AN INVESTIGATION OF TURBULENCE AND DIFFUSION WITHIN VEHICLE WAKES AND ON–ROAD MEASUREMENTS USING AN INSTRUMENTED MOBILE CAR AND A STATIONARY ROADSIDE MONITORING SYSTEM

STEFAN J. MILLER

A DISSERTATION SUBMITTED TO THE FACULTY OF GRADUATE STUDIES IN PARTIAL FULFILLMENT OF THE REQUIREMENTS FOR THE DEGREE OF

DOCTOR OF PHILOSOPHY

GRADUATE PROGRAM IN EARTH & SPACE SCIENCE
LASSONDE SCHOOL OF ENGINEERING
YORK UNIVERSITY
TORONTO, ONTARIO

AUGUST 2022

ABSTRACT

Moving motor vehicles emit pollutants that negatively impact human health. Stationary roadside measurements alone are not sufficient to quantify the pollutant–flow interactions that occur behind moving vehicles. The instrumented mobile car however is well–suited for on–road measurements, but has been underutilized for this purpose since limited studies have investigated its accuracy at high vehicle speeds. Thus, this work details two on–road measurement campaigns using an instrumented car, with three main objectives: (1) study the vehicle momentum wake and vehicle–induced turbulence (VIT), (2) investigate the accuracy of the mobile system for measuring atmospheric means, variances and covariances, and (3) quantify the emission of aerosols and CO_2 by on–road vehicles and their subsequent diffusion. Measurements behind on–road vehicles demonstrate that VIT decays with increasing distance following a power law relationship. Comparison of measurements with prior on–road studies suggests a height dependence of VIT in vehicle wakes, and an extended parameterization is outlined that describes the total on–road turbulent kinetic energy (TKE) enhancement due to a composition of vehicles, including a vertical dependence on the magnitude of TKE. Next, a wavelet–based approach to remove the effects of sporadic passing traffic is developed and applied to a measurement period during which a heavy–duty truck passes in the opposite highway lane; removing the times with traffic in this measurement period gives a 10% reduction in the TKE. When sampling uncertainties are considered, the vertical momentum flux measured on the car is found to be not different from roadside measurements in the 95% confidence interval. The first on–road and in–traffic measurements of the vertical turbulent particle number flux and the vertical turbulent CO_2 flux are presented and the results suggest this technique could be further developed to measure individual vehicle emission rates while driving. The lateral width of the wake generated by each passing vehicle is estimated using the stationary roadside measurements, and is determined to be a factor of 5 times greater for heavy–duty trucks relative to sport utility vehicles and passenger cars at a distance of 150 m behind the vehicle.

ACKNOWLEDGMENTS

Firstly, I would like to deeply thank my supervisor, Professor Mark Gordon. Without his support, insight, patience, and guidance, it would not have been possible to complete the field experiments detailed in the following chapters or get my research ready for journal publication. Thank you for the career opportunities you have helped me achieve, and all the time spent helping me improve my written communication. I really cannot thank you enough!

Second, I would like to thank Professor Peter Taylor for his support with my research, even before becoming a graduate student at York University. Thank you for lending your vehicle and assisting with data acquisition, and the great conversations over the past many years.

Thank you to Ralf Stabler and Mike Wheeler of Environment and Climate Change Canada for your useful suggestions and providing the instruments and equipment necessary to complete my research.

Thank you to my committee member, Professor Robert McLaren for your useful feedback over the past few years.

I would like to give my sincere thanks to Sepehr Fathi and Zheng Qi Wang for assisting with the measurement acquisition (as drivers in the 2016 experiment), and for being great friends over the past many years. Also, thank you Brandon Loy for assisting during the assembly process of the mobile laboratory, and lending your drill press.

Table of Contents

List of figures

List of tables

CHAPTER 1

1. Introduction

Moving motor vehicles directly emit pollutants in the gas and particle phase, in addition to greenhouse gases such as CO_2. Particulate phase pollutants result from incomplete fuel combustion, and unburned fuel and lubricating oil, and may consist of long chain (C20 to C32) alkanes (Harrison et al. 2018), polycyclic aromatic hydrocarbons (PAH) and phenols (Perrone et al. 2014; Lu et al, 2019), for example. Except for small particles < 30 nm, hydrocarbons and organic compounds are typically present in the form of adsorbed and condensed material, coating carbonaceous aggregates (Maricq, 2007). Diesel exhaust is known to cause pulmonary inflammation, genotoxicity, and oxidative stress in humans, with its toxicity dependant on the total surface area of the particles inhaled and the particles' total organic and metallic fraction (Ristovski et al. 2011 and references therein).

The diffusion and advection of these emitted particles and gases is complicated, since immediately after their release, they are impacted by complex flow structures induced by the moving vehicle. Theory to describe the momentum far–wake of a block–shaped vehicle during weak ambient flow ($\bar{u}$ < 1 m s^{-1}) is outlined by Eskridge and Thompson (1982). The far–wake is typically defined as $x > 10h$ downwind (Baker, 2001), where h is the height of the vehicle and x is the physical distance downwind of the vehicle's backend. Vehicle wake theory predicts that turbulent kinetic energy,

$$e \propto Q^2 \left(\frac{x}{h}\right)^{-1.2} F(\chi, \omega), \tag{1.1}$$

where Q is the vehicle relative wind speed and $F(\chi, \omega)$ is a structure function, which in Eskridge and Thompson (1982), is determined by a polynomial fit to wind tunnel measurements. ω and χ are non–dimensional vertical and lateral distances, respectively. Thus, vehicle wake theory predicts a power law decay of e with increasing non–dimensional distance, as $(x/h)^{-1.2}$.

The theory developed by Eskridge and Thompson (1982) was later incorporated into the highway air pollution model 'ROADWAY', to account for the impact of momentum wakes generated by moving traffic on pollutant diffusion (Rao et al. 1986). The interest in understanding the interactions between emitted pollutants and the vehicle wake has only continued to grow since the work of Eskridge and Thompson (1982). Wang and Zhang (2012) used a coupled turbulence and aerosol dynamics model to investigate how the vehicle wake interacts with emitted aerosols within a diesel plume, and affects particle development, growth, and diffusion. Their results show that vehicle–induced turbulence (VIT) has the effect of quickly diffusing the emitted plume near the tailpipe, and so particle nucleation occurs very close

to the tailpipe and the total particle number drops off rapidly, within a few meters of the vehicle's backend, in the near–wake region. The near wake is often defined as the region at $x/h < 10$ (Baker, 2001). Especially for block–shaped vehicles, the near–wake is characterized by a recirculation region (i.e., reversed flow) and intense shear layers that emerge from each wall of the trailer, extending downwind (McArthur 2016; Lo and Kontis, 2017). Numerical modelling has shown that the recirculation region can trap aerosols, leading to elevated concentrations in the near wake region (Wang and Zhang 2012).

Despite increasing modelling research, in–situ and on–road studies investigating VIT and how VIT interacts with emitted aerosols and gases are limited. Rao et al. (2002) investigated VIT directly behind an isolated full–sized van of height 2.1 m, but only for $x/h < 2.32$. More recently, Gordon et al. (2012) described the first measurements of VIT made by chasing different vehicles on highways, in real–world traffic conditions. Their investigation used a large van that was outfitted with two three–dimensional sonic anemometers (held at a height of 3 m), a video recording system, and a GPS system, referred to as a "mobile laboratory". Despite in–situ studies that report VIT, there has not yet been an on–road experiment aimed at measuring turbulent fluxes of emitted pollutants, probably because there is limited literature surrounding the accuracy of an instrumented mobile measurement system for variance and covariance measurement at high vehicle speeds. The first study to examine the accuracy of an instrumented car equipped with a sonic anemometer was completed by Belušic et al. (2014). Their results demonstrated the practicality of measuring atmospheric means, variances and covariances from an instrumented car, but not without difficulties imposed by flow non–stationarity, which can result in anomalously large car–measured velocity variances.

The research presented in Chapters 2 through 4 surrounds the use of an instrumented car that was equipped with a sonic anemometer, CO_2/H_2O gas analyzer, optical scattering particle sizer and video recording/GPS system, for mobile on–road measurement. Measurements were obtained during two different campaigns, in 2016 and 2019. The instrumented car setup and instrumentation used in 2016 and 2019 are detailed in Chapter 2 and 4, respectively. The on–road measurements were collected to investigate vehicle wakes and their interaction with emitted aerosols and trace gases, and to evaluate the low–cost system for measuring atmospheric means, variances and covariances, when the goal is not to measure on–road traffic but rather the ambient environment. Chapter 2 investigates the spatial variation of VIT measured behind on–road vehicles and, by comparing to previous on–road studies, what impact measurement height has on the measured VIT. Chapter 3 examines the accuracy of the instrumented car for measurements made in low–traffic situations, but where impacts from other traffic (i.e., VIT) and roadside structures are still present. And Chapter 4 studies the interaction of VIT with aerosols and trace gases emitted by heavy–duty diesel vehicles. Chapter 4 also investigates the size characterization of diesel exhaust nanoparticles (60 to 1000 nm), and the feasibility of measuring on–road turbulent fluxes of aerosols and CO_2 gas emitted from

heavy–duty vehicles, while travelling at highway speeds of 100 km h^{-1}. The final study outlined in Chapter 5 switches to a stationary perspective – specifically, Chapter 5 presents high–frequency measurements made by a stationary tripod placed at the side of a highway. The tripod–mounted instrumentation measured isolated vehicles traveling at high speeds near 80 km h^{-1}, providing a unique opportunity to explore the flow and turbulence generated by vehicle wakes in near–isolation. The study described in Chapter 5 uses high–frequency velocity measurements to estimate the lateral spread of vehicle wakes generated by heavy–duty trucks and passenger vehicles, and considers the viability of near–highway wind energy generation.

1.1 Publication status and author contributions

Chapter 2 is published in Boundary Layer Meteorology (Miller et al. 2019). Chapter 3 has been submitted to Atmospheric Measurement Techniques and is currently under review in status 'final response' (Miller and Gordon, 2022). Chapter 4 and Chapter 5 have not yet been submitted to a journal.

Peter Taylor provided useful suggestions, proof–reading, and minor text editing during the preparation of Chapter 2 and 3 for journal submission. In addition, Peter Taylor provided the sport utility vehicle that served as the instrumented car used in this work and was a driver during the 2019 measurement campaign. Ralf Stabler provided useful suggestions and proof–reading during preparation of Chapter 2. In addition, Ralf Stabler provided the CO_2/H_2O gas analyzer used in Chapter 4. Mike Wheeler provided the flow controller, pump, and some fittings necessary to perform on–highway aerosol sampling and provided useful suggestions on the measurement setup used in Chapter 4. Mark Gordon provided proof-reading, minor editorial adjustments, helpful suggestions/feedback and assisted with performing and designing both field experiments. I completed all data analysis and all writing.

CHAPTER 2: A study of the spatial variation of vehicle–induced turbulence on highways using measurements from a mobile platform

Stefan J. Miller[1], Mark Gordon[1], Ralf M. Staebler[2], Peter A. Taylor[1]

[1]Department of Earth & Space Science & Engineering, York University, 4700 Keele Street, Toronto, ON M3J 1P3, Canada

[2]Air Quality Processes Research Section, Air Quality Research Division, Atmospheric Science and Technology Directorate, Science and Technology Branch, Environment and Climate Change Canada, 4905 Dufferin Street, Toronto, ON M3H 5T4, Canada

Publication status: Published as Miller et al. (2019) in Boundary Layer Meteorology

Abstract

During July 2016, an on–road study was conducted in and around the Toronto, Canada region to investigate the spatial variation of vehicle–induced turbulence on highways. The power spectral density of turbulent kinetic energy (TKE) while following on–road vehicles is significantly enhanced for frequencies greater than 0.5 Hz. This increase is not present while driving isolated from traffic, demonstrating that TKE is enhanced considerably on highways in the presence of vehicles. The magnitude of normalized TKE is found to decay following a power–law relationship with increasing normalized distance behind on–road vehicles, which is most pronounced behind heavy–duty trucks. The results suggest that the TKE in the vehicle wake is maximized in the upper shear layer near the vehicle top. An extended parametrization is outlined that describes the total on–road TKE enhancement due to a composition of vehicles, which includes a vertical dependence on the magnitude of TKE.

2.1 Introduction

Motor vehicles are a ubiquitous feature of the modern world, and their combustion engines generate air pollution, such as nitrogen oxides (NO_x) and particulate matter, that has been shown to cause cardiovascular and respiratory disease in humans (Hoek et al. 2013). Once emitted from the tailpipe, the pollutants disperse to the surrounding environment where their human impacts are felt. The turbulence generated by on–road vehicles, referred to hereafter as vehicle–induced turbulence, is a major factor that affects pollutant dispersion and transport processes on highways. Therefore, to accurately predict pollutant concentrations near highways, vehicle–induced turbulence should be correctly parametrized in numerical prediction models such as A Unified Regional Air–quality Modelling System (Makar et al. 2010).

A moving vehicle on a highway generates a momentum wake that trails behind the rear of the vehicle. The initial analytic theory that describes the vehicle momentum wake can be found in Eskridge and Hunt (1979), who demonstrated that in the wake of a moving vehicle, the normalized turbulent kinetic energy (TKE) decays with downwind distance following a power–law relationship. This initial analytic theory was later modified by Eskridge and Thompson (1982) based on wind–tunnel measurements of two block–shaped, model vehicles (1:8 and 1:32 scale models). From their measurements, they estimated the vertical profile of the longitudinal turbulent velocity variance ($\overline{u'^2}$) at several non–dimensional downwind distances demonstrating that TKE varies not only horizontally, but also vertically within vehicle wakes.

Since the work of Eskridge and Thompson (1982), additional wind–tunnel studies have examined flow properties in vehicle wakes (Kastner–Klein et al. 2000; Baker 2001; Carpentieri et al. 2012; McArthur et al. 2016; Lo and Kontis 2017) and an increasing number of studies have been conducted numerically (Bäumer et al. 2005; Lee and Choi 2009; Wang and Zhang 2009, Wang and Zhang 2012; Wang et al. 2011; Huang et al. 2014; Bhautmage and Gokhale 2016; Kim et al. 2016; Sterken et al. 2016). The measurement domains of selected studies relevant to the current investigation are given in Table 2.1; each measured distance (horizontally downwind, x_m and vertically upward, z_m) is normalized by an approximate vehicle height (h), giving a normalized distance behind the vehicle, and a normalized height above the ground. These studies provide invaluable insight into the flow structure in the vicinity of on–road vehicles and demonstrate the high spatial variability of vehicle–induced turbulence, both horizontally and vertically, which has yet to be fully resolved from in situ measurements. Figure 2.1 displays qualitatively the flow regions in the x–z plane behind a high–speed, block–shaped tractor–trailer based on past wind–tunnel and modelling studies (Wang and Zhang 2012; Lo and Kontis 2017).

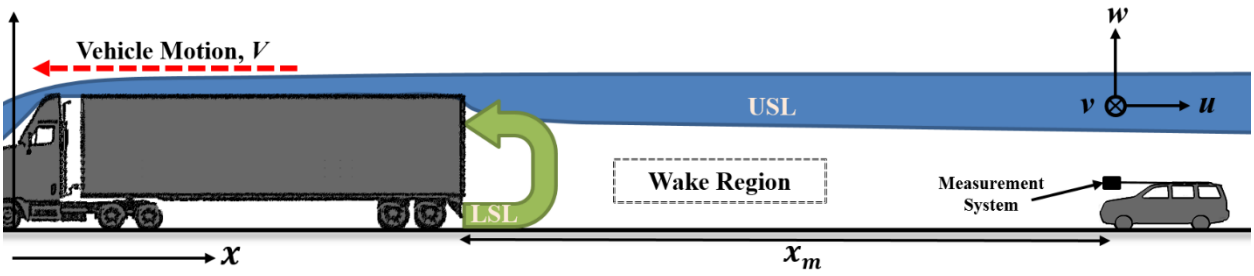

Figure 2.1: A qualitative schematic (not to scale) of a tractor–trailer travelling on a high–speed freeway (i.e., vehicle speed, $V > 15$ m s^{-1}) being followed by a passenger vehicle. Shown are the time–averaged locations of the upper shear layer (USL), the lower shear layer (LSL), and the wake region. Here x_m is the following distance and u, v, and w are the measured (unrotated) longitudinal, lateral, and vertical measured velocity components respectively (see Sect. 2.3.1). The circle with an "x" represents a positive v–component into the page. Adapted from Wang and Zhang (2012) and Lo and Kontis (2017)

Lo and Kontis (2017) performed a wind–tunnel experiment aimed at visualizing the flow field of a model tractor–trailer (1:20 scale model) for $x_m \leq 1.5h$. They demonstrate that flow separation occurs at the rear–end roof of the tractor–trailer, with a large energetic upper shear layer extending downwind. A less energetic lower shear layer is shown to originate from the gap between the ground and trailer underbody (see Fig. 2.1), which forms a vortex as it moves downwind. Two additional shear layers also develop along each side of the tractor–trailer, but these are not shown in Fig. 2.1. Lo and Kontis (2017) reveal that the most intense turbulence is found in the upper shear layer, while the wake region below it has only moderate levels of turbulence. Similar results regarding the magnitude of turbulence in the upper shear layer are presented in Lee and Choi (2009) and graphically in Wang and Zhang (2012). Wang and Zhang (2012) modelled the TKE behind a block–shaped van of $h = 2.1$ m using an environmental turbulent–reacting flow model. For a vehicle speed (V) of approximately 22 m s^{-1} they demonstrate the existence of an elevated region of enhanced turbulence near the vehicle height, presumably due to the upper shear layer that trails behind the vehicle to at least $x_m = 8h$. They also show that the TKE decreases rapidly above $z_m = 0.87h$, with an approximate decrease of 70% to 90% in the measured TKE from $z_m = 0.87h$ to $z_m = 1.29h$.

Baker (2001) separated the momentum wake of ground vehicles into two regions (a) the near–wake, and (b) the far–wake, based on wind–tunnel results of the wake structure behind a tractor–trailer and high–speed train at different non–dimensional times. Baker (2001) then defines the near–wake for these vehicles as the region up to ten vehicle heights behind the vehicle ($x_m < 10h$); beyond $10h$ is defined as the far–wake. These definitions are adopted herein. Bhautmage and Gokhale (2016) used a computational fluid dynamics model to simulate the TKE behind a commercial bus with $h = 3$ m in a highway road tunnel with $V \approx 28$ m s^{-1}. They present the vertical profile of TKE behind the bus at $x_m = 0.33h$ ($x_m = 1$ m) to represent the near–wake and at $x_m = 10h$ to represent the far–wake, following Baker (2001). In the near wake at $x_m = 0.33h$ the TKE maximizes slightly above $z_m = h$, while below $z_m = h$ the TKE decreases before

maximizing again close to the ground. In the far–wake at $x_m = 10h$ however, the TKE is found to maximize lower at $z_m \approx 0.4h$, while the secondary maximum near the ground disappears.

Field studies that examine vehicle–induced turbulence have been primarily carried out using roadside towers (Chock 1980; Rao et al. 1979; Kalthoff et al. 2005; Alonso–Estébanez et al. 2012). Only two known studies have obtained in situ measurements from within–vehicle wakes. Rao et al. (2002) and Hosker et al. (2003) detail the first such measurements made on an isolated airport runway in Rockwood, Tennessee. Since the airport runway was isolated, interference from other vehicle wakes was not a factor. The measurements were completed by placing an array of sonic anemometers secured to adjustable pipe scaffolding on an open trailer. The array consisted of three sonic anemometers placed laterally – one at the centreline, and two others located ± 0.91 m from the centreline – at two different measurement heights. The sonic anemometers collected data at a sampling frequency (f_s) of 10 Hz. The trailer was then towed behind a full–sized van of $h = 2.1$ m, and measurements were obtained behind the rear of the vehicle, at x_m between $0.29h$ and $2.32h$, and at z_m between $0.86h$ and $1.74h$ (summarized in Table 2.1).

More recently, Gordon et al. (2012) measured vehicle–induced turbulence during the summer on highways in the Toronto, Canada area using a mobile laboratory equipped with two sonic anemometers, a dashcam and a GPS system. The two sonic anemometers sampled at $f_s = 20$ Hz and were mounted to a metal frame at a measurement height of $z_m = 3$ m (level with the vehicle's roof, above the front bumper). To perform data analysis, they classified the on–road vehicles into three categories: (1) heavy–duty trucks (either 10 or 18 wheeled), (2) mid sized vehicles and (3) passenger cars. They developed a parametrization based on their in–situ measurements to model the on–road TKE enhancement resulting from these three vehicle classes, assuming that TKE does not vary with height within vehicle wakes. Using output from the Global Environmental Multiscale model in tandem with their parametrization they found that vehicle–induced turbulence increased the vertical diffusion coefficient over highways by more than 80% in the early morning.

We here continue the investigation of Gordon et al. (2012) by exploring the magnitude of TKE within vehicle wakes as a function of height and extend the parametrization describing on–road TKE enhancement to include a height dependence. For a typical heavy–duty truck ($h = 4.1$ m) we made measurements at $z_m = 0.4h$ while Gordon et al. (2012) measured at $z_m = 0.7h$. Since $z_m = 0.7h$ is located closer to the upper shear layer, it is expected to feature a larger magnitude of TKE than measurements made at $z_m = 0.4h$, for the same following distance in the near wake. Behind mid sized vehicles, however, the Gordon et al. (2012) measurements were made above the wake zone at $z_m = 1.5h$ and are expected to have a significantly lower value of TKE than our measurements made within the wake zone and the measurements obtained by Rao et al. (2002). We will give an overview of the study, outlining the experimental setup and reviewing the methodology used. In situ measurements obtained at a measurement

height of 1.7 m are then presented, beginning with power spectral densities of TKE for various near–highway and in–traffic scenarios. We explore the decay rate of TKE as a function of normalized distance behind different vehicle classes and compare our results to past on–road studies to demonstrate the vertical variation of TKE within vehicle wakes. We conclude by extending the parametrization of on–road TKE enhancement, originally developed by Gordon et al. (2012), to include a height dependence on the magnitude of the TKE.

Table 2.1: A summarized list of selected studies related to ground vehicle wakes. Indicated are the study type, vehicle type(s) studied and their height(s), h. The normalized horizontal measurement domain (x_m) behind the rear of the vehicle (i.e., horizontally parallel to the vehicle motion) and normalized vertical measurement domain (z_m) of each study are given. Two types of heavy–duty trucks are detailed (see Sect. 2.2.6): heavy–duty trucks class A (HD–A) and heavy–duty trucks class B (HD–B).

Study	Study Type	Vehicle Type and Height, h	Normalized Distance Behind Vehicle, x_m	Normalized Vertical Domain, z_m
Gordon et al. (2012) *	In situ	1) HD–B truck, h = 4.1 m 2) Mid size, h = 2 m 3) Car, h = 1.4 m	$2.5h \leq x_m \leq 24.4h$	$z_m = 0.73h$
Hosker et al. (2003) & Rao et al. (2002)	In situ	Mid size, h = 2.1 m	$0.29h \leq x_m \leq 2.32h$	$0.86h \leq z_m \leq 1.74h$
This study*	In situ	1) HD–A truck, h = 3 m 2) HD–B truck, h = 4.1 m 3) Mid size, h = 2 m 4) Car, h = 1.4 m	$2.5h \leq x_m \leq 24.4h$	$z_m = 0.41h$
Bhautmage and Gokhale (2016)*	Numerical model	1) HD–A truck, h = 3 m 2) Mid size, h = 2 m	$x_m = 0.33h$, $x_m = 10h$	$0 \leq z_m \leq 1.67h$
Wang and Zheng (2012)	Numerical model	Mid size, h = 2.1 m	$0 \leq x_m \leq 10h$	$0 \leq z_m \leq 4.75h$
Eskridge and Thompson (1982)	Wind tunnel	Mid size, 1:32 scale model, h = 0.043 m	$10h \leq x_m \leq 60h$	$0 \leq z_m \leq 3h$
Lo and Kontis (2017)	Wind tunnel	HD–B truck, 1:20 scale model, h = 0.196 m	$0 \leq x_m \leq 1.5h$	$0 \leq z_m \leq 1.5h$

***The measurement domains listed in the final two columns of this table have been determined by using an HD–B truck of h = 4.1 m to scale physical distances, or in the case of Bhautmage and Gokhale (2012) using h = 3 m.**

2.2 Study overview and experimental setup

2.2.1 Study domain

The on–road study was conducted between 6 July and 15 July 2016 in Toronto and the surrounding area. The measurements used in the analysis were obtained on Highway 400 between Toronto and Craighurst, on Highway 401 between York University and Toronto Pearson International Airport, on Jane Street, which runs parallel to Highway 400 (1 km east) and on various side roads in the area. Measurements were also made between 12 and 15 July 2016 while the mobile laboratory was stationary near Highway 400. The locations where measurements were obtained are shown on the map in Fig. 2.2. A total of six hours of highway measurements were made over six days of highway driving. Highway 400 and Highway 401 are bi–directional multi–lane freeways (with six or more lanes) of speed limit 100 km h^{-1} (28 m s^{-1}), split by an embankment at the highway centre. Jane Street is a bi–directional side road of speed limit 80 km h^{-1} (22 m s^{-1}) with a maximum of four lanes, and without a centre embankment. The terrain is generally flat and agricultural, but areas of trees are present, primarily located along the roadsides of Highway 400 and Jane Street.

2.2.2 Traffic conditions

Figure 2.2 shows the 2016 annual average daily traffic (AADT) for highways in the study domain (MTO 2016). The AADT ranges from about 18,000 in the most northern part of the study domain (near Craighurst), to more than 150,000 in the most urban regions inside the City of Toronto. Despite the large AADT values shown, the on–road measurements presented herein were generally obtained without much surrounding traffic. It has been demonstrated using computational fluid dynamics modelling that a vehicle travelling in a neighbouring highway lane has little effect on the TKE measured in the target lane (except perhaps under extreme crosswinds, see Sect. 2.2.3) since the vehicle wake has a limited lateral spread (Kim et al. 2016). Despite this, we exclude any periods where a heavy–duty truck was in a neighbouring lane, except for the analysis presented in Sect. 2.4.1. The length of continuous measurements required in Sect. 2.4.1 precluded removing periods while a heavy–duty truck was passing in a neighbouring lane. In general, measurements made while a mid sized vehicle or passenger car was in a neighbouring lane are not excluded.

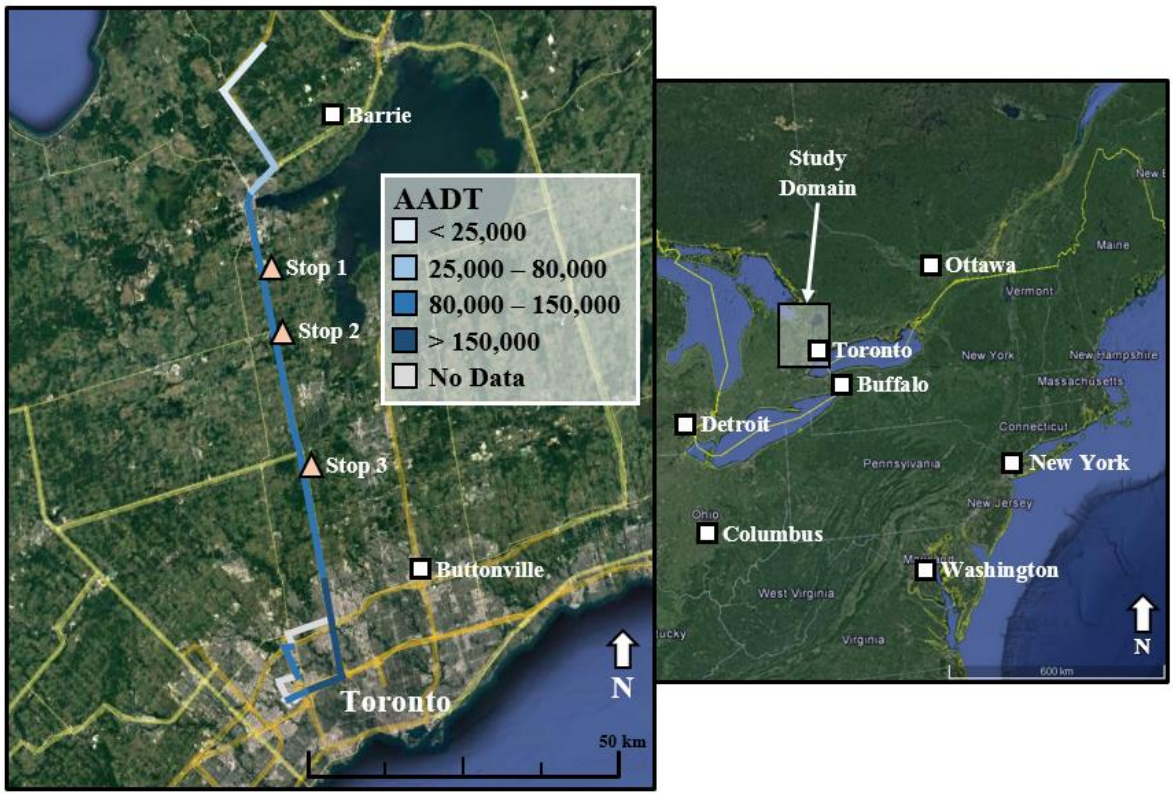

Figure 2.2: The locations where measurements were obtained are shown as different shades of blue or grey (see legend) in the left map. These colours represent the annual average daily traffic (AADT) for 2016. Also shown are the Environment and Climate Change Canada (ECCC) weather stations (squares) and the stationary locations (triangles) where measurements were made during this study. © Google Earth Images.

2.2.3 Meteorology

During the study sky conditions varied from full sun to mostly cloudy, with one day (14 July) featuring overcast skies for the entire drive. The final portion of the drive that was completed on 7 July was towards a thunderstorm located over the City of Toronto, although no measurements were made during precipitation. Table 2.2 summarizes the local meteorological conditions during each day's entire drive. The 10–m wind speed (u_{10}) and 10–m wind direction (γ_{10}) presented are from the Environment and Climate Change Canada (ECCC) Buttonville Airport weather station (BU) and ECCC Barrie–Orillia weather station (BA). These two weather stations are located at opposite ends of the study domain and are displayed in Fig. 2.2 as white squares. The values of u_{10} and γ_{10} in Table 2.2 are the mean values of the entire drive, calculated from hourly measurements. From these data the atmospheric stability is then estimated according to a modified Pasquill stability classification (Mohan and Siddiqui, 1998), using irradiance values obtained from the CNR1 radiometer (Campbell Scientific) at the York University weather station (EMOS, 2016). The stability classifications are A: extremely unstable, B: moderately unstable, C: slightly unstable and D: neutral.

Table 2.2 The meteorology during each drive. Shown in the table are the date and local time of each drive and the prevailing weather conditions. The 10–m wind speed (u_{10}) and 10–m wind direction (γ_{10}) shown are the Environment and Climate Change Canada (ECCC) Buttonville weather station (BU) and ECCC Barrie–Orillia weather station (BA). The final column is a stability classification based on a modified Pasquill stability class.

Day	Time period (local time)	Weather conditions	u_{10} (m s^{-1})		γ_{10} (° true)		Atmospheric stability
			BU	BA	BU	BA	
06 July	13:00 – 14:00	Partly cloudy	5.0	3.8	200	135	Unstable, B–C
07 July	12:00 – 14:00	Partly cloudy, thunderstorm	2.7	3.2	50	345	Unstable, A–B
11 July	11:00 – 13:00	Mainly cloudy	4.8	2.7	110	145	Unstable, B
12 July	10:00 – 13:00	Partly cloudy	4.8	4.3	150	155	Unstable, B
14 July	10:00 – 12:00	Overcast	4.7	3.8	235	245	Unstable, C
15 July	10:00 – 12:00	Mainly sunny	5.8	6.9	255	295	Unstable, C

A wind direction of approximately 170° or 350° runs parallel to the majority of Highway 400 so that a wind direction of 080° or 260° is perpendicular to it. On 14 and 15 July, the wind direction was within ± 30° of being perpendicular to the highway, suggesting the possibility of crosswinds. The mean wind speed at our measurement height (see Appendix B), coupled with the vehicle speed, indicates that crosswinds would not be significant until the followed vehicle (or a vehicle in a neighbouring lane) is at a following distance exceeding 30 m. The measurements for following distances less than 100 m on these two days are not considerably different than the measurements made on 7, 11 and 12 July when the wind direction was closely parallel to the highway, suggesting crosswinds do not significantly affect the measurement of TKE in this study. Therefore, measurements made on 14 and 15 July (about 20% of the data shown in Sect. 2.5.1) are included in our analysis.

2.2.4 Experimental setup

Measurements were made from a mobile laboratory with instrument–mounting hardware constructed at York University. Instrumentation was mounted to a roof rack and then secured to a sport–utility vehicle. The mobile laboratory was equipped with a sonic anemometer (model type A from Applied Technologies, Inc.) placed at the vehicle centreline at a height of 1.7 m; the sonic anemometer made measurements of the three orthogonal velocity components (u, v, w) and the sonic temperature. The boom arm included an enclosed accelerometer to measure the three components of acceleration (a_x, a_y, a_z). All data obtained from the sonic anemometer were digitally recorded at f_s= 40 Hz, with the sonic anemometer internally sampling at 200 Hz and constructing 0.025–s non–overlapping block averages to provide the desired 40 Hz signal. The position and speed (V) of the mobile laboratory (based on GPS information) were recorded at 1 Hz using a dashcam (model Thinkware F750) installed behind the windshield. The dashcam also captured the forward scene in mp4 video format, which was used to classify target vehicles and estimate the following

distance. Additional instrumentation included an open–path H_2O/CO_2 analyzer (LI–COR Inc, LI–7500) and an ultra–high sensitivity aerosol spectrometer (Droplet Measurement Technology). The data acquired by the UHSAS and gas analyzer are presented and discussed in Chapter 4. Figure 2.3 shows the mobile laboratory with the instrument positions.

Figure 2.3: The mobile laboratory developed at York University. Shown are the location of the sonic anemometer, the LI–COR gas analyzer and the dashcam. Physical measurements are superimposed.

2.2.5 Following distance

The following distance is defined as the distance between the measurement location and the back end of the target vehicle, in the same highway lane (see Fig. 2.1) and was estimated using the video recorded from the Thinkware dashcam. A single greyscale image was extracted from each second of video (the dashcam records at 30 frames s^{-1}). The location of the target vehicle was then estimated from its ground projected shadow, which manifests as a step change in greyscale values between the sunlit highway surface and the shadow behind the vehicle. Automated software was developed to determine the location of this step change

for each image frame, with all output results manually verified to reject erroneous values resulting from non–vehicle shadows (e.g., from trees) or abnormalities in the highway surface. Any gaps due to erroneous data were replaced by linear interpolation before being used in the analysis. Once a pixel location representing the following distance was identified, it was converted to a physical distance using the method outlined in the supplementary material of Gordon et al. (2012). A full derivation of the method is provided in Appendix A.

2.2.6 Vehicle classification

During the investigation many different vehicle types were followed for varying amounts of time. Four categories are used to classify the vehicle types: (a) passenger cars, (b) mid sized vehicles, (c) heavy–duty trucks class A (HD–A) and (d) heavy–duty trucks class B (HD–B), with approximate vehicle heights of h = 1.4, 2, 3 and 4.1 m respectively. These heights are chosen such that they correspond with the on–road study of Gordon et al. (2012) to allow for comparison. An additional class, HD–A, was added here to represent heavy–duty trucks that have heights near 3 m. This class consists mainly of block–shaped geometry, but dump trucks that are not block–shaped are also included. It should be noted that the mid sized vehicles class comprises of vans, flatbed pickup trucks and sport–utility vehicles. The slant geometry of individual vehicles was not investigated.

2.3 Measurement of TKE

2.3.1 Corrections

Flow distortion modified the streamlines around the mobile laboratory, altering the velocity measurements made by the sonic anemometer. To quantify the effects of flow distortion, short periods of driving are examined (referred to as runs), with each run consisting of two parts: part A was performed in the forward direction toward a point and part B was performed in the opposite direction away from that point. If stationarity of the wind speed and direction is assumed during each run that consists of two parts (A and B) performed in opposite directions at the same vehicle speed, then the average longitudinal velocity component (u) measured by the sonic anemometer should be equal to the vehicle speed (V). Likewise, the average lateral (v) and vertical (w) velocity components calculated from these two passes should be equal to zero, assuming there is zero contribution from sensor misalignment or flow distortion (Belušic et al. 2014) and that the mean vertical wind velocity is zero. To calculate the average velocity component at a specific value of V during a run, binning is applied separately to each part of the run (A and B), and each velocity component is binned according to V using a bin size of 1 m s^{-1}. Two separate runs were completed on side roads (Runs 1 and 2), and one run was completed on Highway 400 (Run 3). While it was not possible to remain completely isolated for the entirety of Run 3, any vehicles (either mid sized or passenger car)

were located far ahead of the mobile laboratory. Run 3 represented the most isolated period of driving on Highway 400. Runs 1 and 2 were completed on the way to and from stationary measurement locations and therefore a period of up to 17 min elapsed between each part of the run. Runs 1 and 2 both featured isolated driving conditions, except for an occasional passing vehicle travelling in the opposite direction.

The results from Runs 1 to 3 (and the highway drive from each day as a whole) demonstrate that v and w increase approximately linearly with increasing vehicle speed. To correct for sensor misalignment and flow distortion, the entire drive is rotated first by angle θ about the y–axis (R_y), followed by a second rotation by angle φ about the z–axis (R_z), giving $\overline{w}_r = 0$ and $\overline{v_r} = 0$ for all vehicle speeds respectively. A subscript r denotes a final rotated quantity. The rotations (see Fig. 2.4) are respectively, following Wilczak et al. (2001),

$$\begin{bmatrix} u_1 \\ v_1 \\ w_1 \end{bmatrix} = \begin{bmatrix} \cos\theta & 0 & \sin\theta \\ 0 & 1 & 0 \\ -\sin\theta & 0 & \cos\theta \end{bmatrix} \begin{bmatrix} u \\ v \\ w \end{bmatrix}, \tag{2.1}$$

and

$$\begin{bmatrix} u_r \\ v_r \\ w_r \end{bmatrix} = \begin{bmatrix} \cos\varphi & -\sin\varphi & 0 \\ \sin\varphi & \cos\varphi & 0 \\ 0 & 0 & 1 \end{bmatrix} \begin{bmatrix} u_1 \\ v_1 \\ w_1 \end{bmatrix}, \tag{2.2}$$

where a positive rotation angle is defined as a clockwise rotation when looking toward the origin from the positive rotation axis.

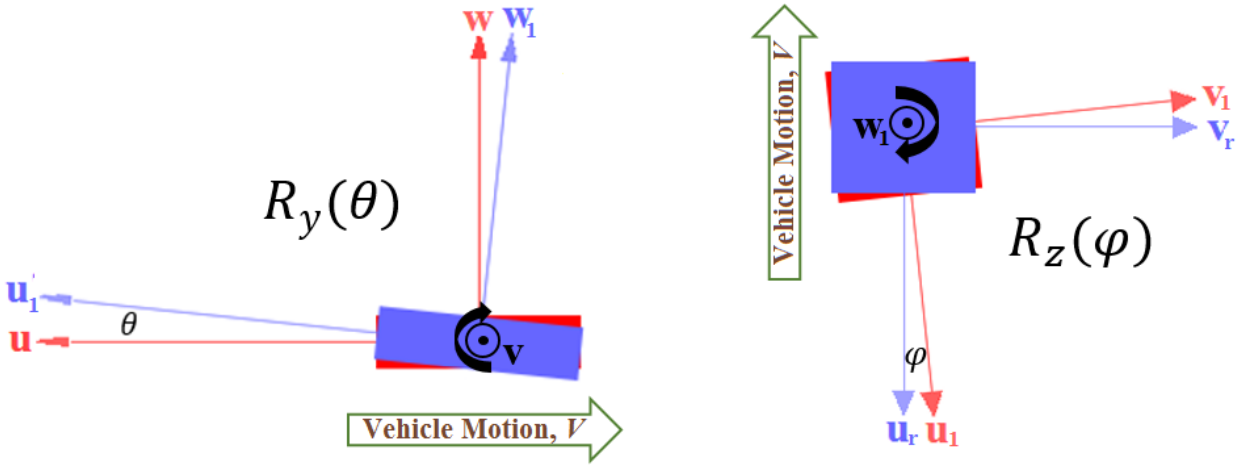

Figure 2.4: The rotation conventions used in this paper. A circle with a dot represents a positive wind component out of the page, toward the reader.

During Runs 1 and 2 there was little variation in the calculated y–axis rotation angle, θ, which is found to be near 6.0°, except for Run 3 when it is near 5.5°. The z–axis rotation angle, φ, is near 1.5° during Runs 1 and 2, but increased to 2.4° during Run 3, perhaps suggesting augmented misalignment for higher vehicle speeds. Testing each day's entire highway drive produces values of θ and φ very similar to those obtained during Runs 1 to 3, with small variations likely due to effects of followed vehicles or changing sensor misalignment. An inclinometer within the instrument–housing measured an anemometer misalignment of approximately $\theta = -3°$. This suggests that, if the anemometer was properly aligned, flow distortion would result in a rotation angle, θ, of about 9°. Wang et al. (2013) performed a wind–tunnel experiment (with a freestream velocity of 30 m s^{-1}) on a block model that had a shape very similar to our sampling vehicle (a sport–utility vehicle). They demonstrate graphically that the streamlines take on a tilt of approximately 10° at the location of this study's anemometer, which is similar to our measured value.

Figure 2.5 (a) to (c) displays the binned (with respect to vehicle speed, V) values of the longitudinal velocity component measured by the sonic anemometer (u_r) for Runs 1 through 3 respectively, after application of Eq. 2.1 and Eq. 2.2. Parts A and B of each run are shown as lines with blue squares and red circles respectively while the black triangles are averages of the two–run means. The markers in each panel represent an average value of a specific vehicle–speed bin, while the error bars represent ± 1 standard deviation from the mean for run parts A and B. The dashed grey line gives the expected one–to–one relationship assuming stationarity of the mean wind speed and direction (i.e. $\langle u_r \rangle = V$, where $\langle \ldots \rangle$ represents an average of the averages of parts A and B within the bin). During Runs 1 and 2 we found little difference between $\langle u_r \rangle$ and V in the 1 m s^{-1} bins, while in the higher speed Run 3, the $\langle u_r \rangle$ measurement was low by about 1 m s^{-1}. Mejia et al. (2016) present the modelled flow around a station–wagon with a freestream velocity near 19.5 m s^{-1}. They demonstrate a slight deficit in the longitudinal velocity component near the windshield, potentially extending to the measurement location used herein. Therefore, it is possible that the slight deficit in $\langle u_r \rangle$ found during Run 3 is the result of flow distortion, but it could also be related to other

factors, such as other on–road vehicles and their associated wake velocity deficits. Given the uncertainty surrounding the cause of this 1 m s^{-1} deficit in $\langle u_r \rangle$ during Run 3, the magnitude of u_r is not modified.

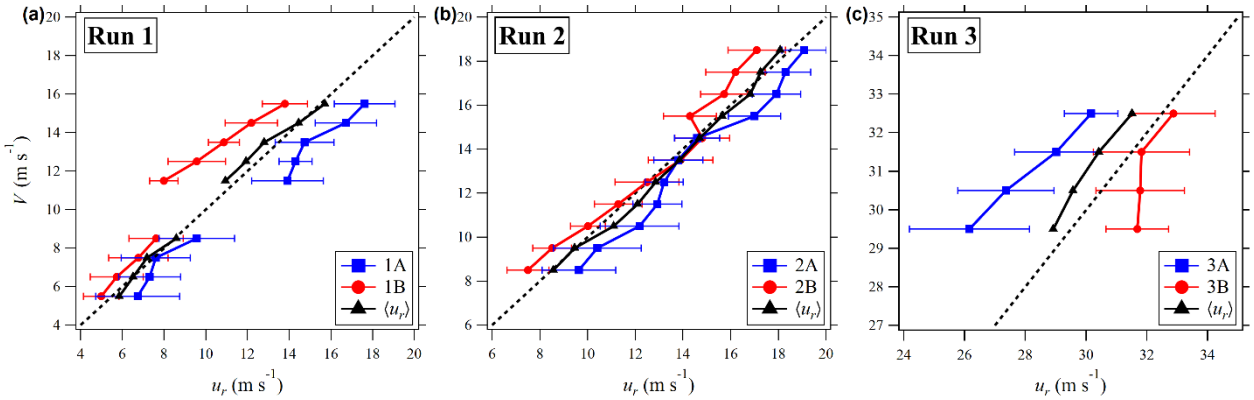

Figure 2.5: The binned (with respect to vehicle speed, V) rotated longitudinal velocity (u_r) of (a) Run 1, (b) Run 2 and (c) Run 3. Part A of the run is shown as a blue line (squares), Part B as a red line (circles) and the average of the averages of parts A and B within the bin, $\langle u_r \rangle$, is shown as a black line (triangles). The error bars represent ± 1 standard deviation. The dashed black line gives the expected one–to–one relationship assuming stationarity of the mean wind speed and direction and no flow distortion (i.e., $\langle u_r \rangle = V$, where $\langle \ldots \rangle$ represents an average of the averages of parts A and B within the bin).

2.3.2 TKE calculation

After correction for the effects of flow distortion, each 1 Hz measurement of vehicle speed is removed from the 40 Hz measurement of the rotated longitudinal wind component as

$$u_s = u_r - V. \tag{2.3}$$

By removing the mobile laboratory's velocity from the sonic anemometer measurement, we obtain the longitudinal velocity component in a frame of reference fixed relative to the ground. Rapid variations in the speed of the mobile laboratory (should they occur) do not therefore contribute to calculated variances used to determine the TKE. The average TKE per unit mass is then calculated as

$$\bar{e} = 0.5\left(\overline{u_s'^2} + \overline{v_r'^2} + \overline{w_r'^2}\right), \tag{2.4}$$

where $\overline{u_s'^2}$, $\overline{v_r'^2}$ and $\overline{w_r'^2}$ are the longitudinal, lateral, and vertical velocity variances respectively (an overbar denotes an average value) calculated for an averaging period (T) of 10 s, which has been adopted from Gordon et al. (2012). A short period of 10 s is chosen for T since highway driving results in a large distance covered in a short time period. The 10–s averaging time is chosen as a balance between homogeneity of

conditions on the highway versus adequate averaging time for statistical significance of the mean values. This choice of averaging time is discussed in Sect. 2.4.1.

A modelling study of the flow around an SUV (using a free stream velocity ≈ 28 m s^{-1}) performed by Sterken et al. (2016) shows that the TKE is not enhanced at the front end of the vehicle, except immediately near the windshield and in the vehicle's undercarriage near the front tires. For the data presented herein while following on–road vehicles, 89% of measurements were made at $V \leq 24$ m $s^{-1} \leq 32$ m s^{-1}, with a mean of $V = 28$ m s^{-1} (less than 3% were made at $V < 20$ m s^{-1}). Considering these results and our own findings, no flow distortion correction was applied to our TKE measurements.

2.4 Results

2.4.1 TKE underestimation

In the calculation of atmospheric wind velocity variances, averaging periods are generally on the order of 30 min (Kaimal and Finnigan, 1994), as opposed to the 10–s period adopted here. Stationary measurements made over a 10–min period with a mean wind speed of 5 m s^{-1} corresponds to a distance of 3000 m, while 10 s of highway driving at $V = 30$ m s^{-1} corresponds to a distance of only 300 m. Therefore, eddies contributing to the TKE at length scales larger than 300 m will be neglected in the 10–s averaging period, causing the TKE to be underestimated. In Gordon et al. (2012), it was estimated that only 66% of the TKE was captured using an averaging period of $T = 10$ s compared to $T = 13$ min. Here, a similar analysis was completed by splitting a 13–min interval while following behind a HD–B truck and an 11–min interval while following behind a commercial bus, with vehicle speeds ranging between 23 m $s^{-1} \leq V \leq 27$ m s^{-1} and 24 m $s^{-1} \leq V \leq 32$ m s^{-1} respectively, into blocks of period T and then calculating the TKE for each block. The resulting blocks were then averaged over the entire interval, giving a TKE value for that specific T. By incrementing through T, starting at $T = 5$ s and ending at $T = 13$ min (or $T = 11$ min for the bus), the TKE as a function of T was estimated. The results are displayed in Fig. 2.6, where it is estimated that between 84 and 85% of the TKE is captured at $T = 10$ s compared to $T = 11$ min or $T = 13$ min. The difference between these two studies may be related to the sampling frequency, which is 40 Hz herein compared to 20 Hz in Gordon et al. (2012), or related to following distance, which had a greater variance in this study for both the HD–B truck and commercial bus. The following distance was generally between $4h \leq x_m \leq 12h$ for the HD–B truck and between $5h \leq x_m \leq 15h$ for the commercial bus, but for a brief period in both cases this increased toward $x_m = 18h$. In Gordon et al. (2012) measurements were obtained closer to the HD–B truck and the range of following distances was slightly smaller, ranging between $2.9h \leq x_m \leq 8.5h$. Given the uncertainty in the underestimation correction, the analysis to follow has been completed without applying an increase to the magnitude of the measured TKE, unless noted. Since the past on–road studies used a similar value of T to calculate the TKE (i.e., 10 s to 1 min), the results are expected to be comparable

without modification. Furthermore, Rao et al. (2002) did not calculate the underestimation of the measured TKE due to the use of a short 1–min averaging period (here we estimate that using T = 1 min captures about 90% of the TKE).

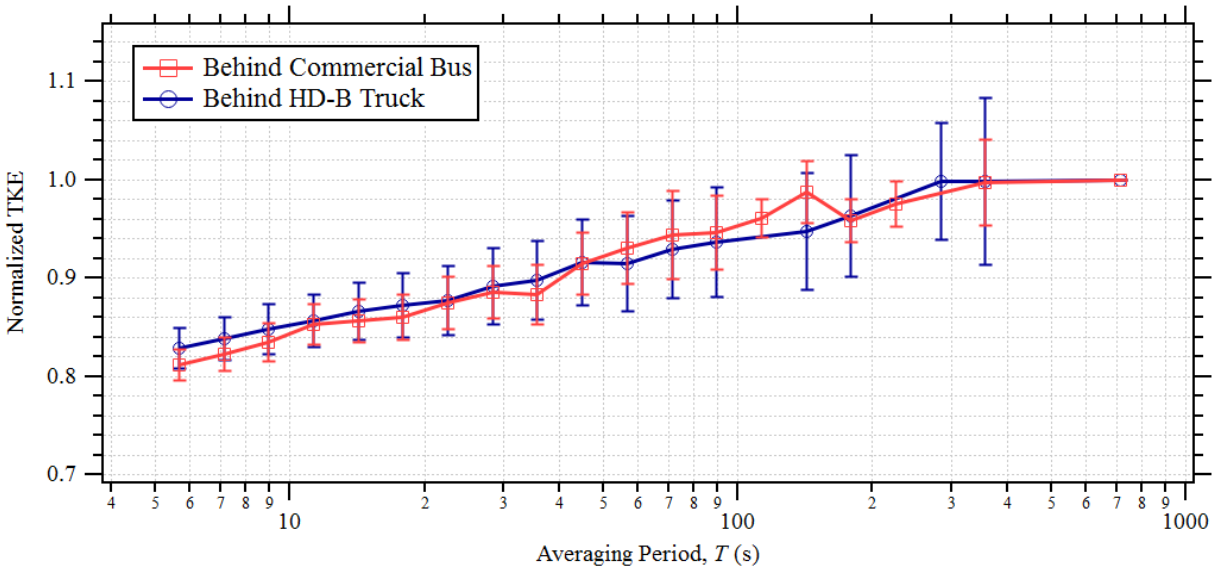

Figure 2.6: Normalized TKE (normalized by the TKE calculated using T = 11 min for the bus and T = 13 min for the HD–B truck) at various averaging periods. The error bars represent the standard error of the normalized TKE for each averaging period.

2.4.2 Power spectral density of TKE

a. Near highway spectra

Stationary measurements were obtained near Highway 400 at Stop 3 (see Fig. 2.2) on three separate days, between 12 and 15 July. Appendix B details the local meteorological conditions during these stationary measurements. On 15 July, the ambient wind direction was perpendicular to Highway 400, placing Stop 3 in a downwind location relative to the highway. During measurements made on 12 July however, the ambient wind direction was closely parallel to the highway, placing Stop 3 in a slightly upwind location. Stop 3 is located approximately 35 m from the highway edge. Figure 2.7 displays the binned power spectral density (multiplied by frequency so that the values represent energy contributions per increment $\log_{10} f$) of TKE calculated for a 15–min period at Stop 3 on 12 and 15 July. All power spectral densities presented herein are binned with respect to the logarithm of frequency (with 10 points per decade except at low frequency) and are plotted against normalized frequency, $f_n = z_m f/\bar{u}$, where z_m is the measurement height, f is the frequency in Hz and $\bar{u}$ is the mean wind speed (given as $\bar{u}_{1.7}$ in Table 2.5). For power spectra calculated during driving, the frequencies are normalized by $U_M = \overline{u_s} + \bar{V}$ (the sum of the mean vehicle speed and mean velocity component in the flow parallel to the direction of vehicle motion) instead of $\bar{u}$. Superimposed on the figure is a dashed black line representing a slope of − 2/3.

The power spectral density of TKE measured downwind of the highway at Stop 3 is consistently greater than the power spectral density measured during parallel ambient flow for $f > 0.014$ Hz ($f_n > 0.01$). Kalthoff et al. (2005) show the power spectra of the orthogonal velocity components (u, v, and w) measured at a stationary roadside tower located 3 m downwind of a highway ($z_m = 4.75$ m; $\bar{u} = 1.7$ m s^{-1}). They found that the power spectral densities measured downwind of the highway were greater than those measured upwind for $f > 0.05$ Hz, which is similar to our findings, and they show a distinct jump near $f = 0.1$ Hz ($f_n \approx 0.3$), which is present in each velocity component. Our TKE power spectrum measured downwind of the highway shows some evidence of an increase near $f = 0.1$ Hz ($f_n \approx 0.07$), but it is not as distinct as in Kalthoff et al. (2005). The jump found by Kalthoff et al. (2005), however, is similar to the broad maximum found near $f_n \approx 0.2$ while following heavy–duty trucks.

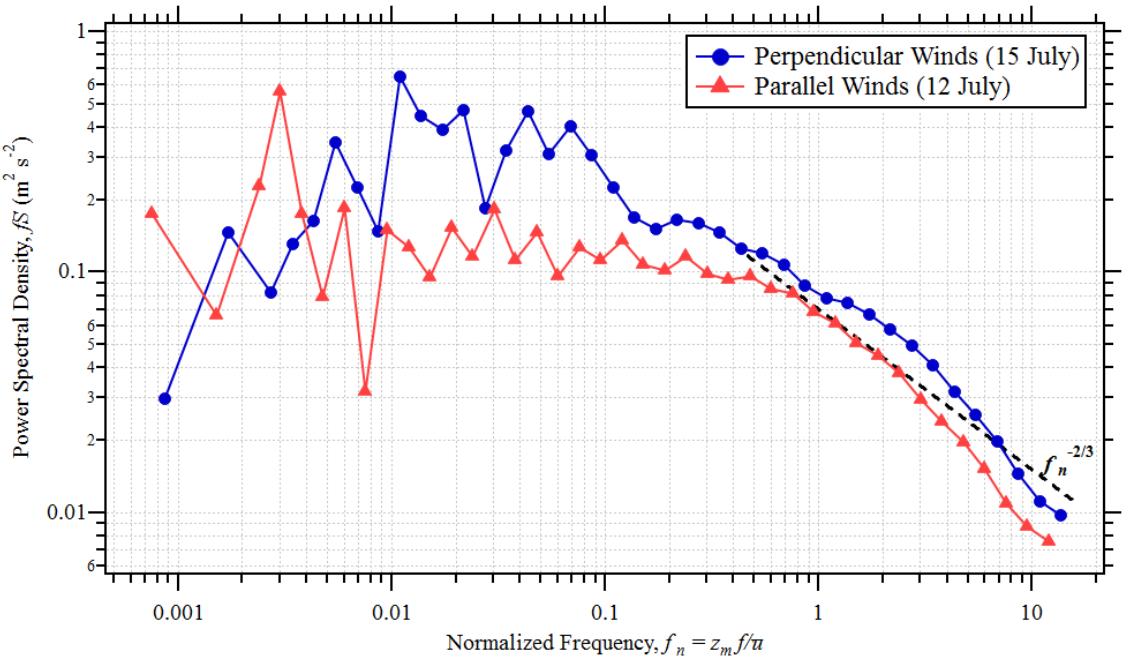

Figure 2.7: The 15–min binned (with respect to $log_{10}f$ with 10 points per decade except at low frequency) power spectral density (multiplied by f) of TKE measured while stationary near Highway 400 on 12 July (corresponding to slightly upwind measurements) and on 15 July (corresponding to downwind measurements). The power spectra are plotted against the normalized frequency, f_n where z_m is the measurement height and $\bar{u}$ is the mean wind speed calculated over the 15–min averaging period.

b. On–road spectra

Figure 2.8 displays the binned power spectral density of TKE (multiplied by frequency) calculated for a 1–min period while following: (A to B) a tractor–trailer (HD–B truck) with 10 to 16 wheels, (C) a commercial bus, (D) a passenger car, and (E to F) while driving isolated from traffic at V = 14 m s^{-1}, 22 m s^{-1} and 31 m s^{-1} respectively. The tractor–trailer analyzed in case A and B is displayed in Fig. 2.11 of Appendix A as the

followed vehicle. A short period of 1 min is necessary to obtain power spectra at a relatively constant following distance and vehicle speed. Superimposed on Fig.2.8 are dashed black lines representing a slope of – 2/3, while the details related to each case are summarized in Appendix C.

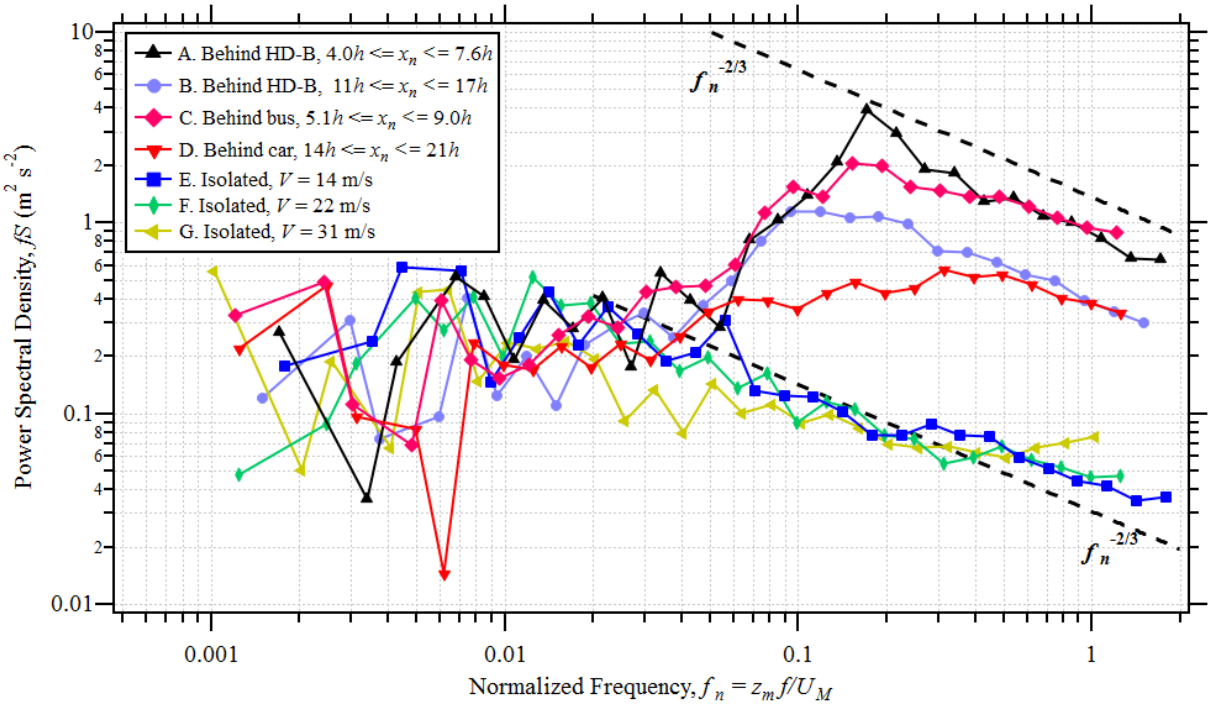

Figure 2.8: The 1–min binned (with respect to $\log_{10} f$ with 10 points per decade except at low frequency) power spectral density (multiplied by f) of TKE for seven cases, listed as A through G in the legend of the figure. The black dashed lines at the high frequency end represent a −2/3 slope. The power spectra are plotted against the normalized frequency where z_m is the measurement height and U_M is the sum of the mean vehicle speed and the mean velocity component in the flow parallel to the direction of vehicle motion (i.e., $U_M = \overline{u_s} + \bar{V}$).

The TKE power spectral densities measured in the near–wake region of the tractor–trailer and commercial bus (cases A and C respectively) both show a broad maximum centred near a normalized frequency of $f_n = 0.2$ ($f \approx 2$ Hz and wavelength $\lambda \approx 10$ m). The case–A maximum is more distinct behind the tractor–trailer than behind the bus (case C). In the far–wake ($x_m \approx 13h$) behind the same tractor–trailer (case B), the maximum near $f_n = 0.2$ broadens and decreases in magnitude. For all cases following a vehicle, the spectra begin to increase significantly for $f_n > 0.04$ ($f \approx 0.5$ Hz). During periods of isolated driving at various speeds (cases E to G), the spectra peaks near $f_n = 0.008$ ($f \approx 0.08$ Hz) and decreases thereafter, demonstrating that TKE is significantly enhanced on highways at $f > 0.5$ Hz in the presence of on–road vehicles. While driving isolated at $V = 22$ m s^{-1} and $V = 31$ m s^{-1} (cases F and G respectively), the spectra begin to increase slightly for $f_n > 0.5$ and $f_n > 0.4$ respectively (corresponding to $f > 7$ Hz), deviating away

from the expected − 2/3 slope. Since the spectral densities for $f_n > 0.1$ while following on–road vehicles are at least an order of magnitude greater than those measured during isolated driving, the increase seen in cases F and G should not significantly impact our interpretation of the TKE spectra measured in traffic. The high frequency increase seen during F and G may be related to aliasing, or perhaps related to other factors such as frame vibrations.

Only Rao et al. (2002) and Gordon et al. (2012) present the power spectral density of TKE calculated from measurements obtained from within a vehicle wake. Rao et al. (2002) displays the power spectra of TKE measured at $z_m = 0.87h$ and $x_m = 1.4h$ behind a full–sized van. Gordon et al. (2012) present power spectra of TKE measured at $z_m = 0.73h$ and $3.7h \leq x_m \leq 6.1h$ behind an HD–B truck and at $z_m = 2.1h$ and $11h \leq x_m \leq 18h$ behind a passenger car. The power spectra of TKE measured in both of these studies demonstrated that there is a large amount of turbulence production in the wake of on–road vehicles. The spectral density was found to increase or remain steady with increasing frequency for $f > 1$ Hz behind the full–sized van in Rao et al. (2002) and increase with increasing frequency for $f > 0.2$ Hz ($f_n > 0.03$) behind the HD–B truck in Gordon et al. (2012). In both of these cases, the spectra lacked an inertial subrange. The same continuous increase in the TKE power spectra for $f > 0.2$ Hz was not found behind the passenger car in Gordon et al. (2012) however, where the spectra peak near $f = 0.4$ Hz ($f_n \approx 0.06$) and decrease thereafter. In our study, the power spectra of TKE behind the tractor–trailer and commercial bus begin to show an increase with increasing frequency for $f > 0.1$ Hz ($f_n > 0.01$), which is similar to the findings behind the HD–B truck in Gordon et al. (2012). However, for $f > 2$ Hz ($f_n > 0.2$), the power spectral density begins to decrease, and at high frequencies, $f_n > 0.4$ ($\lambda < 4$ m) the spectra show a slope near − 2/3, indicating the presence of an inertial subrange. These results are in contrast to the TKE power spectra presented in Gordon et al. (2012) behind the HD–B truck and in Rao et al. (2002) behind the full–sized van.

The main differences between the present study and the past on–road studies are, (i) the sampling frequency, and (ii) the location of measurements used to calculate the power spectra (see Sect. 2.1). For the full–sized van in Rao et al. (2002) and the HD–B truck in Gordon et al. (2012), the power spectra were obtained near the upper shear layer (see Fig. 2.1) and for smaller x_m than for our study. Additionally, Rao et al. (2002) and Gordon et al. (2012) used a lower sampling frequency ($f_s = 10$ Hz and $f_s = 20$ Hz respectively), while driving at comparable vehicle speeds during similar atmospheric conditions.

2.4.3 TKE decay with downwind distance

To estimate the decay rate of TKE, the 10–s TKE value (e_{10s}) was normalized by U_M^2, where U_M is the sum of the mean vehicle speed and the mean velocity component in the flow parallel to the direction of vehicle motion (i.e. $U_M = u_s + V$) which may be in opposite directions. Note that $U_m = \overline{u_r}$, the averaged rotated longitudinal velocity component measured by the sonic anemometer. This represents an

approximation of the velocity difference between the airflow along the road in the freestream above the wake and in the wake immediately behind the vehicle. The initial shear production of vehicle–induced turbulence is then assumed proportional to U_M^2. Figure 2.9 shows the normalized 10–s TKE binned by the normalized (with respect to vehicle height) following distance for mid sized vehicles and passenger cars (Fig. 2.9 (a)) and heavy–duty trucks (Fig. 2.9 (b)). Superimposed on each plot are coloured dashed lines showing the least squares fit to $e_{10s}/U_M^2 = \exp(a)\,(x_m/h)^b = A(x_m/h)^b$ for each vehicle class. Table 2.3 displays statistics related to each least squares fit, noting that all analysis in this section is restricted to following distances less than 100 m (see Appendix A).

Wakes behind both classes of heavy–duty trucks, as well as mid sized vehicles, demonstrate a strong power–law decay of normalized 10–s TKE with increasing normalized following distance, with the strongest decay rate found for the HD–B class. Data from passenger car wakes also reveal a decay of TKE with increasing normalized following distance but given the limited dataset and higher standard error (see Table 2.3), there is much less confidence in the results for this class. The decrease of 10–s TKE with normalized distance ceases for mid sized vehicles and passenger cars beyond about $35h$, which may demonstrate that the wake has dissipated by this distance and an on–road background level (e_{bg}) remains. For isolated vehicles the U_M^2 scaling is no longer relevant for the background level, but on busy roads with multiple vehicles travelling at similar speeds, it may still be appropriate.

Gordon et al. (2012) analyzed their data by performing a least squares fit on the normalized 10–s TKE as a function of normalized following distance for HD–B trucks, mid sized vehicles and passenger cars. Their results show that HD–B trucks have the fastest rate of decay, with $e_{10s}/U_M^2 = 0.0821(x_m/h)^{-0.92}$. For our measurements behind HD–B trucks, the decay rate of the normalized 10–s TKE is found to be slightly greater than that, but perhaps the most striking differences between the two studies are in the results found for mid sized vehicles and passenger cars. Our measurements for passenger cars have values below most measurements of Gordon et al. (2012) and the rate of TKE decay is found to be greater. For mid sized vehicles, our measured values are above those of Gordon et al. (2012) for distances less than $15h$, also resulting in a greater rate of TKE decay. The difference for mid sized vehicles between the two studies is primarily in the near–wake region (i.e., less than $10h$) and can likely be attributed to the measurement heights (see Sect. 2.1). Another possible reason for the differences in the calculated decay rates of the two studies could be related to individual vehicle geometry within each class.

Rao et al. (2002) measured the TKE behind a full–sized van ($h = 2.1$ m) for $x_m < 2.3h$, and developed a least squares fit of the normalized TKE as a function of normalized following distance, giving $e/U_M^2 = 0.0099(x_m/h)^{-0.19}$. The decay rate found by Rao et al. (2002) is much lower than the decay rate found herein behind mid sized vehicles, which may be a consequence of their limited measurement domain (see Table 2.1).

Table 2.3: Statistics related to the least squares fit to $e_{10s}/U_M^2 = exp(a)\,(x_m/h)^b = A(x_m/h)^b$. Also shown are the fits of Gordon et al. (2012) and Rao et al. (2002). Here SE is the standard error, n is the number of 1 Hz data for each vehicle class, and r^2 is the coefficient of determination.

Study	Class	a	$A = \exp(a)$	b	r^2	SE(a)	SE(b)	n
This Study	Car	–3.351	0.0350	–0.76	0.27	0.180	0.0545	515
This Study	Mid size	–3.204	0.0406	–0.71	0.39	0.076	0.0240	1348
This Study	HD–A	–2.341	0.0962	–0.90	0.46	0.053	0.0190	2619
This Study	HD–B	–2.116	0.1205	–1.11	0.62	0.033	0.0144	3565
Gordon et al. (2012)	Car	–4.689	0.0092	–0.23	0.05	0.037	0.0109	8306
Gordon et al. (2012)	Mid size	–4.382	0.0125	–0.34	0.12	0.025	0.0083	11923
Gordon et al. (2012)	HD–B	–2.500	0.0821	–0.92	0.64	0.014	0.0065	11227
Rao et al. (2002)	Mid size	–4.615	0.0099	–0.19	–	–	–	–

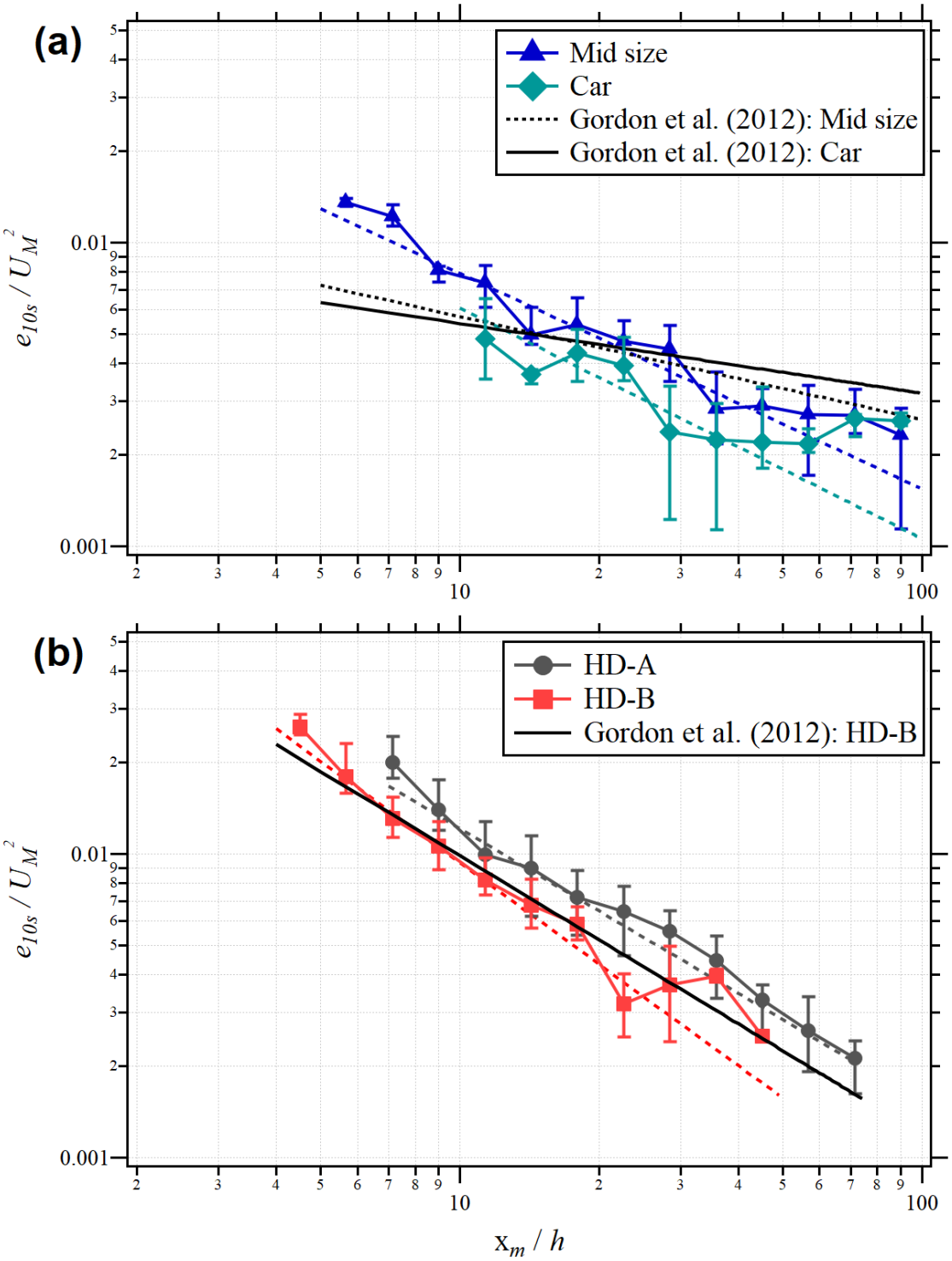

Figure 2.9: Quartiles of the binned normalized 10–s TKE (e_{10s}/U_M^2) at various normalized (with respect to vehicle height, h) following distances (x_m) for (a) passenger cars and mid sized vehicles, and (b) HD–A and HD–B trucks. U_M is the sum of the mean vehicle speed ($\overline{V}$) and the mean velocity component in the flow parallel to the direction of vehicle motion ($\overline{u_s}$) (i.e., $U_M = \overline{V} + \overline{u_s}$). Solid coloured lines for each vehicle class represent the median and error bars represent the 25th (bottom) and the 75th (top) percentile. Also shown are dashed coloured lines representing a least squares fit to $ln(e_{10s}/U_M^2) = a + bln(x_m/h)$ for each vehicle class. The least–squares fits of Gordon et al. (2012) are indicated as black solid or dashed lines, detailed in the legend of each figure.

2.5 Discussion

2.5.1 Height dependence of TKE: study comparisons

We present the non–normalized 10–s TKE (e_{10s}) as a function of following time (t_m) where $t_m = x_m/U_M$ (Gordon et al. 2012; Huang et al. 2014). The following time represents the time taken for the mobile laboratory to arrive at and sample an air parcel that was disturbed by the target vehicle. In meteorological and air–quality prediction models, the vehicle flow rate (s^{-1}) is a common input, making t_m an appropriate variable to estimate the on–road TKE enhancement (Sect. 2.5.2). Assuming exponential decay of the non–normalized 10–s TKE with following time, as $e_{10s} = e_{bg} + N\,exp(-Dt_m)$, where e_{bg} is the on–road background TKE ($m^2\ s^{-2}$), N is a constant ($m^2\ s^{-2}$) and D is the exponential decay constant (s^{-1}), produces a root–mean–square error (r.m.s.) for HD–B trucks of 0.91 $m^2\ s^{-2}$. If instead e_{10s} is assumed to decay exponentially with following distance (x_m), the r.m.s. error for HD–B trucks is found to be greater at 1.24 $m^2\ s^{-2}$. This demonstrates that e_{10s} is best modelled as decay in t_m instead of decay with x_m, possibly related to varying vehicle speeds, or because of other factors that are unaccounted for (i.e., velocity deficits, ambient conditions). Figure 2.10 displays the quartiles of e_{10s} at various t_m for each vehicle class together with quartiles of the 10–s TKE from Gordon et al. (2012), and the average 1–min TKE behind the full–sized van in Rao et al. (2002). Our data shown in Fig. 2.10 and those of Gordon et al. (2012) are from different measurement days, and no limit on x_m has been imposed. The results shown for the Rao et al. (2002) study were obtained from Hosker et al. (2003) and the supplementary material of Wang and Zheng (2012). The results of Bhautmage and Gokhale (2016) were obtained from the graphical results for a commercial bus of 3 m height (shown as black stars). Figure 2.10 is split into two parts, each displaying a specific height range: (a) 2 m ≤ z_m < 4 m and (b) 0 m < z_m < 2 m. Refer to Table 2.1 for the measurement domain of each of these studies.

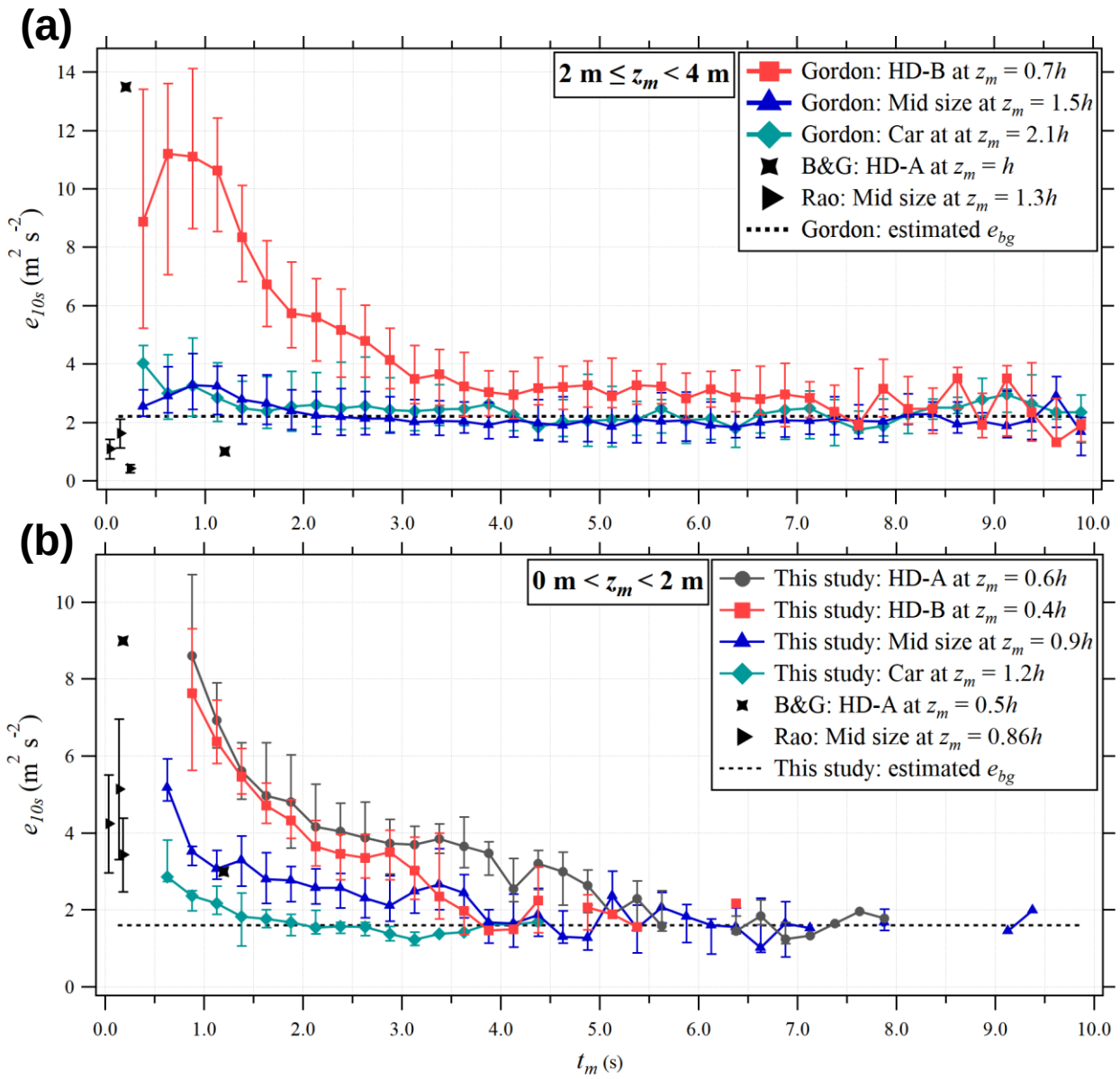

Figure 2.10: Quartiles of the 10–s TKE (e_{10s}), binned according to following time (t_m) in 0.25–s bins. Shown in the figure are two panels representing different height ranges: (a) 2 m ≤ z_m < 4 m and (b) 0 < z_m < 2 m. All data are shown (i.e., no limit is imposed on the following distance, x_m). Each linked marker represents a median value, while the error bars give the 25th (bottom) and 75th (top) percentiles. The measurements (mean values calculated over 1 min averaging intervals) behind the full–sized van from Rao et al. (2002) are shown as black sideways triangles; the error bars give ± 1 standard deviation from the mean. Finally, the modelled results from Bhautmage and Gokhale (2016) for a commercial bus of 3–m height are displayed as black stars

From Fig. 2.10 (b), the most rapid decline of e_{10s} occurs at t_m < 2 s for heavy–duty trucks and at t_m < 1 s for mid sized vehicles and passenger cars. Our results show that e_{10s} reaches an asymptote at t_m > 6 s for mid sized vehicles and HD–A trucks. A similar asymptote is seen in the data from Gordon et al. (2012) around t_m = 6 s, except for HD–B trucks which were found to asymptote later at t_m > 7.5 s. If we

assume there is no interference from other vehicles while measuring at large t_m, then this asymptotic value represents the median on–road background TKE

$$e_{bg} = e_A + e_{RIT}, \tag{2.5}$$

where e_A is the ambient turbulence (resulting from local meteorology) and e_{RIT} is the road–induced turbulence. The variable e_{RIT} refers to turbulence that is generated by barriers on the highway (i.e., an embankment), by roadside structures such as trees, or thermally induced by solar heating of the highway surface (Rao et al. 1979; Wang and Zheng 2009). We can estimate e_{bg} for 15 July from the downwind measurements made at Stop 3, where the TKE was found to be 1.74 $m^2\ s^{-2}$. The TKE value measured during this period includes both components of Eq. 2.5, namely e_A and e_{RIT}; Stop 3 is located approximately 35 m from the highway edge during essentially perpendicular ambient flow, with a mean wind of $\bar{u}_{1.7}$ = 2.21 $m\ s^{-1}$. Thus, an air parcel disturbed by on–road traffic will take about 16 s to arrive at Stop 3 and be sampled.

From Fig. 2.10 (b), e_{bg} can be estimated as the average binned e_{10s} for mid sized vehicles and HD–A trucks at $t_m > 6$ s, giving $e_{bg} \approx 1.6\ m^2\ s^{-2}$ (if the underestimation in Sect. 2.4.1 is assumed, then $e_{bg} \approx 1.9\ m^2\ s^{-2}$). This value of e_{bg} is very similar to the value found downwind of the highway at Stop 3 during measurements made on 15 July. There is an uncertainty in the value of e_{bg} since data were amalgamated from drives that occurred on different days, leading to variations in e_A and e_{RIT}. Performing a similar analysis on the data obtained by Gordon et al. (2012) in Fig. 2.10 (a) behind mid sized vehicles and passenger cars at $t_m > 6$ s, gives a value for that study of $e_{bg} \approx 2.2\ m^2\ s^{-2}$. The values of e_{bg} from these two campaigns are similar in magnitude since measurements were obtained in the same geographic location during the summer months, at a similar time of day.

In Gordon et al. (2012) HD–B trucks were found to have the largest magnitude of e_{10s}, peaking at t_m = 0.63 s with $e_{10s} - e_{bg} \approx 9.0\ m^2\ s^{-2}$ (see Fig. 2.10 (a)). The TKE measured behind HD–B trucks in Gordon et al. (2012) is much greater than the TKE measured behind either HD–A or HD–B trucks in our study for $t_m < 3$ s. For example, behind HD–B trucks at t_m = 0.88 s we obtained $e_{10s} - e_{bg} \approx 6\ m^2\ s^{-2}$, which is a decrease of about 33% compared to e_{10s} measured behind HD–B trucks at t_m = 0.88 s in Gordon et al. (2012). If the underestimations in Sect. 2.4.1 are taken into consideration, then this decrease becomes 48%. Behind the commercial bus of h = 3 m in Bhautmage and Gokhale (2016), the modelled TKE at $t_m \approx 0.20$ s is similar to the aforementioned findings behind HD–B trucks at t_m = 0.88 s. At $t_m \approx 0.20$ s they found that the TKE maximizes near $z_m = h$ and decreases approximately linearly until $z_m = 0.33h$, with an estimated decrease of about 40% between $z_m = h$ and $z_m = 0.33h$. By t_m = 1.2 s however, the TKE is found to maximize much lower at $z_m = 0.4h$, with the TKE decreasing approximately linearly with height up to

$z_m = 1.2h$. This is in contrast to the measurements behind HD–B trucks, where TKE at $z_m = 0.7h$ is consistently larger in magnitude than TKE measured at $z_m = 0.4h$ for $t_m < 3$ s. In the modelling investigation of Bhautmage and Gokhale (2016), the TKE was simulated within an enclosed road tunnel opposed to the open atmosphere, which may account for the differences noted here.

Behind mid sized vehicles, our measurements show a pronounced increase in the 10–s TKE at $t_m < 1.5$ s, while Gordon et al. (2012) report only a minor increase at $t_m < 1$ s. At $t_m = 0.63$ s behind mid sized vehicles, we found $e_{10s} - e_{bg} \approx 3.6$ m^2 s^{-2}, while Gordon et al. (2012) found $e_{10s} - e_{bg} \approx 0.7$ m^2 s^{-2}, giving a decrease of about 81% between $x_m = 0.9h$ and $x_m = 1.5h$ (75% when considering the underestimates in Sect. 2.4.1). This is similar to the 70% to 90% decrease found behind the full–sized van between $x_m = 0.87h$ and $x_m = 1.29h$ in Wang and Zhang (2012) and Rao et al. (2002). Furthermore, the magnitude of TKE behind the full–sized van in Rao et al. (2002) is comparable in magnitude to our measurements behind mid sized vehicles, when on–road background levels are considered. The Rao et al. (2002) study had $e_{bg} \approx 0$ (Hosker et al. 2003).

Performing an atmospheric stability analysis (not shown here) on the measurement days of Gordon et al. (2012) (using the same method outlined in Sect. 2.2.3), produces stability classifications very similar to those given in Table 2.2. This suggests that the differences noted between our results and Gordon et al. (2012) are not the result of atmospheric stability. For our measurements, there is no significant difference in the magnitude of TKE behind on–road vehicles while the atmospheric stability was slightly unstable (14 and 15 July), compared to measurements made during more unstable atmospheric conditions (7, 11 and 12 July). Thus, in summary, the differences noted between our measurements and Gordon et al. (2012) while following behind HD–B trucks and mid sized vehicles are likely a result of measurement height and overall proximity to the upper shear layer (Sect. 2.1). Lee and Choi (2009) note that the flow within both the wake region and the upper shear layer contains small–scale vortices, however in the upper shear layer these vortices are particularly strong and concentrated, leading to enhanced levels of turbulence.

2.5.2 Height–integrated parametrization of on–road turbulence enhancement

In Gordon et al. (2012) a parameterization of on–road turbulence enhancement (Δe_q) due to vehicle class q, was developed by integrating the binned 10–s TKE (e_q) measured at z_m = 3 m over all t_m (Fig. 2.10 (a)), giving

$$\Delta e_q = F_q \int_0^\infty (e_q - e_{bg}) \mathrm{d}t_m = F_q I_q, \tag{2.6}$$

where F_q is the number of q vehicles per unit time (s^{-1}), I_q ($m^2\ s^{-1}$) is the value of the integral in Eq. 2.6 and e_{bg} is the on–road background level of the 10–s TKE (Eq. 2.5). Gordon et al. (2012) estimated e_{bg} as the average of e_q (calculated from all vehicle classes) at t_m > 8 s. It was assumed in their formulation that the measured TKE did not vary with height behind the target vehicle. Following the evidence presented in Sect. 2.5.1, this parametrization of on–road TKE enhancement should be extended to include a height–dependence.

To represent the vertical variation of TKE for vehicle class q, the vertical domain (z_c) impacted by vehicle–induced turbulence is split into n layers of thickness Δz. The TKE enhancement in each layer (i) is calculated by numerical integration of Eq. 2.6, or by using a suitable function to describe $e_q(t_m)$. The total TKE enhancement (i.e., the sum of $\Delta e_q \Delta z$ from each layer) is then averaged over the entire domain, z_c, yielding an estimated vertically averaged on–road TKE enhancement ($\overline{\Delta e_q}$) due to vehicle class q,

$$\overline{\Delta e_q} = \frac{1}{z_c}\sum_{i=1}^{n} \Delta e_{q_i} \Delta z_i = \frac{F_q}{z_c}\sum_{i=1}^{n} I_{q_i} \Delta z_i. \quad (2.7)$$

From our median binned measurements and those of Gordon et al. (2012) (from Fig. 2.10), we can model the data as $e_q(t_m) = e_{bg} + N\exp(-Dt_m)$, allowing direct calculation of I_q from Eq. 2.6. Table 2.4 lists the coefficients (N, D and e_{bg}) of this fit for cars ($q = C$), mid sized vehicles ($q = M$) and HD–B trucks ($q = HD$). The benefit of applying this modelled fit, as opposed to numerically integrating the median values, is the extrapolation of the dataset to t_m < 1 s. This is crucial since this missing portion of the t_m domain features a very large value of TKE, significantly impacting the final value of I_q. This method also allows direct estimation of e_{bg}, which is found to range between 1.5 and 1.6 $m^2\ s^{-2}$ for our study and 2.0 and 2.3 $m^2\ s^{-2}$ for Gordon et al. (2012). The values of e_{bg} found from the exponential fits are similar to the value of e_{bg} estimated for each study in Sect. 2.5.1, demonstrating respectable agreement between the fits and median measurements.

Table 2.4: Details related to the fit $e_q(t_m) = e_{bg} + N\,exp(-Dt_m)$ for this study and Gordon et al. (2012). Here e_{bg} is the on–road background TKE ($m^2\ s^{-2}$), N is a constant ($m^2\ s^{-2}$) and D is the exponential decay constant (s^{-1}). The standard deviation (SD) of each fitted variable is also shown. I_q is the value of the integral in Eq. 2.6 for each exponential fit.

Study	Class, q	e_{bg}	N	D	$SD(N)$	$SD(D)$	$SD(e_{bg})$	I_q
		$m^2\ s^{-2}$	$m^2\ s^{-2}$	s^{-1}	$m^2\ s^{-2}$	s^{-1}	$m^2\ s^{-2}$	$m^2\ s^{-1}$
This study	HD	1.64	11.8	0.80	1.220	0.103	0.208	14.8
This study	M	1.62	4.50	0.73	0.683	0.149	0.120	6.2
This study	C	1.48	3.96	1.67	0.906	0.308	0.050	2.4
Gordon et al. (2012)	HD	2.34	11.4	0.56	0.838	0.072	0.242	20.4
Gordon et al. (2012)	M	2.01	1.36	0.61	0.273	0.203	0.068	2.2
Gordon et al. (2012)	C	2.30	2.70	1.46	0.724	0.418	0.052	1.8

If we assume a height domain of z_c = 4 m (in reality this would extend higher) and split it into two levels (n = 2, Δz = 2 m), we can then apply Eq. 2.7 to estimate the vertically averaged on–road TKE enhancement, by letting our measurements represent the first level (i = 1), corresponding to 0 m < z_m < 2 m (Fig. 2.10 (b)) and the measurements made during Gordon et al. (2012) represent the second level (i = 2), corresponding to 2 m ≤ z_m < 4 m (Fig. 2.10 (a)). The value of I_q at each level can be calculated by integrating the exponential fit (Eq. 2.6) giving $I_q = N/D$ (the results are displayed in Table 2.4). For Highway 400, Gordon et al. (2012) measured a total traffic flow rate of F_T = 2.2 s^{-1}, consisting of 89.9% cars, 4.8% mid sized vehicles and 5.3% HD trucks. This gives $F_C \approx 1.98\ s^{-1}$, $F_M \approx 0.11\ s^{-1}$ and $F_{HD} \approx 0.12\ s^{-1}$ respectively. Using these values in Eq. 2.7 gives $\overline{\Delta e_C} \approx 4.2\ m^2\ s^{-2}$, $\overline{\Delta e_M} \approx 0.45\ m^2\ s^{-2}$ and $\overline{\Delta e_{HD}} \approx 2.1\ m^2\ s^{-2}$. Summing these values gives the total vertically averaged on–road TKE enhancement due to a composition of vehicles

$$\overline{\Delta e_T} = \overline{\Delta e_C} + \overline{\Delta e_M} + \overline{\Delta e_{HD}}, \tag{2.8}$$

with $\overline{\Delta e_T} \approx 6.8\ m^2\ s^{-2}$ and an average per unit flow enhancement of $\overline{\Delta e_T}/F_T \approx 3.1\ m^2\ s^{-1}$. If the traffic composition contains even a marginally higher fraction of HD–B trucks, then the amount of the on–road TKE enhancement will be significantly higher. Ideally this method of estimating $\overline{\Delta e_T}$ would use more than two levels measured over a wider range of heights, and include a more diverse selection of vehicle classifications, demonstrating the need for additional in–wake measurements.

It should be noted that $z < z_c$ is the portion of the boundary layer affected by vehicle–induced turbulence and relates to the lowest vertical level in a numerical prediction model. Increasing z_c (i.e., decreasing the model's vertical resolution) decreases the estimated on–road TKE enhancement, since the same amount of vehicle–induced turbulence will be averaged over a larger vertical region. However, as the

resolution of numerical forecasting models increases, it will become increasingly necessary to include a vehicle–induced turbulence parametrization to accurately predict vertical diffusion near highways. Makar et al. (2010) found that AURAMS overpredicted surface NOx concentrations in grid squares covering highways when the model was executed using a horizontal resolution of 15 km. It has been suggested that this overprediction may be related to insufficient dispersive processes, possibly due to the absence of a vehicle–induced turbulence parametrization in the numerical model (Makar et al. 2010; Gordon et al. 2012). In Gordon et al. (2012), their measured value of Δe (from Eq. 2.6) was added to the Global Environmental Multiscale model value of e_A to determine the influence of vehicle–induced turbulence on the vertical diffusion coefficient (K_z). The Global Environmental Multiscale model has a variable vertical resolution with the lowest vertical model level being 42 m (Gordon et al. 2012). They found that K_z is increased by 10 to 25% as a result of vehicle–induced turbulence, except in the early morning when K_z is increased by more than 80%, demonstrating the importance of including an accurate vehicle–induced turbulence parametrization in numerical models.

2.6 Conclusions

The power spectral density of TKE while following behind on–road vehicles increases significantly for $f > 0.5$ Hz ($f_n > 0.04$), consistent with the results behind an HD–B truck in Gordon et al. (2012) and a full–sized van in Rao et al. (2002). The same increase is not seen while driving isolated from traffic, which demonstrates the large enhancement of TKE in the presence of on–road vehicles. Furthermore, a broad peak in the TKE power spectra centred near a frequency of 2 Hz ($f_n \approx 0.2$, $\lambda \approx 10$ m) is observed while following behind a tractor–trailer and a commercial bus. Beyond $f \approx 5$ Hz ($f_n > 0.4$, $\lambda < 4$ m) the power spectral density begins to decrease with increasing frequency with a clear indication of an inertial subrange. This is in contrast to Gordon et al. (2012) behind an HD–B truck and Rao et al. (2002) behind a full–sized van, where the TKE power spectra remains relatively flat for $f > 1$ Hz. The TKE power spectrum measured while stationary downwind of the highway is found to be consistently greater than the power spectrum measured slightly upwind of the highway during parallel ambient flow for $f > 0.015$ ($f_n > 0.01$). This is consistent with Kalthoff et al. (2005) for measurements obtained downwind of a German motorway, and in Gordon et al. (2012) for measurements made near Highway 400.

The normalized TKE produced by on–road vehicles was found to decay with increasing following distance according to a power–law relationship, with decay rates (b from Table 2.3, with following distance normalized by vehicle height) of 0.76, 0.71, 0.90 and 1.11 for passenger cars, mid sized vehicles, HD–A trucks and HD–B trucks respectively. The results for heavy–duty trucks compare reasonably well with Gordon et al. (2012). However, for mid sized vehicles, the decay rate is much greater, probably because we obtained measurements at $z_m = 1.7$ m which is within the wake zone of mid sized vehicles of $h = 2$ m.

From our results and those of Gordon et al. (2012), the variation of TKE with height is quantified. Comparison between the present results and those obtained by Gordon et al. (2012) suggests that TKE maximizes in the upper shear layer and decreases quickly above it. For mid sized vehicles at t_m = 0.63 s, the TKE decreases by about 81% from a height of $0.9h$ to a height $1.5h$. This decrease agrees with the findings behind the full–sized van in Rao et al. (2002). Below the upper shear layer, the TKE decreases are more moderate; for HD–B trucks at t_m = 0.88 s, the TKE was found to decrease by about 33% from a height of $0.7h$ to a height of $0.4h$.

The parametrization developed in Gordon et al. (2012) is extended to include a height dependence on the magnitude of vehicle–induced turbulence. By splitting the measurement domain into levels, the on–road enhancement of TKE in each level is calculated. Using only two levels, the total on–road TKE enhancement per unit traffic flow is found to be $\overline{\Delta e_T}/F_T \approx 3.1$ m^2 s^{-1} for a typical peak traffic pattern on Highway 400. As model resolution increases it will become crucial to include the variation of on–road TKE enhancement with height in order to properly model vertical diffusion over highways and pollutant levels in the vicinity.

There is a need for additional on–road measurements to obtain a more detailed vertical profile, especially for z_m < 1.5 m and z_m > 3 m. Future on–road measurement campaigns should also be performed in the overnight and early–morning hours, and in different seasons, to assess the effect of atmospheric stability and varying weather conditions on the magnitude of vehicle–induced turbulence. With additional measurements, future work should also attempt to relate the TKE enhancement behind on–road vehicles to the standard deviation of the crosswind, along–wind and vertical displacement of pollutants (σ_x, σ_y, σ_z) used in Gaussian diffusion models.

CHAPTER 3: The measurement of mean wind, variances and covariances from an instrumented mobile car in a rural environment

Stefan J. Miller[1], Mark Gordon[1]

[1]Department of Earth and Space Science and Engineering, York University, Toronto ON, M3J 1P3, Canada

Publication status: Submitted and under review as Miller and Gordon (2022) in Atmospheric Measurement Techniques

Abstract

Turbulence near the surface can be intermittent and may have a large variation over a short distance. The car offers an affordable and practical way to sample atmospheric turbulence near the surface over a large spatial domain, but limited studies have investigated the instrumented car's ability to measure atmospheric means, variances and covariances, especially in less ideal conditions. On 20 and 22 Aug 2019, a small tripod was outfitted with a sonic anemometer and placed in a highway shoulder to compare with measurements made on an instrumented car as it travelled past the tripod. The rural measurement site in this investigation was selected so that the instrumented car travelled past many upwind surface obstructions and experienced the occasional passing vehicle. To obtain an accurate mean wind speed and mean wind direction on a moving car, it is necessary to correct for flow distortion and remove the vehicle speed from the measured velocity component parallel to vehicle motion (for straight–line motion). In this study, the velocity variances and turbulent fluxes measured by the car are calculated using two approaches: (1) eddy–covariance and (2) wavelet analysis. The results show that wavelet analysis can better resolve low frequency contributions, and this leads to a reduction in the horizontal velocity variances measured on the car, giving a better estimate for some measurement averages when compared to the tripod. A wavelet–based approach to remove the effects of sporadic passing traffic is developed and applied to a measurement period during which a heavy–duty truck passes in the opposite highway lane; removing the times with traffic in this measurement period gives approximately a 10% reduction in the turbulent kinetic energy. The vertical velocity variance and vertical turbulent heat flux measured on the car are biased low compared to the tripod. This low bias may be related to a mismatch in the flux footprint of the car versus the tripod, or perhaps related to rapid flow distortion at the measurement location on the car. When random measurement uncertainty is considered, the vertical momentum flux is found to be not different from the tripod in the 95% confidence interval, and significantly different than zero for most measurement periods.

3.1 Introduction

Measurements of atmospheric means, variances and covariances obtained from an instrumented mobile car can provide low cost, in situ observations close to the ground, and over a large measurement domain. Hereafter 'instrumented mobile car' refers to all potential on–road vehicles that could serve as a measurement platform, including cars, sport utility vehicles, pickup trucks, minivans, or larger mobile laboratories that use a heavy–duty truck. Previous investigations have largely used instrumented mobile cars for the measurement of near–surface atmospheric means, but minimal attention has been given to their use for the measurement of turbulence (i.e., variances and covariances). In the nocturnal boundary layer characterized by stable conditions and weak flow, turbulence near the surface mainly originates from poorly understood non–stationary mechanical shear and submesoscale motions (Mahrt et al. 2012; Van De Wiel et al. 2012) such as low–level jets, thermotopographic wind systems (i.e., katabatic flow) and breaking gravity waves (Salmond and McKendry, 2005). In the very–stable boundary layer the generated turbulence is often intermittent and results in the vertical transport of scalars (i.e., heat, pollutants), but stationary towers may be too isolated and "site–specific" to adequately sample the temporally and spatially localized turbulence (Salmond and McKendry, 2005). The mobile car, however, can measure along a driven path, which may provide a more representative sample of turbulence near the surface compared to a stationary tower. In addition, the mobile car may also be used to obtain in situ wind and turbulence measurements near the surface within the urban boundary layer, measurements that may help validate high–resolution, street–level models. In the near–surface urban boundary layer, the strength of the wind and the intensity of turbulence are influenced by the composition of buildings and trees (Mochida et al. 2008; Gromke and Blocken 2015; Hertwig et al. 2019; Krayenhoof et al. 2020), and can have a significant impact on pedestrian comfort (Hunt et al. 1976; Yu et al. 2021), and neighborhood–level pollutant dispersion (Aristodemou et al. 2018; Su et al. 2019). The mobile car involves less logistical limitations (i.e., permits, vandalism) and potentially affords a greater spatial coverage when compared to the installation of a stationary tower in a high–density urban area. Furthermore, as the resolution of numerical weather prediction models continues to improve, the measurement of localized variations in near–surface heat, momentum and moisture fluxes may improve the prediction of convective storms (Markowski et al. 2017).

The instrumented mobile car has been used in various investigations to measure atmospheric means near the surface (Bogren and Gustavsson 1991; Straka et al. 1996; Achberger and Bärring 1999; Armi and Mayr 2007; Mayr and Armi 2008; Taylor et al. 2011; Smith et al. 2009; White et al. 2014, Currey et al. 2016; de Boer et al. 2021). Gordon et al. (2012) and Miller et al. (2019) used the instrumented car for the measurement of velocity variances on highways to quantify vehicle–induced turbulence. Despite the increasing number of investigations using instrumented mobile car systems for atmospheric measurements,

there are limited studies that examine their performance and accuracy for the measurement of the mean flow, velocity variances and covariances.

Achberger and Bärring (1999) investigated the accuracy of mean temperature measurements made on a minibus in low–speed driving conditions (8 to 11 m s^{-1}) by installing four thermocouples at various heights (0.5 m, 1 m, 2 m, and 4 m). From their results they developed a spectral correction for the measured air temperature to remove the effects due to thermal inertia of the thermocouples. More recently, Anderson et al. (2012) evaluated the feasibility of using passenger vehicles (9 in total) to collect mean air temperature and air pressure measurements on roads, with the end goal of improving road weather forecasts to reduce weather–related traffic fatalities. They found good agreement for mean air temperature measurements made on passenger vehicles when compared to mean air temperature measurements made by stationary weather stations, and poor agreement for air pressure.

Figure 3.1: A front view of instrumented car (also referred to as a mobile car platform or mobile car laboratory) used in this investigation.

Belušic et al. (2014) is the first known study to evaluate a three–dimensional sonic anemometer (model CSAT3, sampling frequency of 20 Hz) affixed to a passenger vehicle for its accuracy at measuring atmospheric variances and covariances, in addition to atmospheric means. In their setup the sonic anemometer was supported by a sophisticated arm and lattice aluminum frame; the arm held the sonic above the vehicle's top at a height of 3 m from the ground, positioned slightly ahead of the vehicle's front end. Recently, Hanlon and Risk (2020) investigated how the placement of a sonic anemometer on the vehicle affects the accuracy of velocity measurements, by applying computational fluid dynamics modelling in

combination with mobile car measurements. The anemometers were placed vertically upward on top of the vehicle's roof.

If 1 min averages are assumed, then measurements (i.e., wind velocity, gas concentration) obtained from an instrumented car travelling at near–highway speeds (i.e., 15 to 25 m s^{-1}) are made over a significant spatial path on the order of 10^3 meters, where surface variations (i.e., vegetation, building structures, other traffic) can be significant. A single spatial path measured by the vehicle may therefore feature flow conditions that are not stationary and an upwind surface that is not homogenous. This calls into question the applicability of the eddy–covariance (EC) method which requires near–stationary conditions to reduce uncertainties in the estimation of variances and covariances. During their investigation Belušic et al. (2014) made car measurements on a nearly flat, homogenous portion of remote rural highway, without traffic and without large upwind obstacles such as trees and houses. Therefore, their investigation represented an "idealized" case. Even so, they found instances where the car–measured horizontal velocity variances were significantly overestimated compared to measurements made by a nearby stationary tower. They concluded that non–stationarity of the flow was the likely cause leading to the anomalously large car–measured horizontal velocity variances. Their results demonstrate that non–stationarity of the flow cannot be ignored when measuring on an instrumented mobile car. Recently Schaller et al. (2017) applied wavelet analysis as an alternative technique to estimate turbulent methane fluxes measured by a fixed tower in non–stationary conditions. For periods fulfilling the stationarity requirement, the wavelet flux was in excellent agreement with eddy–covariance flux, but for periods where the stationarity requirement was violated, the wavelet flux was found to be more reliable and provided a better estimate. Since their work, wavelet analysis applied to analyze turbulent fluxes has become more common (von der Heyden et al. 2018; Göckede et al. 2019; Conte et al. 2021).

The present work investigates an instrumented mobile car setup (shown in Fig. 3.1) by comparing car–based measurements with measurements made by a small roadside tripod. Our setup differs from Belušic et al. (2014) in two main ways which are necessary to make the vehicle safe for on–road driving with other vehicles: (1) our sonic anemometer is held closer to the vehicle and situated over the vehicle's front end and (2) the sonic anemometer is held closer to the ground at a height of 1.7 m, which is near the height of the vehicle's top. We selected this design to investigate whether the sonic anemometer can be held closer to the vehicle and still provide measurements that are representative of the mean flow and turbulence near the surface, allowing road–safe vehicle operation without compromising the measured data. While farmland is common in our measurement domain, the car also travelled past many large trees, houses, and experienced the occasional passing vehicle traveling in the opposite direction. Therefore, we investigate if the mobile car measurements are still representative of the turbulence statistics near the surface in a less idealized case, where the upwind surface and terrain is not homogenous, and the measured flow is affected

by many surface obstacles including other traffic. Thus, this work aims to help design a low–cost experiment to measure and analyze on–road velocity variances and covariances using an instrumented car, in the presence of sporadic passing traffic and upwind surface inhomogeneities. This study investigates how these inhomogeneities affects the calculated statistics. Wavelet analysis is considered as an alternative technique to eddy–covariance for the estimation of velocity variances and covariances measured on the car and is applied to quantify and remove the effects of sporadic passing traffic. The potential sources of measurement uncertainty on the car are quantified and discussed.

3.2 Methodology

3.2.1 Instrumented car

A sport utility vehicle (SUV) was outfitted with instrumentation fastened to the vehicle using a roof rack as shown in Fig. 3.1. A 40 Hz, three–dimensional sonic anemometer (Applied Technologies, Inc., model type "A" or "Vx") was installed on a support arm located at the front end of the vehicle, at a height of z_m = 1.7 m. Since the "A" type is rated for higher flow velocities, once it became available for use it was installed and the "Vx" type was removed. This change was done to test how the specific sonic anemometer model affects the measured velocities. The "A", "Vx", and "V" type sonic anemometers ("V" is used on the roadside tripod) have an accuracy of ± 0.1 m s^{-1} within a measurement range of ± 60 m s^{-1}, ± 20 m s^{-1}, and ± 15 m s^{-1} respectively. To limit the effect of vibrations on the measurements made by the sonic anemometer, the horizontal arm holding the anemometer was supported by two metal rods attached to the vehicle's front end. The forward scene was recorded by a Thinkware F750 dashcam (30 frames per second), which encodes 1 Hz measurements of latitude, longitude, and vehicle speed (s) as metadata in each mp4 file.

The coordinate system of the sonic anemometer on the car is defined (assuming an observer is sitting inside of the vehicle facing toward the front hood) so that measured velocity parallel to vehicle motion (u_m) is positive toward the car, the measured lateral velocity (v_m) is positive toward the right, and the measured vertical velocity (w_m) is positive upward. Subscript m denotes a raw measured value.

3.2.2 Roadside tripod

On 20 and 22 Aug 2019 a small tripod was assembled and placed at the roadside (i.e., in the highway shoulder) to compare with measurements made by the instrumented car as it travelled past the stationary tripod. The tripod was equipped with a three–dimensional sonic anemometer (Applied Technologies, Inc., model type "V") that recorded at either a frequency of 10 Hz (20 Aug) or 20 Hz (22 Aug). Each day the sonic was installed at a measurement height of z_m = 1.4 m. On 22 Aug, the tripod also had a Thinkware X700 dashcam (30 frames per second) installed to record passing traffic. To investigate the effect of tripod

vibrations on the measurements, we tied down the system with guy wires on the 22 Aug, but left it free to vibrate on the 20 Aug.

3.2.3 Measurement site

The measurement site was agricultural fields located on either side of a two–lane highway. The traffic on 22 Aug passing our measurement site was more significant than on 20 Aug; the traffic composition on 22 Aug included occasional large trucks and we did not observe any large trucks passing our measurement site on 20 Aug. Both days featured fair weather, with sky conditions ranging from mainly sunny on 20 Aug to partly cloudy on 22 Aug. The wind direction measured at nearby Egbert weather station (maintained by Environment and Climate Change Canada with measurements obtained at a height of 10 m) ranged between 160º and 200º on 20 Aug and 310º and 340º on 22 Aug. The mean wind ranged between 4.2 m s^{-1} and 5.6 m s^{-1} on 20 Aug and 3.8 m s^{-1} and 5.0 m s^{-1} on 22 Aug. The Egbert weather station is located about 16 km north of the measurement site.

The road is relatively flat near the tripod location, but in general, the terrain is not flat and homogenous in this area. The study area (which spans about 10 km) has several hills with slopes up to 10º. The elevation ranges between 200 and 300 m above mean sea level and there are areas with numerous trees and some structures located upwind of the highway. The tripod was located at an elevation of 277 m on 20 Aug, and at an elevation of 222 m on 22 Aug (estimated from Google Earth). For reference, the Egbert weather station is at an elevation of 251 m.

In this work a *measurement track* refers to the specific ground path driven by the vehicle, while a *measurement pass* refers to a specific set of measurements made on a particular track. Each measurement pass can be further divided into "A" and "B", representing the specific direction driven by the vehicle on a particular track. On each day, two different 1000 m tracks (Track #1 and Track #2) are chosen to compare with measurements made on the tripod. Track #1 is centered on the location of the tripod and consists of an equal amount of highway on either side of the tripod (i.e., 500 m before the tripod and 500 m after the tripod). Track #2 however begins 120 m away from the tripod and continues for 1000 m, thus it does not include the highway directly in front of the tripod. Track #1 and Track #2 (for each day) are displayed in Fig. 3.2 as yellow and blue lines, respectively. The location of the tripod in Fig. 3.2 is displayed as a marker with a star enclosed. Track #1 and Track #2 are chosen to examine how the choice of measurement track impacts the comparison of turbulence statistics between the car and tripod. Table 3.1 gives the number of measurement passes performed on each day, and the amount of measurement passes that are excluded due to traffic ahead of the instrumented car. Two extra unique measurement passes corresponding only to Track #2 were also analyzed on 22 Aug, where the car was parked at the tripod and then drove away (a constant vehicle speed was attained before 120 m).

Table 3.1: The number of measurement passes completed on 20 and 22 Aug.

Date	Track #1	Track #2	Unique Measurement Passes	Excluded (traffic ahead)
20 Aug	6	6	7	1
22 Aug	5	7	9	2

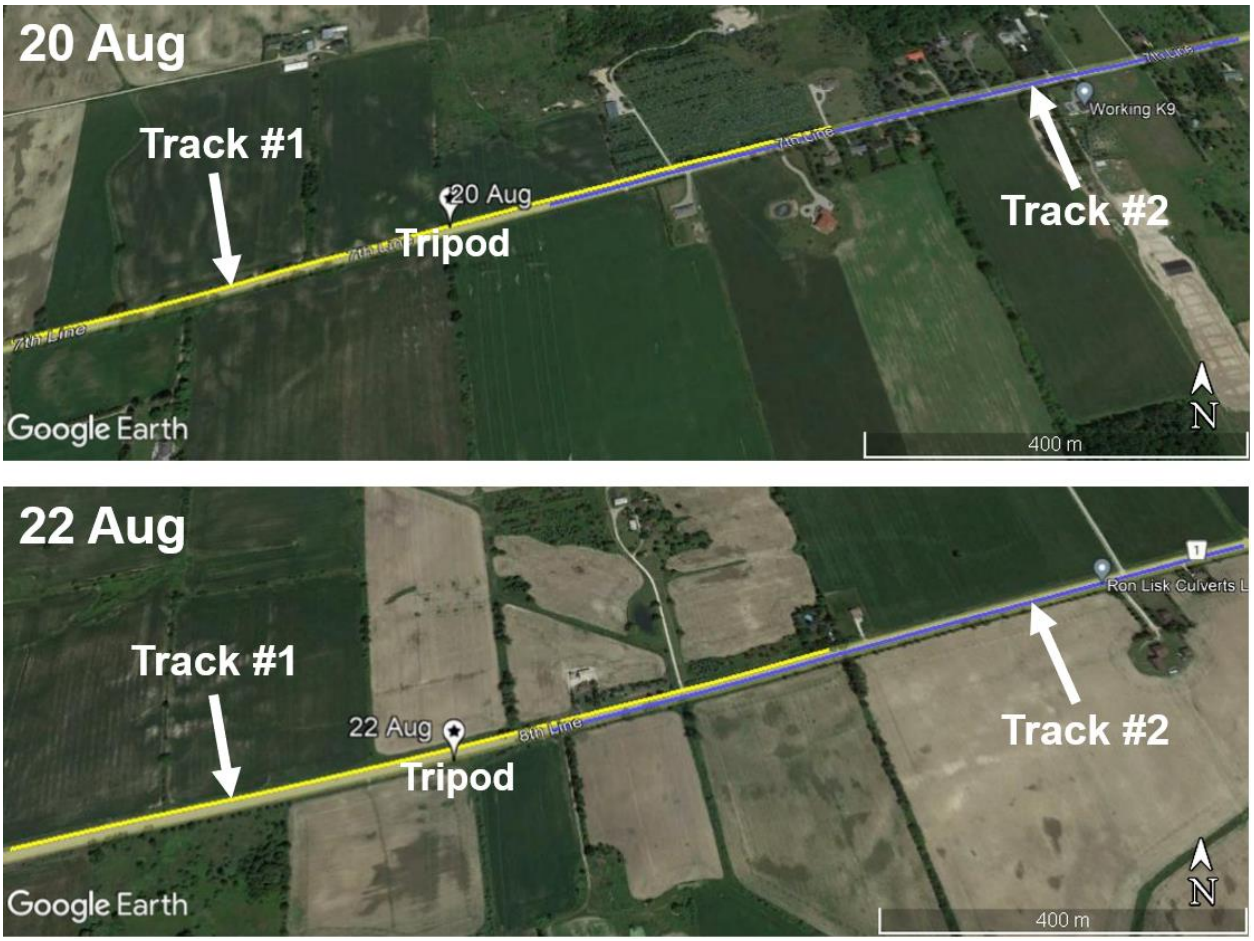

Figure 3.2: The measurement site on 20 Aug (top) and 22 Aug (bottom) with the 1000 m tracks driven by the car superimposed. Track #1 is shown as a yellow line and Track #2 is shown as a blue line. Track #1 is centered on the location of the tripod and therefore 500 m of highway is included in Track #1 on either side of the tripod location. Track #2 begins 120 m away from the tripod and therefore it does not include any measurements made on the highway directly in front of the tripod. © Google Earth Images.

3.2.4 Flow distortion and senor corrections

Measurements made on an instrumented car may be significantly impacted by flow distortion. Flow distortion originates from vehicle movement (speed s) and from the ambient horizontal wind (u_H) that is present even when the vehicle is stationary; u_H may be at an angle to the vehicle, potentially leading to flow distortion in both components of the measured horizontal velocity (i.e., u_m, v_m). Further impacts on the measurements can occur from sensor misalignment and sensor limitations that occur while measuring

in high flow velocities. Flow distortion at the location of the sonic anemometer is investigated by analyzing measurement passes that are separated into part A and B. A and B are each driven on the same length of highway, but in opposite directions (following Belusic et al. 2014). Before investigating flow distortion, the sonic anemometer data are filtered for spikes. Here a spike is defined as an unrealistic sequence of 2 or less data points and is identified by applying a non–linear median filter according to Starkenburg et al. (2016). For the measurements considered in this paper, the effect of this spike removal on the calculated statistics is minimal (i.e., in any measurement pass there are 2 or less flagged values). Measurements flagged as spikes are removed and replaced with linearly interpolated values. If it is assumed that the mean ambient vertical velocity $\overline{w} \approx 0$ m s^{-1} and that the flow is in steady state during A and B with measurements made at a constant vehicle speed s then following Belusic et al. (2014) and Miller et al. (2019), we can assume three relationships (here an uppercase variable (U, V, W, S) represents an averaged or binned value, while a lowercase variable represents an individual measurement).

I. Without flow distortion, the average measured vertical velocity (W) at any measured longitudinal velocity (U) is expected to be equal to 0, over a sufficiently long record. That is, W is not expected to have any dependence on U. However, in the presence of flow distortion on the mobile car, W becomes a function of U.

II. The average velocity recorded over both travel directions (U_{AB} as a function of S) is expected to follow the relationship $U_{AB}(S) = 0.5(U_A(S) + U_B(S)) = S$, since any wind component parallel to the direction of vehicle motion is cancelled out by travelling the same distance in both directions.

III. The lateral velocity V measured over all of A and all of B is expected to follow the relationship $V_{AB} = 0.5[V_A + V_B] = 0$, since the coordinate system rotates 180° when the vehicle changes direction.

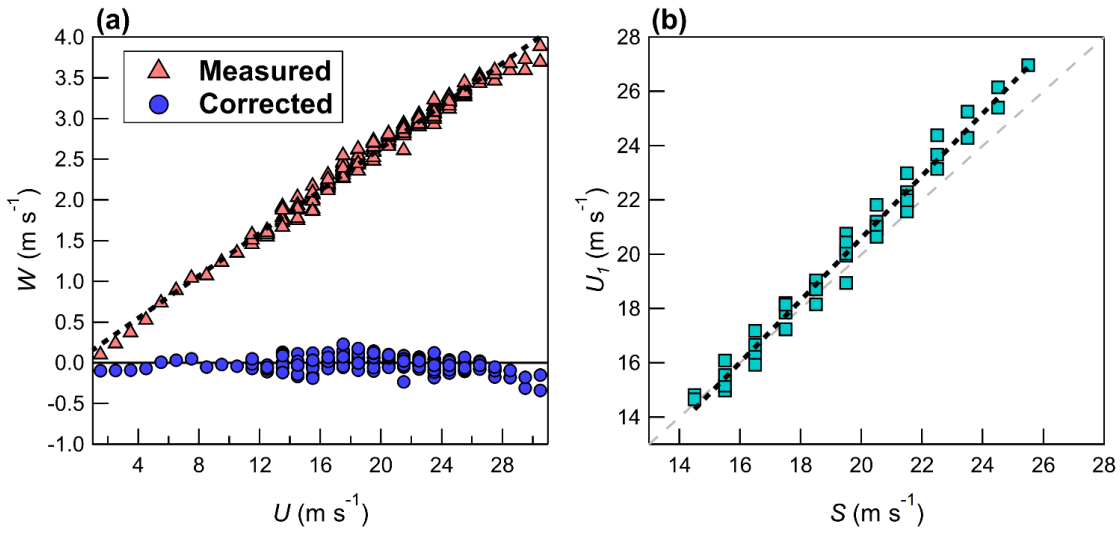

Figure 3.3: (a) The measured vertical velocity W (red) plotted as a function of the measured longitudinal velocity U and the corrected vertical velocity W_c (blue) after application of Eq. 3.1; (b) the measured U_1 as a function of vehicle speed S (after application of Eq. 3.1). Measurements are binned using a bin size of 1 m s^{-1}. Data shown are for both 20 and 22 Aug. Black dashed lines give a least square fit: (a) $W = 0.03 + 0.13U$ ($R^2 = 0.99$) and (b) $U_1 = -2.34 + 1.147S$ ($R^2 = 0.98$).

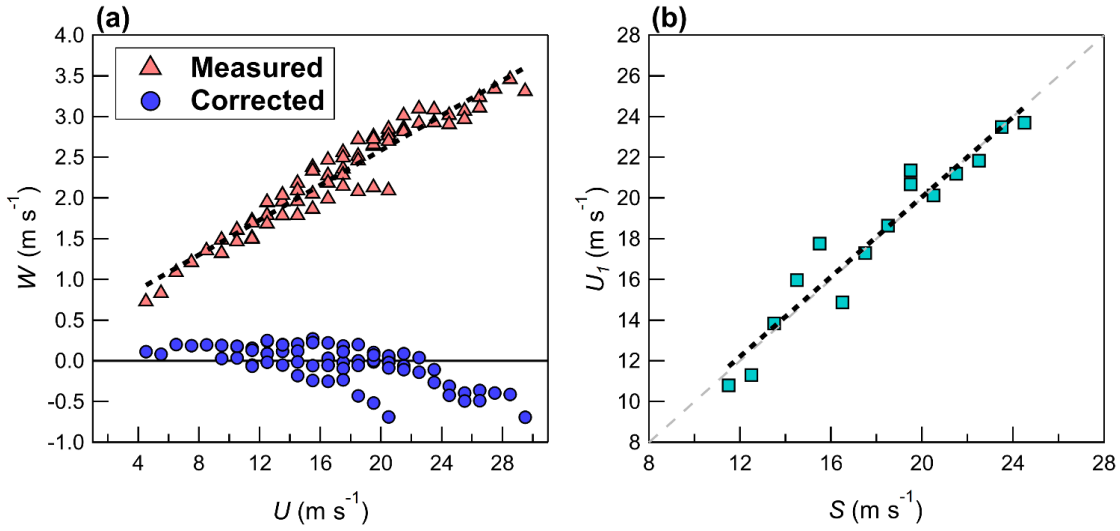

Figure 3.4: Corrections as shown in Fig. 3.3, except for 30 Aug. Black dashed lines give a least square fit: (a) $W = 0.45 + 0.11U$ ($R^2 = 0.96$) and (b) $U_1 = 0.44 + 0.98S$ ($R^2 = 0.92$).

Figure 3.3 (a) shows W binned according to U, with binning completed using a bin size of 1 m s^{-1}. The data shown in Fig. 3.3 includes all back–and–forth passes completed on 20 and 22 Aug. The anemometer was not removed from the vehicle between 20 and 22 Aug, therefore the results should be consistent across both days. Figure 3.3 (a) demonstrates that flow distortion at the measurement location is significant in this study, and W increases linearly with increasing U (coefficient of determination, $R^2 = 0.99$). The measured

velocity field is corrected by applying a coordinate rotation to give a zero mean vertical velocity (assuming there is no flow distortion effect in v_m) as

$$u_1 = u_m \cos\theta + w_m \sin\theta, \quad (3.1\text{ a})$$

$$w_c = -u_m \sin\theta + w_m \cos\theta. \quad (3.1\text{ b})$$

Here θ is set to the median of θ_b, where $\theta_b = \text{atan}(W_b/U_b)$ and subscript b represents individual binned values of 1 m s^{-1} size (i.e., from Fig. 3.3 (a)). θ_b does not show any dependence on U for the vehicle speeds investigated in this study (i.e., for S > 15 m s^{-1}; see Fig. D1 in the supplementary material). For the data shown in Fig. 3.3 (a), θ = 7.54º (interquartile range of 0.32º).

Figure 3.3 (b) shows U_1 binned according to S. In Fig. 3.3 (b) at S > 17 m s^{-1} the results suggest that U_1 is overestimated. The same analysis performed on 30 Aug did not show this overestimation in U_1 for higher S (Fig. 3.4 (b)), however the setup on 30 Aug used a sonic anemometer that is rated for higher flow velocities, up to 60 m s^{-1} (Applied Technologies, model "A"). This suggests that the overestimation in U_1 on 20 and 22 Aug for S > 17 m s^{-1} is likely an instrument–related limitation rather than a direct effect of flow distortion. Taking the difference between the least square fit and the expected relationship (i.e., $U_1 = S$) the overestimation in u_1 (i.e., after applying Eq. 3.1) is

$$u_{excess}(s) = \max(0, -2.34 + 0.147s). \quad (3.2)$$

The overestimation, $u_{excess}(s)$ is then removed from u_1 to give u_c as

$$u_c(s) = u_1(s) - u_{excess}(s). \quad (3.3)$$

No corrections are applied to v_m since there is no clear relationship with any measured variable (i.e., U, S; see Fig. D2). The corrections outlined in Eq. 3.1 through Eq. 3.3 are applied to all vehicle measurements from 20 and 22 Aug, for which s > 0 m s^{-1}. After correction for flow distortion the 1 Hz vehicle speed is linearly interpolated to 40 Hz and then removed from u_c to give the meteorological wind speed component parallel to the direction of motion as (Belusic et al. 2014)

$$u = u_c - s. \tag{3.4}$$

3.2.5 Wavelet analysis and the quantification of sporadic passing traffic

The continuous wavelet transform of a discrete time series x containing N data points, measured at a time step Δt is calculated as (Torrence and Compo, 1998)

$$G_n^x(a) = \sum_{n'=0}^{N-1} x_{n'}\, \psi_0^* \left(\frac{(n'-n)\Delta t}{a}\right). \tag{3.5}$$

The wavelet coefficients are calculated as the convolution of x with a dilated (a) and translated (n) wavelet function ψ_0, where a is referred to as the wavelet scale and n is a localized time (position) index. If ψ is complex, then the complex conjugate ($*$) is used to calculate $G_n^x(a)$. Following Torrence and Compo, (1998), the analyzing wavelet is normalized to have unit energy, so that

$$\psi_0 = \sqrt{\frac{\Delta t}{a}}\psi. \tag{3.6}$$

Where ψ in this work is the complex Morlet wavelet,

$$\psi(\eta) = \pi^{-0.25} e^{6i\eta} e^{-\eta^2/2}. \tag{3.7}$$

The Morlet wavelet is chosen since it has been shown to be well suited for the analysis of atmospheric turbulence (Strunin and Hiyama, 2004; Salmond 2005; Schaller et al. 2017). The total energy (or wavelet variance) of the entire time series is preserved in the wavelet transform and can be recovered by summing the scaled–averaged wavelet power over all scales (j) and times (n),

$$\sigma_x^2 = \frac{\Delta j \Delta t}{C_\delta N} \sum_{n=0}^{N-1} \sum_{j=0}^{J} \frac{1}{a_j} \left|G_n^x(a_j)\right|^2, \tag{3.8}$$

where Δj = 0.25 determines the spacing between discrete scales $a_j = a_0 2^{j\Delta j}$ (a_0 = 2Δt) and $C_\delta = 0.776$ is a wavelet specific reconstruction factor for the Morlet wavelet. The Morlet wavelet scale can be converted to an equivalent Fourier scale (i.e., period) as $\tilde{a}_j = 1.03 a_j$. Like the wavelet variance, given time series x_n and y_n, the wavelet covariance (or turbulent flux) can be calculated as

$$\overline{x'y'} = \frac{\Delta j \Delta t}{C_\delta N} \sum_{n=0}^{N-1} \sum_{j=0}^{J} \frac{1}{a_j} \Re[G_n^x(a_j) G_n^{y*}(a_j)], \quad (3.9)$$

where the real part ($\Re$) of the wavelet cross–spectrum defines the wavelet co–spectrum, and the imaginary part gives the wavelet quadrature spectrum (Strunin and Hiyama, 2004; Paterna et al. 2016). For a 1000 m track consisting of $N_T = T/\Delta t$ ($T \in \mathbb{Z}$ is the integer second length of the track) measurements the wavelet variance including time scales up to index a^* can be calculated as

$$\sigma^2_{x\,1\text{ km}} = \frac{\Delta j \Delta t}{C_\delta N_T} \sum_{n=0}^{N_T-1} \sum_{j=0}^{a^*} \frac{1}{a_j} \left|G_n^x(a_j)\right|^2. \quad (3.10)$$

In Eq. 3.10 index value a^* represents the maximum wavelet scale, which is set to match T as closely as possible. $G_n^x(a_j)$ is calculated from a time series with a temporal length 11 times that of $\sigma^2_{x\,1\text{ km}}$, and the times corresponding to $\sigma^2_{x\,1\text{ km}}$ are at the center of the period. The additional data before and after $\sigma^2_{x\,1\text{ km}}$ (equivalent to about 10 km) represents driving in the vicinity of the tripod, and in most cases on the same road. The instrumented car did not come to rest during this additional driving, except briefly (< 5 s) at a stop sign or to reverse directions. The inclusion of the extra time series before and after the actual track ensures that the wavelet transform coefficients used to calculate wavelet variances and covariances are not impacted by edge effects for scales up to a^* (i.e., they do not lie outside of the cone of influence), while still retaining good computational efficiency (Torrence and Compo, 1988; Schaller et al. 2017). $\sigma^2_{x\,1\text{ km}}$ can be decomposed to give the wavelet variance for each second of the track (likewise with scales up to index a^*), as

$$\sigma^2_{x_i\,1\,s} = \frac{\Delta j \Delta t}{C_\delta N} \sum_{n=i/\Delta t}^{(i+1)/\Delta t-1} \sum_{j=0}^{a^*} \frac{1}{a_j} \left|G_n^x(a_j)\right|^2, \quad (3.11)$$

where $i = 0, 1, \ldots, T-1$, $N = 1/\Delta t$ and

$$\sigma^2_{x\,1\text{ km}} = \frac{1}{T} \sum_{i=0}^{T-1} \sigma^2_{x_i\,1\,s}. \quad (3.12)$$

The wavelet variance calculated for each second allows the effects of sporadic passing traffic to be removed by excluding times when traffic is likely affecting the measurements made on the car (as determined by manual inspection of the video recordings), calculated as

$$\sigma_{x}^{2}{}_{F\,1\text{ km}} = \frac{1}{T_f}\sum_{i=0}^{T-1}\delta_i\sigma_{x_i}^{2}{}_{1\,s}, \tag{3.13}$$

where $\delta_i = \begin{cases} 0, & \text{if traffic} \\ 1, & \text{otherwise} \end{cases}$ and $T_f = \sum_{i=0}^{T-1}\delta_i$.

Using the real part of the wavelet coefficients, the original time series x can be reconstructed at each n. By limiting the scales (for example selecting scales $j = J_{\min}$ to $j = J_{\max}$) a wavelet filtered time series can be constructed at each n as

$$x_n^f = \frac{\Delta j\sqrt{\Delta t}}{C_\delta \psi_0(0)}\sum_{j=J_{\min}}^{J_{\max}}\frac{1}{\sqrt{a_j}}\Re\left[G_n^x(a_j)\right], \tag{3.14}$$

where $\psi_0(0) = \pi^{-0.25}$ for the Morlet wavelet. Calculation of the wavelet transform is computationally intensive when Eq. 3.5 is used. By applying the convolution theorem, the wavelet transform can be completed much faster in Fourier space and this approach is used here; the software developed to perform the continuous wavelet transform has been converted to IGOR Pro from Matlab code available online by Torrence and Compo (1998).

3.2.6 Coordinate rotation

To compare the measurements made on the tripod to those made on the car, the coordinate systems must be consistent. The initial step is to rotate the individual measurements made on the vehicle into a meteorological coordinate system (i.e., u_{met} positive toward the east and v_{met} positive toward the north) using the vehicle's heading. This rotation is necessary since the vehicle's heading may change along the measurement path, leading to a varying sonic anemometer coordinate system along a driven path. For driven paths with large curvature, not performing the transformation to meteorological coordinates gives incorrect mean values (and variances) that are used to determine the rotation angles needed for transformation into a streamwise coordinate system. For the highways investigated in this study, the vehicle heading remains rather consistent over their length; hence our analysis only applies to straight vehicle motion, and we do not determine uncertainties due to measurements through road curvature.

After rotation into meteorological coordinates, each track (on the car and tripod) is then rotated into a mean streamwise coordinate system following Wilczak et al. (2001), where $\bar{u}$ is the mean wind and $\bar{v} = \bar{w} = 0$. The wavelet variances and covariances are likewise rotated into mean streamwise coordinates (unless otherwise indicated) using the same rotation angles applied to rotate the eddy–covariance results.

3.2.7 Sampling errors

a. Random measurement uncertainty

For the calculation of turbulence statistics, the use of a finite record length gives rise to a random measurement uncertainty since the record will not contain enough independent samples to accurately represent the ensemble mean (Lenschow et al. 1994). Further random measurement uncertainty can be introduced by non–stationarity in the record and white noise in the measured signal (Rannik et al. 2016). In this work, the magnitude of the random measurement uncertainty is estimated using two methodologies. All uncertainty estimations are after correction for flow distortion and rotation into a streamwise coordinate system. The first method developed by Mann and Lenschow (1994) can be defined as

$$\delta_{ML} = |\overline{w'q'}| \left(\frac{2I_{wq}}{T}\right)^{\frac{1}{2}} \left(\frac{1+r_{wq}^2}{r_{wq}^2}\right)^{\frac{1}{2}} (1 - az^*), \tag{3.15}$$

with the integral time scale (I_{ws}) calculated as

$$I_{wq} = \int_0^\infty R_{wq}(\tau)\, \mathrm{d}\tau. \tag{3.16}$$

I_{wq} is estimated by numerically integrating the autocorrelation function to the first zero crossing. In Eq. 3.15, $z^* \cong 0$ near the surface, $r_{wq} = \frac{\overline{w'q'}}{\sigma_w \sigma_q}$ is the correlation coefficient between w and q, and T is the averaging period (in seconds) over which the covariance is calculated. For neutral stability, I_{wq} can be approximated as z/s (Finkelstein and Sims, 2001). For a vehicle with a measurement height of z_m = 1.7 m, a mean wind speed of $\bar{u} \approx 2.5$ m s^{-1}, and a constant vehicle speed of s = 25 m s^{-1}, $I_{wq} \approx 0.07$ s. For the stationary tripod (s = 0) at a slightly lower height of z_m = 1.4 m, I_{wq} = 0.56 s for the same wind speed. For a covariance of scalar q with the vertical velocity w, the instantaneous flux is calculated as $\varphi' = w'q' = (w - \bar{w})(q - \bar{q})$ and φ' is used to estimate the autocorrelation function needed for calculation of the integral

time scale (I_{wq}) from Eq. 3.16 (Rannik et al. 2016). The instantaneous flux is introduced since the cross–correlation is an asymmetric function making it unsuitable for estimation of the I_{wq}.

The second methodology outlined in Finkelstein and Sims (2001) gives an estimation of the variance of a covariance (δ_{FS}),

$$\delta_{FS} = \sqrt{var(\overline{w'q'})} = \left[\frac{1}{N}\left(\sum_{p=-m}^{m} \hat{\gamma}_{q,q}(p)\hat{\gamma}_{w,w}(p) + \sum_{p=-m}^{m} \hat{\gamma}_{q,w}(p)\hat{\gamma}_{w,q}(p)\right)\right]^{1/2}, \quad (3.17)$$

where m is the number of samples required to ensure the integral time scale (ITS) is sufficiently captured. $\hat{\gamma}_{w,w}(p)$ and $\hat{\gamma}_{w,q}(p)$ are the unbiased autocovariance and cross–covariance respectively, expressed as

$$\hat{\gamma}_{w,w}(p) = \frac{1}{N-p}\sum_{i=1}^{N-p}(w_i - \overline{w})(w_{i+h} - \overline{w}), \quad (3.18)$$

and

$$\hat{\gamma}_{q,w}(p) = \frac{1}{N-p}\sum_{i=1}^{N-p}(q_i - \overline{q})(w_{i+h} - \overline{w}). \quad (3.19)$$

The value of m is determined by calculating δ_{FS} as a function of m and choosing the value at which δ_{FS} reaches a constant or asymptotic value as m is further increased. For the roadside tripod a value of $m = 300$ s is determined, while for the vehicle measurements $m = 30$ s (see Fig. D4 and Fig. D5)

For wavelet analysis, Eq. 3.14 is applied to generate a wavelet reconstructed time series (q_f and w_f) for scales up to a^*. Thus, the reconstructed time series will exclude low frequency contributions attributed to wavelengths λ > 1000 m. The reconstructed time series are then rotated into mean streamwise coordinates and subsequently used in Eq. 3.18 and Eq. 3.19 to estimate δ_{FS} for the wavelet covariance (and likewise for wavelet variances).

b. Random measurement uncertainty due to instrument noise only

The sonic anemometer's signal may be impacted by white noise, a form of random measurement uncertainty. Lenschow et al. (2000) consider a stationary time series with its mean removed (i.e., $w'(t)$) that is impacted by (uncorrelated) white noise, $\epsilon(t)$, where the autocovariance function is

$$\gamma_{w,w}(\tau) = \overline{(w' + \epsilon')(w'_{t+\tau} + \epsilon'_{t+\tau})} = \overline{w'w'_{t+\tau}} + \overline{w'\epsilon'_{t+\tau}} + \overline{w'_{t+\tau}\epsilon} + \overline{\epsilon'\epsilon'_{t+\tau}}. \quad (3.20)$$

Since $w(t)$ and $\epsilon(t)$ are uncorrelated, $\epsilon(t)$ is present only at zero lag and so $\overline{w\epsilon} = 0$. Equation 3.20 then reduces to $\gamma_{w,w}(\tau) = w'w'_{t+\tau}$, with $\gamma_{w,w}(0) = \overline{w'^2} + \overline{\epsilon'^2}$. Based on the inertial subrange theory by Kolmogorov, the autocovariance function is expected to follow (Lenschow et al. 2000; Wulfmeyer et al. 2010; Bonin et al. 2016),

$$\gamma_{w,w}(\tau) = \overline{w'^2} - C\tau^{\frac{2}{3}}, \quad (3.21)$$

where constant C is associated with turbulent eddy dissipation. To estimate $\overline{\epsilon'^2}$, Eq. 3.21 is typically fit to the first 5 lags of the autocovariance function, corresponding to time lags of 0.1 to 0.5 s for a 10 Hz signal of a sonic anemometer (Rannik et al. 2016). For Doppler lidar measurements of the vertical velocity in convective conditions, Bonin et al. (2016) fit Eq. 3.21 to the autocovariance function for time lags up to half the integral time scale (i.e., $\tau = 0.5I_{ww}$). The fit is then extrapolated back to zero lag to give $\gamma_{w,w}(\rightarrow 0)$, and the variance attributed to white noise in the measured signal is then estimated as (Lenschow et al. 2000; Mauder et al. 2013)

$$\overline{\epsilon'^2} = \Delta\gamma_{w,w} = \gamma_{w,w}(0) - \gamma_{w,w}(\rightarrow 0). \quad (3.22)$$

Some authors report a poor fit to Eq. 3.21 and instead apply a linear fit extrapolation back to zero lag to determine Eq. 3.22 (Lenschow et al. 2000; Mauder et al. 2013; Langford et al. 2015). For measurements obtained on the tripod and instrumented car, a linear fit extrapolation in addition to Eq. 3.21 are used to estimate $\overline{\epsilon'^2}$. For tripod measurements time lags up to 0.5 s are used to determine the fit, but for the car travelling at vehicle speeds near 20 m s^{-1}, only the first 3 points (up to 0.075 s) of the autocovariance function are used. Eq. 3.21 may lead to an extrapolated value at zero lag larger than $\gamma_{w,w}(0)$, which gives 'negative' and thus undefined $\overline{\epsilon'^2}$. Bonin et al. (2016) noted a similar finding in their investigation when fitting the autocovariance function to Eq. 3.21 for the vertical velocity measured from Doppler lidar. They hypothesize that the undefined $\overline{\epsilon'^2}$ occurs when the genuine white noise in the signal is minimal and the smallest scales of turbulence remain unresolved. Therefore, when $\overline{\epsilon'^2}$ is negative and undefined we assume that the true white noise is minimal and that $\overline{\epsilon'^2} \approx 0$. Thus, for the analysis herein $\overline{\epsilon'^2} = \max(\overline{\epsilon'^2}, 0)$.

3.2.8 Comparison of mobile car measurements to tripod measurements

In this work, we follow the approach of Belusic et al. (2014) and select a fixed ground path to investigate means, variances and covariances on the car. Two different fixed 1000 m ground paths (L) are considered, referred to as Track #1 and Track #2, and these tracks are compared to measurements made by the tripod (see Sect. 3.2.3).

The averaging period (T) on the tripod is set to 5 min for atmospheric means, but for atmospheric variances and covariances T varies depending on the mean wind speed measured by the tripod ($\bar{u}$) according to Taylor's frozen hypothesis as $T = L/\bar{u}$, where L = 1000 m. For the two measurement days investigated here, T on the tripod ranges between 6 and 8 min. For consistency, the averaging period used for calculation of the tripod means, variances and covariances is centered on the time that the instrumented car passes the tripod (for both Track #1 and Track #2). Refer to Table 3.1 for the number of measurement passes corresponding to each day. For the car, any measurement pass that follows closely behind a vehicle is excluded from the results.

3.3 Results and discussion

3.3.1 Mean wind speed and mean wind direction

Figure 3.5 shows a scatter plot of (a) the 5 min mean wind direction on the tripod compared to the mean wind direction measured on the mobile car and (b) the 5 min mean wind speed measured on the tripod compared to the mean wind speed measured on the mobile car. The mean wind speed shown is after rotation into streamwise coordinates. The grey lines in Fig. 3.5 denote a specific percentage of the tripod measured value (i.e., 100% gives a one–to–one relationship) and this convention is used in the figures that follow. The mean bias error, $\mathrm{MBE} = (1/N)\sum_{i=1}^{N}(M_c - M_t)$, and the root mean squared error, $\mathrm{RMSE} = (1/N)\sum_{i=1}^{N}\sqrt{(M_c - M_t)^2}$ are given in Table 3.2. Here, the subscripts c and t refer to the car and the tripod. The tripod is therefore used as a 'ground truth' for the car measurements.

Table 3.2: Statistics calculated over all measurement passes (i.e., on both tracks on 20 and 22 Aug). Subscript EC denotes a statistical variance or a covariance calculated using eddy–covariance. A subscript W denotes a variance or covariance calculated using wavelet analysis.

	MBE_{EC}	MBE_{W}	RMSE_{EC}	RMSE_{W}	Mean_{EC} Car	Mean_{W} Car	Mean_{EC} Tripod
$\overline{u'^2}$ (m^2 s^{-2})	0.90	0.44	1.44	0.75	2.15	1.69	1.26
$\overline{v'^2}$ (m^2 s^{-2})	0.20	0.04	0.61	0.44	1.38	1.21	1.19
$\overline{w'^2}$ (m^2 s^{-2})	–0.11	–0.12	0.12	0.13	0.17	0.16	0.29
$\overline{u'w'}$ (m^2 s^{-2})	0.005	0.02	0.08	0.08	–0.13	–0.11	–0.14
$\overline{w'T'}$ (K m s^{-1})	–0.05	–0.04	0.06	0.06	0.08	0.08	0.13
$\bar{u}$ (m s^{-1})	0.04		0.53		2.45		2.42

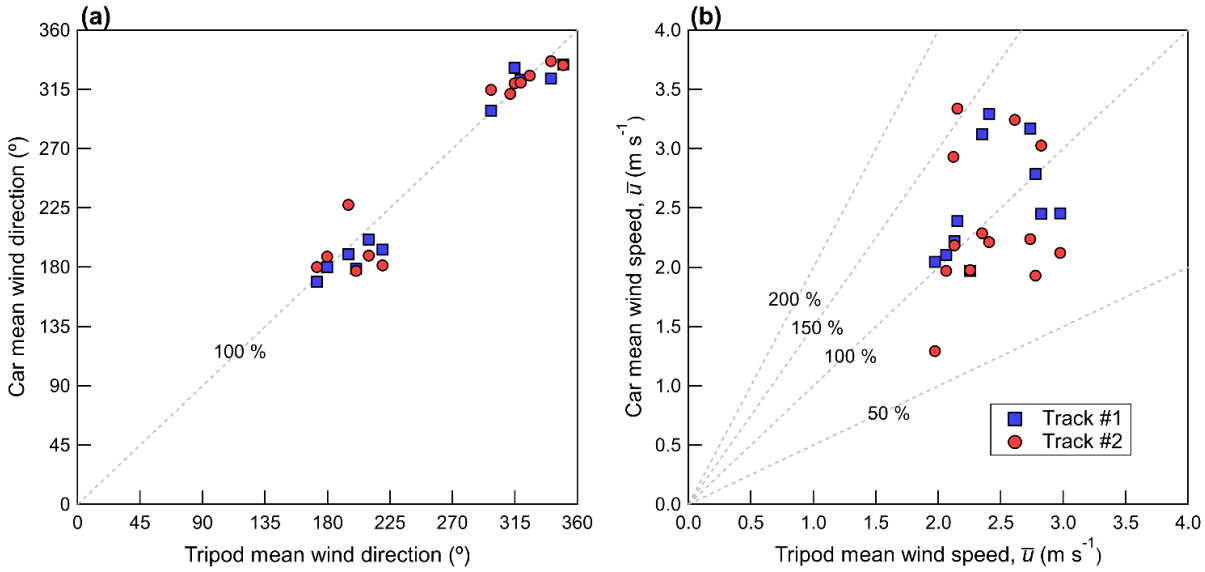

Figure 3.5: A scatter plot showing the mean wind direction (a) and mean wind speed (b) measured by the tripod and compared to the mobile car. Dashed grey lines denote constant percentages of the independent variable.

The mean wind speed shown in Fig. 3.5 (b) shows relatively good agreement between the car and tripod; the car $\bar{u}$ = 2.45 m s^{-1} while the tripod $\bar{u}$ = 2.42 m s^{-1} (car RMSE = 0.53 m s^{-1}). When the analysis is separated by tracks, the agreement is best for Track #1; RMSE = 0.43 m s^{-1} and 0.71 m s^{-1} for Track #1 and Track #2 respectively (see Table D1 and Table D2). If $\bar{u}$ measured on the tripod is used as a normalizing factor, the normalized root–mean squared error of $\bar{u}$ (NRMSE) is 18% and 30% for Track #1 and Track #2 respectively. The mean wind direction on the car agrees well with the tripod on both Track #1 and Track #2 as shown in Fig. 3.5 (a), where most points fall within 20º of the one–to–one line.

To investigate how the car performs for shorter averaging periods, non–overlapping intervals of 10 s duration are examined on 20 and 22 Aug. There are 263 and 250 such intervals on 20 and 22 Aug respectively and these represent times that the vehicle is driving in the vicinity of the tripod (i.e., within about 10 km) and not necessarily on a 1000 m track. The results are shown in Table 3.3, which displays the average meteorological wind components (u_{met} and v_{met}), the mean wind direction, and the mean wind speed (after rotation into streamwise coordinates). Statistics are also shown in Table 3.3, including the median, maximum and minimum values in each set and the interquartile range (IQR). The standard deviation of the wind direction is calculated using the Yamartino algorithm (Turner, 1986). The results show that the wind direction is rather consistent on both days for a shorter averaging period of 10 s, where the wind direction standard deviation is 38° on 20 Aug and 31° on 22 Aug. While the average of all 10 s mean wind speeds on 20 and 22 Aug is consistent with the measurement passes shown in Fig. 3.5 (b), there can be significant variation in each individual interval as demonstrated by the large IQR and maximum/minimum values (IQR = 1.30 m s^{-1} and 1.86 m s^{-1} on 20 and 22 Aug respectively). This

demonstrates that using short averaging periods on the mobile car allows measurement of localized flow variations, where the magnitude of the flow may vary significantly but the direction remains relatively constant in comparison.

Table 3.3: Statistics of the mean flow measured by the car on 20 and 22 Aug. The averaging period is 10 s; therefore, the statistics are calculated from a set of n non–overlapping intervals. Shown are the wind components in a meteorological coordinate system (u_{met}, v_{met}), the mean wind direction calculated from u_{met} and v_{met}, as well as the mean wind speed after rotation into a streamwise coordinate system. Note that $\overline{u}$ includes a component due to the vertical velocity, and hence it may exceed the horizontal wind speed calculated as $u_h = \sqrt{u_{met}^2 + v_{met}^2}$. The standard deviation of the wind direction is calculated using the Yamartino algorithm (Turner, 1986).

	20 Aug (n = 263)						22 Aug (n = 250)					
	Mean	**Std Dev**	**Max**	**Min**	**Median**	**IQR**	**Mean**	**Std Dev**	**Max**	**Min**	**Median**	**IQR**
u_{met} (m s^{-1})	0.30	0.82	—	—	0.26	1.07	1.37	0.96	—	—	1.29	1.35
v_{met} (m s^{-1})	1.63	1.03	—	—	1.56	1.41	–1.73	1.26	—	—	–1.64	1.75
θ (°)	190	38.2	—	—	191	41.9	322	31.0	—	—	318	34.0
$\overline{u}$ (m s^{-1})	1.90	0.92	4.54	0.18	1.72	1.30	2.42	1.23	6.30	0.14	2.40	1.86

3.3.2 Velocity variances and covariances

Figure 3.6 shows the velocity variances measured on the instrumented car compared to the velocity variances measured on the tripod. Figure 3.6 (a), (b) and (c) show $\overline{u'^2}$, $\overline{v'^2}$ and $\overline{w'^2}$ respectively. The velocity variances measured on the car are calculated using the typical statistical approach, denoted as EC (i.e., for time series x with N points, $\sigma_x^2 = (1/N)\sum_{i=1}^{N}(x - \bar{x})^2$) or wavelet analysis (i.e., Eq. 3.10). Only statistical velocity variances measured by the tripod (and covariances calculated using eddy–covariance) are presented herein. For measurements made on the tripod the effect of applying wavelet analysis to calculate variances and covariances is minimal compared to the instrumented car (see Fig. D3). Furthermore, for some measurement passes the Morlet wavelet applied to the tripod suffers from edge effects that cannot be avoided, since the tripod recordings were abruptly ended at the end of each measurement day. For wavelet analysis, the maximum wavelet scale (index a^*) is chosen to correspond as closely as possible to the temporal length of the measurement track to ensure that both calculation methods retain the same spatial scales and are therefore comparable (see Sect 3.2.5). For the car measurement tracks investigated here, the temporal length ranges between 40 and 60 s, and all measurement tracks have a maximum spatial scale of approximately 1000 m.

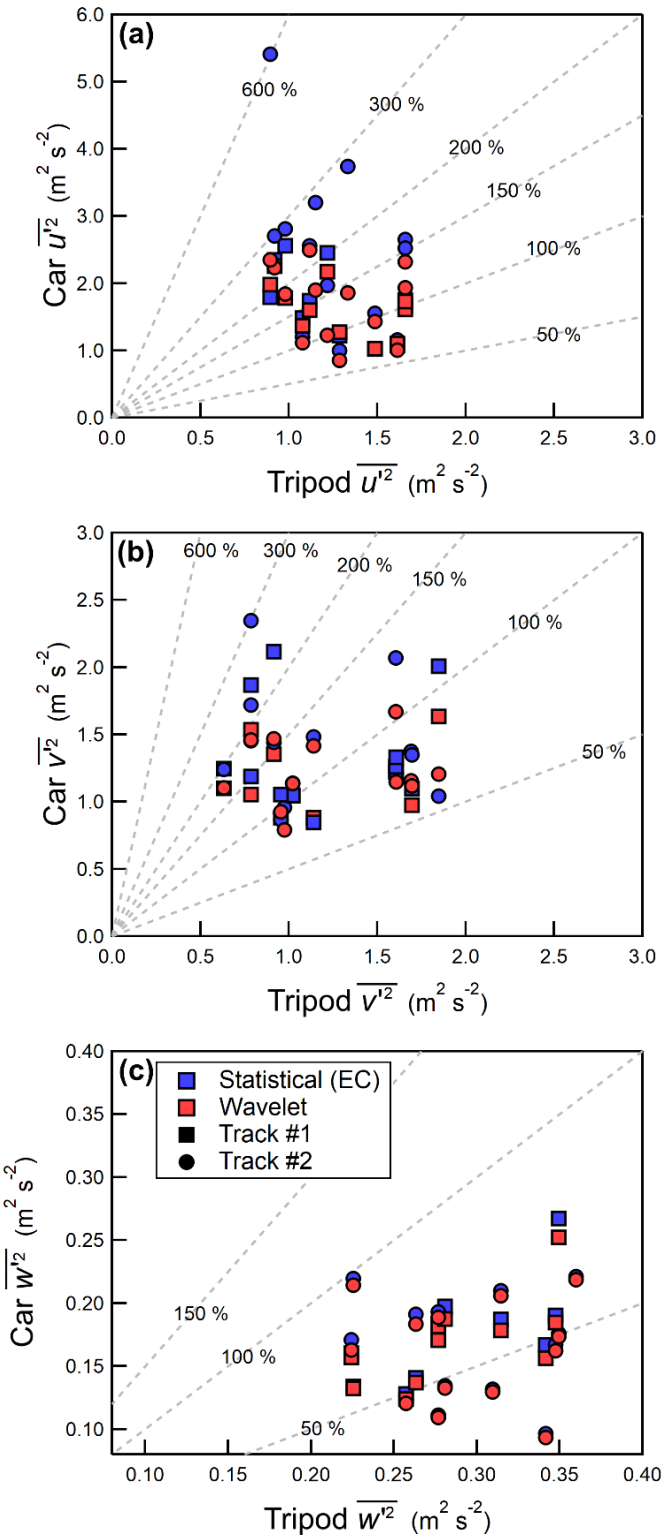

Figure 3.6: The horizontal streamwise velocity variance, $\overline{u'^2}$ (a), the lateral velocity variance, $\overline{v'^2}$ (b) and the vertical velocity variance, $\overline{w'^2}$ (c) measured by the tripod (horizontal) and compared to the instrumented car (vertical). Variances calculated using either wavelet analysis or EC and are shown as red and blue markers respectively. Dashed grey lines denote constant percentages of the independent variable.

Applying wavelet analysis to estimate the horizontal velocity variances leads to a significant reduction in the magnitude compared to EC for some passes, specifically for those passes reporting the largest horizontal velocity variances as shown in Fig. 3.6 (a) and (b). This reduction results in an improved agreement between the two measurement systems; for $\overline{u'^2}$, wavelet analysis gives $\mathrm{RMSE_W}$ = 0.75 m^2 s^{-2} compared to $\mathrm{RMSE_{EC}}$ = 1.44 m^2 s^{-2} for EC. However, retaining larger scales in the wavelet variance calculation (i.e., corresponding to spatial scales exceeding 1000 m) gives horizontal velocity variances that are larger and more similar to EC. This suggests that wavelet analysis can better resolve low frequency variations occurring at spatial scales near and exceeding 1000 m, compared to EC. Low frequency contributions on the car may arise from variation in the flow that results only from a changing upwind environment, and therefore this effect would not be captured by a stationary monitoring station. As discussed in Sect 3.2.5, wavelet analysis is applied to a time series with a temporal length 11 times longer than the time series used to calculate the EC variances, giving wavelet analysis superior low frequency resolution compared to eddy–covariance.

Despite the improved agreement when wavelet analysis is applied to estimate the horizontal velocity variances, there are still instances where $\overline{u'^2}$ and $\overline{v'^2}$ measured by the mobile car are larger than what is measured by the roadside tripod. Given the public highway where the study was conducted, some measurement passes inevitably have sporadic traffic that was travelling in the opposite direction as the mobile car (as determined by visual inspection of the video). The passing traffic can significantly impact the velocity variances measured on the car due to vehicle–induced turbulence, especially in the case of passing heavy–duty trucks (Gordon et al. 2012; Miller et al. 2019). For the measurement passes shown in Fig. 3.6, there are two instances where a heavy–duty truck travelled in the lane opposite to the instrumented car, as well as a few occasions where passenger vehicles (i.e., SUV, cars) travelled past the car.

Figure 3.7 displays the 1 s wavelet variance calculated using Eq. 3.11 for three different measurement passes from Track #2 (on 22 Aug); Fig. 3.7 (a) had 2 simultaneous passing sport utility vehicle (SUV), and Fig. 3.7 (c) had a passing heavy–duty truck followed in quick succession by an SUV. Wavelet analysis is performed on the measured velocities in a meteorological coordinate system (i.e., u_{met}, v_{met}), with a^* extending up the temporal length of the measurement pass (i.e., the same a^* used for the wavelet variances presented in Fig. 3.6). Each measurement pass shown in Fig. 3.7 was performed in the same direction and in the highway lane closest to the tripod (i.e., on the downwind side of the highway). Traffic is denoted by a circled area in the respective figure panel. With these instances of traffic included, the velocity variances are 1.68 m^2 s^{-2}, 1.38 m^2 s^{-2} and 0.21 m^2 s^{-2} for $\overline{u_{met}'^2}$, $\overline{v_{met}'^2}$ and $\overline{w_c'^2}$ respectively. Removing the 1 s wavelet variances corresponding temporally with these passing vehicles (9 seconds in total), gives a $\overline{u_{met}'^2}$, $\overline{v_{met}'^2}$ and $\overline{w_c'^2}$ of 1.47 m^2 s^{-2}, 1.29 m^2 s^{-2} and 0.17 m^2 s^{-2} respectively, representing

about a 10% reduction in the turbulent kinetic energy during this measurement pass. This demonstrates that even limited traffic travelling in the highway lane adjacent to the car (and in the opposite direction) can substantially increase the magnitude of the velocity variances measured by the car on a 1000 m track, especially heavy–duty trucks. In Fig. 3.7 (a), two SUVs passed by the mobile car in quick succession, but the passage of these vehicles is not discernable as a localized increase of the 1 s wavelet variances. This suggests that the vehicle wakes did not advect past the instrumented car during this measurement pass, and thus no removal is warranted.

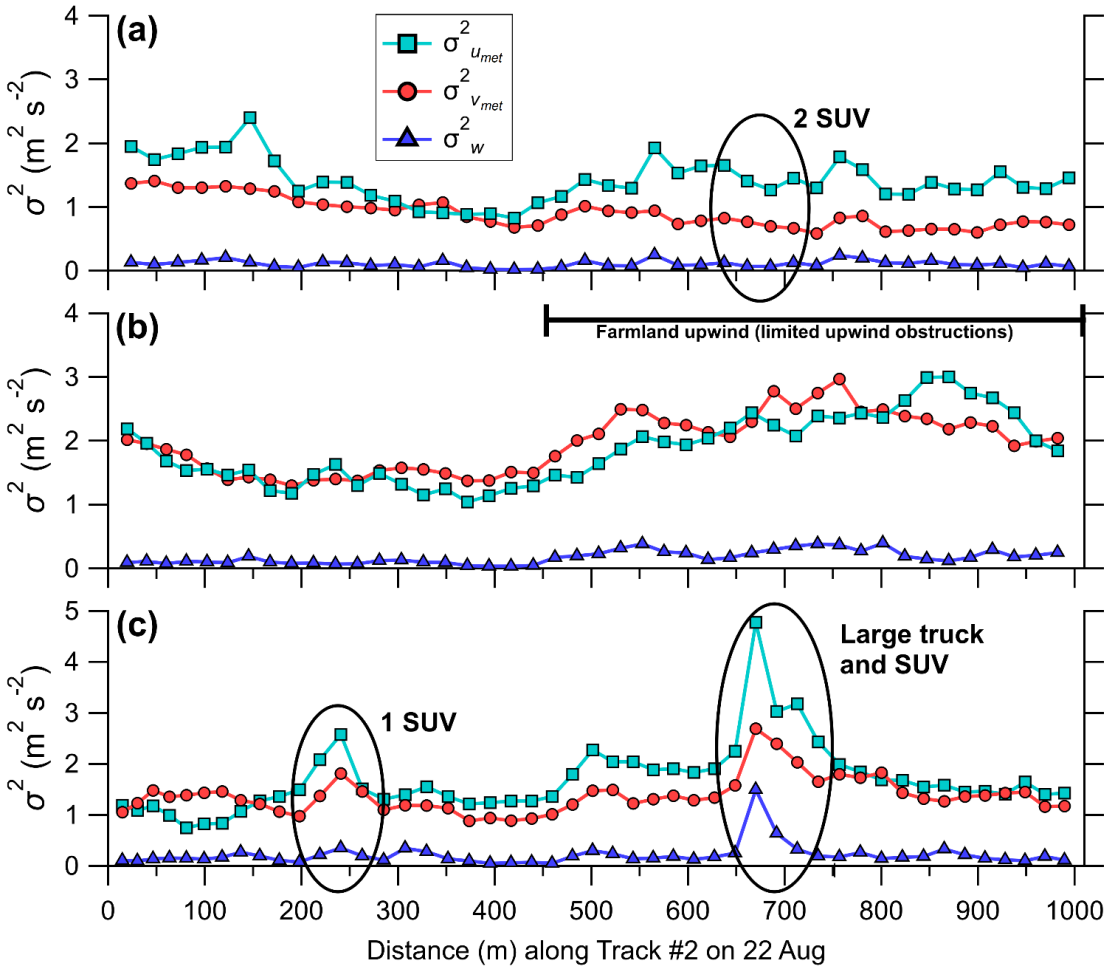

Figure 3.7: Car–measured velocity variances on 3 different 1000 m tracks calculated every second using wavelet analysis. The data shown are from 22 Aug. The black circled areas denote the passage traffic in the lane adjacent to the instrumented car (i.e., traveling in the opposite direction), as determined from visual inspection of the dashcam video. The text located to the right of the circle gives the traffic composition. The data shown are measurements from the lane closet to the tripod. The velocity variances shown are in a meteorological coordinate system.

For the measurement pass shown in Fig. 3.7 (b) there is a noticeable increase in the 1 s horizontal velocity variances about 450 m into the measurement track. A similar trend is also seen in Fig. 3.7 (c).

Before 450 m there are many large trees and houses upwind of the highway, but after 450 m the upwind environment becomes open farmland (i.e., limited obstructions to the mean flow). The presence of many trees and houses in close proximity acts as a windbreak, forcing the flow to accelerate and rise over the surface obstructions. The flow is reduced downwind of the surface obstruction (Taylor and Salmon, 1993; Mochida et al. 2008), and close to the surface just after the obstruction (i.e., the near wake) is the "quiet zone", where the horizontal velocity variances are reduced in comparison with the undisturbed upwind flow (Lee and Lee, 2012; Lyu et al. 2020). Therefore, the reduced horizontal velocity variances for the first few hundred meters of the track may be related to the quiet zone generated by the many trees and houses upwind of the road. After about 450 m the upwind environment becomes relatively open and the flow measured on the car increases, and this increase continues over the remainder of the track. The changing wind speed along the track introduces a trend in the horizontal velocity record measured on the car.

Figure 3.6 (c) displays $\overline{w'^2}$ measured on the mobile car compared to $\overline{w'^2}$ measured on the tripod. The instrumented car $\overline{w'^2}$ is biased low by 30 to 50% ($\mathrm{MBE_{EC}} = -0.11$ m^2 s^{-2}) and applying wavelet analysis to estimate $\overline{w'^2}$ does not improve the agreement between the two measurement systems. The removal of vehicle–induced turbulence from the car measurements (and not the tripod) further decreases $\overline{w'^2}$, in turn increasing the bias between the car and tripod.

Figure 3.8 (a) displays the vertical momentum flux ($\overline{u'w'}$) and Fig. 3.8 (b) shows the sonic heat flux ($\overline{w'T'}$). Figure 3.8 follows the same conventions as Fig. 3.6. Like $\overline{w'^2}$, the sonic heat flux ($\overline{w'T'}$) measured by the mobile car in this study also has a low bias by 30 to 50% compared to the tripod ($\mathrm{MBE_{EC}}$ = –0.05 K m s^{-1}). There is no improvement in the statistical measures if wavelet analysis is used to estimate $\overline{w'T'}$.

The discrepancy between the car and the tripod for $\overline{w'^2}$ and $\overline{w'T'}$ may be related to a mismatch in the flux footprint or possibly related to the rapid flow distortion experienced at the location of the sonic anemometer on the vehicle. The road produces a distinct upward heat flux and an increase in $\overline{w'^2}$ on sunny days because it has a significantly lower albedo than the surrounding grasses and farmland. On 22 Aug we parked on the upwind side of the highway for approximately 30 min, but the car was also parked on the downwind side of the highway during assembly and disassembly of the tripod. For three independent 8 min periods, the average $\overline{w'^2}$ and $\overline{w'T'}$ on the upwind side of the highway are measured at 0.15 m^2 s^{-2} and 0.085 K m s^{-1} respectively. Downwind of the highway $\overline{w'^2}$ and $\overline{w'T'}$ are found to be larger, near 0.33 m^2 s^{-2} and 0.109 K m s^{-1} on average (from 6 independent samples), which are more like the measurements made on the tripod. These findings for $\overline{w'^2}$ are similar to Gordon et al. (2012) who measured $\overline{w'^2}$ = 0.27 m^2 s^{-2} downwind of a four–lane highway on a sunny day.

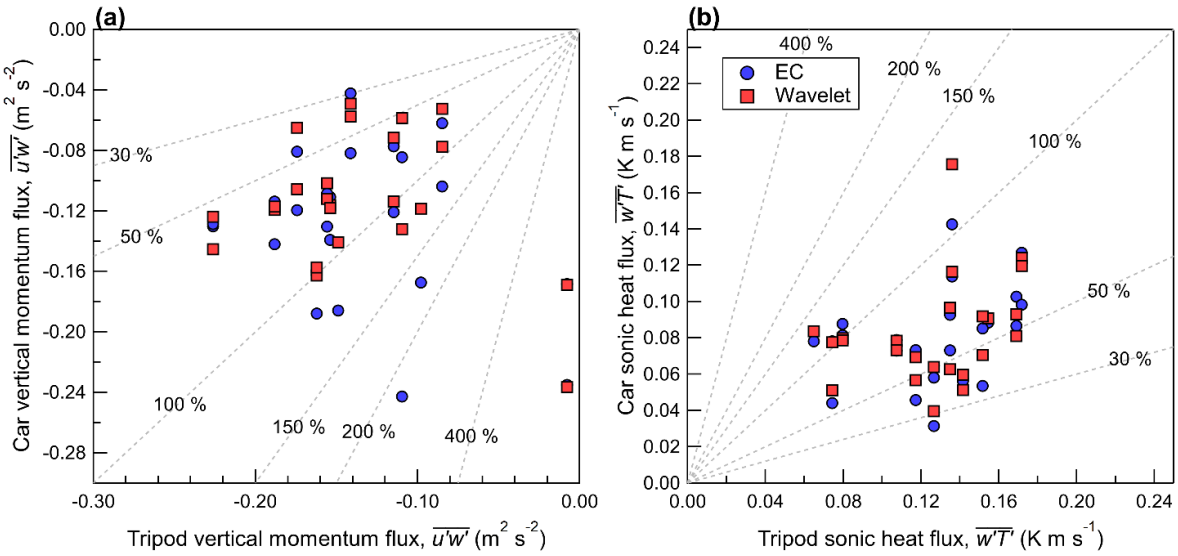

Figure 3.8: The vertical momentum flux, $\overline{u'w'}$ (a) and the sonic heat flux, $\overline{w'T'}$ (b) measured by the tripod (horizontal) and compared to the mobile car (vertical). Covariances calculated using wavelet analysis and EC are shown as red and blue markers respectively. Dashed grey lines denote constant percentages of the independent variable.

To investigate the flux footprint of the tripod versus the instrumented car, the footprint model of Kljun et al. (2015) is applied with $\bar{u}$ = 2.5 m s^{-1}, a boundary layer height of h = 1500 m, a friction velocity of u_* = 0.35 m s^{-1}, an Obukhov length of L = –30 m, $\overline{v'^2}$ = 1.5 m^2 s^{-2} and a wind direction that is assumed perpendicular to the highway. These meteorological values represent estimations based on measurements made on 22 Aug. For the car $z_m \approx$ 1.7 m but for the tripod $z_m \approx$ 1.4 m. However, flow distortion on the mobile car results in the measurements being representative of a lower height than the height at which the instrumentation is installed. Achberger and Bärring (1999) explored the displacement due to flow distortion on a mini–bus and estimated that the displacement at 2 m height was typically on the order of 0.2 m. Therefore, measurements obtained at z_m = 1.7 m on the mobile car in this study are probably representative of a slightly lower height between 1.5 and 1.6 m. For the upper height limit of z_m = 1.7 m, the footprint model predicts that the maximum location of influence to the flux is about 4.2 m upwind of the measurement location. For z_m = 1.5 m it is about 3.7 m upwind. Since the tripod is positioned in the shoulder of the highway, 3.7 m upwind of the tripod is near the center of the highway. Assuming the instrumented car is in the lane closest to the tripod (or about 1.75 m from the edge of the highway), the maximum location of influence to the flux is near 6 m, or near the edge of the highway furthest from the tripod. Therefore, when the car is in the lane closest to the tripod, the measurements have a flux footprint that includes less influence from the highway. The footprint model predicts that the influence from the road is minimized when the car is driving in the lane furthest from the tripod, but for measurements made during this study there is not a significant statistical difference in $\overline{w'^2}$ and $\overline{w'T'}$ for the close versus far highway lane. The footprint model

applied here is strongly impacted by the mean wind speed $\bar{u}$ – a lower $\bar{u}$ gives a location of maximum influence to the flux that is closer to the measurement system.

Another factor that may influence the velocity measurements made by the sonic anemometer is rapid distortion of the flow caused by the moving vehicle. Wyngard (1988) shows that the variance of scalar quantities (such as the sonic temperature or a gas concentration) remains unchanged during rapid flow distortion. The velocity variances, however, may be altered during stretching and compression of the flow as it is forced to rise over the front end of the vehicle, in analogy to isotropic turbulence and flow over a symmetric hill (Britter et al. 1981; Gong and Ibbetson 1989). If it is assumed that the low bias in the measured $\overline{w'^2}$ on the car is caused by rapid flow distortion alone (i.e., no effect from the highway asphalt), then rapid distortion theory would predict a proportional increase in the velocity variance measured parallel to the vehicle motion. However, in the case of the measurements of $\overline{w'^2}$ made during this study, there is likely a contribution from rapid distortion of the flow in addition to a contribution from the flux footprint mismatch between the car and tripod, but it is not possible to separate the effects in this work.

The vertical momentum fluxes, $\overline{u'w'}$ measured by the car and tripod are displayed in Fig. 3.8 (a). For EC there is no significant bias for $\overline{u'w'}$ measured on the car compared to $\overline{u'w'}$ measured on the tripod. The tripod measurements of $\overline{u'w'}$ generally fall within the 95% confidence interval of $\overline{u'w'}$ measured on the car (see Sect. 3.3.4–b). There are instances where $\overline{u'w'}$ measured by the two systems differ significantly however, and this suggests a better estimate of $\overline{u'w'}$ can probably be obtained by averaging multiple passes. The horizontal momentum flux, $\overline{u'v'}$, measured on the tripod does not agree with measurements made on the mobile car (not shown), and when sampling errors are considered $\overline{u'v'}$ measured on the car is not found to be significantly different than zero within the 66 % confidence interval.

3.3.3 Velocity spectra

Figure 3.9 displays the binned power spectral density (multiplied by frequency) of the velocity components for measurement Pass 5 (Fig. 3.9 (a)), Pass 7 (Fig. 3.9 (b)), and Pass 8 (Fig. 3.9 (c)) from Track #1. These three measurement passes have been chosen since they demonstrate unique features in the car spectra, which are representative of the spectra from the remaining measurement passes not shown (see Fig. D6). The frequencies are normalized to give a wavelength as $\lambda = \bar{u}/f$ where f is the frequency (Hz) and $\bar{u}$ is the mean ambient wind on the tripod or the car relative flow on the mobile car. Each panel displays the spectra of u (top), v (middle) and w (bottom). In general, the shape of the spectra measured on the mobile car agree well with the spectra measured by the tripod, however there are some notable differences: (1) Unlike the tripod, the power spectra of u and v measured on the car during Pass 7 and 8 increase at high frequencies ($\lambda < 5$ m). This increase may be related to white noise in the measured signal or perhaps aliasing and is

present in about 75% of the measured spectra from Track #1. Langford et al. (2015) show that the power spectra of the sonic temperature increase linearly with a +1 at high frequencies (in the inertial subrange) in the presence of white noise, resembling the findings in this study for u and v. One potential source of white noise in the measured horizontal velocity components may be road unevenness (Schiehlen, 2006). Belusic et al. (2014) found distinct peaks in their car measured v spectra near a frequency of 7 Hz which they attribute to frame vibrations, and by comparing the sonic measurements to GPS–INS motion they concluded that road unevenness did not impact the high frequency portion of the velocity spectra. (2) For u in Pass 7 and 8 as λ increases past 100 m, the power spectral density increases on the car while on the tripod the power spectral density decreases. (3) In Pass 7 and 8, w appears to be under–sampled since the car spectra do not extend through the entire inertial subrange. Therefore, sampling at high vehicle speeds (> 15 m s^{-1}) would probably benefit from a sampling rate greater than 40 Hz. Additionally, in Pass 5 and 8 there is a general underestimation of the power spectral density of w on the car compared to the tripod for λ between about 5 to 80 m, and this underestimation is a common feature in the measured car spectra.

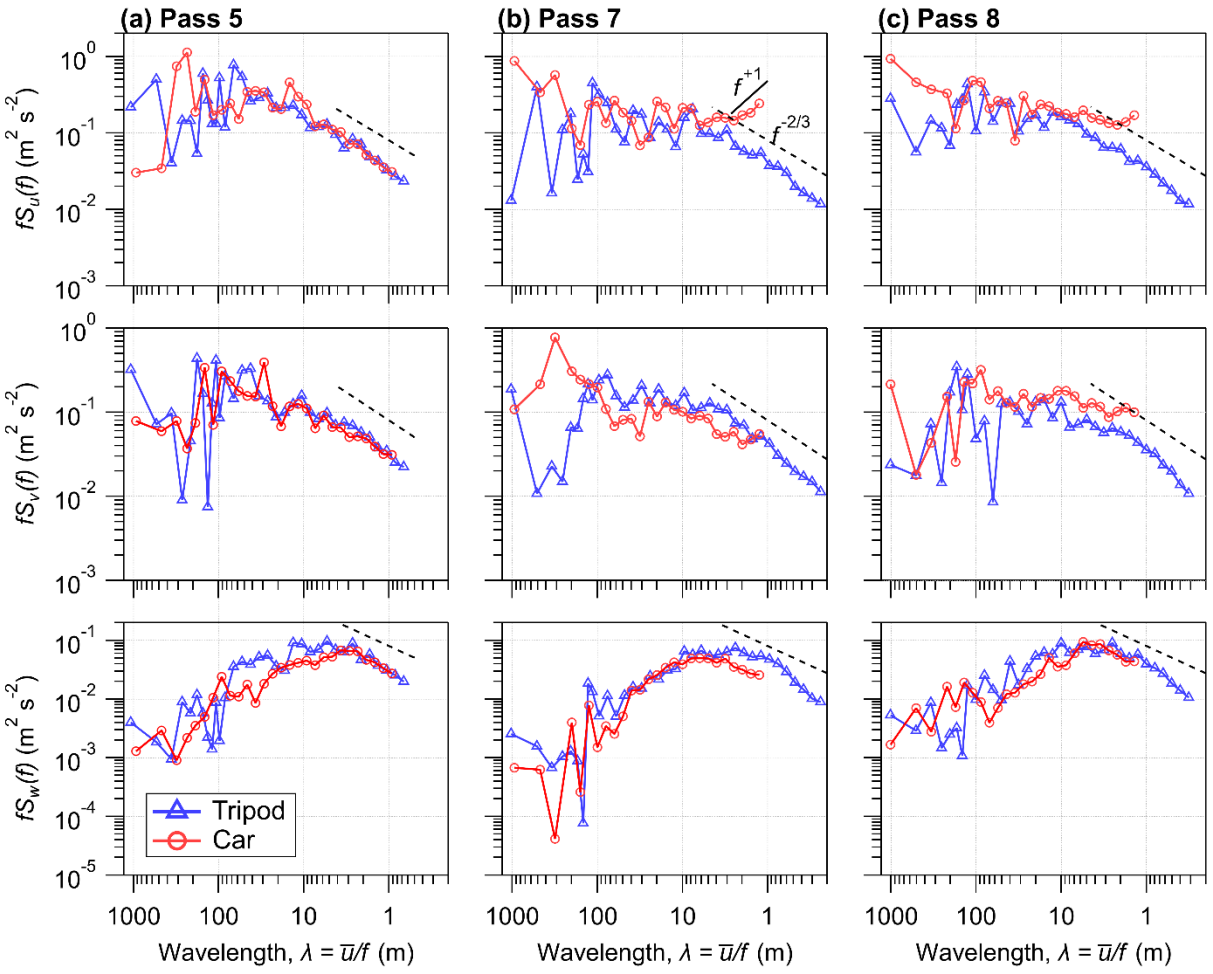

Figure 3.9: Binned power spectral density (multiplied by frequency) of the velocity components u (top), v (middle), and w (bottom) measured by the roadside tripod (triangles) and the mobile car (circles). The frequencies are normalized to give a wavelength (λ) as $\overline{u}/f$ where f is the frequency (Hz) and $\overline{u}$ is the mean ambient wind speed (or car relative flow for the mobile car).

3.3.4 Measurement uncertainties

a. Flow distortion correction angle, θ

Despite the rather strong relationship between the measured vertical velocity (W) and the measured longitudinal velocity (U) discussed in Sect. 3.2.4, there is still an uncertainty in the rotation angle (θ) used to correct for the effect of flow distortion on the vertical velocity. The median of θ calculated using all binned values is 7.54º, with the lower and upper quartile (25th and 75th) being 7.38 and 7.70º respectively (IQR = 0.32º). If instead θ = Q25 = 7.38º is used for the flow distortion correction, the mean vertical velocity measured on the car during all measurement passes increases, giving $\overline{w}$ = 0.06 m s^{-1} (using θ = Q50 = 7.54º gives $\overline{w}$ = 0.00 m s^{-1}). In addition, there is an increase in the magnitude of $\overline{w'^2}$, $\overline{w'T'}$ and $\overline{u'w'}$, giving a marginally better statistical agreement between the car and tripod for $\overline{w'^2}$, $\overline{w'T'}$ as shown in Table 3.4. These results demonstrate that reducing θ to give $\overline{w}$ > 0 m s^{-1} is not sufficient to improve the agreement among all turbulence statistics and will not remove the bias noted in Sect. 3.3.2 for $\overline{w'^2}$ and $\overline{w'T'}$. Similarly, increasing θ from 7.54 º does not remove the bias or improve the agreement between the car and tripod.

Table 3.4: Statistics calculated over all measurement passes (i.e., Track #1 and Track #2), but with θ = 7.38º.

	MBE$_{EC}$	**MBE$_{W}$**	**RMSE$_{EC}$**	**RMSE$_{W}$**	**Mean$_{EC}$ Car**	**Mean$_{W}$ Car**	**Mean$_{EC}$ Tripod**
$\overline{u'^2}$ (m^2 s^{-2})	0.89	0.44	1.43	0.75	2.14	1.68	1.26
$\overline{v'^2}$ (m^2 s^{-2})	0.20	0.04	0.61	0.44	1.38	1.21	1.19
$\overline{w'^2}$ (m^2 s^{-2})	–0.10	–0.11	0.11	0.12	0.18	0.17	0.29
$\overline{u'w'}$ (m^2 s^{-2})	–0.04	–0.02	0.10	0.08	–0.18	–0.15	–0.14
$\overline{w'T'}$ (K m s^{-1})	–0.04	–0.03	0.05	0.05	0.09	0.09	0.13
$\overline{u}$ (m s^{-1})	0.04	—	0.53	—	2.44	—	2.42

b. Sampling errors

A significant concern when obtaining atmospheric measurements from an instrumented mobile car is the impact of sampling errors. Sampling errors on the mobile car may result from (i) the use of a record length that is too short to be representative of an ensemble mean, (ii) non–stationarity of the flow introduced by microscale variations or inhomogeneities in the terrain and surrounding structures (i.e., trees, buildings), or (iii) white noise and persistent structured signals introduced by vehicle resonance and vibrations.

In this work three methods to quantity the random measurement uncertainty are investigated: (1) the method of Finkelstein and Sims (2001) referred to as F&S (i.e., Eq. 3.17), (2) the method of Mann and Lenschow (1994) referred to as M&L (i.e., Eq. 3.15) and (3) the method of Lenschow et al. (2000) (Eq. 3.22). F&S and M&L give an estimate of the overall random measurement uncertainty, while Lenschow et al. (2000) gives an estimate of random measurement uncertainty attributed only to white noise in the measured signal. The method of Lenschow et al. (2000) does not include contributions from persistent structured signals that may occur at a specific frequency (i.e., from vehicle resonance or some other cause of vibrations such as speed bumps).

Figure 3.10 displays the random measurement uncertainty of the horizontal velocity variances ($\overline{u'^2}$ and $\overline{v'^2}$) measured on the car plotted as a function of the magnitude of the variance. Likewise, Fig. 3.11 shows the random measurement uncertainty of the vertical velocity variance ($\overline{w'^2}$) and Fig. 3.12 displays the random measurement uncertainty of the measured covariances ($\overline{u'w'}$ and $\overline{w'T'}$). The random uncertainty estimates calculated from M&L and F&S agree well on the mobile car platform for velocity variances when m = 30 s. However, for m = 30 s F&S tends to give a slightly greater magnitude of random measurement uncertainty than M&L for covariances (i.e., Fig. 3.12). This is similar to the findings of Finkelstein and Sims (2002), who note that method of F&S contains a contribution from both the autocovariance and cross–covariance function leading to a larger magnitude and more conservative estimate of the sampling error compared to M&L. Rannik et al. (2016) note that F&S gives an estimate of the "total" random measurement uncertainty.

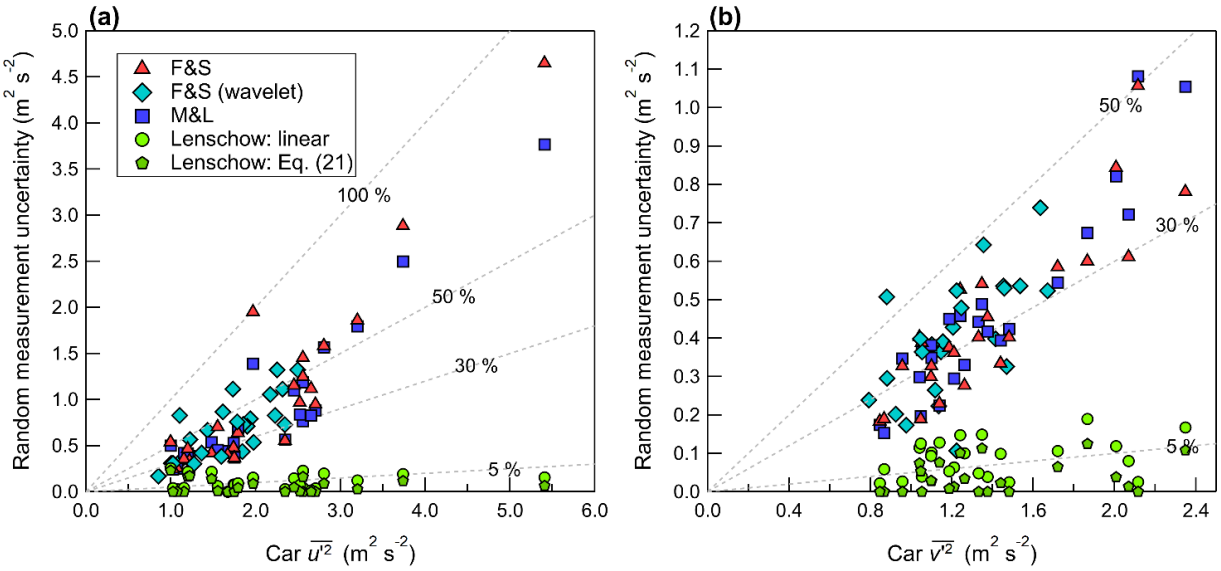

Figure 3.10: Random measurement uncertainty of the horizontal velocity variance measured on the car, plotted as a function of (a) the longitudinal velocity variance $\overline{u'^2}$ and (b) the lateral velocity variance, $\overline{v'^2}$. Dashed grey lines denote constant percentages of the independent variable.

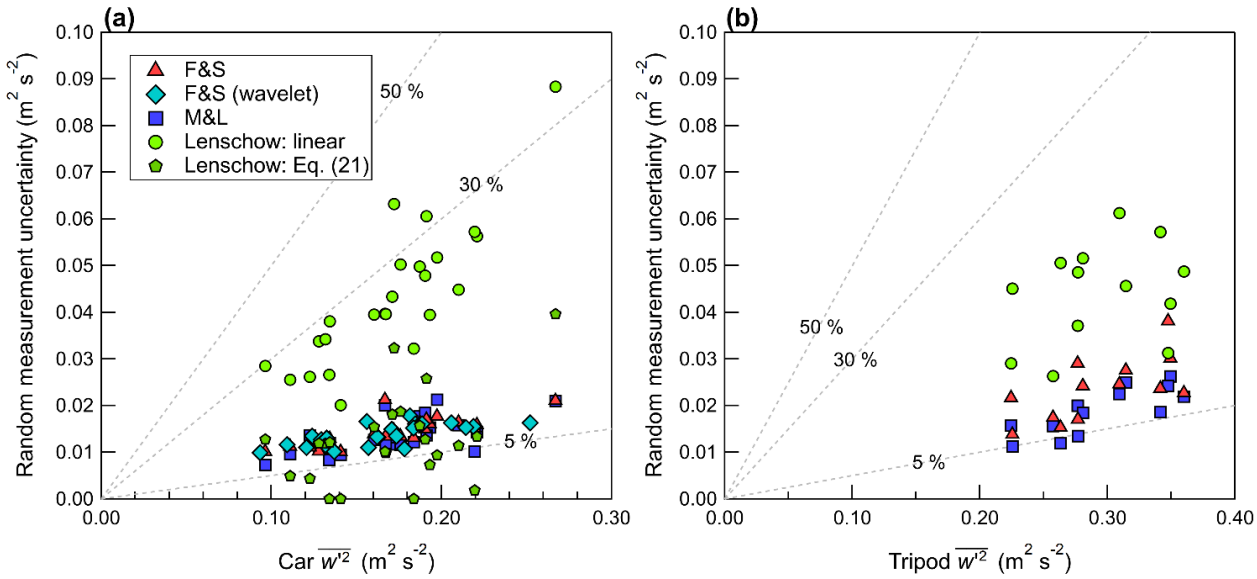

Figure 3.11: Random measurement uncertainty of the vertical velocity variance measured (a) on the car and (b) on the tripod, plotted as a function of $\overline{w'^2}$. Dashed grey lines denote constant percentages of the independent variable.

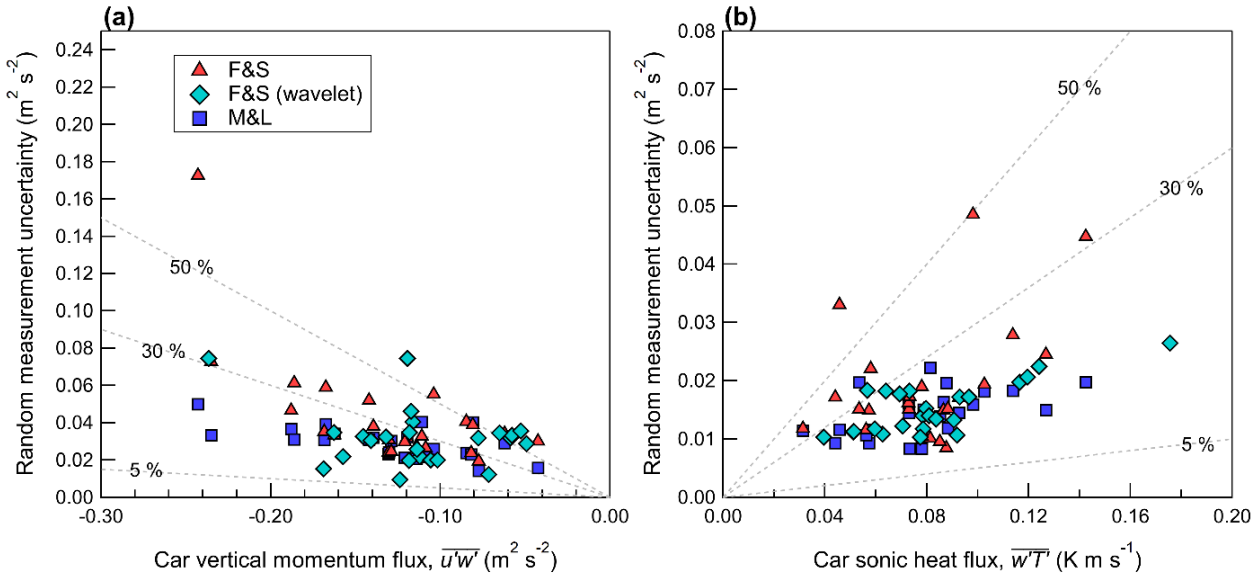

Figure 3.12: Measurement uncertainty of (a) the vertical turbulent momentum flux $\overline{u'w'}$ and (b) the vertical turbulent sonic heat flux $\overline{w'T'}$ measured on the car and plotted as a function of the flux magnitude. Dashed grey lines denote constant percentages of the independent variable.

The random measurement uncertainty calculated from F&S and M&L scales approximately linearly with increasing magnitude of the velocity variance or covariance, as shown in Fig. 3.10 to Fig.

3.12. For Track #2 there are several instances where $\overline{u'^2}$ is large (i.e., 2 to 5 $m^2\ s^{-2}$) and δ_{FS} is on the order of $\overline{u'^2}$. δ_{FS} and δ_{ML} give 1 standard deviation of the random measurement uncertainty of a measured variance or covariance and represents the 68 % confidence interval (Rannik et al. 2016); $1.96\delta_{FS}$ and $1.96\delta_{ML}$ gives the 95 % confidence interval. Thus, $\overline{u'^2}$ measured on Track #2 is not significantly different than 0 in the 95 % confidence interval for some measurement passes. A trend in the velocity record results in an autocorrelation function that does not fall to zero as expected and instead remains elevated at large time lags. This suggests that δ_{FS} in this study includes a contribution from non–stationarity in the record, which is consistent with the conclusions of Rannik et al. (2016) for measurements made on stationary towers, who found that δ_{FS} continues to increase as m is increased to 300 s.

Reconstructing the time series using wavelet analysis produces a filtered time series, where the resolved low frequency contributions are excluded. Applying F&S to the reconstructed time series gives an estimate of δ_{FS} for the wavelet variances and covariances (shown in Figs. 3.10 to 3.12 as diamonds). For $\overline{u'^2}$, wavelet estimates of δ_{FS} follow a similar trend to the uncertainty estimates found using the unfiltered time series, that is, as the magnitude of the wavelet variance increases, so does δ_{FS}. However, for times when wavelet analysis predicts a smaller $\overline{u'^2}$, δ_{FS} is also found to be proportionally reduced.

Figures 3.10 and 3.11 show the random measurement uncertainty due to white noise in the measured signal (δ_L) estimated according to Lenschow et al. (2000). For the measurement tracks investigated here the use of a linear fit to estimate δ_L gives a much larger uncertainty than Eq. 3.21. In the case of the vertical velocity, δ_L estimated using a linear fit extrapolation is 3 to 4 times larger than the total random measurement uncertainty according to δ_{FS}. δ_L is expected to represent a contribution to the total random measurement uncertainty and therefore $\delta_L < \delta_{FS}$ (Rannik et al. 2016). This suggests that the linear fit significantly underestimates the true variance and overestimates the amount of white noise for w. If a power law fit (Eq. 3.21) is used instead of a linear fit, δ_L is reduced and for several measurements passes $\delta_L < \delta_{FS}$. The difficulty estimating δ_L for w on the car is not unexpected, since w has an integral time scale (ITS) of 0.05 to 0.1 s for vehicle speeds near 20 m s^{-1} and this is only 2 to 4 times the sampling interval of the sonic anemometer. This limits the amount of autocovariance function time lags that lie within the inertial subrange, giving a poor fit. Lenschow et al. (2000) note that for a successful power law fit to the autocovariance function, the ITS must be "several times larger" than the sampling interval of the instrument. For w measured on the tripod, the use of Eq. 3.21 gives undefined $\overline{\epsilon'^2}$ while a linear fit gives $\delta_L > \delta_{FS}$ as shown in Fig. 3.11 (b).

Compared to w, the measured horizontal velocity components on the car (u, v) have a larger ITS (on the order of 1 s) and a larger signal–to–noise ratio (SNR). Rannik et al. (2016) argue that the method proposed by Lenschow et al. (2000) is best suited for closed–path sensors as opposed to open–path sensors

and high–precision instrumentation such as sonic anemometers. They found that the method of Lenschow et al. (2000) gives a relatively unbiased estimate of the white noise when the SNR is small and applied the method to estimate δ_L only for w (not for u or v). For u and v in this study, δ_L typically represents a small contribution to the total random measurement uncertainty, except for weaker signals (i.e., lower measured horizontal variances). The presence of white noise in the measured u and v signals is also supported by the spectra shown in Fig. 3.9 (b), where a near +1 slope appears at high frequencies within the inertial subrange. This is not the case for w, where the spectra do not show a +1 slope at high frequencies and hence w spectra have no evidence of white noise impacting the measured signal. This may suggest that δ_L overestimates the magnitude of white noise present in w, and so δ_L is likely not a reliable estimate of white noise in the vertical velocity for car measurements made at high vehicle speeds near 20 m s^{-1}.

In addition to Track #1 and Track #2, the car was driven on a gravel road at relatively high vehicle speeds (s between 20 and 23 m s^{-1}) for a short (< 5 min) period. The effect of the gravel road is investigated by splitting the short period into non–overlapping intervals of 49 s (yielding 5 unique samples), and performing the same analysis as outlined in Sect. 3.2. The car measurements on the gravel road are similar to car measurements obtained on the paved road, for a comparable s. The magnitude of the variances and covariances on the gravel road are not different from measurements on the paved road within the 95 % confidence interval, and the uncertainty estimates (δ_{FS}, δ_{ML} and δ_L) are the same order of magnitude. The measured velocity variances and uncertainty analysis for the gravel road are displayed in the supplemental material (Fig. D7). These measurements suggest that the road surface types investigated in this study have a limited influence on the measured turbulence statistics.

c. Tripod velocity record contamination from passing traffic

Since the study was designed to investigate measurements in non–idealized conditions, the highway locations have public access and therefore other vehicle traffic was present during the measurements. The traffic consisted largely of passenger vehicles (such as cars, pickup trucks, sport utility vehicles and minivans), but the traffic on 22 Aug was more significant and was comprised of occasional large trucks (dump trucks and tractor–trailers). For measurement passes on 22 Aug (with video recordings available on the tripod), the dashcam recorded between 26 and 40 total passing vehicles, of which 0 to 4 were large trucks. The car takes about 45 s to complete a track, but on the tripod the equivalent averaging period is between 6 to 8 min. For some measurement passes, the mobile car does not experience any traffic contamination, but this is not the case for the tripod. Therefore, the tripod will measure a different composition and amount of passing traffic than the car, potentially leading to differences in the measurements made by the two systems.

Large trucks produce a significant amount of vehicle–induced turbulence, but passenger cars and sport utility vehicles produce much less in comparison (Miller et al. 2019; Gordon et al. 2012). Furthermore, the wake has limited lateral spread relative to the vehicle travel direction (Kim et al. 2018), except perhaps for times with significant advection, so the most noticeable effect on the tripod will be from traffic in the adjacent highway lane (i.e., closet to the tripod). For measurements on the car, passing traffic (particularly large trucks) is found to enhance the measured velocity variances (i.e., Fig. 3.7 (c)). Like the car, the main effect of passing traffic on the tripod measurements would also be an enhancement of the velocity variances. Thus, for times when there is no traffic contamination on the car, the differences shown in Fig. 3.6 between the car and tripod–measured velocity variances may be underestimated, since the tripod velocity variances are enhanced due to passing traffic, but the car measurements are not. Therefore, the presence of traffic measured by the tripod and not the car introduces an additional uncertainty into the measurement comparisons shown in Sect. 3.3. Vehicle wake measured by the roadside tripod are investigated in more detail in Chapter 5.

3.4 Conclusions

The results presented in Sect. 3.3 demonstrate that the instrumented car design used in this study can successfully measure the mean atmospheric boundary layer close to the surface, but the car measurements may vary significantly based on the surrounding features such as trees, buildings, and other traffic. Therefore, the interpretation of the car–based measurements depends largely on the specific application, since the car may measure turbulence that is localized and not represented in single–point measurements made at a stationary tower. In the previous study of Belušic et al. (2014) there was limited upwind surface obstructions and no other traffic during their measurements. Despite the more idealized environment, their measurements revealed times when the horizontal velocity variances ($\overline{u'^2}$ and $\overline{v'^2}$) measured on the car were significantly larger than a nearby stationary tower, and they suggest that intense, temporally limited flow structures are to blame. These events dominate the measurements made on the car, but not on the tripod since the averaging period is longer. In this investigation, $\overline{u'^2}$ and $\overline{v'^2}$ on the car calculated using EC are also found to be much larger than measured on tripod for some measurement passes (i.e., a factor between 2 and 5 for $\overline{u'^2}$ with $\mathrm{RMSE}_{EC\ Car}/\mathrm{Mean}_{EC\ Tripod} = \mathrm{NRMSE}_{EC} \approx 114\%$). When the measurement uncertainty in Sect 3.3 is considered, these large $\overline{u'^2}$ are not significantly different than 0 in the 95% confidence interval, since $\delta_{FS} \approx \overline{u'^2}$. Applying wavelet analysis to calculate $\overline{u'^2}$ and $\overline{v'^2}$ gives significantly reduced magnitudes for some measurement passes, particularly those measurement passes with the largest estimated EC variances. This results in an improved agreement between the mobile car and tripod for $\overline{u'^2}$ and $\overline{v'^2}$ (for $\overline{u'^2}$ $\mathrm{RMSE}_{W\ Car}/\mathrm{Mean}_{EC\ Tripod} = \mathrm{NRMSE}_{W} \approx 60\%$). The improved agreement

using wavelet analysis suggests that wavelet analysis resolves length scales near and exceeding the length of the measurement track (i.e., 1000 m); in this study the change in surface features on Track #2 (from a windbreak to an open field) may yield an artificial low frequency contribution in the velocity record. Thus, when measuring from an instrumented car it is important to be aware of changes in terrain and land usage, which can strongly impact the near–ground measurements.

Evidence from this investigation shows that passing traffic (especially large trucks) can also lead to an increase in the velocity variances measured on the car. However, if the passing traffic is sporadic, the resulting increase in the measured velocity variances from vehicle–induced turbulence can be identified and removed using wavelet analysis. For a measurement pass in this study that experienced a passing heavy–duty truck and sport utility vehicle, removing the times when the traffic passes the mobile car (9 out of 46 s) decreases the turbulent kinetic energy by about 10%. This highlights the importance of video recordings in conjunction with sonic anemometer measurements on a car, so that times with possible traffic contamination can be identified in applications where its measurement is not intended.

The sampling uncertainties in Sect. 3.3 suggest that it is possible to measure a statistically significant vertical momentum flux on the mobile car at vehicle speeds near 20 m s^{-1}. $\overline{u'w'}$ measured on the car is typically found to be not different from the tripod within the 95% confidence interval, but for some passes $\overline{u'w'}$ measured on the car is small (< 0.06 m^2 s^{-2}) and not significantly different than 0 in the 95% confiendence interval. Therefore, for measurements obtained on the mobile car a better estimate of $\overline{u'w'}$ can probably be obtained by averaging multiple passes with a spatial extent of 10's of kilometers. Random measurement uncertainty estimates of $\overline{u'w'}$ by F&S and M&L (which give 1 standard deviation of the uncertainty) have magnitudes that are typically 10 to 40% of the measured flux. Furthermore, there is no significant bias in $\overline{u'w'}$ measured on the car when the entire set of measurement passes is considered ($\mathrm{MBE}_{EC\ Car}/\mathrm{Mean}_{EC\ Tripod} = \mathrm{NMBE}_{EC} \approx$ –4% and $\mathrm{MBE}_{W\ Car}/\mathrm{Mean}_{EC\ Tripod} = \mathrm{NMBE}_{W} \approx$ –14%).

The vertical velocity ($\overline{w'^2}$) and vertical sonic heat flux ($\overline{w'T'}$) measured in this study are found to be biased low compared to measurements made on the tripod ($\mathrm{NMBE}_{EC} \approx$ –38% for both $\overline{w'^2}$ and $\overline{w'T'}$). The low bias on the car is probably due to the combination of two factors: (1) the footprint measured by the car contains less of the low–albedo highway than the tripod and (2) rapid flow distortion at the measurement location on the car. Interestingly, there is evidence of a similar low bias in $\overline{w'^2}$ (but not $\overline{w'T'}$) measured by the car in Belusic et al. (2014), where only 4 out of the 19 completed passes measured a greater $\overline{w'^2}$ on the car than the stationary tower (i.e., their Fig. 4). This demonstrates that wind tunnel testing or computational flow modelling of each specific instrumented car design may be useful to quantify the effects of rapid flow distortion on the measured velocity variances and covariances. Applying the method of Lenschow et al. (2000) to estimate the magnitude of white noise in the measured vertical velocity signal at vehicle speeds

near 20 m s^{-1} likely underestimates the true signal variance and overestimates the amount of white noise and therefore is not recommended.

The mean wind speed and mean wind direction were found to be consistent with measurements made on the tripod. For $\bar{u}$ measured on Track #1 and Track #2, the NMBE ≈ 2% and NRMSE ≈ 22% respectively. Even a short averaging period of 10 s for car measurements made at a vehicle speed near 20 m s^{-1} provides a reliable estimate of mean wind direction on the car; for about 250 unique intervals on 20 and 22 Aug the interquartile range of the wind direction is 42 and 34° respectively. Despite the rather consistent wind direction, the mean wind speed in any individual 10 s averaging period may vary considerably; the interquartile range for $\bar{u}$ is 1.3 and 1.9 m s^{-1} on 20 and 22 Aug respectively. The large variation in the 10 s mean wind speed likely represents more localized flow that exists in a specific location. Therefore, the instrumented car may prove invaluable for studies that require precise measurement of localized flow, providing simultaneous measurement of wind speed and direction over a large domain. This study shows that even when the sonic anemometer is placed particularly close to the vehicle (compared with Belusic et al. (2014), for example), it is still possible to correct for flow distortion effects and obtain measurements of the mean wind and turbulence that are not different within the 95% confidence interval from measurements made by a nearby stationary tripod.

The results presented in this investigation demonstrate that car–based measurements of turbulence require care when selecting the appropriate spatial and temporal averaging, and when selecting the measurement location, to ensure that the measurements obtained are representative of the specific application. This is demonstrated in our measurements, where the highway surface/flux footprint, upwind obstructions and passing traffic are all found to have a significant effect on the measured values but are not necessarily errors since they do represent real features that can generate atmospheric turbulence.

CHAPTER 4: Characterization of heavy–duty diesel vehicle emission plumes using high–frequency on–road measurements

Stefan J. Miller[1], Mark Gordon[1], Ralf M. Staebler[2], Michael Wheeler[2]

[1]Department of Earth & Space Science & Engineering, York University, 4700 Keele Street, Toronto, ON M3J 1P3, Canada

[2]Air Quality Processes Research Section, Air Quality Research Division, Atmospheric Science and Technology Directorate, Science and Technology Branch, Environment and Climate Change Canada, 4905 Dufferin Street, Toronto, ON M3H 5T4, Canada

Publication status: Not yet submitted

Abstract

Vehicles emit pollutants that negatively impact human health. While many studies have used instrumented cars to measure vehicle emissions in–situ on highways, there has not been an in–situ investigation using an instrumented car that has aimed to quantify turbulent fluxes or concentration variances. During 2016 and 2019 an instrumented mobile car was used to sample particulate emissions and turbulence generated by heavy–duty diesel vehicles (HDDVs) on highways while travelling at high vehicle speeds near 100 km h^{-1}. The instrumentation was co–located and included an aerosol spectrometer, CO_2/H_2O gas analyzer and sonic anemometer, allowing quantification of vertical turbulent fluxes of aerosols (total number) and CO_2 while chasing HDDVs. This study presents the first in–situ measurements of the vertical turbulent flux of aerosols and CO_2 obtained behind HDDVs on highways. The direction of the vertical flux at a height of 1.7 m is found to be consistent with the exhaust location on the measured heavy–duty vehicle (HDV): negative for HDVs with an exhaust located on the vehicle's top (near 4 m) and positive for HDVs with an exhaust located on the vehicle's bottom (near 0.5 m), signifying a plume expanding downward and upward through the measurement location, respectively. The most significant downward fluxes of aerosols behind HDVs with a top exhaust occur only during times with a large negative vertical momentum flux, suggesting a relationship between vertical momentum transport in the wake and the vertical diffusion of aerosols. The emission of CO_2 from a commercial bus is found to be distinctly related to vehicle acceleration, with the measured CO_2 mass density increasing nearly exponentially with increasing vehicle acceleration. Furthermore, we present evidence of a shift in the mode diameter of accumulation mode particles measured behind a commercial bus during periods of vehicle acceleration. Specifically, the median size distribution measured during the release of a visible plume has a mode diameter that is about 20 nm larger than the median size distribution calculated from the entire record behind the commercial bus. The results show that the mode diameter of accumulation mode particles has decreased by about 10 nm between 2016 and 2019, which we suggest may be related to an increasing percentage of biodiesel mixed into diesel fuel in Ontario.

4.1 Introduction

Vehicular traffic is known to emit aerosols that can negatively impact human health, causing cardiovascular and pulmonary disease and cancers (Pope III et al. 2002) because of toxic organic and inorganic chemical components such as black carbon (BC), polycyclic aromatic hydrocarbons and carbonyl compounds, present in both the gas and particulate phase (Perrone et al. 2014; Casal et al. 2014; Dallmann et al. 2012; Pang and Mu, 2007). BC is a significant component of vehicular emissions in North America. Liggio et al. (2012) measured BC in the Toronto, Canada region using an on–road mobile laboratory, demonstrating that BC emission from heavy–duty diesel vehicles (HDDV) is significant (mean BC emission factor of approximately 600 mg kg_{FUEL}^{-1}) and BC emission factors from gasoline vehicles, as of 2012, were underestimated by a factor of nine in Canada (mean BC emission factor of approximately 115 mg kg_{FUEL}^{-1}). A reduction in particulate emissions from motor vehicles over time has been demonstrated by measurements in Toronto Canada, however particulate emissions from motor vehicles remains a significant health concern. Sabaliauskas et al. (2012) show that total number concentration of particles with diameters < 50 nm decreased by 23 % (in the winter months) between 2006 and 2011; for particles with diameters between 50 and 100 nm and 100 and 300 nm, the decrease was 17 and 24 % respectively. They partially attribute the decrease with time to improved NO_x emission control technologies used on gasoline vehicle engines.

The fate of pollutants released from an isolated vehicle's exhaust are determined by complex interactions of the ambient boundary layer with the vehicle–generated flow perturbations. It is well known that the geometry of the vehicle's rear end has a significant impact on the wake structure (Ahmed, 1981). Kanda et al. (2006) used a wind tunnel to investigate a model passenger car (scale 1/20 of an actual vehicle) for low vehicle speeds near 5.6 m s^{-1} (20 km h^{-1}) and an exhaust located under the vehicle. They measured large $\overline{w'^2}$ over the trunk and immediately downwind of the vehicle, which has the effect of enhancing vertical diffusion of the plume directly behind the car. After the initial vertical diffusion, the plume is mainly diffused laterally and downwind. Thompson and Eskridge (1987) demonstrate that a moving passenger car may have a counterrotating longitudinal vortex pair, each vortex forming along each side wall of the vehicle, which forces the flow above the vehicle to descend into the central portion of the vehicle wake, flushing out pollutants. The flow behind square–back vehicles (i.e., tractor–trailers, commercial buses) is similarly complex, owing to the presence of shear layers that emerge along the walls of the vehicle and from the vehicle's underbody (Lo and Kontis, 2017; Xie et al. 2020). The near wake is thus characterized by a recirculation region, where pollutants become trapped and concentrations may be significantly enhanced (Chang et al. 2009; Wang and Wang, 2021). The pollutants may be removed periodically from the recirculation region through low–frequency wake oscillations or settle downwind of the vehicle in the far wake at distances up to 150 m (Baker, 2001; Xie et al. 2020).

When more than one vehicle is present, wake interactions become important. Of particular interest is the so called "vehicle platoon," where a series of vehicles travel together in a group at a similar speed. He et al. (2019) performed a numerical simulation of a platoon of eight 1/20 scale model heavy–duty trucks with trailers (box–shaped trailer with a full–scale height of 3.5 m). They present the flow and vorticity in the $y - x$ plane, demonstrating that the lateral spread of the wake is least for the first vehicle in the platoon and greatest for the last vehicle. Similarly, vorticity presented in the $x - z$ plane shows that the wake height is greater behind the final vehicle than the initial vehicle in the platoon. A similar increase in the vertical spread of the wake for each successive vehicle in the platoon is demonstrated by Ebrahim and Dominy (2020) who performed a numerical simulation of the flow field generated by a group of three passenger cars. The increased vertical and lateral spread of the wake imply greater mixing lengths and hence greater pollutant diffusion in these directions (Makar et al. 2021).

According to theory developed by Eskridge and Thompson (1967), the wake should be dependent on vehicle speed, both in terms of its strength and height – that is, for greater vehicle speeds the wake turbulence increases and the wake spreads to greater vertical heights with downwind distance behind the vehicle. Groneskei (1988) used roadside measurements (1, 10, 30 and 70 m from the edge of the road) in conjunction with two cars emitting a tracer gas (either SF_6 or $CBrF_3$) to investigate the effect of vehicle speeds (11 or 22 m s^{-1}) on the dispersion of exhaust gases. They found that increasing the vehicle speed resulted in greater vertical diffusion of the exhaust gas, noting a linear relationship between the vertical diffusion parameter (σ_z) and the theoretical wake length scale (l_w) close to the road. Furthermore, they found that a Gaussian distribution with a maximum concentration at ground level is a good fit to the vertical profile of the exhaust gas; Xie et al. (2020) similarly found the Gaussian distribution is a good fit to pollutant dispersion in the far wake of a heavy–duty truck (with a trailer) using large eddy simulation. Eskridge et al. (1991) predict that the effect of increased vehicle speed on vertical diffusion in the vehicle wake is most significant during stable atmospheric conditions. Vehicle speed also has a substantial impact on emitted aerosols, since it modifies the dilution ratio, which influences the physical processes governing aerosol growth and formation.

Another factor that has a significant impact on the dispersion and mixing of an exhaust plume is the location of the exhaust on the vehicle. Chang et al. (2009) investigated the impact of different exhaust positions on a passenger vehicle (all beneath the vehicle) and found that a side–exit exhaust (i.e., oriented perpendicular to the vehicle's travel direction) results in the highest dilution ratio and the lowest number of pollutants being trapped in the recirculation region of the near wake (about 10 to 30% of emitted pollutants are trapped). When the exhaust is oriented parallel to the vehicle's travel direction, and at the back–center of the vehicle, the number of pollutants trapped is maximized and the dilution ratio is minimized. They also investigated an upright exhaust on a heavy–duty truck without a trailer and found a concentration maximum

in the near wake near the vehicle's top. Chang et al. (2009) note that compared to a passenger vehicle, there is greater vertical spread and less lateral spread of the plume released from a heavy–duty truck (without a trailer) with a top exhaust.

The actual number of pollutants (i.e., CO_2, aerosols) that are emitted from a moving motor vehicle is dependent on the vehicle's operating parameters, such as engine load and the vehicle's age. The vehicle's engine load is affected by the driving speed, rate of acceleration, and the road grade – the engine load is proportional to the amount of fuel consumed (Wang and Rhkha, 2017). Lapuerta et al. (2003) measured an increased particle number concentration with increasing engine load for all particle sizes, except at the highest engine load where the number of small particles with diameters < 250 nm is reduced in favor of particles with diameters > 250 nm. They suggest that at the highest engine loads, agglomeration of particles increases the mean particle diameter, leading to a measurable reduction in the number of particles with diameters < 250 nm. Kim et al. (2017) found a similar result, but specifically for vehicle acceleration and suggest periods of high acceleration favor particle agglomeration and therefore larger sized particles.

There are considerable modelling and wind tunnel studies investigating the dispersion of emitted pollutants from moving vehicles, but there is a need for in–situ measurements to validate the results. Therefore, based on these previous studies, some questions this work will consider are: (1) For measurements made at a fixed height of 1.7 m behind a moving vehicle, is there a significant difference in concentration statistics (i.e., mean, variance, vertical flux) depending on the location of the vehicle exhaust? (2) Do the measurements taken within vehicle wakes demonstrate pollutant trapping? (3) Do in–situ measurements support the existence of vehicle–induced shear layers, and if so, can they be linked to vertical pollutant diffusion? (4) Do measurements demonstrate a relationship between acceleration and the emission of gases or aerosols? (5) Can the pollutant concentration downwind of the moving vehicle and within the vehicle wake be predicted using a Gaussian plume model?

There have been numerous "chasing" experiments that have measured particulate matter emitted by on–road vehicles, focusing on the measurement of aerosol size distributions or particulate emission factors (Bukowiecki et al. 2002; Canagaratna et al. 2004; Kittelson et al. 2004; Kolb et al. 2004; Pirjola et al, 2004; Giechaskiel et al. 2005; Johnson et al. 2005; Dallmann et al. 2012; Gordon et al. 2012; Liggio et al. 2012; Jezek et al. 2015; Wren et al. 2018). An on–road study concentrating on the measurement of particle number concentration statistics and vertical turbulent number fluxes behind motor vehicles has not yet been attempted to the authors' knowledge. This may be due to the difficulty in obtaining simultaneous high–frequency and co–located measurements of the vertical velocity and particle number concentration, and measurement uncertainties resulting from non–stationarity (Miller and Gordon, 2022; Belusic et al. 2014). While sampling at highway speeds near 100 km h^{-1} (28 m s^{-}), high frequency instrumentation and short averaging periods are likely necessary for the generation of accurate concentration statistics. Recently,

wavelet analysis has been used to calculate turbulence quantities from non–stationary time series and can provide estimates for short averaging periods of 1 to 10 s while still retaining longer timescales (Schaller et al. 2017). Typically for an observing station fixed on the ground, concentration statistics including the mean ($\overline{N}$), variance (σ_N^2), intermittency factor, fluctuation intensity ($\sqrt{\sigma_N^2}/\overline{N}$) and probability distributions are used to quantify the plume (Hanna 1984a; Hanna 1984b; Mylne and Mason, 1991). The intermittency factor is defined as the "fraction of time that material from a continuous source is present at a receptor" (Wilson et al. 1985). For determination of this fraction, typically the amount of time the instrument measures "zero" concentration is required; practically this requires background levels to be removed to give a zero–mean concentration over the record length of interest. However, while measuring on a highway at speeds near 100 km h^{-1}, the background concentration of aerosols and trace gases such as CO_2 and H_2O are highly variable at time scales < 10 s, making the determination of an intermittency factor challenging.

This study presents on–road measurements of aerosols (with diameters between 60 and 1000 nm) and CO_2 gas obtained from highways in the Toronto, Canada region. Using high frequency and co–located instrumentation, we present the first in–situ measurements of the vertical turbulent number flux measured while following behind heavy–duty vehicles in real–world traffic conditions. The intermittency factor behind heavy–duty vehicles is estimated from frequency distributions generated from measurements obtained in the near and far wake region. Through assessment of the in–situ measurements, this study investigates how flow within the vehicle wake impacts vertical pollutant diffusion behind heavy–duty vehicles. Section 4.4.2 gives a brief survey of aerosol characteristics in vehicle exhaust emissions, with a focus on diesel exhaust which is utilized by most heavy–duty vehicle engines in North America.

4.2 Characteristics of exhaust aerosol emissions

The particles in an exhaust plume of an on–road diesel vehicle typically consist of 3 overlapping lognormal modes: (a) the nucleation mode with particle diameters between 3 and 30 nm, (b) the accumulation mode with particle diameters between 30 and 500 nm, and (c) the coarse mode with particle diameters between 500 and 2500 nm. While rigid boundaries are given here for the size ranges, it should be understood these are approximations and the modes may extend into each other (Kittelson and Kraft, 2014). Gasoline engines produce an asymmetric size distribution with a smaller mean diameter of 40 to 80 nm, compared to 60 to 120 nm for diesel engines (Harris and Maricq, 2001).

4.2.1 Nucleation mode

The nucleation mode consists of volatile compounds (i.e., sulfuric acid, condensable hydrocarbons) that form during the dilution and cooling of the exhaust. These volatile compounds remain in the vapor phase within the tailpipe and then undergo gas–to–particle phase transition after they are released into the ambient

environment to form semi–volatile droplets (Kittelson et al. 2014). In addition to these volatile compounds, the nucleation mode may consist of solid metallic ash and small solid carbonaceous aggregates (Kittelson et al. 2022).

The formation of a nucleation mode is influenced by (i) the presence of other particles, (ii) the dilution ratio and residence time, (iii) the ambient conditions (i.e., air temperature and relative humidity), and (iv) the sulfur content of the fuel and lubricating oil. If soot dominates the plume relative to ash, then the formation of a nucleation mode will be suppressed since the semi–volatile compounds and metallic ash will be scavenged (i.e., adsorption and condensation) by the carbonaceous accumulation mode particles (Kittelson et al. 2000). Soot in the context of vehicle exhaust is defined as an aggregate of carbonaceous particles, which may contain ash, organic and inorganic components as absorbed material. Greater than 90% of the particles by number reside in the nucleation mode, but < 10% by mass. (Kittelson et al. 2004).

4.2.2 Accumulation mode

The accumulation mode (or the soot mode) consists of fractal–like carbonaceous agglomerates made up of potentially hundreds of spherical monomers. The agglomerates are highly non–spherical, especially as their size increases toward 250 nm (China et al. 2014). The accumulation mode contains most of the particle mass. (Kittelson et al. 2000).

Soot particles are formed within the diesel engine system and not after release from the tailpipe, and polycyclic aromatic hydrocarbons (PAH) are considered a significant precursor for soot formation (i.e., naphthalene $C_{10}H_8$, pyrene $C_{16}H_{10}$, coronene $C_{24}H_{12}$) (Kittelson and Kraft, 2014). The carbonaceous agglomerates of the soot grow by condensation and adsorption, but also through coagulation which is considered a dominant growth process. The coagulation–dominant growth of soot is expected to result in a self–preserving size distribution, dependent only on the Knudsen number (Friedlander & Wang, 1966). However, Harris and Maricq, (2001) have shown deviations from this expected form (which is not lognormal), and they suggest other soot particle growth processes (i.e., soot oxidation, surface growth, particle fragmentation) are important.

Additional, non–engine related emissions may also occur, such as tire ware due to friction with the road surface, producing an accumulation mode in the 30 to 60 nm range during full–stops, turning sharp corners, or during periods of rapid acceleration (Mathissen et al. 2011). Additional accumulation mode particles may be generated by brake ware (Grigoratos and Martini, 2015).

4.2.3 Coarse mode

2 to 20% of the particles by mass reside in the coarse mode (Kittelson et al. 2000). Coarse mode particles may be accumulation mode particles that get recirculated through the engine system or crankcase emissions

(i.e., from lubricating oil) and engine/tire wear (Kittelson and Kraft, 2014; Grigoratos and Martini, 2015). Additional coarse mode particles may arise due to suspension of dust; dust suspension by vehicle induced turbulence is particularly prominent on unpaved roads and roads with a gravel–based shoulder (Williams et al. 2008; Moosmuller et al. 1998).

4.3. Methodology

4.3.1 Instrumentation and experimental setup

The data presented in this study were collected in 2016 and 2019. A complete description of the instrumented car design and sonic anemometers used in 2016 and 2019 are described in Miller et al. (2019) and Miller and Gordon (2022) respectively. As a brief description, a roof rack was secured to the top of a sport utility vehicle. A steel frame with an extended arm was attached to the roof rack to hold the instrumentation and an aerosol sampling line near the front end of the vehicle (i.e., over the front bumper). Instrumentation in 2016 included a sonic anemometer (Applied Technologies Inc.), an open–path CO_2/H_2O gas analyzer (LI–COR, model LI–7500) and an ultra high sensitivity aerosol spectrometer (UHSAS, Droplet Measurement Technologies, Inc). Only the sonic anemometer and UHSAS were present during the 2019 study. The gas analyzer was installed on the front arm, co–located with the sonic anemometer, and sampled at a rate of 20 Hz. The UHSAS sampled from a stainless–steel sampling line, with the line entrance co–located with the sonic anemometer. Aerosol sampling during this study is described in detail in the following subsection.

a. Aerosol sampling

Measurements of aerosols with optical particle diameters between 60 and 1000 nm were obtained by the UHSAS. Size–resolved optical particle diameters were measured at 1 Hz, and each sample is stored as a histogram consisting of 99 logarithmically spaced size bins. The UHSAS measures the aerosols' scattering signature produced by illumination with a 1054 nm laser (~ 1 kW of power). It then infers the particle diameter from a calibration curve (which assumes spherical particles); for particles with diameters < 300 nm, infrared scattering is proportional to the sixth power of the particle diameter (i.e., the Rayleigh regime). The sample flow rate of the UHSAS was held constant at 50 sccm during the 2019 study and 90 sccm during the 2016 study. The UHSAS sampled from a stainless–steel main line (inner diameter = 4.2 mm; outer diameter = 6.35 mm) at a tee junction located at the rear driver's side window. During the 2019 study, a tip was installed on the main line (outer diameter = 3.18 mm, inner diameter = 2.16 mm, length = 0.3 m) and isokinetic sampling at vehicle speeds near 100 km h^{-1} (28 m s^{-1}) was maintained by a pump with a flow controller (set to 6 lpm), used to draw air through the main line. During 2016, the setup did not have a flow controller, and the main line did not include the 0.3 m tip extension (pump flow rate of 10 lpm) and

consequently featured subisokinetic sampling at the main line entrance. For a tube aligned with the flow streamlines, subisokinetic sampling leads to oversampling of larger particles and an overestimation of the number concentration at the tube entrance (Hinds 1999). A photo of the 2019 setup inside of the instrumented car is shown in Fig. 4.1 and the entire setups used during 2016 and 2019 are described graphically in Fig. E1 and numerically in Table E1. For the setups in 2016 and 2019 we estimated the total particle loss using the particle loss calculator provided online by von der Weiden et al. (2016) and the results are shown in Fig. E2. The particle loss is estimated to be most significant during the 2016 study, with a size–dependent particle loss between 4 and 11%. In either setup, the greatest estimated particle loss is for particles with diameters < 100 nm and particles with diameters > 700 nm, because of deposition to the walls of the tube, due to diffusion and sedimentation, respectively.

Figure 4.1: The aerosol sampling setup used during the 2019 study. A view of the inside of the instrumented car is shown.

The UHSAS has known deficiencies that may affect the measurements which determine the detection limit of the instrument. Cai et al. (2008) found that ammonium sulfate with a particle diameter of 62 ± 2 nm is only detected 50 % of the time and suggest this as a lower size cut–off for the UHSAS; at times when the total particle number concentration exceeds 3000 cm^{-3} and is increased further toward 5000 cm^{-3}, the UHSAS detection efficiency declines toward 90 % (when compared to measurements by a scanning mobility particle sizer). Cai et al. (2008) attribute this decreased detection efficiency at high particle number concentrations to “counting coincidence”. Counting coincidence occurs when two particles

pass through the optics at the same time, but only the particle closest to the laser scatters radiation and so the second particle passes through undetected. The probability of counting coincidence therefore increases as the number concentration increases and becomes a significant factor affecting the UHSAS measurements when the number concentration exceeds 3000 cm^{-3}. Moore et al. (2021) found that the UHSAS performs well for non–absorbing aerosol species, but significantly undersizes (> 20 %) highly absorbing particles (fullerene soot and nigrosine dye particles) with diameters greater than 80 nm. Howell et al. (2021) similarly found that the UHSAS undersized highly absorbing aerosol particles, particularly black carbon. They demonstrate that black carbon can be significantly heated by the laser beam to its vaporization point, causing the diameter of the particle to decrease as it evaporates. They suggest a similar effect (i.e., decrease in particle diameter) may occur for particles that are coated with volatile materials, which char to form black carbon and then are further heated by the laser reducing their diameters.

We investigated the performance of our UHSAS in a lab by comparing its results to a condensation particle counter (CPC) for total number concentration and to a differential mobility particle sizer (DMPS) for ammonium sulfate and polystyrene latex for particle diameter. Testing was carried out about three weeks prior to the start of the 2019 study. For ammonium sulfate particles in the 200 to 500 nm range, the UHSAS is found to underpredict the total number concentration by up to 24% when compared to the CPC, with the greatest differences found for the largest particle concentrations, consistent with Cai et al. (2008). The diameter of ammonium sulfate particles measured by the UHSAS compares well (within ± 5%) to DMPS measurements for particle diameters < 200 nm, but the UHSAS underestimates the particle diameter in an almost linear fashion as the particle diameter increases toward 500 nm. At 500 nm the UHSAS measured particle diameter of ammonium sulfate is about 15% lower than the diameter measured by the DMPS. For polystyrene latex particles the particle diameter measured by the UHSAS agrees with the DMPS within ±5 %.

b. CO_2 sampling

The number density of CO_2 and H_2O were measured using a fast-response open path infrared gas analyzer (LI-7500, LI-COR Inc.). Measurements of CO_2 and H_2O number density were recorded at a frequency of 20 Hz, and the gas analyzer was collocated with the sonic anemometer. Since the LI-7500 measures number density, an accurate air temperature is not required. For example, at an air temperature of 50°C and 100% relative humidity, an error in the temperature of 10°C results in an error of < 0.01% in the CO_2 number density. The LI-7500 is susceptible to vibrations at 132 Hz and 172 Hz when sampling at 20 Hz; the LI-7500 is not impacted by vibrations < 132 Hz and has minor impacts from vibrations > 172 Hz (LI-7500 Manual, 2004). At a sampling frequency of 20 Hz, the LI-7500 has an RMS noise of 0.27 mg m^{-3} at an ambient CO_2 concentration 370 ppm. Other sources of uncertainty in the CO_2 number density results from

zero drift with changing air temperature (maximum of ±0.5 mg m^{-3} per ℃ change from 25℃), gain drift with changing air temperature (maximum of ±0.1 mg m^{-3} per ℃ change from 25℃) and cross sensitivity to H_2O. These sources of measurement uncertainty define the detection limit of the instrument.

4.3.2 Study domain and meteorology

The study consists of two sets of data, collected in 2016 and 2019. The study domain and meteorology corresponding to the 2016 dataset is detailed in Miller et al. (2019). The data collected in 2019 were obtained on Highway 407 (ON–407) and Highway 400 (ON–400), located in the Toronto Canada region, both having a speed limit of 100 km h^{-1} (27.8 m s^{-1}). Measurement days in August included 20, 22, 28, 29 and 30, and meteorology (from Environment and Climate Change Canada) is given in Table 4.1. For measurement days driving on ON–400, the Egbert weather station is given for meteorological comparisons, but for days driving on ON–407, Toronto Pearson International Airport is reported instead.

Table 4.1: Meteorology measured by Environment and Climate Change Canada weather stations during the 2019 study. For ON–400 Egbert weather station data are shown, but for ON–407, Toronto Pearson International Airport is reported instead. The measurement height of data is 10 m.

	Temperature (℃)	Relative humidity (%)	Wind speed (m s^{-1})	Wind direction (°)	Highway studied
20 Aug	26.4. – 28.4	53 – 59	4.2 – 5.6	160 – 200	ON–400
22 Aug	17.8 – 20.8	51 – 60	3.8 – 5.0	300 – 340	ON–400
28 Aug	24.9 – 26.9	32 – 48	2.8 – 6.7	210 – 270	ON–400 / ON–407
29 Aug	21.1 – 23.6	45 – 50	4.2 – 7.5	210 – 290	ON–407
30 Aug	18.8 – 21.7	34 – 50	4.2 – 5.6	260 – 310	ON–400

4.3.3 Aerosol number concentration

The UHSAS generates a histogram of the particle sizes, recorded over time interval Δt, which is here set to the fastest possible rate of 1 s. The UHSAS can record the timing of each individual particle count with millisecond precision, known as the "particle–by–particle" (PbP) functionality. Occasionally the data stream can overload the computer CPU, and to avoid excessive data loss any data stored in the internal buffer are discarded and not reported in the histogram or PbP data. However, the UHSAS will report the number of known missing particles for which sizing and timing data were discarded. The total number is not discarded, and the size distributions are scaled upward to account for the missing particles. Only the 2019 study had working PbP data, which is necessary to generate a 40 Hz time series of particle number concentration for turbulent flux calculation (see Fig. E3 for an example of a 40 Hz time series). The maximum sampling rate of the UHSAS in 2016 was 1 Hz. The UHSAS used a sample flow (F_s) rate of

either 50 or 90 sccm in 2019 and 2016 respectively, which is corrected to standard pressure and temperature P_r = 101325 Pa and T_r = 273.15 K respectively. The aerosol number density (N_t, # cm^{-3}) can then be calculated from the 1 s particle count (C_{1s}, # s^{-1}) each second as

$$N_t = \frac{C_{1s}}{F_s}. \tag{4.1}$$

Here $C_{1s} = C_1 + C_2 + \cdots + C_{99}$, is the sum of counts from all 99 size bins measured over a period of 1 s. Each individual bin can also be normalized to give n_i. The UHSAS histogram can be converted to a number distribution (n_N) based on $\log D_p$ by dividing each n_i by the corresponding size range ($d \log D_p$). The UHSAS in this study sampled using logarithmically spaced size bins, so that $d\log D_p$ = 0.01234. $d\log D_p$ is unitless when using a reference diameter of 1 μm (i.e., $\log(D_p/1)$), so that the number distribution has units of cm^{-3}.

Aerosol size distributions measured from highways are often described as the sum of k = 3 lognormal distributions (corresponding to the 3 modes discussed in Sect. 4.4.2),

$$n_N(\log D_p) = \sum_{i=1}^{k} \frac{N_i}{\sqrt{2\pi}\log\sigma_{g_i}} \exp\left(-\frac{\left(\log(D_p)-\log(\mathrm{CMD}_i)\right)^2}{2\left(\log\sigma_{g_i}\right)^2}\right) \tag{4.2}$$

where N is the total aerosol number concentration, CMD is the count median diameter and σ_g is the geometric standard deviation. For a lognormal distribution, the CMD is equal to the geometric mean diameter (Hinds, 1999). For this study only the accumulation mode is considered, and so k = 1. Fitting of measured data to Eq. 4.2 is completed using IGOR Pro.

4.3.4 Calculation of CO_2 and aerosol fluxes

Flow distortion correction is applied to the measured w and u, as described previously in Chapter 2 and Chapter 3. Following Schaller et al. (2017) and Miller and Gordon (2022) (i.e., Chapter 3), the vertical turbulent flux of CO_2 (or aerosol number concentration) is calculated using wavelet analysis, to give a wavelet covariance ($\overline{w'\rho_c'}$) between the vertical velocity (w) and the CO_2 mass density (ρ_c) (or between w and N_t). Wavelet analysis in this work includes time scales up to 60 s, regardless of the averaging period (T) used. Coordinate rotation to give $\overline{w}$ = 0 is not applied here, since the averaging periods used are very short (1 to 10 s) and the horizontal velocity may change quickly even over such short time periods when travelling at 100 km h^{-1}. Since measurements obtained by the sonic anemometer and gas analyzer are not perfectly co–located, a time delay occurs between w and ρ_c. To account for this, ρ_c is shifted to maximize

the cross–correlation prior to calculating any turbulence statistics. The sonic anemometer data is not shifted since it is synchronized with the GPS velocity and the video recordings. For the data presented here, the time delay between w and ρ_c is typically on the order of 1 s. Since the LI–COR gas analyzer records at 20 Hz, the sonic anemometer data is down–sampled to 20 Hz prior to the calculation of $\overline{w'\rho_c'}$. For $\overline{w'\rho_c'}$**,** the raw vertical CO_2 flux is corrected according to Webb et al. (1980) and the sonic temperature is converted to an absolute temperature following Van Dijk et al. (2004), Eq. 3.53. The Webb correction is applied to account for density fluctuations in the measured trace gas resulting from the heat flux and water vapor flux (i.e., rising air parcels have a lower density than descending air parcels). Since the LI–COR measures the CO_2 number density, a correction to $\overline{w'\rho_c'}$ is therefore required.

A similar procedure is applied to calculate covariances between w and N_t, that is, N_t is shifted to maximize the cross–correlation with w, and for 2016 measurements, w is down–sampled to 1 Hz to match the sampling frequency of the UHSAS. The time delay between w and N_t is between 2 and 3 s, due to residence time in the inlet lines.

4.3.5 Plume identification

A plume is identified as a significant enhancement of the measured CO_2 concentration over background levels. During a typical vehicle chasing record of sufficient duration, there will likely be periods where the instrumented car measures the background concentration due to plume meandering (Cassiani et al. 2020). Ideally, a plume should consist of at least one local maximum bounded by local minima. A single plume may have several local maxima, therefore further conditions must be imposed to separate the individual plumes, and we apply an approach similar to Wren et al. (2018):

I. The background level for CO_2 is set to the 5th percentile of ρ_c calculated from a 90 s moving window. The background level ($\rho_{c_{BG}}$) is removed from ρ_c, giving the perturbation of the CO_2 mass density above the background level attributed to vehicle emissions (ρ_{C_e}).

II. Local maxima and minima of ρ_{C_e} (determined from the first derivative) are excluded if they are deemed too insignificant, that is any minimum > $0.015\rho_{c_{BG}}$ (i.e., 1.5% of background) and any maximum ≤ $0.04\rho_{c_{BG}}$ (i.e., 4.0% of background).

III. Boundaries defining the start and end of each plume are identified by searching on either side of a local maximum (or set of maxima) for the first minimum.

IV. ρ_{C_e} integrated over a measured plume must be greater than 10 mg m^{-3} s and have a duration of at least 10 s, otherwise the plume is rejected. The limit of 10 mg m^{-3} is chosen to ensure that the plume

has an integrated background concentration that exceeds the detection limit of the LI-7500 and to avoid introducing unrealistic emission ratios into the analysis.

V. The same boundaries defining each CO_2 plume are used to extract the corresponding particle number concentration, N_t. In this way it is assumed that ρ_{C_e} should correlate with N_t and consequently they share nearly identical boundaries. The background levels are removed from N_t identical to step (I), giving N_{t_e}

VI. All identified plumes are visually inspected to eliminate cases where there is little correlation between ρ_{C_e} and N_{t_e}.

4.3.6 Particle number emission factors

An emission factor (ER) for particle number concentration is determined from a carbon balance method and calculated by integrating the background removed ρ_c and N_t over the duration of a measured plume (Canagaratna et al. 2004; Jezek et al. 2015; Wren et al. 2018),

$$\mathrm{ER} = \frac{\int_{t_1}^{t_2} N_{t_e}\,\mathrm{d}t}{a\int_{t_1}^{t_2} \rho_{C_e}\,\mathrm{d}t} w_C, \tag{4.3}$$

where a is the molar ratio between C and CO_2 ($a = M_C/M_{CO_2}$ = 12 g mol^{-1} / 44 g mol^{-1} = 0.2727) to convert to equivalent carbon, w_c = 0.87 is the carbon fraction of the followed vehicle's fuel, N_{t_e} is the total number concentration after removing background levels (# m^{-3}) and ρ_{C_e} is the mass density of carbon dioxide after removing background levels (kg m^{-3}). The total number concentration is calculated over the size range of 60 to 1000 nm and hence represents the accumulation mode particles and not the nucleation mode. The EF is determined between time t_1 and time t_2 which represents the duration of the plume. For N_t, EF has units of # kg^{-1} fuel burned. If the number concentration is used to estimate total mass, the units of the EF become g kg^{-1} fuel burned, but this conversion is not applied here due to large uncertainties. Specifically, a density profile of the measured particle size distribution must be assumed. For diesel exhaust particles, the effective particle density decreases from 1.0 g cm^{-3} to 0.2 g cm^{-3} as the particle mobility diameter increases from 50 to 300 nm, but there is a ± 20% range in the measured densities in the literature (Park et al. 2003; Maricq and Xu, 2004; Olfert et al. 2006). The mobility diameter of an irregularly shaped particle is defined as the diameter that a spherical particle would have if it had the same charge and migration velocity as the particle in question, while moving through a steady–state electric field (Kittelson et al. 2022, DeCarlo et al. 2004). A second uncertainty arises from potential errors in the optical particle diameter measured by the UHSAS (see Sect 4.3.1–a), since mass requires calculation of the volume distribution which for spherical particles

is proportional to the particle diameter cubed. The assumption of particle sphericity when calculating the volume distribution is a third uncertainty, since soot in diesel exhaust become highly non spherical as their particle diameter increases from 50 to 300 nm (Park et al. 2003; China et al. 2014). Integration in Eq. 4.3 should also include carbon monoxide and total hydrocarbons, but these components have been shown to be small (about 10% of the total carbon) compared to CO_2 (Dallmann et al. 2012).

4.3.7 Estimating fuel consumption of heavy–duty vehicles

For a heavy–duty diesel vehicle (HDDV) the fuel consumption in liters per second (l s^{-1}) can be modelled to a good approximation as (Wang and Rakha, 2017),

$$FC(t) = \alpha_0 + \alpha_2 P(t) + \alpha_3 P(t), \tag{4.4}$$

where α_0, α_1 and α_2 are vehicle specific constants and $P(t)$ is the power (kW) required for operation of the vehicle. The power can be approximated as

$$P(t) = \left(\frac{R(t)+1.1ma(t)}{3600\eta}\right) S(t), \tag{4.5}$$

where S is the vehicle speed (km h^{-1}), a is the instantaneous vehicle acceleration (m s^{-2}), η = 0.94 is the driveline efficiency, m is the vehicle mass and R is the resistance force acting on the vehicle (N). R is calculated as

$$R(t) = \frac{\rho_{std}}{25.92} C_d C_h A_f S(t)^2 + 9.8m\frac{C_r}{1000}(c_1 S(t) + c_2) + 9.8mG(t), \tag{4.6}$$

where p_{std} = 1.23 kg m^{-3} is the air density at sea level (assuming an air temperature T = 288 K), C_d = 0.78 is the drag coefficient, $C_h = 1 - 0.085h_g$ is a correction factor for height h_g (km) above mean sea level and $A_f \approx 10$ m^2 is the frontal area of the HDDV. C_r, c_1 and c_2 are unitless rolling resistance parameters. In this work it assumed that the road is made of asphalt in good condition, giving C_r = 1.25 (Rakha et al. 2001). For c_1 and c_2 we follow Wang and Rakha (2017), and therefore c_1 = 0.0328 and c_2 = 4.575. Finally, $G(t)$ is the road grade which is assumed to be zero since the highway is relatively flat in the study domain. Assuming diesel fuel has a mass of 0.832 kg l^{-1} then the amount of fuel consumed (kg s^{-1}) is $FC_m = 0.832FC(t)$.

4.4 Results

4.4.1 A case study: CO_2 and particle emissions from a commercial bus

For approximately 20 minutes the instrumented car followed behind a Coach Canada commercial passenger bus, at following distances ranging between 10 and 80 m (median ≈ 34 m, interquartile range (IQR) of 13 m). The vehicle speed is generally near 28 m s^{-1}, but there are two traffic slowdowns due to congestion, where the bus decelerates and then accelerates back toward highway speeds. The Coach Canada bus (manufacturer MCI, model J4500, year 2006) uses a Detroit Diesel Series 60 engine, with its exhaust pipe located at the bottom rear of the vehicle, near the ground. This vehicle had many visible plumes that were recorded by the dashcam video. Figure 4.2 (top image) shows an example of a plume released by the commercial bus; the series of images shown in the bottom of Fig. 4.2 demonstrates emission of a plume from a HDDV. While following behind the commercial bus there is visual evidence of emission at all vehicle speeds, and the visible plumes released from the commercial bus correlate temporally with increasing N_t and CO_2 measured on the instrumented car. However, there are times when a plume is detected in the measurements of N_t and CO_2 without any visible plume recorded on video.

Figure 4.2: Top: still image while chasing a Coach Canada bus on a highway after it has emitted a visible black plume from its exhaust (from the 2016 study). Bottom: a series of still images (each consecutive second) behind a tractor–trailer as it changes lanes, showing the emission of a visible plume (from the 2019 study).

Figure 4.3 (a) shows the 1 s vehicle speed and 1 s following distance while chasing the commercial bus. Gaps in the time series represent occasions when another vehicle entered the lane ahead of the instrumented car, and then subsequently changed lanes again. As seen in Fig. 4.3 (a), there were two periods when the traffic flow moved at speeds less than 20 m s^{-1} (~80 km h^{-1}). These slow periods were followed by a period of acceleration back to near 28 m s^{-1} (100 km h^{-1}). The estimated 1 s acceleration of the bus (a_t) is displayed in Fig. 4.3 (b); also shown in Fig. 4.3 (b) is a_t smoothed with a 6–s running mean. The portion of highway where the commercial bus is sampled does not have any noticeable curvature, therefore only straight–line acceleration is considered. Figure 4.3 (c) is the 1 s averaged CO_2 mass density (ρ_c) calculated from 20 Hz measurements and the 1 s particle number concentration (N_t). Performing a cross–correlation between ρ_c and a_t gives a time lag of 3 s, and about 5 s for N_t and a_t. This time lag results from the travel time required for the CO_2 gas, and particles generated in the engine and during dilution of the exhaust, to arrive at and be sampled by the measurement system affixed to the car. For aerosols this time includes three parts: (1) the travel time between the engine to emission from the tailpipe, (2) from the tailpipe to the inlet of the sampling line and (3) from the inlet of the sampling line to sampling by the UHSAS. For CO_2/H_2O gas, only (1) and (2) are included in the time lag; the inlet for aerosol sampling is co–located with the gas analyzer. Therefore, the results have been shifted by 3 s and 5 s to maximize the cross correlation between ρ_c and a_t, and N_t and a_t, respectively.

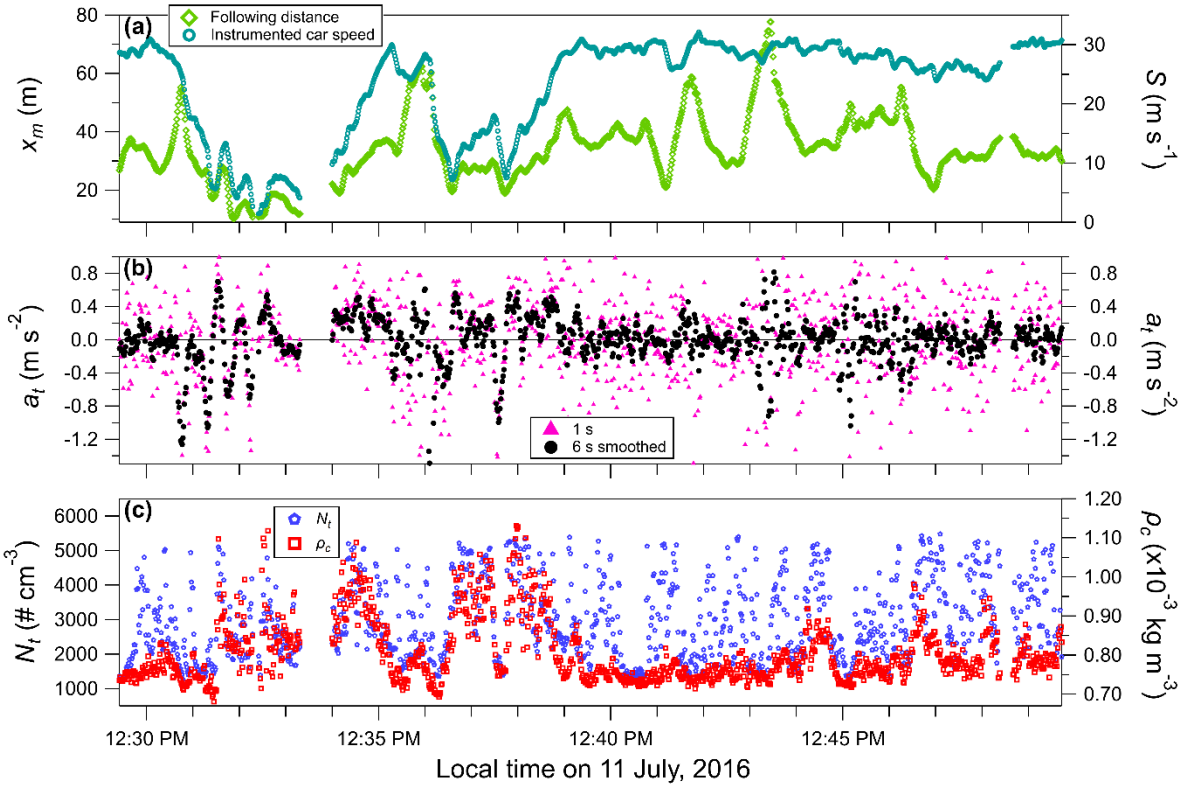

Figure 4.3: (a) The 1 s following distance (x_m) of the commercial bus and 1 s vehicle speed of the instrumented car (S), (b) the estimated 1 s acceleration of a commercial bus (a_t) and the acceleration smoothed with a 6–point running mean, and (c) The 1 s averaged CO_2 mass density (ρ_c) and 1 s aerosol number concentration (N_t). Data are from 11 July 2016. Data in panel (c) are not background removed.

Figure 4.4 shows (a) ρ_c and (b) N_t binned according to the smoothed 6–s a_t of the commercial bus, using a bin size of 0.1 m s^{-2}. The median of each bin is shown as a marker while error bars (upper and lower respectively) give the 75th and 25th percentile of each bin. If a bin has less than 20 data points, then that bin is excluded from the results presented in Fig. 4.4. The median ρ_c increases as the acceleration increases past 0.1 m s^{-2} in an exponential fashion, indicating that vehicle acceleration is a significant cause of CO_2 emission from the commercial bus. While N_t is greatest during acceleration, there is not a significant change in N_t as the acceleration is increased and N_t remains relatively constant in the median. For times when the bus is driving at a nearly constant speed (i.e., $a_t \approx 0$ m s^{-2}), the measured N_t remains large, suggesting significant particle emissions even while travelling at a nearly constant speed. For periods of deceleration, the median ρ_c is reduced and remains relatively constant (with a reduced interquartile range). If unsmoothed data are used instead of smoothed data to generate Fig. 4.4, then the effect is to increase the magnitude of $a_t > 0$ m s^{-2}, and to give a less significant increase of ρ_c in the median and 25th percentile with increasing

a_t. Nonetheless, both the smoothed and unsmoothed binned a_t suggest that larger a_t produces greater CO_2 emission.

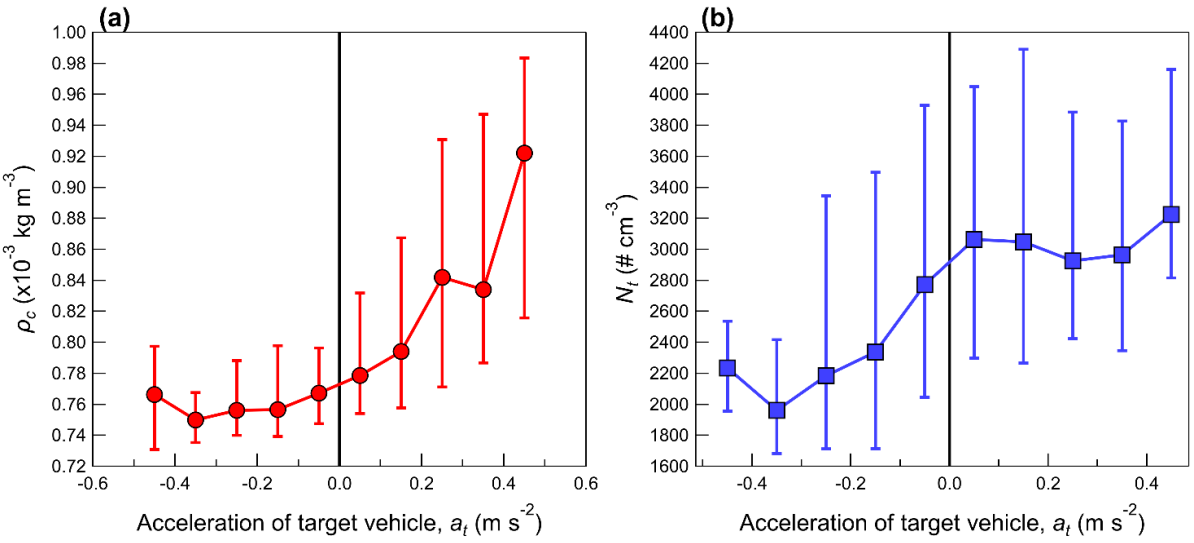

Figure 4.4: (a) 1 s averaged CO_2 mass density (ρ_c) and (b) the 1 s number concentration (N_t) binned according to the 6 s smoothed acceleration (a_t), for measurements made behind the commercial bus (i.e., data shown in Fig. 4.3). Solid markers connected by lines show the median, and the upper and lower error bar gives the 75th and 25th percentile of each bin, respectively. Data are not background removed.

4.4.2 Particle size distributions

Figure 4.5 displays image plots of the time varying (second resolution) aerosol size distribution ($dN/d\log D_p$) for particles with diameters between 62 and 204 nm measured behind two different HDDVs: (a) a tractor–trailer and (b) a commercial bus. Emissions from these two vehicles were both measured during the 2016 study, with following distances typically between 20 and 50 m and vehicle speeds of 24 to 32 m s^{-1}. Superimposed in Fig. 4.5 is a black dashed line which displays the mode diameter, D_{mode}, which is defined as the particle diameter (D_p) at which $dN/d\log D_p$ is maximized. Even though diameters greater than 204 nm are not shown, D_{mode} measured behind these HDDVs never exceeds this upper range. There are times behind both vehicles when D_{mode} occurs in the 60 to 62 nm range (the lowest size bin measured by the UHSAS), which suggests the presence of a nucleation mode. However, the full nucleation mode consists of particles with diameters that are too small to be sized by the UHSAS. Thus, the size bin 60 to 62 nm is excluded in the determination of D_{mode} and is not shown in Fig. 4.5. Figure 4.5 (a) and (b) use different ranges for the color scale to allow variations in the number concentration to be emphasized. The image plots demonstrate the there is a large temporal variation in the number concentration while chasing behind HDDVs. D_{mode} has some degree of time variation behind both vehicles within the measured plumes. However, behind the commercial bus the variation of D_{mode} is more distinct and follows a well–defined

pattern: an increase, a maximum and a subsequent decrease, referred to here as an 'event'. Events with the largest variation in D_{mode} are denoted as circled areas in Fig. 4.5 (b), but there are other events where variation exists in D_{mode}, however it is less significant and similar to the variation measured behind the tractor–trailer shown in Fig. 4.5 (a). In both measurement years (2019 and 2016), we did not measure any other vehicles that had as much variation in the magnitude of D_{mode} as the commercial bus. The sharp cut–off in the size distribution of the tractor–trailer around a particle diameter of 130 nm (a similar region of reduced concentration exists behind the commercial bus), is related to the instrument calibration (i.e., overlapping gain stages), and thus is not an actual artifact of the measured distribution.

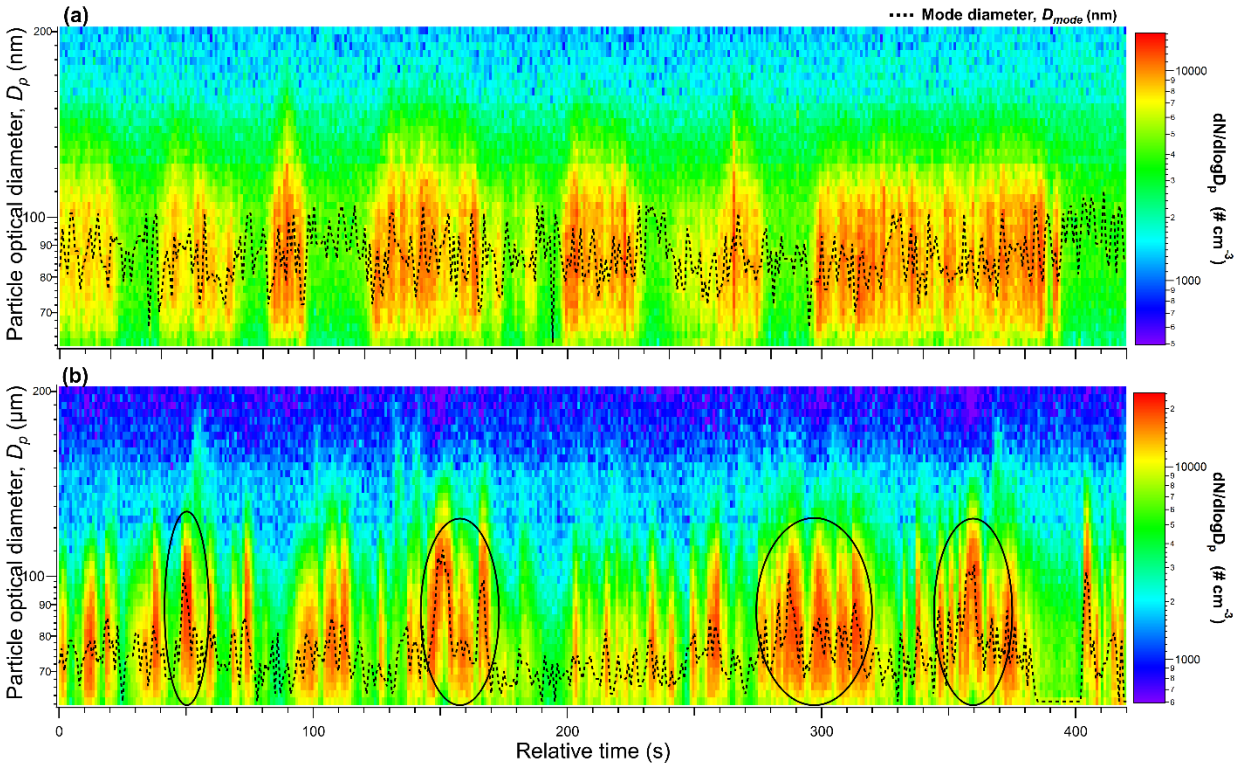

Figure 4.5: dN/dlogD_p for D_p between 62 and 204 nm measured each second behind (a) a tractor–trailer with an exhaust location on the vehicle top and (b) a commercial bus with an exhaust location near the ground. The dashed black line gives the mode diameter, D_{mode}. The panels use different color scales for dN/dlogD_p to emphasize variations. Size distributions are not background removed, and not corrected for particle loss.

The aerosol number distributions while chasing various HDDVs are shown in Fig. 4.6. Only times when N_t is greater than the 75th percentile are included in Fig. 4.6, to avoid including periods more representative of background levels. The 75th percentile is determined from the entire record behind a chased vehicle (5 to 15 min). Solid lines in Fig. 4.6 therefore show the median of all data that exceeds the 75th percentile for a particular chasing record. The data are presented in two panels based on the measurement year: (a) shows 2019 data and (b) 2016 data. The data presented in Fig. 4.6 were obtained

relatively close to the back of the vehicle, with x_m < 80 m and typically between 20 and 50 m. For the median size distributions from 2019 shown in Fig. 4.6 (a), a fit to Eq. 4.2 is successful only for Transport #3, #5, #9 and #10. Here a fit is deemed successful if it can capture the accumulation mode with a fit that is representative of the measured data (by visual inspection) – the fits that are deemed unsuccessful appear linear over the entire range of measured particle diameters. These parameters of the function fit to Eq. 4.2 are given in Table 4.2. For most HDDVs measured in 2019 the shape of the number distribution is remarkably similar, irrespective of the measurement day. A fit to Eq. 4.2 is possible for all measured number distributions shown in Fig. 4.6 (b), but not Fig.4.6 (a).

For the data collected in 2019 versus 2016 there are two major differences in the number distributions, which is revealed by the lognormal fits shown in Table 4.2. First, the CMD is on the order of 10 nm larger in 2016 than 2019; and second, apart from the commercial bus, σ_g is greater in 2016 than 2019. N, however, is similar between both 2019 and 2016. For the data collected during both 2016 and 2019, particle emission included mainly particles with diameters < 200 nm; thus the 200 to 1000 nm range is not shown in Fig. 4.6.

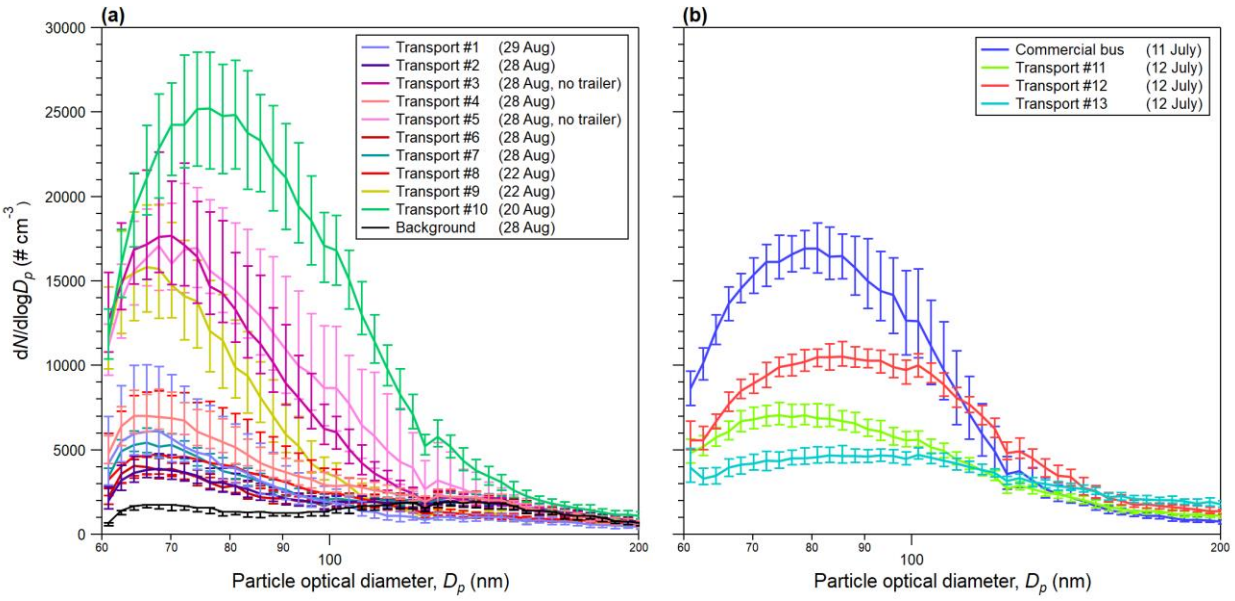

Figure 4.6: The median (solid), 25th percentile (lower error bar) and 75th percentile (upper error bars) of dN/dlogD_p made while chasing HDDVs for (a) measurements obtained during 2019 and (b) measurements obtained during 2016. The background levels are not removed. Size distributions are not background removed, and not corrected for particle loss.

Table 4.2: Lognormal fit of Eq. 4.2 to the size distributions shown in Fig. 4.6. CB refers to the commercial bus. The "#" reference is consistent with those shown in Fig. 4.6. The value of each fit parameter is shown ± 1 standard deviation.

Date / Transport ID	N (# cm^{-3})	σ_g	CMD (nm)
20 Aug 2019 / #10	7389 ± 100	1.32 ± 0.01	79 ± 0.3
22 Aug 2019 / #9	3942 ± 134	1.27 ± 0.01	66 ± 1
28 Aug 2019 / #3	5497 ± 138	1.38 ± 0.01	71 ± 1
28 Aug 2019 / #5	5071 ± 171	1.33 ± 0.01	68 ± 1
11 July 2016 / CB	4959 ± 50	1.31 ± 0.004	81 ± 0.2
11 July 2016 / #11	3090 ± 82	1.53 ± 0.02	77 ± 1
11 July 2016 / #12	3843 ± 55	1.40 ± 0.01	87 ± 0.5
11 July 2016 / #13	2912 ± 65	1.82 ± 0.03	85 ± 1

4.4.3 CO_2 and particle number fluxes

a. Variation with following distance

Figure 4.8 displays (a) $\overline{w'\rho_c'}$, (b) the CO_2 mass density variance ($\sigma_{\rho_c}^2$) and (c) the CO_2 mass density (ρ_c) measured at z_m = 1.7 m and binned according to following distance using a bin size of 5 m. Likewise, Fig. 4.8 (d), (e) and (f) show $\overline{w'N'}$, σ_N^2 and N_t respectively, calculated from 22, 28, and 29 Aug 2019 data. All means, variances and covariances shown in Fig. 4.8 are calculated using an averaging period of 10 s. 2019 data almost exclusively measured behind HDDVs with top exhausts, with an estimated exhaust located at a height of 4.1 m. In the analysis presented here, 20 Aug is not included since only one HDDV was sampled, and it produced anomalously large emissions (see Fig. 4.6 and Table 4.2), likely due to emissions from other HDDVs that were travelling in its vicinity. Furthermore, measurements on 30 Aug did not sample closely behind HDVs, and so no data from that day are included here. Upper and lower error bars denote the 75th and 25th percentile respectively, and this convention is used in all figures that follow. The measurements are sorted into two groups based on exhaust location. The exhaust location is determined by visually inspecting the video: triangles are box shaped HDVs that have an exhaust location on the vehicle's bottom (BE–HDVs) and circles are box shaped HDDVs that have an exhaust location on the vehicle's top (TE–HDVs). An example of a TE–HDV and BE–HDV emitting a black carbon abundant plume, while travelling at a speed near 100 km h^{-1} with negligible ambient flow, is shown in Fig. 4.7.

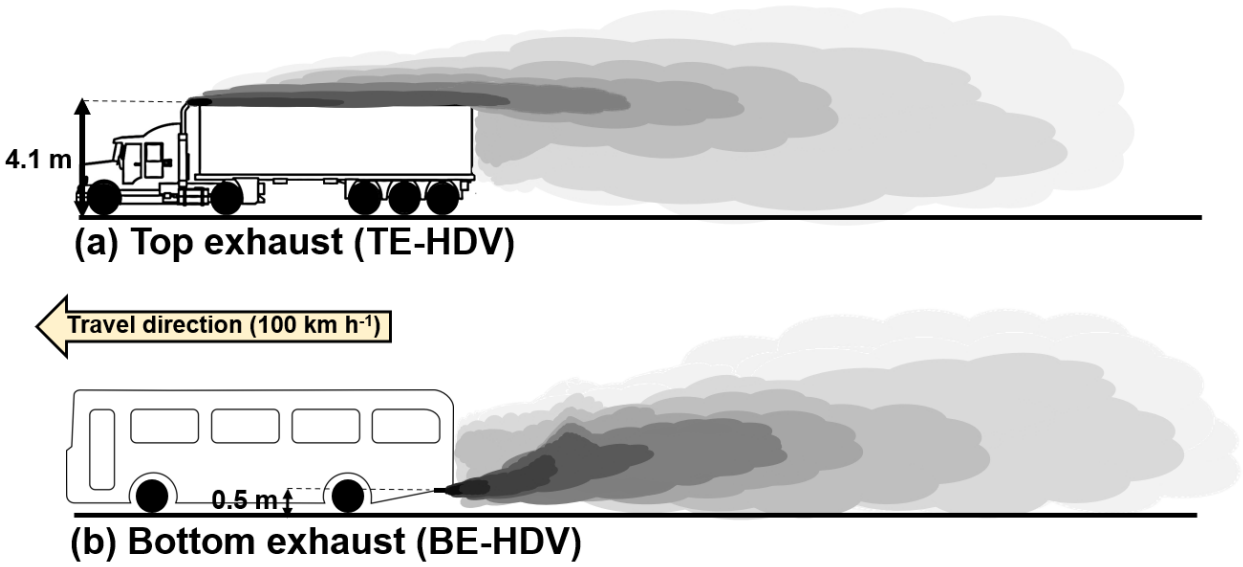

Figure 4.7: Interpretation of (a) a top exhaust (TE–HDV) and (b) a bottom exhaust (BE–HDV) vehicle emitting a black carbon plume that is spreading with time and interacting with the vehicle induced flow perturbations. Ambient winds are assumed to be weak and negligible (< 1 m s^{-1}). Depiction is of the $x - z$ plane.

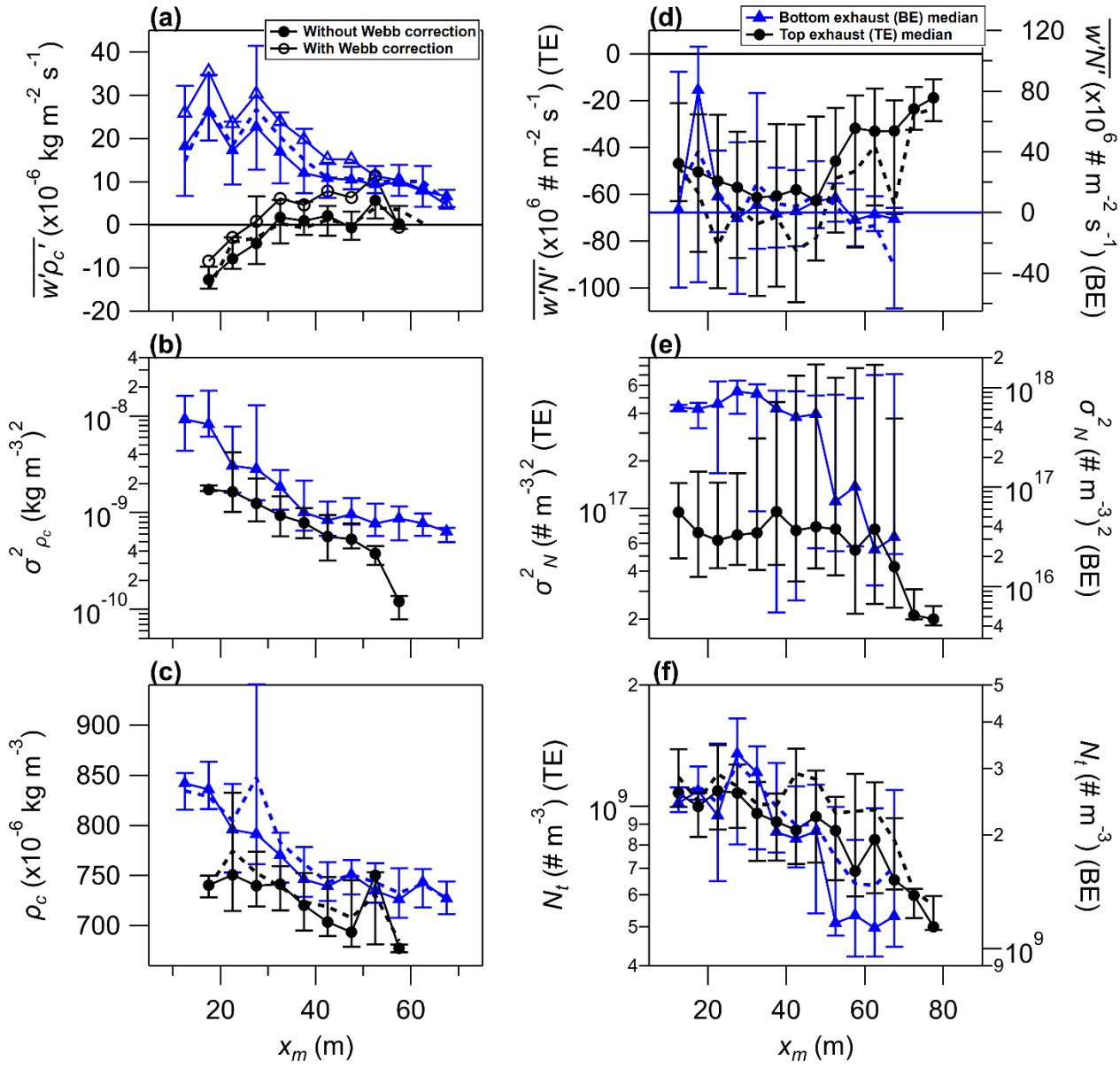

Figure 4.8: The median (solid marker), 25th percentile (lower error bar) and 75th percentile (upper error bars) of (a) the vertical turbulent flux of carbon dioxide ($\overline{w'\rho_c'}$), (d) the vertical turbulent flux of aerosols ($\overline{w'N'}$), (c) the variance of the CO_2 mass density ($\sigma^2_{\rho_c}$), (e) the variance of the aerosol number concentration (σ^2_N), (c) the average CO_2 mass density (ρ_c) and (f) the average aerosol number concentration (N_t) made while chasing HDVs with either a bottom exhaust (BE) or top exhaust (TE). Dashed lines give the bin mean. For aerosols, the measurements shown for BE vehicles were recorded at 1 Hz, but for TE the measurements shown were recorded at 40 Hz. All measurements for CO_2 were recorded at 20 Hz (for BE and TE vehicles). All statistics are calculated over a 10 s averaging period. Panel (c) and (f) are not background removed.

The median $\overline{w'\rho_c'}$ < 0 behind TE–HDVs at x_m < 20 m (< 35 m if no Webb correction is applied) and $\overline{w'N'}$ < 0 at all x_m measured. Behind TE–HDVs the largest negative $\overline{w'N'}$ are at x_m between 20 and 45 m, but the largest negative $\overline{w'\rho_c'}$ occur closer to the trailer, between 15 and 20 m, which is the lower limit of measured x_m during the 2016 study. There is a drop–off in $\sigma_{\rho_c}^2$ near x_m = 50 m, and likewise in σ_N^2 near x_m = 60 m measured behind TE–HDVs. At x_m < 50 m, $\sigma_{\rho_c}^2$ increases steadily with decreasing x_m but σ_N^2 remains relatively constant and shows little trend with decreasing x_m. ρ_c and N_t are similar to $\sigma_{\rho_c}^2$ and σ_N^2 respectively, except at x_m < 35 m where ρ_c and N_t remain relatively constant. All TE–HDVs investigated have a trailer accompanying the main cab, with a length of about 15 m. Therefore, the actual distance between the instrumented car and the exhaust location is about 15 m greater than x_m presented in Fig.4.8 (and Fig. 4.10).

Behind BE–HDVs, $\overline{w'\rho_c'}$ > 0 at all x_m measured (in the 25th, median and 75th percentiles), and the median $\overline{w'\rho_c'}$ is maximized at x_m between 15 and 20 m. The median $\overline{w'N'}$ shows a similar maximum at x_m between 15 and 20 m, and $\overline{w'N'}$ is typically positive or near zero at all x_m measured. Therefore, downward (negative) fluxes of $\overline{w'\rho_c'}$ and $\overline{w'N'}$ are much less likely to occur for measurements made at z_m= 1.7 m behind BE–HDVs compared to TE–HDVs. Behind BE–HDVs, there is a significant drop in σ_N^2 and N_t around x_m = 50 m, suggesting a transition region near this distance. It is useful to point out that σ_N^2 and $\overline{w'N'}$ measured behind BE–HDVs are calculated from 1 Hz sampling. While measuring at high vehicle speeds, 1 Hz sampling neglects high frequency contributions occurring at frequencies > 0.5 Hz (these contributions are evident in the cospectra of $\overline{w'N'}$ measured behind TE–HDVs, see Sect 4.4.4).

The effect of applying the Webb correction to $\overline{w'\rho_c'}$ in this work is to increase the flux, increasing the flux magnitude when $\overline{w'\rho_c'}$ > 0 and decreasing the flux magnitude when $\overline{w'\rho_c'}$ < 0. The magnitude of the Webb correction is dominated by the heat flux (not shown).

To investigate the distribution of N_t in the wake of TE–HDVs, 1 s averaged measurements of N_t are separated into two groups defined by x_m: Group 1 consists of measurements at x_m < 50 m and Group 2 contains measurements at 50 ≤ x_m< 80 m. As demonstrated from the results presented in Fig. 4.8 (f), these two groups represent distinctly different regions of the wake – Group 1 is likely representative of the near wake region and Group 2 the far wake region. A frequency and cumulative frequency distribution generated from each group of data are shown in Fig. 4.9: Group 1 is shown in Fig. 4.9 (a) and Group 2 shown in Fig. 4.9 (b). The frequency distribution of Group 1 is unimodal and positively skewed, peaking between 945 and 1015 × 10^6 # m^{-3}. Group 2 is bimodal, and less positively skewed compared to Group 1. Group 2 has a dominant peak (frequency ≈ 0.165) between 595 and 665 × 10^6 # m^{-3}, and a second less defined peak between 875 and 1015 × 10^6 # m^3 that is consistent with the peak of Group 1. The cumulative

frequency distribution shows that in Group 1 about 22 % of N_t are < 735× 10^6 # m^{-3} while for Group 2 approximately 48 % of N_t are < 735× 10^6 # m^{-3}.

It is likely that the dominant peak in the far wake (Group b) can be attributed to "background levels". In this case, the cumulative frequency distribution at the minimum located between each peak gives a threshold to define the "background levels". For the data shown in Fig. 4.9 (b) this corresponds to 735× 10^6 # m^3, with the fraction of time spent at "zero concentration" then f_{zero} = 0.48. The intermittency factor is then $I = 1 - f_{zero}$ = 0.52 or 52 %. Using the same threshold in the near wake region (Group 1) gives f_{zero} = 0.22 and I = 78 %.

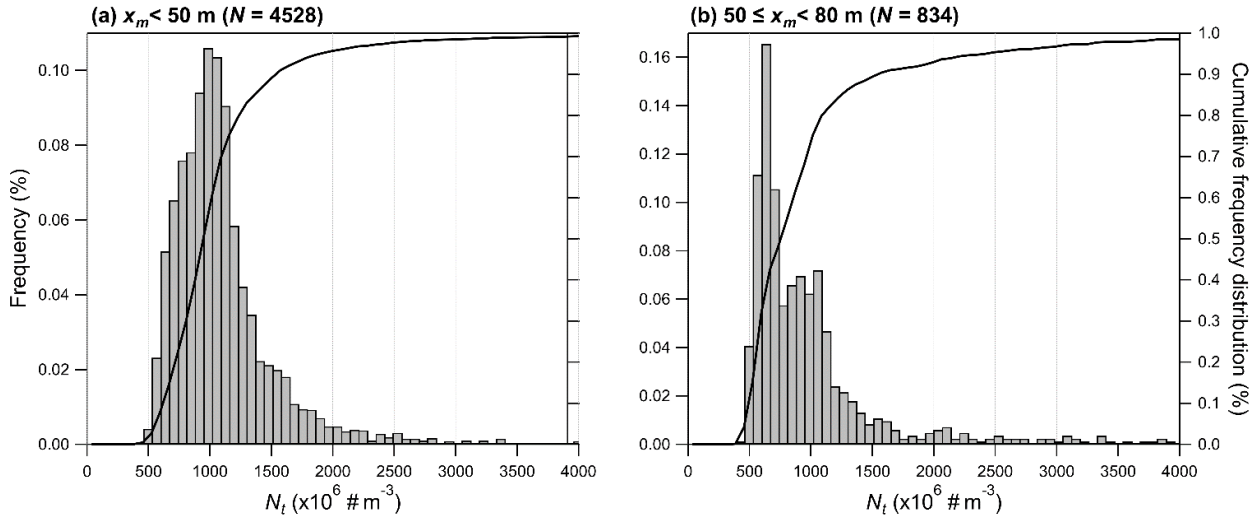

Figure 4.9: The left axis shows a frequency distribution of the particle number concentration (N_t) and the right axis shows a cumulative frequency distribution, measured behind TE–HDV for (a) following distances (x_m) < 50 m and (b) 50 ≤ x_m < 80 m. The distributions are generated from 1 s averages of N_t.

b. Impact of averaging period

While measuring at high vehicle speeds near 100 km h^{-1}, 10 s corresponds to about 278 m of elapsed distance. Further, as was shown in Sect. 4.4.2 there are rapid variations in the aerosol size distribution on short time scales of 1 to 5 s, and this may suggest that an averaging period less than 10 s is more appropriate for the calculation of concentration statistics. Thus, in this section the averaging period is reduced to 1 s (from 10 s). Figure 4.10 (c), (d) and (f) show $\overline{w'N'}$, $\overline{w'\rho_c{}'}$ (without Webb correction applied) and N_t respectively, binned according to x_m using a bin size of 5 m and calculated using an averaging period of 1 s. Therefore, Fig. 4.10 (b), (c) and (f) demonstrate the impact of using a 1 s averaging period to calculate $\overline{w'N'}$, $\overline{w'\rho_c{}'}$ and N_t, when compared to analysis completed using a 10 s averaging period as shown in Fig. 4.8 (d), (a) and (f) respectively. Since 2016 used 1 s sampling for aerosols, it is not possible to calculate a

1 s $\overline{w'N'}$ for BE–HDVs. For TE–HDVs, using a 1 s averaging period gives a more defined minimum in the median and 25th percentile for $\overline{w'N'}$, between 30 and 40 m. The 75th percentile of $\overline{w'N'}$ calculated using a 1 s averaging period also suggests that the magnitude of $\overline{w'N'}$ is reduced toward zero at x_m < 15 m and x_m > 60 m. Using a 1 s averaging period to calculate $\overline{w'\rho_c{}'}$ reduces the magnitude of the flux for both BE–HDVs and TE–HDVs. This results in a median $\overline{w'\rho_c{}'} \approx 0$ for all x_m behind TE–HDVs and for BE–HDVs, the peak in the median $\overline{w'\rho_c{}'}$ between 15 and 20 m is less evident.

c. Vehicle–induced turbulence

Figure 4.10 (a) shows $\overline{w'N'}$ and (d) shows $|u'v'|$, binned according to turbulent kinetic energy (e) using a bin size of 1 m^2 s^{-2}. Figure 4.10 (e) shows the turbulent kinetic energy binned according to x_m using a bin size of 5 m. Like the previous section, a 1 s averaging period is used to generate Fig. 4.10 (a), (d) and (e). In Fig. 4.10 (d) the absolute value of $\overline{u'v'}$ is presented ($|\overline{u'v'}|$) since modelling studies suggest the sign of $\overline{u'v'}$ will reverse while measuring behind a box shaped HDV, dependent upon which side wall shear layer is being measured (McArthur et al. 2016; He et al. 2019). For a scatter plot of $|\overline{u'v'}|$ plotted against e, a power law fit matches the median binned measurements well, with $|u'v'| = -0.09 + 0.11e^{1.42}$, and this fit is displayed in Fig. 4.10 (d) as a red dashed line. A linear fit gives R^2 = 0.48 with $|u'v'| = -0.74 + 0.37e$ (see Fig. E4) but gives a poor fit for large and small magnitudes of $|\overline{u'v'}|$. The linear fit does not give a reasonable y–intercept (–0.74 m^2 s^{-2}) while the power law fit gives a physically reasonable y–intercept near zero when uncertainty in the intercept is considered (i.e., standard deviation of the y-intercept of power law fit is 0.06 m^2 s^{-2}).

Vehicle–induced turbulence has previously been quantified using turbulent kinetic energy from on–road measurements, where a clear relationship with following distance was demonstrated (Rao et al. 2002; Gordon et al. 2012; Miller et al. 2019/Chapter 2). Likewise, Fig. 4.10 (e) shows that the 1 s turbulent kinetic energy (e) measured behind TE–HDVs (from 2019 data) has a clear relationship with x_m, decreasing with increasing x_m, which is consistent with prior on–road studies. The drop off in e is most rapid within the first 30 m downwind of the trailer, decreasing from 8.9 m^2 s^{-2} at x_m = 12.5 m to 5.4 m^2 s^{-2} by x_m = 28 m. The relationship between $|\overline{u'v'}|$ and e is quite pronounced for measurements behind TE–HDVs, and despite a linear regression to measurements giving a poor fit for large and small $|\overline{u'v'}|$, the results suggest about 48 % of the variance in e can be explained by $|\overline{u'v'}|$. The relationship between $\overline{w'N'}$ and e is less pronounced, but the results demonstrate that the largest $\overline{w'N'}$ are coincident with large e. Therefore, vehicle–induced turbulence facilitates rapid vertical diffusion of pollutants behind TE–HDVs travelling at high speeds.

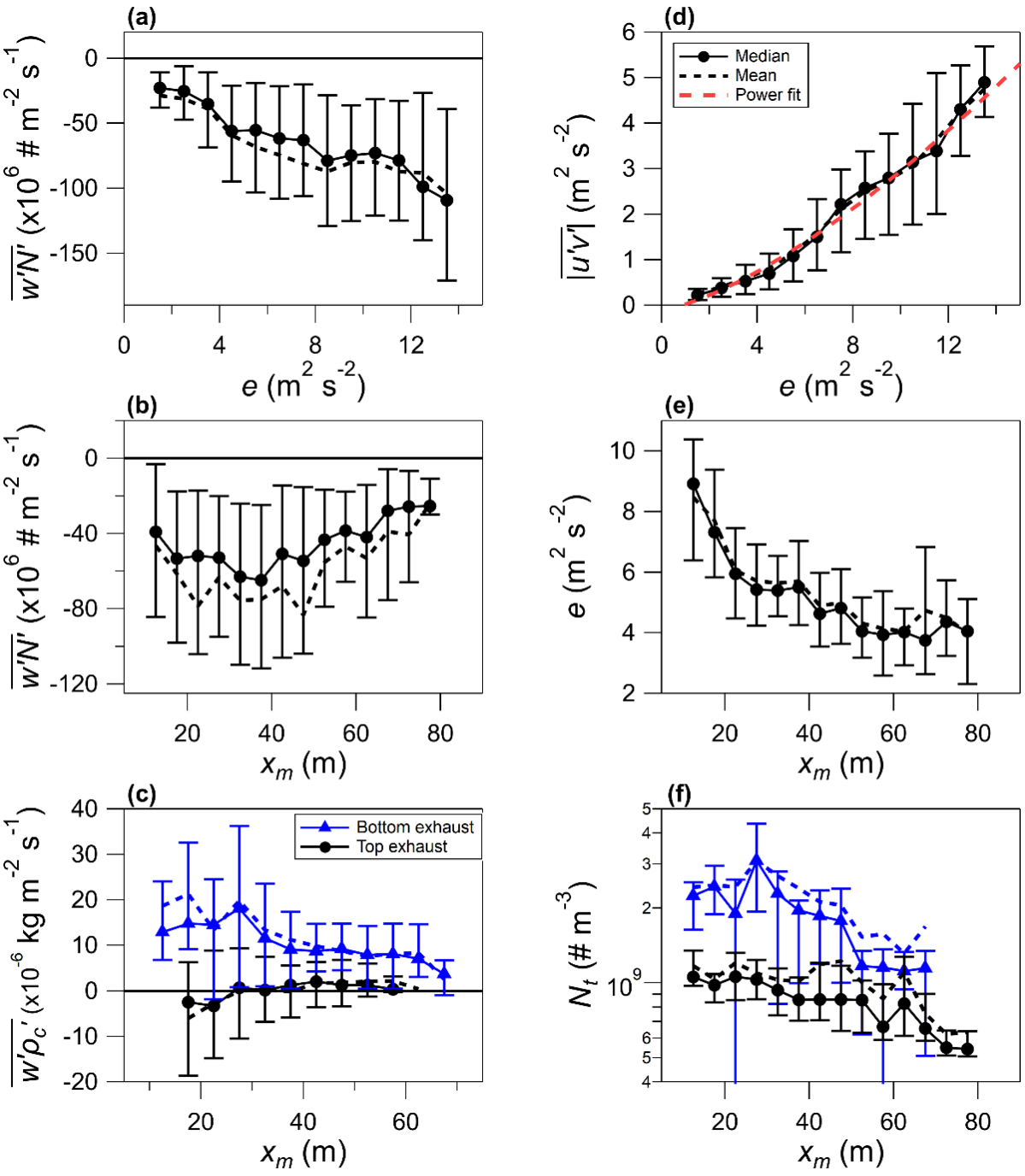

Figure 4.10: The median (solid marker), 25th percentile (lower error bar) and 75th percentile (upper error bars) of (a) the vertical turbulent aerosol number flux ($\overline{w'N'}$) and (d) the vertical turbulent momentum flux ($\overline{u'w'}$) binned according to turbulent kinetic energy (e). Panel (b) shows $\overline{w'N'}$, (c) the vertical turbulent CO_2 flux ($\overline{w'\rho_c'}$), (e) the turbulent kinetic energy and (f) the average aerosol number concentration (N_t) binned according to following distance (x_m). Measurements were obtained while chasing HDVs with either a bottom exhaust (BE) or top exhaust (TE). Dashed lines give the bin mean. All measurements for CO_2 were recorded at 20 Hz (for BE and TE vehicles). All statistics are calculated over a 1 s averaging period. Panel (f) is not background removed.

Fig. 4.11 (a) displays $\overline{w'N'}$ binned according to $\overline{u'w'}$, and Fig. 4.11 (b) shows $\overline{u'w'}$ binned according to e. The vertical momentum flux ($\overline{u'w'}$) has a distinct relationship with $\overline{w'N'}$. The most significant downward $\overline{u'w'}$ (i.e., < –1.5 m^2 s^{-2}) are coincident with the most significant downward $\overline{w'N'}$ (i.e., < –150×10^6 m^{-2} s^{-1}) measured behind TE–HDVs. The median $\overline{u'w'}$ decreases nearly linearly with increasing e up to 7 m^2 s^{-2}. For large e > 10 m^2 s^{-2}, downward momentum fluxes are most significant but there are times when $\overline{u'w'}$ > 0 (i.e., upward). For measurements behind TE–HDVs, we do not observe $\overline{u'w'}$ > 0 for significant downward $\overline{w'N'}$, and therefore when $\overline{u'w'}$ > 0, the downward turbulent transport of aerosols is limited.

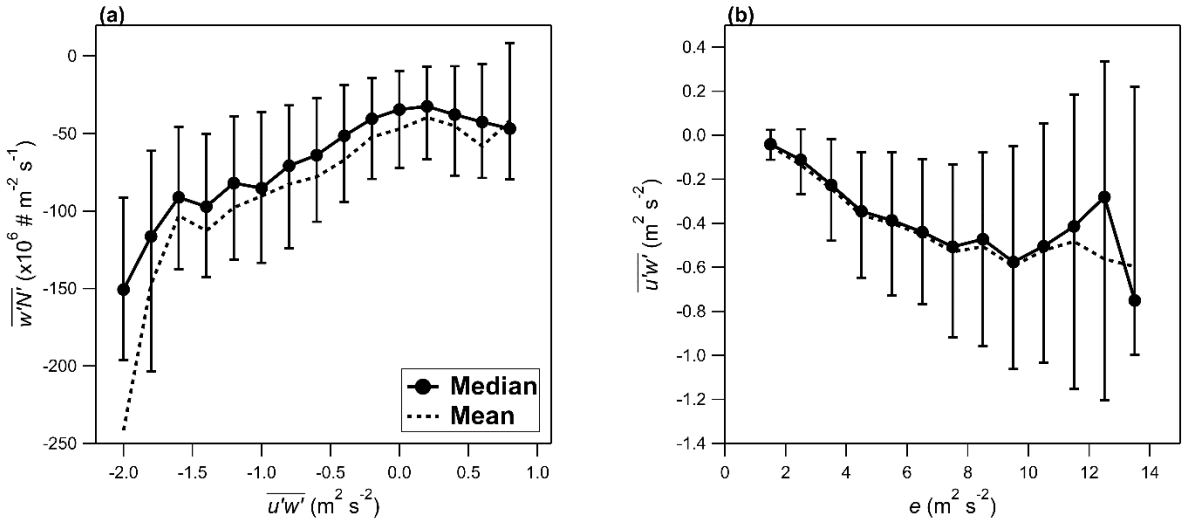

Figure 4.11: (a) the vertical turbulent number flux ($\overline{w'N'}$) binned according to the vertical turbulent momentum flux ($\overline{u'w'}$) using a bin size of 0.2 m^2 s^{-2}, and (b) $\overline{u'w'}$ binned according to turbulent kinetic energy (e) using a bin size of 1 m^2 s^{-2}. Data are from TE–HDV. Variances and covariances are calculated using a 1 s averaging period.

4.4.4 Spectra and cospectra

Figure 4.12 displays 1 min wavelet power spectra of (a) the turbulent kinetic energy and (b) the number concentration. Fig. 4.12 (c) shows the wavelet cospectrum between w and N_t. The frequency axis has been converted to an equivalent wavelength, $\lambda = u_m/f$, where u_m is the measured flow parallel to vehicle motion and f is the frequency. This normalization assumes that Taylor's hypothesis is valid. Each panel shows three different spectra of TE–HDVs in different scenarios measured in 2019: one case is without a trailer (denoted 'no box') and two are with a trailer (denoted 'with box'). Spectra for a period isolated from traffic are included for comparison. All spectra were measured at a height of 1.7 m. For a single HDV with a trailer, there is a distinct peak in the turbulent kinetic energy between λ = 10 and λ = 20 m. For two HDVs side–by–side, the peak is lower, between λ = 8 and λ = 10 m. When the trailer is removed, the peak broadens

and becomes much less distinct. Comparing with the background spectrum, length scales less than 60 m are responsible for enhanced turbulent kinetic energy in the vehicle wake. The concentration spectra however have influences from much longer wavelengths. These longer wavelength contributions may be due to variation of the background levels, due to plume meandering resulting from crosswind flow, or due to variations in the emission rate and following distance. The emission rate and following distance are not necessarily constant over the entire 1 min period used to calculate the spectra. However, the following distance remains within a small range of about 10 m, and therefore should not significantly impact the measured spectra. The concentration spectra do not demonstrate an inertial subrange, unlike the spectra of turbulent kinetic energy, and have less slope at high frequencies. Cospectra of $\overline{w'N'}$ demonstrate an increase in a similar range as the turbulent kinetic energy spectra, with the main contributions to $\overline{w'N'}$ from $\lambda < 50$ m. There are significant contributions to $\overline{w'N'}$ at frequencies > 0.5 Hz (the Nyquist frequency of the 2016 aerosol data), and therefore $\overline{w'N'}$ reported for BE–HDVs in Fig. 4.8 (d) are likely underestimated. Removal of the trailer has little effect on the shape of the cospectra for $\lambda < 20$ m.

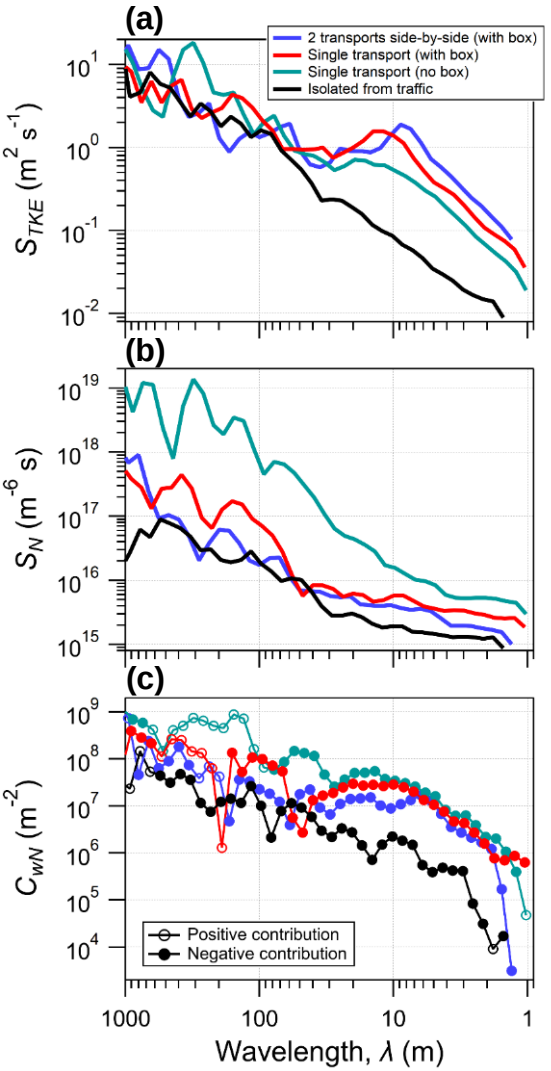

Figure 4.12: 1 min wavelet power spectra of (a) the turbulent kinetic energy and (b) the number concentration. Panel (c) shows the 1 min wavelet cospectrum of the vertical velocity and the aerosol number concentration. Measurements were obtained in 2019 behind heavy–duty vehicles with top exhausts. The frequency axis is normalized to give an equivalent wavelength, $\lambda = u_m/f$, where u_m is the measured flow parallel to vehicle motion and f is the frequency.

4.4.5 Emission factors

Figure 4.13 shows a frequency and cumulative frequency distribution of the particle number emission factors calculated from data collected during 2016. About 59% of the emission factors are $\leq 0.19\times10^{14}$ # kg^{-1}, and approximately 90% are $\leq 0.69\times10^{14}$ # kg^{-1}. Large emission factors $> 0.7\times10^{14}$ # kg^{-1} are therefore relatively uncommon (< 10 %). If the emission factors are separated by vehicle classification, as HDVs or LDVs (light–duty vehicles), then HDVs clearly produce the largest emission factors. Emission factor statistics for each vehicle class are shown in Table 4.3. LDVs include passenger vehicles such as cars, sport utility vehicles and pickup trucks, while HDVs include dump trucks, tractor–trailers (with or without a box) and commercial buses. There are times when the instrumented car is isolated with no traffic in the highway

lanes ahead, except maybe 100's of m away. During these isolated times there are still plumes being recorded since there are times with correlated ρ_c and N_t. The video reveals that while there is no traffic directly ahead of the instrumented car, there is still significant traffic in the highway lanes moving in the opposite direction (i.e., across the center highway embankment). Thus, it is likely that LDV emission factors are impacted and biased high as a result, since there may be HDVs which have much higher emissions travelling in the opposite direction, and these plumes can be advected across the highway while measuring behind a low emission LDV. This is supported by a maximum emission factor for LDVs, which is 0.95×10^{14} # kg^{-1}; emission factors this large account for < 7% of all emission factors calculated during 2016. Given these results we do not focus on LDV plume dynamics in this study, since HDV exhaust is clearly impacting measurements while sampling behind low emission vehicles, giving rise to a large uncertainty for the LDV class. These values are compared to previous studies in Sect 4.5.2.

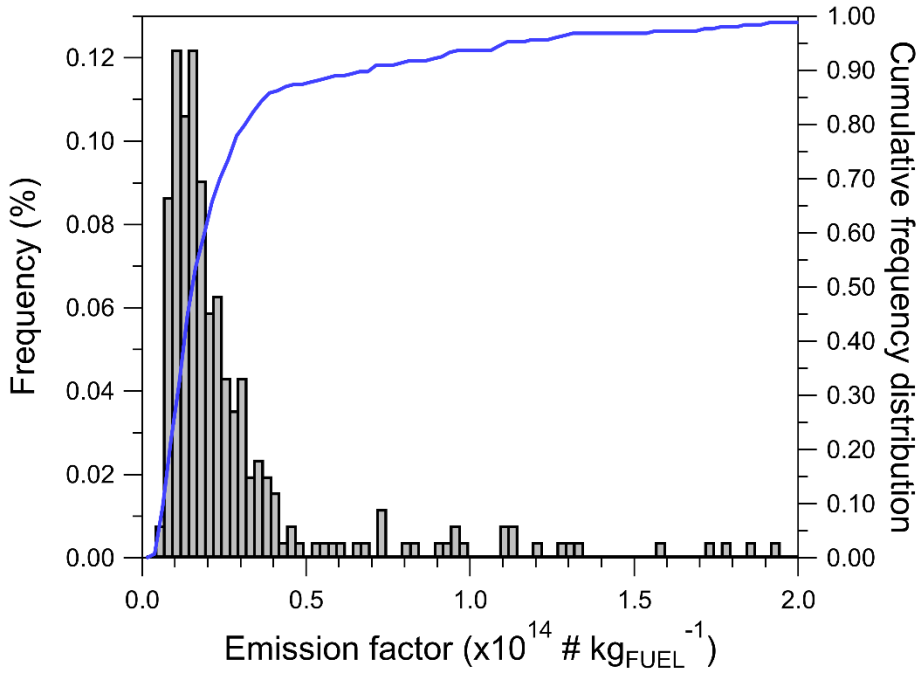

Figure 4.13: Frequency (left axis) and cumulative frequency (right axis) distribution of emission factors calculated from 07 to 15 July 2016.

Table 4.3: Emission factor statistics based on vehicle classification, as either heavy–duty vehicles (HDV) or light–duty vehicles (LDV). See text for description of vehicle types included in each classification. Emission factors have units of $\times10^{14}$ # kg^{-1} and include particles with diameters between 60 and 1000 nm. Data are calculated from measurements obtained between 07 and 15 July 2016.

Vehicle Type	No. Plumes	Median	Q25	Q75	Mean	Min	Max
HDV	115	0.23	0.14	0.39	0.43	0.04	3.50
LDV	40	0.13	0.10	0.18	0.15	0.07	0.95

4.5. Discussion

4.5.1 Pollutant transport and wake characteristics behind heavy–duty vehicles

For BE–HDVs, the effluent is released directly into the vehicle's wake (in the absence of strong crosswinds). Immediately after release, the plume undergoes rapid dilution and cooling resulting from the enhanced turbulence generated by the lower shear layer which emerges from the vehicle's underbody. The rapid dilution limits the amount of buoyancy–driven plume rise, and so plume rise is dominated by advection and turbulent transport as the plume interacts with the lower and side shear layer (Xie et al. 2020). For BE–HDVs measured in this study the exhaust is estimated to be near the ground, at a height of 0.5 m. While following closely behind BE–HDVs, we measured a positive $\overline{w'N'}$ and $\overline{w'\rho_c{}'}$ at a height of 1.7 m, which is consistent with release from a near–ground level source and a plume expanding upward through the detection system. For HDVs with a box–shaped trailer and an exhaust location on the vehicle's top near a height of 4.1 m, the effluent is not emitted directly into the wake region, but instead it is emitted above the trailer. The trailer is on the order of 15 m, and so the trailer must travel past the emitted pollutants, or the emitted pollutants must be advected downwind, to be released into the wake region. For measurements made at a height of 1.7 m and x_m < 30 m, we measured $\overline{w'\rho_c{}'} < 0$ behind TE–HDVs, and for all x_m investigated we measured $\overline{w'N'} < 0$. This is consistent with release from an elevated source and a plume expanding downward toward the measurement height of 1.7 m. Thus, our instrumented setup can successfully measure the general evolution of a chased vehicle's exhaust plume while driving at vehicle speeds near 100 km h^{-1}, since our turbulent flux directions (i.e., positive versus negative) are consistent with the actual pollutant release point on the targeted vehicle.

For a block–shaped vehicle traveling at highway speeds, a side shear layer emerges from each side wall of the vehicle, extending downwind (McArthur et al. 2016; Lo and Kontis, 2017). Based on previous modelling studies, the side shear layer should be evident as a region of enhanced horizontal Reynolds shear stress ($\overline{u'v'}$) extending downwind of either side wall. When measuring behind a block–shaped HDV, these same modeling studies suggest that $\overline{u'v'} < 0$ in the passenger side shear layer and $\overline{u'v'} > 0$ in the driver side shear layer (McArthur et al. 2016; He et al. 2019), where the opposite sign of $\overline{u'v'}$ in either side shear layer indicates that horizontal velocity fluctuations are orientated inward toward the wake center (McArthur et al. 2016). We investigated the direction of $\overline{u'v'}$ in relation to the ambient wind's impact direction on the instrumented car, relative to its travel direction: 0° for ambient flow opposite to the travel direction, –90° for ambient flow perpendicular to and toward the passenger's side, –180° for ambient flow in the direction of travel and +90° for ambient flow perpendicular to and toward the driver's side. If the sign of measured $\overline{u'v'}$ behind block shaped HDVs is dependent on which side shear layer is being sampled, then under crosswind flow it is expected that one side shear layer will be preferentially sampled, and hence one sign

(i.e., positive, or negative) should dominate $\overline{u'v'}$. Carrying out this analysis on the measurements behind TE–HDVs (see Fig. E5 and Fig. E6) indicates that when the ambient flow is toward the passenger's side of the vehicle, $\overline{u'v'} < 0$, but when the ambient flow is toward the driver's side, $\overline{u'v'} > 0$. The measurements in this study are biased since the mean ambient flow is oriented more often toward the passenger's side of the vehicle (compared to the driver's side) and coincident with small x_m. As a result, we find that a histogram of $\overline{u'v'}$ measured behind TE–HDVs is negatively skewed with larger magnitudes for $\overline{u'v'} < 0$ (see Fig. E7). As demonstrated in Sect. 4.4.3–c from a least–squares fit to measurements, about 50% of measured variance in the turbulent kinetic energy behind TE–HDVs can be explained by $\overline{u'v'}$ alone. Combined, these results indicate the presence of two side shear layers extending downwind of block shaped HDVs, that produce significant turbulence at a height of 1.7 m and are most intense close to the vehicle at x_m < 25 m. Furthermore, the sign of $\overline{u'v'}$ is found to be dependent upon which side shear layer is being measured – negative for the passenger's side and positive for the driver's side, which is consistent with the modelling studies of McArthur et al. (2016) and He et al. (2019).

In addition to the side and lower shear layers, an upper shear layer develops along the top of the trailer. McArthur et al. (2016) and He et al. (2019) demonstrate that the upper shear layer is characterized by an enhanced zone of vertical momentum transport (and e) extending downwind near the top of the trailer. Thus, modelling studies predict a region characterized by a large negative $\overline{u'w'}$ near the trailer's top, that extends downwind. Unlike $\overline{u'v'}$, the relationship between $\overline{u'w'}$ and e measured at a height 1.7 m is weak: linear least squares fit of $\overline{u'w'}$ versus e gives R^2 = 0.17 (not shown), compared to R^2 = 0.48 for $\overline{u'v'}$ versus e. This is not unexpected, since as demonstrated in modelling and wind tunnel investigations, the upper shear layer is positioned near the top of the trailer, and therefore above our measurement height of 1.7 m. Despite this, we find that the most significant downward fluxes of $\overline{w'N'}$ behind TE–HDVs occur only when $\overline{u'w'}$ is minimized (see Fig. 4.11), suggesting a correlation between vertical momentum transport in the wake and the vertical diffusion of aerosols. If the large negative $\overline{u'w'}$ correspond to the upper shear layer as demonstrated in modelling studies, then these results suggest that the upper shear layer has a significant impact on vertical pollutant transport in the near wake region for TE–HDVs, and probably on the initial transport to the vehicle wake (along the top of the trailer).

In the recirculation region (typically less than 10 vehicle heights downwind), numerical simulations show that pollutants are trapped to some degree within the intense vehicle–generated shear layers that bound the wake region (Wang and Zhang, 2012; Xie et al. 2020; Wang and Wang, 2021). This trapping effect might be indicated by the measurements presented in this study (i.e., Fig. 4.8), but the evidence from measurements alone is not conclusive. For example, behind either TE–HDVs or BE–HDVs, the median ρ_c and N_t increases steadily for x_m < 50 m, but for $x_m > 50$ m there is little change in the median ρ_c. These

results are more indicative of a sharp change in the wake behavior near 50 m range, likely representing the transition region of the near wake to far wake region.

The cospectra of w and N_t shown in Fig. 4.12 (c) demonstrate that length scales < 50 m are primarily responsible for vertical turbulent transport of particles in the wake region. The spectra of N_t are expected to attain a –5/3 slope in the inertial subrange (Hanna, 1986). However, the spectra of N_t here do not display any evidence of an inertial subrange. We see a near +1 slope in the high frequency part of the spectrum, when plotted as $fS(f)$ versus f, which may indicate the presence of white noise (Langford et al. 2015). This implies that there is significant noise in the particle–by–particle 40 Hz UHSAS number concentration measurements, leading to an overestimated variance. Nonetheless, the presence of white noise in N_t should not impact the cospectra, since white noise present in N_t will theoretically have zero correlation with w. Fig. 4.12 (b) demonstrates that other factors aside from vehicle-induced flow structures influence the variation of the particle number concentration while measuring on highways, such as variations in the background level with time and much more transient emissions that occur during specific operating conditions (i.e., acceleration). These effects lead to low frequency contributions in the concentration spectra (at length scales greater than 50 m) that are specific to the time series analyzed and do not correlate with vehicle-induced turbulence.

4.5.2 Comparison of measured emission factors and size distributions to past studies

Emission factors calculated from the UHSAS in this study are much lower than any previous North American particle number emission factors published in the available literature. A summary of previous measurement studies is given in Table 4.4. This underestimation is likely due to a difference in the size range between the UHSAS (only diameters > 60 nm) and other instruments used to determine emission factors in other studies. This is especially important since nucleation mode particles are mostly diameters < 60 nm and can encompass up to 90 % of emitted exhaust particles by number. Three studies (Kalafut–Pettibone et al. 2011, Kittelson et al. 2006 and Ban–Weiss et al. 2010) present graphically the size–resolved emission factors (by number) for measurements made in Mexico City, Minnesota, and San Francisco respectively. These studies measured the largest emission factors for particles with diameters between 10 and 30 nm (i.e., the nucleation mode), regardless of vehicle classification. Ban–Weiss et al. (2010) also provides the size–resolved emission factors for LDVs and HDVs as supplementary data (for particle diameters between 10 and 290 nm). Using the data, their emission factors have been recalculated to exclude particles with diameters < 60 nm (shown in Table 4.4). For HDVs, excluding particles with diameters < 60 nm decreases their emission factor from 40×10^{14} # kg_{FUEL}^{-1} to 8.1×10^{14} # kg_{FUEL}^{-1}, which is still about 19× larger than the average emission factor measured behind HDVs in this study. However, Kittelson et al. (2006) measured lower emission factors between 60 and 100 nm for HDVs than Ban–Weiss et al. (2010)

but raw data are not available to recalculate their emission factors. Nonetheless, the lower emission factors between 60 and 100 nm measured by Kittelson et al. (2006) would give a lower emission factor over the larger size range of 60 to 290 nm compared to Ban–Weiss et al. (2010).

Table 4.4: Particle number emission factors from the literature from the last two decades. Only studies that report emission factors in units of # kg_{FUEL}^{-1} are included. Some studies reported with units exponentiated as $\times 10^{15}$ while others report as $\times 10^{14}$. Given our small emission factors, we report only as $\times 10^{14}$ for clarity.

Fleet averaged					
Study	**Study type**	**Vehicle speed** ($m\ s^{-1}$)	**Location**	**Size range** (nm)	**Emission factor** $\times 10^{14}$ # kg_{FUEL}^{-1}
This study	Chasing	10 – 30	Toronto, Canada	60 – 1000	0.30
Wren et al. (2018)	Chasing	10 – 30	Toronto, Canada	4.5 – 3000[1]	3.7 – 20.0
Wang et al. (2015)	Roadside	< 14	Toronto, Canada	7 – 3000	7.53 – 7.57
Kalafut–Pettibone et al. (2011)	Roadside	Not reported	Mexico	11 – 494	15.6
Yli–Tuomi et al. (2005)	Chasing	15 – 28	Finland	> 7	83
Kittelson et al. (2004)	Chasing	< 28	Minnesota, USA	3 – 1000	22 – 110

HDV (heavy–duty vehicles)					
Study	**Study type**	**Vehicle speed** ($m\ s^{-1}$)	**Location**	**Size range** (nm)	**Emission factor** 10^{14} # kg_{FUEL}^{-1}
This study	Chasing	10 – 30	Toronto, Canada	60 – 1000	0.43
Larson et al. (2017)	Chasing	2 – 12	Seattle, USA	> 50	29 – 62
Hudda et al. (2013)	Chasing	13 – 31	Los Angeles, USA	> 10	42
Park et al. (2011)	Chasing	> 13.0	Los Angeles, USA	10 – 1000	14
Ban–Weiss et al. (2010)	Tunnel	Not reported	San Francisco, USA	10 – 290	40
Ban–Weiss et al. (2010)	Tunnel	Not reported	San Francisco, USA	60 – 290[2]	8.1
Ban–Weiss et al. (2009)	Tunnel	8 – 24	San Francisco, USA	> 3	47 – 400

LDV (light–duty vehicle)					
Study	**Study type**	**Vehicle speed** ($m\ s^{-1}$)	**Location**	**Size range** (nm)	**Emission factor** 10^{14} # kg_{FUEL}^{-1}
This study	Chasing	20 – 30	Toronto, Canada	60 – 1000	0.15
Zimmerman et al. (2015)	Roadside	Not reported	Toronto, Canada	2.5 – 3000	3 – 8
Hudda et al. (2013)	Chasing	13 – 31	Los Angeles, USA	> 10	4.3
Park et al. (2011)	Chasing	> 13.0	Los Angeles, USA	10 – 1000	5.5
Ban–Weiss et al. (2010)	Tunnel	Not reported	San Francisco, USA	10 – 290	2.8
Ban–Weiss et al. (2010)	Tunnel	Not reported	San Francisco, USA	60 – 290[2]	0.38

[1]Wren et al. (2018) do not give a size range, except to note their emission factor includes ultrafine particles, which may be considered ambiguous (see for example, Kittelson et al. (2022)). Gordon et al. (2012) also report CRUISER measurements, which the same mobile system used in Wren et al. (2018). They report that the condensation particle counter sizes particles in the range of 4.5 to 3000 nm, and this is the range that is presented here.

[2]Caclulated from supplementary data provided by Ban–Weiss et al. (2010) corresponding to their Fig. 2.

It is useful to point out that Larson et al. (2017) measured accumulation and coarse mode particle emission factors for HDVs in Seattle, USA, and obtained large emission factors more typical of those that include measurement of the nucleation mode. Their measurements were made at lower vehicle speeds < 12 $m\ s^{-1}$ and during September and December (in the Northern hemisphere), which probably represent more

favorable conditions for nucleation mode formation. The formation of a nucleation mode is enhanced at low vehicle speeds, low air temperatures and high relative humidity (Kittelson et al. 2004; Ronkko et al. 2006). Furthermore, nucleation and accumulation mode particles may be better sampled in the lower size range of their instrumentation (50 to 100 nm), since they measured a maximum number concentration near 57,000 # cm^{-3} and a mean number concentration near 20,000 # cm^{-3}. During our 2016 study the maximum number concentration is much lower, around 8000 # cm^{-3}, but the UHSAS has known deficiencies with particle detection especially when the total number concentration is high (i.e., counting coincidence), or when particles have diameters < 100 nm (see Sect. 4.3.1–a). The accuracy of the UHSAS at measuring total number concentrations exceeding 10,000 # cm^{-3} has not been reported, but it is likely that a considerable number of particles are not sampled due to instrument deficiencies. Therefore, the low emission factors presented here, compared to previous studies shown in Table 4.4, are likely due to (1) missing nucleation mode particles, and (2) a low bias in the total number concentration measured by the UHSAS.

If it is assumed that measurements are missing 90% of the total particle number due to a combination of (1) and (2) as described in the previous paragraph, then including this additional 90% would give emission factors that are about 10× larger than those measured by the UHSAS. Thus, for HDVs, the inclusion of 90% more particles would give a mean emission factor of 43 $\times 10^{14}$ # kg_{FUEL}^{-1} and for LDVs 15 $\times 10^{14}$ # kg_{FUEL}^{-1}, which for HDVs is consistent with the emission factors presented in the literature when the nucleation mode is included (except for Larson et al. (2017) who measured low vehicle speeds). As noted in Sect. 4.4.5, there are times that the instrumented car is clearly measuring emission factors from traffic on the opposite side of the highway embankment. If a high emission factor plume is measured while sampling behind a low emission vehicle class (i.e., due to advection), the result will be an artificial inflation of the average emission factor for that vehicle class. This is the likely reason why the average LDV emission factor, when scaled to include probable missing particles, is large compared to the previous studies highlighted in Table 4.4.

As noted in Sect. 4.4.2, there is a clear trend in the data whereby the particle size distributions measured in 2016 suggest larger sized particles than measured during 2019. One reason for this difference could be fuel composition and emission standard changes that were implemented in Canada between the two measurement campaigns. Specifically, in 2017 Canada lowered the allowable limit of sulfur in gasoline from 30 mg kg^{-1} to 10 mg kg^{-1}, but diesel fuel regulations did not change and had an allowable limit of 15 mg kg^{-1} in both 2016 and 2019. However, in Ontario Canada, regulations for biodiesel fuel did change between 2016 and 2019, with the mandated percentage of biofuel blended into diesel fuel increasing from 3% in 2016 to 4% in 2017 as part of the "Greener Diesel Regulations" (Ministry of Environment and Climate Change, Ontario, 2016). Kim et al. (2008) measured a shift in the accumulation mode toward smaller particle diameters, with a reduction between 20 to 30 nm, for biodiesel compared to diesel fuel.

Other investigations have measured a similar result for biodiesel fuel (Chuepeng et al. 2011; Armas et al. 2013; Guo et al. 2017). These same studies have also demonstrated a reduction in the total number of accumulation mode particles for biodiesel fuel, but a reduction in the total number concentration between 2016 and 2019 is not demonstrated by our measurements. Aside from the in–gasoline sulfur content and biodiesel regulations, vehicles produced in the year 2017 onwards were expected to conform to more stringent particulate emission standards. For HDVs the particulate emission standard was reduced from 0.01 to 0.008 g mile^{-1}, with 40 % of all 2019 model year vehicles expected to conform to this emission standard. However, it is unlikely that the implementation of more stringent emission requirements would be a significant factor in our 2019 study, since most HDVs are likely to be older models built before 2017. Aside from fuel and emission standards changes, there is also the possibility that subisokinetic sampling leads to larger particles being measured in 2016 compared to 2019; subisokinetic sampling leads to oversampling of larger sized particles and an overestimation of the particle number concentration at the probe inlet (Hinds, 1999). Therefore, aside from the increase in biodiesel use in Ontario that may result in larger particles being emitted in 2016 compared to 2019, the measured particle diameters may also be biased high in 2016 due to subisokinetic sampling. Furthermore, there is a concern that the limited number of individual vehicles sampled in 2016 (Fig. 4.6b) limits the statistical significance of the comparison between 2016 and 2019, and hence limits the ability to draw firm conclusions about the cause of the difference in particle diameter between 2016 and 2019. Despite the limited number of individual vehicles, each vehicle shown in Fig. 4.6 was sampled continuously for at least 5 min (some as much as 30 min), giving at least 75 independent samples exceeding the 75th percentile that determine each median curve shown in the figure.

The results shown in Fig. 4.5 demonstrate that the mode diameter measured behind HDDVs is not constant and has significant temporal variation on short time periods of 1 to 5 s, and this variation is most pronounced behind the commercial bus. One possibility for the large variations measured behind the commercial bus may be related to changing engine load, since periods of large acceleration favor larger sized particles (Kim et al. 2017). We investigated the relationship of D_{mode} measured behind the commercial bus to vehicle acceleration (Fig. E9) and there is some evidence of larger D_{mode} in the mean at large acceleration. Furthermore, the largest variations in D_{mode} (circled in Fig. 4.5 (b)) correspond almost exclusively to periods of acceleration (not shown), and times that a black plume released from the bus is obvious on dashcam video. Therefore, the rapid variations in D_{mode} are probably caused by acceleration, because during periods of acceleration the bus occasionally emits visible plumes with significant black carbon that have larger optical diameters than typical emissions measured during cruise conditions. Figure 4.14 shows the aerosol size distribution measured behind the commercial bus, during which D_{mode} > 90 nm and a visible plume is obvious on the dashcam video recordings. The solid black line gives the median calculated from 55 independent samples (i.e., 55 s of data) of black carbon plumes, which has D_{mode} =

101.5 nm, and this is about 20 nm larger than the aerosol size distribution calculated from all measurements behind the bus greater than the 75th percentile (shown as a red line in Fig. 4.14). Yokelson et al. (2011) suggest that black carbon is largely undetected by the UHSAS, but the results in Fig. 4.14 demonstrate that the black carbon plumes emitted by the commercial bus are sampled by the UHSAS, and present as a very clear shift in the particle size distribution toward larger particle diameters. The distribution of the measured black carbon plumes is approximately lognormal; the blue line in Fig. 4.14 is a lognormal fit to the median measurements and the error bars give the 25th (lower) and 75th (upper) percentiles.

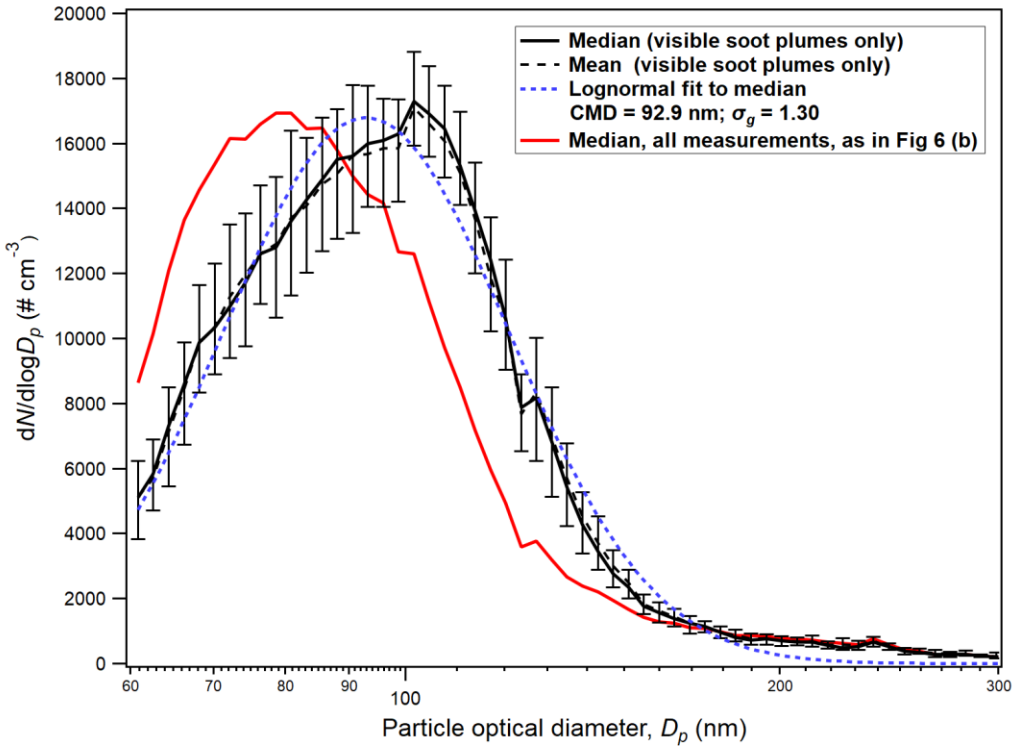

Figure 4.14: The solid black line gives the median aerosol size distribution measured behind the commercial bus, determined from times when a visible plume is obvious on the dashcam video recordings and D_{mode} > 90 nm. The black dash line gives the mean, and the dashed blue line gives a lognormal fit to the median measurements. Error bars give the 25th (lower) and 75th (upper) percentiles. Also shown as a red line is the aerosol size distribution for the commercial bus, as shown in Fig. 4.6 (b). Size distributions are not background removed, or corrected for particle loss.

Previous studies investigating particle size distributions of diesel vehicles have reported a wide range of geometric mean diameters that are representative of the accumulation mode particles, sometimes < 60 nm (Xue et al. 2015), which is below the size range of the UHSAS. A lognormal mode centered below a particle diameter of 60 nm could explain the poor fit to measurements for most HDDVs measured in 2019 (see Fig. 4.6 (a)). Since the detection efficiency of the UHSAS drops off rapidly for particles with diameters less than 100 nm, the result would likely be a measured particle size distribution that is skewed toward

larger particle sizes, giving the appearance of an accumulation mode centered at a diameter > 60 nm. This is similar to the appearance of the size distribution for most HDDVs measured in 2019 and shown in Fig. 4.6 (a). Lognormal distributions fitted to the accumulation mode of diesel exhaust have previously reported σ_g in the range of 1.5 and 2.5 (Abdul–Khalek et al. 1998; Harris and Maricq, 2001; Virtanen et al. 2004; Xue et al. 2015). For the lognormal distributions calculated in this study, σ_g in some cases is found to be below this range, between 1.27 and 1.82. The smallest σ_g are calculated for data measured in 2019; σ_g may also be underestimated if the particle distribution is distorted by the UHSAS at particle diameters < 100 nm.

4.5.3 Plume modelling

The evolution of pollutants in the far wake region (and the region above the wake) have previously been described with good success by a Gaussian distribution (Groneskei 1988; Xie et al. 2020). Recently, Makar et al. (2021) assumed a Gaussian distribution to model the vertical variation of turbulent kinetic energy within vehicle wakes in a numerical prediction model. For a pollutant released downwind of a source, the gradient transport model as described by the advection–diffusion equation can be used to model the plume's evolution

$$\frac{\partial \bar{N}}{\partial t} + \bar{u}\frac{\partial \bar{N}}{\partial x} + \bar{v}\frac{\partial \bar{N}}{\partial y} + (\overline{w} + \overline{w_s})\frac{\partial \bar{N}}{\partial z} = \frac{\partial}{\partial x}\left(K_x \frac{\partial \bar{N}}{\partial x}\right) + \frac{\partial}{\partial y}\left(K_y \frac{\partial \bar{N}}{\partial y}\right) + \frac{\partial}{\partial z}\left(K_z \frac{\partial \bar{N}}{\partial z}\right). \quad (4.7)$$

This is valid only when the plume size has a greater size than the dominant eddy size, and if the plume is assumed to be nonreactive. If advection dominates the downwind diffusion of the plume, then $\bar{u}\frac{\partial \bar{N}}{\partial x} \gg \frac{\partial}{\partial x}\left(K_x \frac{\partial \bar{N}}{\partial x}\right)$. For small particles (< 100 nm) and gases, the settling velocity $\overline{w_s} \approx 0$. If the plume is time–independent (steady–state) ($\partial/\partial t = 0$) and the coordinate system is aligned so that $\bar{v} = \overline{w} = 0$, then Eq. 4.7 reduces to

$$\bar{u}\frac{\partial \bar{N}}{\partial x} = \frac{\partial}{\partial y}\left(K_y \frac{\partial \bar{N}}{\partial y}\right) + \frac{\partial}{\partial z}\left(K_z \frac{\partial \bar{N}}{\partial z}\right). \quad (4.8)$$

The solution to the advection–diffusion equation (without deposition) is the Gaussian plume equation (Ermak 1967),

$$\bar{N}(x,y,z) = \frac{Q}{4\pi x\sqrt{K_y K_z}} e^{\left(-\frac{Uy^2}{4K_z x}\right)}\left[e^{\left(\frac{-U(z-h)^2}{4K_z x}\right)} + e^{\left(\frac{-U(z+h)^2}{4K_z x}\right)}\right], \quad (4.9)$$

where the error term has been neglected. Here we assume that the turbulent number flux is proportional to the number concentration gradient (i.e., Fickian diffusion), and the vertical number flux can be described as

$$\overline{w'N'} = -K_z \frac{\partial \bar{N}}{\partial z}, \tag{4.10}$$

with constant eddy diffusivities (Lushi and Stockie, 2010),

$$K_z = \frac{\sigma_z^2 U}{2x} \text{ and } K_y = \frac{\sigma_y^2 U}{2x}. \tag{4.11}$$

Differentiating (4.9) with respect to height, combined with (4.10) gives

$$\overline{w'N'}(x,y,z) = -K_z \frac{\partial \bar{N}}{\partial z} = \frac{UQ}{16\pi x^2 \sqrt{K_z K_y}} e^{\left(-\frac{Uy^2}{4K_z x}\right)} \left((2z-2h) e^{\left(\frac{-U(z-h)^2}{4K_z x}\right)} + (2z+2h) e^{\frac{-U(z+h)^2}{4K_z x}} \right). \tag{4.12}$$

For a TE–HDV with a trailer, the exhaust is above the main cab, upwind of the trailer. However, based on previous evidence, it is assumed that the end of the trailer can be viewed as a secondary source location: pollutants that are trapped in the upper shear layer are released at the end of the trailer into the wake region, without substantial diffusion along the trailer's top. For the TE–HDVs investigated in this work, the trailer has an estimated height of h = 4.1 m. For median binned measurements of $\overline{w'N'}$ made at z = 1.7 m at various locations downwind of the trailer, estimates of K_y, K_z, Q and U are obtained by iterating through various combinations of these variables to determine which combination will minimize the total normalized root–mean square error (RMSE_T) of Eq. 4.9 and Eq. 4.12 simultaneously,

$$\text{RMSE}_T = \frac{1}{|\overline{w'N'}|_{max,obs}} \left(\frac{1}{n} \sum_{i=1}^{n} \left(\overline{w'N'}_{i,obs} - \overline{w'N'}_{i,model} \right)^2 \right)^{1/2} + \frac{1}{\bar{N}_{max,obs}} \left(\frac{1}{n} \sum_{i=1}^{n} \left(\bar{N}_{i,obs} - \bar{N}_{i,model} \right)^2 \right)^{1/2} \tag{4.13}$$

The RMSE is normalized by the maximum measured concentration ($\bar{N}_{max,obs}$) or maximum magnitude of the measured flux ($|\overline{w'N'}|_{max,obs}$) for Eq. 4.9 and Eq. 4.12 respectively. The total RMSE is calculated as the sum of each normalized RMSE, and this is the variable that is minimized. There are several assumptions implicit in the application of this optimization approach: (1) the following distance has no uncertainties, (2) the instrumented car is always measuring along the plume centerline, (3) crosswind flow

is negligible and hence does not affect the placement of the plume, (4) Q and U are stationary and hence do not vary with time, (5) K_y and K_z are constant in all directions (vertically, laterally and horizontally downwind), (6) there is no effect from vehicle–induced flow structures behind the vehicle (i.e., no recirculation region or shear layers). Furthermore, the data for HDVs are calculated from many different sampled vehicles of the same type. Therefore, this approach does not consider differences that may exist between individual vehicles, such as their emission rate, the length of the trailer or orientation of the exhaust pipe. To remove the need to optimize Q, the measured concentration or flux for each individual vehicle profile could be normalized by the closest measurement (smallest x_m). However, in this study the measurement ranges of each individual vehicle are not identical (i.e., different smallest x_m) which creates a large difference in the normalized profiles preventing them from being combined to form a single profile representative of that vehicle class. There are insufficient data to apply this optimization approach to each individual vehicle, and therefore this approach is not applied here.

It is useful to obtain an initial guess for the source strength Q to compare with the optimized value. For HDVs the median emission factor from Table 4.3 is 0.23×10^{14} # kg_{fuel}^{-1}. Assuming a vehicle speed of 100 km h^{-1} (28 m s^{-1}), no acceleration, h_g = 0 km, vehicle specific constants of α_1 = 2.16×10^{-3}, α_2 = 7.98×10^{-5}, α_3 = 1.0×10^{-8} and a vehicle mass of m = 7092 kg (i.e., convex model of HDDT 8 from Wang and Rakha, (2019), representing a 2001 model vehicle), Eq. 4.4 gives a fuel consumption rate of $FC_m = 0.832FC(t)$ = 0.007298 kg_{fuel} s^{-1}. For an emission factor of 0.23×10^{14} # kg_{fuel}^{-1} and rate of FC_m= 0.007298 kg_{fuel} s^{-1}, an initial guess of the particle emission rate is $Q = 2.02\times10^{11}$ # s^{-1}. The mean wind speed at 10 m height recorded by stationary monitoring stations in the vicinity of the on–road measurements ranged between 3 and 8 m s^{-1} (see Table 4.1).

Two optimizations are presented in Fig. 4.15 for measurements obtained at a height of 1.7 m: (a) and (b) show optimization of ρ_c and $\overline{w'\rho_c'}$ for BE–HDVs (h = 0.5 m) while (c) and (d) show optimization of N_t and $\overline{w'N'}$ for TE–HDVs, respectively. For ρ_c and N_t the background levels are removed following the procedure outlined in Sect 4.3.5. For TE–HDVs the optimized solution predicts a magnitude of N_t that is similar to measurements at x_m > 30 m. However, the Gaussian solution underestimates the decrease in N_t at x_m > 50 m. Furthermore, at x_m < 30 m, the optimized solution gives a poor fit to measurements, since the modelled solution gives decreasing N_t with decreasing x_m while the measurements remain relatively constant. This poor fit for x_m < 30 m is not unexpected, considering the complex flow structure in the near wake region and a recirculation region where pollutants become trapped. The relatively constant N_t for x_m < 30 m might indicate pollutant trapping in the recirculation region, since the optimized solution suggests that N_t should rapidly decrease for x_m < 30 m. Despite the poor fit to N_t, the shape and magnitude of the optimized $\overline{w'N'}$ matches the measurements well (Fig. 4.15 (b)). For BE–HDVs, the optimized solution gives

ρ_c with a magnitude similar to measurements, but the solution does not show an increase in ρ_c at x_m < 20 m which is present in the measurements. The optimized value of Q = 4.2×10^{10} # s^{-1} and 0.0058 kg s^{-1} for N_t and ρ_c respectively. These are lower than the estimates given in the previous paragraph but are of a similar magnitude especially when considering the uncertainties involved.

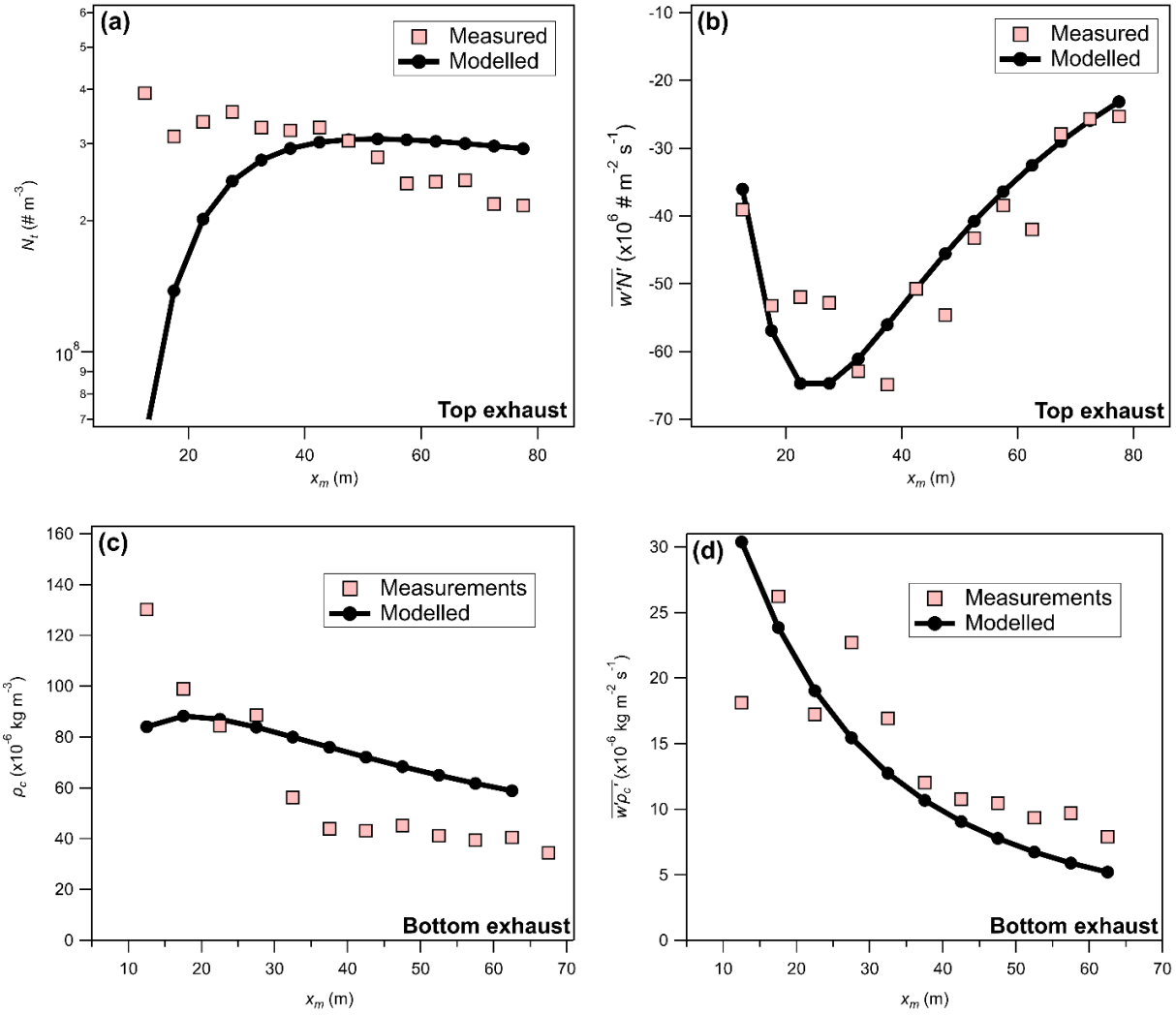

Figure 4.15: (a) and (b) show the optimized solution for N_t and $\overline{w'N'}$ for top exhaust vehicles, with U = 6 m s^{-1}, K_y = 0.038 m^2 s^{-1}, K_Z = 0.175 m^2 s^{-1} and Q = 4.2×10^{10} # s^{-1}. Panel (c) and (d) show the optimized solution for ρ_c and $\overline{w'\rho_c'}$ for bottom exhaust vehicles, with U = 7 m s^{-1}, K_y = 0.14 m^2 s^{-1}, K_Z = 0.19 m^2 s^{-1} and Q = 0.0058 kg s^{-1}. The median measured flux and concentration are used to complete the optimizations, which is completed simultaneously for both Eq. 4.9 and Eq. 4.12. The measured concentrations (ρ_c and N_t) have had background levels removed according to Step I in Sect. 4.3.5. Data in panel (a) and (c) are background removed.

Both optimizations give very similar values of K_z, which is predicted to be 0.175 and 0.19 m^2 s^{-1} for TE–HDVs and BE–HDVs respectively. K_y is optimized to be quite different depending on the exhaust

location, with K_y = 0.038 and 0.14 m^2 s^{-1} for TE–HDVs and BE–HDVs respectively. These results suggest that there is little lateral diffusion behind TE–HDVs compared to BE–HDVs, at our measurement height. Furthermore, for TE–HDVs the optimized results suggest that almost all diffusion is occurring vertically within the vehicle wake. The ROADWAY model parameterizes the vertical diffusion coefficient at height z on highways as $K_z = z\sqrt{\overline{w'^2}}$, where $\overline{w'^2}$ is predicted from vehicle wake theory (Eskridge and Rao, 1986; Eskridge and Rao, 1991). Also, K_z is predicted to increase with increasing vehicle velocity (i.e., $K_z \propto U_r$), leading to increased vertical diffusion at higher vehicle speeds (Eskridge and Rao, 1991). Using measurements of $\overline{w'^2}$ made behind TE–HDVs, the ROADWAY model parameterization suggests that K_z should range between 2 and 3 m^2 s^{-1}, but K_Z = 3 m^2 s^{-1} is about 17 times larger than estimated from the optimized Gaussian fit behind a single TE–HDV (assuming constant K_Z in all directions). Sistla et al. (1979) lists K_Z values used in four different highway models (i.e., their Table 8), that can be used to predict pollutant concentrations downwind of a highway. At a height of 2 m, K_z values used in these models range between 0.05 and 0.55 m^2 s^{-1} under neutral conditions with an assumed roughness length of 1 m. One outlier is the DANARD model which has an upper value of 20 m^2 s^{-1} for K_Z at 2 m height. Sedefian et al. (1981) analyzed data from near–highway stationary towers and estimated K_z due to traffic only at a height of 1.5 m, with values ranging between 0.13 and 1.3 m^2 s^{-1}. Eskridge et al. (1979) suggest slightly larger K_z, more consistent with results from the ROADWAY parameterization applied to measured $\overline{w'^2}$. Nonetheless, the values of K_z reported in the literature from near–highway studies are in a similar range to K_z estimated from the dual–optimization approach applied here, even though K_z in this work represents an in–wake vertical eddy diffusivity near the ground.

4.6. Conclusions

This work investigated the emission and diffusion of CO_2 and accumulation mode aerosols emitted from heavy–duty vehicles using high frequency instrumentation. In Sect. 4.4.1 we asked five questions, and it is worth returning to those now to conclude what this study has demonstrated:

1. The exhaust location is found to impact the concentration statistics measured at a height of 1.7 m behind heavy–duty vehicles. Specifically, measured ρ_c and N_t and their variances are larger behind BE–HDVs than TE–HDVs. Furthermore, the direction of $\overline{w'\rho_c'}$ and $\overline{w'N'}$ is specific to the exhaust location, and $\overline{w'\rho_c'}$ is of greatest magnitude behind BE–HDVs. These results have implications since pedestrians are at ground level (< 2 m height) and so BE–HDVs are more likely to lead to a higher dose of pollutants near ground level. For BE–HDVs, there is a very abrupt decrease in N_t and σ_N^2 near 50 m. For TE–HDVs, this decrease occurs later, near 60 m, and is much less significant compared to BE–HDVs.

2. Measurements combined with plume modelling in Sect. 4.5.3 do support pollutant trapping in the near wake. For TE–HDVs the Gaussian solution predicts a rapid drop in N_t for x_m < 20 m, since under no crosswinds, downward vertical spread can only happen at the end of the trailer, and the downward spread of the plume would take time. Therefore, just downwind of the trailer the total particle number concentration is minimized. However, this is not supported by the measurements, which shows a slight increase in N_t as x_m decreases. For BE–HDVs where less assumptions about the location of the exhaust are required, an optimized Gaussian solution does not give a good fit to ρ_c at small x_m The measured ρ_c increases rapidly at x_m < 20 m, but the optimized solution remains constant or decreases. Thus, the plume model when combined with measurements would suggest that pollutant trapping is occurring at x_m < 30 m.
3. Measurements of $\overline{u'v'}$ behind TE–HDVs do demonstrate the existence of side shear layers. At a measurement height of 1.7 m, $|\overline{u'v'}|$ correlates moderately with measured e, and $\overline{u'v'}$ switches sign depending on the direction of the crosswind flow. The upper shear layer is less defined in our measurements, but there is a clear relationship between $\overline{w'N'}$ and $\overline{u'w'}$; the most significant downward $\overline{w'N'}$ occur only during significant downward $\overline{u'w'}$, which might support the assertion that the upper shear layer entrains pollutants near the start of the trailer that are later released downwind into the near wake region.
4. The emission of CO_2 is found to be distinctly related to vehicle acceleration while measuring behind a commercial bus, as demonstrated by Fig. 4.4 (a). The measured ρ_c increases in a nearly exponential fashion as the bus's acceleration is increased. Like ρ_c, there is a clear relationship between vehicle acceleration and particulate emission, since vehicle acceleration clearly produces larger N_t. However, unlike ρ_c a trend in N_t with increasing acceleration is not clear. For particle size there is evidence that the mode diameter of accumulation mode particles is increased during periods of acceleration. Specifically, periods of acceleration correlate with times that a visible plume is released from the bus. The median size distribution measured during release of the visible plumes has a mode diameter that is about 20 nm larger than the median size distribution calculated from the entire record behind the commercial bus (for which N_t > 75th percentile).
5. Interestingly, for TE–HDVs the optimized Gaussian solution is a good fit to $\overline{w'N'}$ for all x_m measured, even though N_t suggested by the optimized solution is completely different than measurements for small x_m. Therefore, the optimized solution gives the best agreement for the far wake, and worst agreement for the near wake. The conclusions are similar for BE–HDVs.

This investigation demonstrates the feasibility of the instrumented car at measuring on–road vertical turbulent pollutant fluxes and concentration statistics for short averaging periods of 1 to 10 s, while travelling at highway speeds, since the direction of the vertical flux of CO_2 and aerosols are consistent with the exhaust location on the targeted vehicle. Wavelet spectra reveals that length scales < 40 m are responsible for the vertical turbulent transport of aerosols. The results show that the mode diameter of accumulation mode particles has decreased by about 10 nm between 2016 and 2019, which we suggest may be related to an increasing percentage of biodiesel mixed into diesel fuel in Ontario, with a legislated increase from 3 to 4 % in 2017. Furthermore, consistent with previous studies (i.e., Table 4.4), we find that heavy–duty vehicles produce the largest accumulation mode particulate emissions. This work reveals that there is a large uncertainty in the quantification of emission factors from low–emission vehicles when measuring on highways with other traffic, given the significant biases that can occur due to drifting high–emission plumes from heavy–duty vehicles.

CHAPTER 5: Stationary measurements of near–ground wake flow and turbulence generated by isolated vehicles travelling at near–highway speeds

Stefan J. Miller[1], Mark Gordon[1]

[1]Department of Earth and Space Science and Engineering, York University, Toronto ON, M3J 1P3, Canada

Publication status: Not yet submitted

Abstract

Wakes generated by moving vehicles impact pollutant dispersion and may serve as a source of wind power close to the ground but limited in–situ high–frequency measurements of vehicle wakes exist. This study used a small, instrumented tripod placed near the edge of a two–lane highway to investigate vehicle wakes and explore the possibility of harvesting their wind energy. Instrumentation included a video recording system and a sonic anemometer that measured at a height of 1.4 m. The highway in this study was unique, since it featured many different types of vehicles (e.g., passenger cars, sport utility vehicles and transport trucks) travelling at high speeds (near 80 km h^{-1}), and sometimes these vehicles were temporally isolated, allowing analysis of individual vehicle wakes without interference from other traffic. Moving vehicles induce a wake flow, which is most significant behind transport trucks. For a passing transport truck, the wake flow nearly aligns parallel to the road and is oriented in the vehicle's travel direction. The maximum magnitude of the wake–induced flow behind a passing transport truck is measured to be about 2× greater than the mean ambient wind speed. Using the high–frequency measurements, the start and end times of the wake were estimated, and then used to approximate the lateral spread of the vehicle wake generated by each vehicle class. Wakes behind transport trucks have the greatest lateral spread, followed by sport utility vehicles, and passenger cars. The lateral width of the wake generated by a moving transport truck is estimated to be about 5× greater at 150 m behind the vehicle than the wake generated by a moving passenger car or sport utility vehicle. The utility of roadside wind power generation is investigated, and the results suggest that some sections of 400 series highways may have sufficient transport trucks to maintain a consistent wake–induced flow ≥ 3 m s^{-1} during peak traffic. Assuming no wake interactions, only transport trucks and a wind turbine with perfect efficiency, the results from this study suggest that 0.02 kW h (per m^2 swept area) of storable energy could result during peak traffic flow. However, this estimate is probably underestimated, since on real busy highways many vehicles of different types may travel together in groups, leading to wake interactions and potentially compounding flow. In addition to wake–induced flow, passing transport trucks lead to a significant increase in the measured vertical heat flux at a height of 1.4 m for about 5 s following their passage, demonstrating that transport trucks generate significant mixing near the road surface.

5.1 Introduction

Vehicular traffic is known to have many impacts on the atmospheric environment. Aside from pollutants that are directly emitted from the tailpipe, the suspension and subsequent transport of particulate matter (i.e., fugitive dust) can have a significant impact on ground–level air quality (Edvardsson and Magnusson, 2009). This is especially true for vehicles travelling on unpaved roads or roads with an unpaved shoulder (Williams et al. 2008; Moosmuller et al. 1998). The vehicle pulverizes the road material which is then suspended by tire rotation. Following suspension, the particulate matter is diffused by vehicle wake turbulence and advected by the ambient flow. The wake turbulence of a vehicle is dependent on several factors including vehicle speed, which has been shown to affect pollutant diffusion behind vehicles (Eskridge and Thompson, 1982; Eskridge et al. 1991). Field studies investigating fugitive dust emission from on–road vehicles have also found a correlation with vehicle speed and vehicle–induced turbulence (Moosmuller et al. 1998; Etyemezian et al. 2003).

Aside from vehicle related pollutant and particulate emission, recent interest has also focused on the vehicle momentum wake, and the ability to harvest its energy. This energy may then be stored in a battery and used to power streetlights and cameras adjacent to the road (Tian et al. 2020; Hussein et al. 2018; Laponite and Gopalan, 2016). Laponite and Gopalan (2016) show that vehicular motion can generate a significant increase in the flow close to the surface, and this flow represents about a 200% increase in the potential extractable wind power when compared to no vehicular motion. Tian et al. (2020) suggest that vortex cores present near the side of passenger cars are responsible for much of the extractable energy. Despite these numerical investigations demonstrating the feasibility of wind energy extraction from vehicle wakes, in–situ measurement of vehicle–induced flow near highways is lacking.

A limited number of in–situ roadside studies have investigated vehicle–induced turbulence and wake–induced flow. Rao et al. (1979) measured accelerated flow parallel to a highway resulting from traffic travelling at speeds between 75 and 90 km h^{-1} (21 and 25 m s^{-1}). They found that with increased ambient flow perpendicular to the highway (i.e., crosswinds), the vehicle–induced flow parallel to the highway is reduced. Chock (1980) summarizes measurements of the mean wind field that resulted from a pack of vehicles travelling down a highway at speeds of 80 km h^{-1} (22 m s^{-1}). They present measurements made 1.7 m from the edge of the highway, at heights of 1.5, 4.5 and 10 m above the ground. At a height of 10 m, they did not find a distinguishable effect on the mean flow resulting from moving traffic. However, at heights of 1.5 and 4.5 m, there was a clear acceleration of the mean flow in the direction of vehicle travel. Like Rao et al. (1979), their measurements demonstrate that vehicle–induced flow is reduced when ambient crosswind flow increases. Alonso–Estebanez et al. (2012) investigated individual vehicles (a car, a van, and a heavy–duty truck) as they travelled past an array of sonic anemometers placed on guardrails near the edge of a highway. Their study investigated turbulence statistics only and did not investigate vehicle–induced

flow. They present single time–averaged statistics for each vehicle pass, and therefore do not describe the temporally localized variation that occurs as the vehicle passes the sensor.

Previous investigations have measured spectra near the highway, but for longer averaging periods of 15 to 30 min, which is representative of a period with many different types of passing vehicles. Rao et al. (1980) measured spectra near a highway in New York, USA. They found that traffic mainly affected the spectra in the 0.1 to 1.0 Hz frequency range, with a maximum difference near 0.25 Hz. Kalthoff et al. (2005) measured turbulence spectra 2.5 m from a highway (at a height of 3.75 m), and likewise show an enhancement in the spectra at frequencies > 0.1 Hz in the presence of moving traffic. Measurements of spectra have also been made behind vehicles. Baker (2001) presents instantaneous wavelet spectra of velocity measured behind a model lorry and model train at different non–dimensional times, averaged from many different realizations. When the non–dimensional time was small, they found a significant and distinct peak in the wavelet spectra at a frequency of 0.5 Hz, but as the non–dimensional time increased, the peak quickly disappeared. The wavelet spectra also demonstrate that a second peak exists between 0.05 to 0.1 Hz. Baker (2001) argues that the peak near 0.5 Hz is due to "instability in the separated shear layers", and represents the main length scale of the wake. The peak near 0.5 Hz agrees with 1 min Fourier spectra presented in Miller et al. (2019) (Chapter 2) for measurements obtained behind heavy–duty trucks, where the dominant length scale is found to be consistent with the length of the attached trailer (~ 10 to 15 m). A similar increase in the high frequency portion of the velocity spectra was also measured on–road by Gordon et al. (2012) and Rao et al. (2002).

This study presents in–situ measurements of wake flow and turbulence measured near a highway, at a height of 1.4 m. The highway speed limit was 80 km h^{-1} (22 m s^{-1}), and the traffic was sparse, providing a unique opportunity to sample different vehicle types in near–isolation. In this work, three vehicle types are common: passenger cars, sport utility vehicles and heavy–duty trucks (also referred to as a tractor–trailer or transport). We thus describe the variation in the wake flow for each 0.1 s as these different vehicle types pass the sensor – measurements which have not yet been reported in the available literature. Using the high–frequency measurements of vehicle–induced flow, we develop a simple parameterization to estimate the lateral width of the wake with increasing distance behind the vehicle. The amount of extractable wind power is estimated as a function of vehicles per minute, to investigate the feasibility of road–side energy generation. Finally, we present average wavelet power spectra of the measured flow velocity generated by passing heavy–duty trucks. The wavelet spectra presented in this work are calculated for each 2 s period after the passage of a vehicle, to investigate the temporal variation of the spectra in the vehicle wake.

5.2 Methodology

5.2.1 Experimental setup

As discussed in Chapter 3, a small, instrumented tripod was assembled and placed in a highway shoulder for measurement of on–road traffic (on 22 Aug 2019). The instrumentation consisted of a sonic anemometer (Applied Technologies, Inc., model type "V") that sampled at 20 Hz and a Thinkware X700 dashcam video recording system (30 frames per second). The video recording system used in this work has a limited storage capacity, and so some of the recorded video near the start of the measurement period was lost and overwritten by subsequent recordings; the dashcam documents each minute as a separate individual video file. The sonic anemometer was installed at a height of 1.4 m and was secured with guy lines to limit vibrations.

Figure 5.1: The tripod setup used on 22 Aug 2019.

Agricultural fields were located on either side of the two–lane highway. The highway has a posted speed limit of 80 km h^{-1} (22 m s^{-1}) with traffic consisting of passenger vehicles (i.e., cars, sport utility vehicles and pickup trucks) and the occasional heavy–duty truck, hereafter also referred to as "transport trucks". 22 Aug featured fair weather conditions, with partly sunny skies, consisting of mainly cumulus and cirrus clouds. The instrumented tripod and sky conditions are shown in Fig. 5.1. Figure 5.2 shows a top–down view of the location shown in Fig. 5.1, with the shoulder width and lane width estimated from Google Earth superimposed. The tripod is located at the edge the shoulder, about 2.7 m from the edge of the

highway. The wind measured at nearby Egbert weather station (16 km north at an elevation of 251 m) was between 3.8 and 5.0 m s^{-1} at 10 m height with a wind direction between 310 and 340°. This wind direction corresponds to a flow across the highway, toward the sensor. Egbert weather station measured an air temperature between 18.5 and 20.8°C and relative humidity between 51 and 58%. The tripod is located at an elevation of 222 m, estimated from Google Earth.

Figure 5.2: A schematic showing the location of the sonic anemometer and the estimated distances of the highway (estimated from Google Earth). The coordinate system of the sonic anemometer used in this investigation is given in the image (the vertical velocity component is upward, but it is not shown in the figure), as well as the vehicle travel directions.

5.2.2 Coordinate Rotation

The sonic anemometer on 22 Aug was tilted slightly downward with respect to the road, giving a mean vertical velocity ($\overline{w}$) < 0. The coordinate system is rotated parallel to the mean flow (giving $\overline{w}$ = 0) over the entire measurement period by applying a planar fit correction using non–overlapping 5–min mean velocities (36 in total or 3 hours of measurements). The planar fit method assumes the vertical wind speed can be described by (Wilzak et al. 2001),

$$\overline{w_m} = b_0 + b_1\overline{u_m} + b_2\overline{v_m}. \quad (5.1)$$

For the measurements at the tripod on 22 Aug, b_0 = 0.118 m s^{-1}, b_1 = –0.111 and b_2 = –0.02. While the planar fit approach gives $\overline{w}$ = 0 over the entire measurement period (3 hours), individual periods may not necessarily have $\overline{w}$ = 0. Since this work investigates short periods (15 s) while vehicles pass the tripod, it is not practical to rotate each individual period given the limited sample size, and thus the planar fit approximation is used instead of single–run rotations. Table 5.1 gives statistics for each measured velocity

component, calculated from the entire measurement record, after applying a planar fit rotation. As expected from application of the planar fit method, $\overline{w} = 0$. The maximum measured flow velocities are quite large, for example maximum w and v are measured at 7.6 m s^{-1} and 14.3 m s^{-1} respectively. However, as will be demonstrated in Sect. 5.2.3 and Sect. 5.3.2, these high flow velocities measured by the tripod are correlated with passing vehicular traffic. Typically, a spike removal algorithm is applied to sonic anemometer data to remove unrealistic velocities. Unrealistic velocities may be due to electronic noise, or result from insects, large particles or precipitation passing through the sensor. In this study, spike removal is not applied since there is no evidence of unrealistic values in the short time series when the effect of passing traffic is considered.

In the analysis that follows (and Table 5.1), the velocity components are presented so that u is perpendicular to the highway (positive toward the tripod), v is parallel to the highway (in the direction of traffic flow of the closest lane) and is positive toward the right when looking across the highway (from the tripod), and w is positive upward. This coordinate system is chosen so that it aligns with the wake axis that is generated by passing traffic (assuming no crosswind flow). The coordinate system is shown in Fig. 5.2 for reference.

Table 5.1: Velocity component statistics after rotation, calculated from the entire record (about 3 hours).

Velocity component	Mean	Standard deviation	Max	Min	Q25	Median	Q75
u (m s^{-1})	1.82	1.01	7.97	–6.71	1.18	1.77	2.42
v (m s^{-1})	1.19	1.37	14.3	–6.59	0.33	1.21	2.02
w (m s^{-1})	0.00	0.54	7.58	–7.92	–0.30	–0.01	0.30
T (°C)	21.1	0.93	30.3	18.8	20.4	21.0	21.7

5.2.3 Passing Traffic

For the approximately two hours of video recordings, there were 432 vehicles that passed by the tripod. The amount of vehicles separated by vehicle type is given in Fig. 5.3, and the number of vehicles from each class travelling in the close lane is shown as medium red shading. To perform analysis on different vehicle classes, the recorded 'event' must be isolated in time, so that the measurements are representative of that vehicle class alone and not other traffic in the vicinity. A vehicle passing the tripod is therefore considered *isolated* if there is no other traffic for at least 10 s preceding the event and for 10 s following the event in either highway lane. For the period investigated, there were a total of 110 vehicles meeting this criterion (about 25% of the total number); Table 5.2 gives the number of isolated vehicles for different vehicle classifications. Only three vehicle classifications have enough samples of isolated vehicles to generate meaningful statistics for both highway lanes: passenger cars, sport utility vehicles (SUV) and transport

trucks (tractor–trailers). To ensure consistency among sampled vehicles, an 'event' (or vehicle passing) is defined as the time that the front end of the vehicle is directly in front of the tripod, as recorded by the dashcam. Here we assume that all vehicles are travelling at the same speed of 80 km h^{-1} (i.e., the speed limit of the highway). The clock that recorded the sonic anemometer measurements was different from the clock that recorded the tripod tower video. This clock mismatch introduces an uncertainty in the recorded times that is on the order of ±0.5 s, but time–based error bars are omitted from the graphics presented herein.

Table 5.2: The number of vehicles in each vehicle class that travelled in the close or far highway lane and were deemed to be isolated. Bolded rows are investigated in this work.

Vehicle Type	Isolated close lane	Isolated far lane
Passenger car	**22**	**13**
SUV	**16**	**14**
Passenger van	3	4
Commercial van	2	2
Pickup truck	7	4
Jeep	2	0
Small truck	1	0
Other	1	0
Transport	**10**	**9**
Motorcycle	0	0

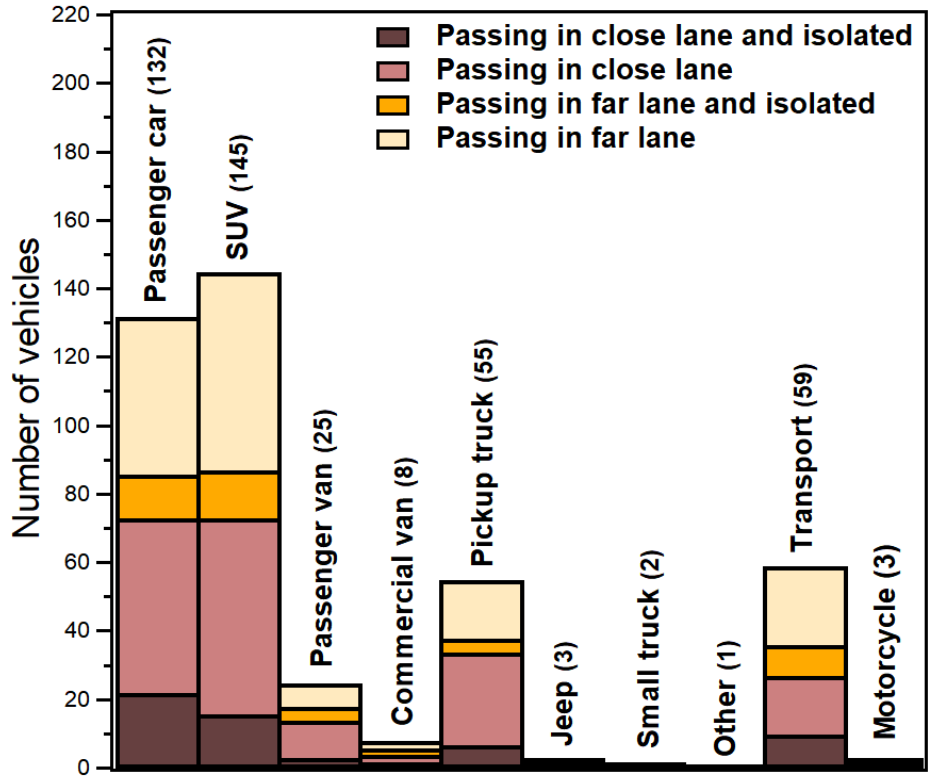

Figure 5.3: The vehicles passing the tripod on 22 Aug (433 in total), separated by vehicle class. The number in brackets gives the total amount of vehicles in that vehicle class. The area of each shaded region is proportional to the legend description, that is: (1) dark red are vehicles that passed in the close lane and were isolated, (2) medium red are the remaining vehicles passing in the close lane (not isolated), (3), medium orange are vehicles passing in the far lane that were isolated and (4) light orange are the remaining vehicles passing in the far lane (not isolated).

5.2.4. Calculation of variances, covariances and means

The procedure to calculate wavelet variances and covariances is detailed in Miller and Gordon (2022) (Chapter 3, Sect 3.2.5) and references therein. For wavelet analysis in this work, variances and covariances for every individual event are calculated for each 0.1 s of measured data and include time scales up to approximately 2 min. Mean values for each event are also calculated for each 0.1 s of measured data (i.e., using 2 data points). The statistics for each event are grouped according to vehicle type and the highway lane of travel, giving a set of n recorded events. The set of n recorded events is used as a basis to generate median values and quartiles for each 0.1 s of measurement.

5.3. Results and discussion

5.3.1 Wake Flow

Figure 5.4 shows the measured horizontal flow (i.e., u and v) as (a) transport trucks, (b) SUVs and (c) passenger cars travelled past the tripod. Refer to Sect. 5.2.3 for filtering criteria. The top panel of Fig. 5.4 shows the u component of velocity, and the bottom shows v; each velocity component is further separated by the highway lane of travel relative to the tripod location (i.e., close, or far). The yellow shading shows the interquartile range. The wake flow is clear in the measured horizontal velocity components and is most significant behind transport trucks in the close lane. Between 1.9 and 2.4 s, the median u quickly increases from 1.4 m s^{-1} to 3.0 m s^{-1}. Between 2.5 and 2.7 s v is negative, indicating that during this time the flow direction is reversed and opposes the vehicle's travel direction. From 3.4 to 6.1 s, the most intense vehicle–induced flow is measured, and the flow direction nearly aligns with the direction of vehicle travel (i.e., $v \approx$ 4 m s^{-1} and $u \approx$ 0.5 m s^{-1}). Measured flow oriented with the vehicle travel direction is consistent with previous near–highway studies performed by Rao et al. (1978) and Chock (1980) when the measured flow is averaged over several seconds, but these previous investigations did not resolve the short 0.3 s period of reversed flow that is demonstrated in Fig. 5.4. However, the 75th percentile of u suggests that even in the most intense part of the wake between 3.4 and 6.1 s, the flow can still have considerable variation in its direction. The horizontal flow in the most intense part of transport truck vehicle wakes exceeds the ambient wind speed by about a factor of 2. For transports travelling in the close lane, the wake flow does not appear in the measurements until about 2 s after the start of the event. This 2 s delay results from the time required for the trailer to fully pass the tripod, plus the time required for the edge of the vehicle wake to spread laterally or be advected to the sensor. Even transport trucks travelling in the far lane show a significant vehicle–induced flow, but with flow oriented in the opposite direction than is generated by vehicles traveling in the close lane. The weakening of the wake flow is much more gradual compared to the initial increase, which is abrupt over about 1 s.

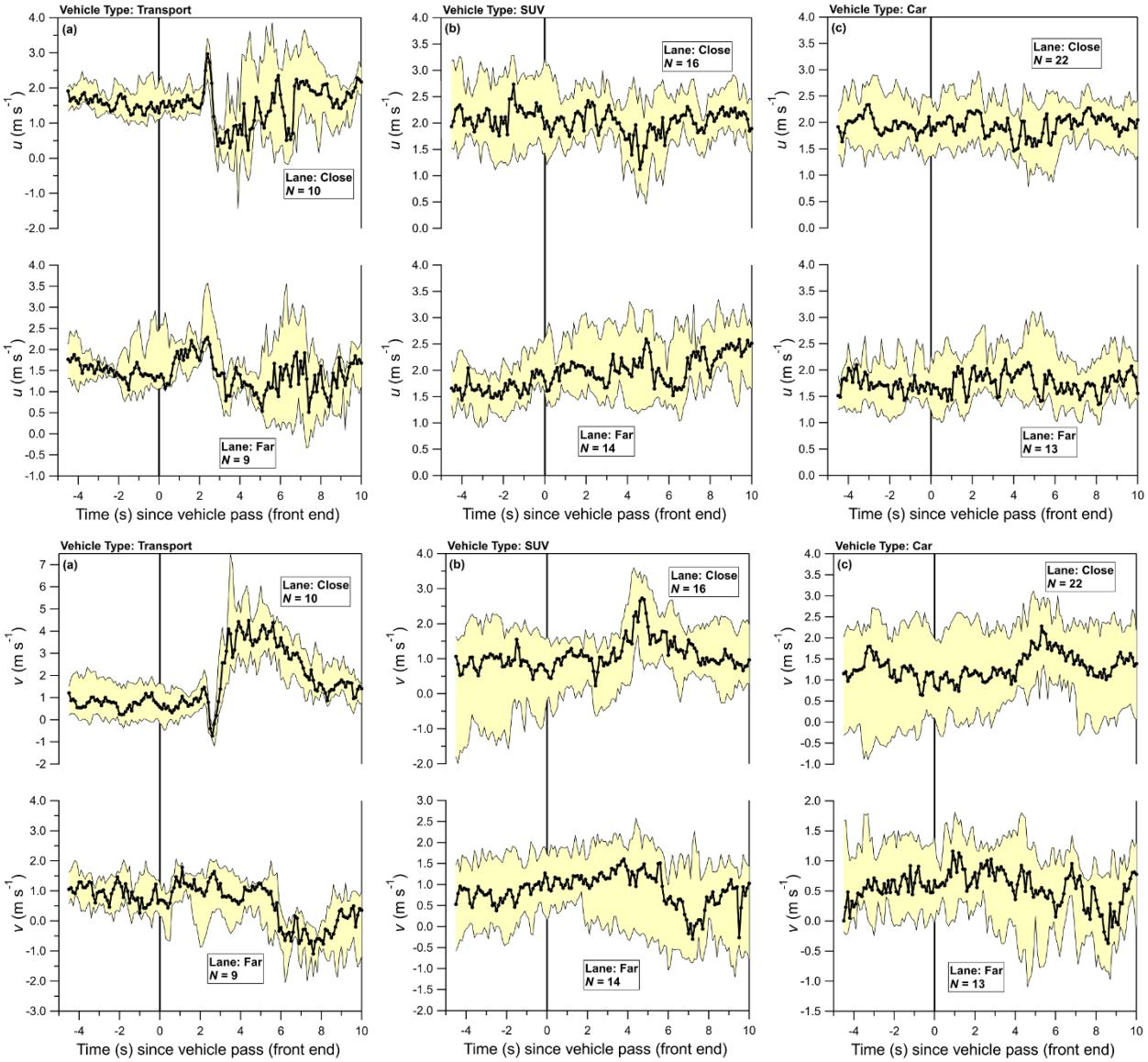

Figure 5.4: The velocity measured as (a) transport trucks, (b) sport utility vehicles (SUV) and (c) passenger cars traveled past the tripod. Each vehicle type has two panels showing the measured velocity: the top shows u (aligned perpendicular to the road) and the bottom shows v (aligned parallel to the road). The median of N events are shown as thick solid lines; the thin upper and lower lines give the 75th and 25th percentiles respectively.

SUVs also show evidence of vehicle–induced flow in the median and 75th percentile, and to a lesser extent passenger cars. For SUVs travelling in the close lane, v begins to show an increase in the median at 3.6 s, with a similar time for u. For passenger cars travelling in the close lane, the effect on the measured v is similar to sport utility vehicles, but for u, the effect of passenger cars travelling in the close lane is more muted and evident mostly in the 25th percentile. There is no visible effect on the measured horizontal velocity components from passenger cars travelling in the far lane. For SUVs travelling in the far lane, there is no visible effect in u, but evidence of their motion exists in the median v, between 5.8 and 8.2 s, since

during this period v decreases from near 1.2 m s^{-1} to –0.3 m s^{-1}. Therefore, these results demonstrate that SUVs induce a greater wake flow than passenger cars, at a measurement height of 1.4 m. At the same time, the wake flow generated by moving passenger cars and SUVs is much less significant than the wake flow generated by moving transport trucks.

a Lateral wake spread

Using the measurements shown in Fig. 5.4, the start and end time of the wake for each vehicle class travelling in the close lane can be estimated. Here v is used to define the temporal start (t_1) and end (t_2) of the wake. The velocity component parallel to the highway is chosen since it shows the most dramatic increase in flow velocity with passing traffic. Furthermore, v has the most clearly defined temporal boundaries, especially for SUVs and cars. Table 5.3 gives the estimated t_1 and t_2 measured for each vehicle class, estimated from Fig. 5.4. Using the start and end time, the lateral spread of the vehicle wake can be estimated after applying some assumptions: (1) vehicles travel at a constant speed of 22 m s^{-1}, (2) all vehicles of a particular class have the same length (L) and width (W), (3) vehicles are exactly centered in their highway lane, (4) the ambient wind speed and direction are stationary, (5) the wake spreads linearly with time and begins at the back end of the vehicle and (6) there is no significant timing uncertainty in the measurements shown in Fig. 5.4. Under strong headwinds and crosswind flow, the wake may not begin at the back of the vehicle as assumed here, but instead begin along the side wall (i.e., see Fig. 5.1 in Rao et al. 2002). For the approximations here, the following dimensions are used for each vehicle class: L = 20 m, 5.0 m, 4.3 m and W = 2.6 m, 2.0 m and 1.7 m for transports, SUVs, and cars respectively.

Table 5.3: The temporal start (t_1) and end (t_2) of the vehicle wake, and the distance d_1 and d_2 (see Fig. 5.5). The vehicle speed (S) is assumed to be the speed limit of the highway, which is 80 km h^{-1} (22.2 m s^{-1}) and is used to estimate the lengths d_1 and d_2.

Vehicle type (close lane)	Temporal wake start, t_1	Temporal wake end, t_2	$d_1 = S(t_1) - L$	$d_2 = S(t_2) - L$	β_1	β_2
Units	**(s)**	**(s)**	**(m)**	**(m)**	**(°)**	**(°)**
Transport	1.9	7.8	22	150	82.1	2.16
SUV	3.6	7.6	75	160	87.4	1.92
Car	4.0	7.9	85	170	87.6	1.75

Two distances d_1 and d_2 can be estimated from the measurements shown in Fig. 5.4, representing the distance the vehicle has travelled at time t_1 and t_2 respectively. This is shown graphically in Fig. 5.5. Using d_1 and d_2, the angles β_1 and β_2 can be determined (see Fig. 5.5) and used as a basis to estimate functions that describe the edge of the wake in the $x - y$ plane. This is demonstrated in Fig. 5.6 (b) for

transports and SUVs, where the black or blue lines denote the edge of the vehicle's wake determined at time t_1 and t_2 using angles β_1 and β_2 respectively. For transports, SUVs and cars, the lateral wake width at distance x behind the vehicle can be estimated as the difference between the functions describing the initial and final edge of the vehicle wake, giving

$$LW(x) = [\tan(\beta_2) - \cot(\beta_1)][d_2 - x] + \frac{d_2 - d_1}{\tan(\beta_1)} \quad \text{for } x \leq d_2. \tag{5.2}$$

Given that we do not observe any visible effects from passenger cars travelling in the far lane (and little effect from SUVs), this likely implies that wakes of these vehicles have very little lateral spread and have essentially dissipated by the time they are advected through the sensor (at a height of 1.4 m). However, for transports there is a clear effect from vehicles travelling in the far lane, suggesting much greater lateral spread of the wake for that vehicle class. These assertions are supported by the lateral wake width estimated from Eq. 5.2 and shown graphically in Fig. 5.6. The results suggest that at 150 m behind transport trucks, the lateral width of the wake is near 18 m. At the same distance behind passenger cars and SUVs, the lateral width of the wake is estimated to be 3.7 and 3.3 m respectively, about 5× less than the lateral wake width estimated for transport trucks. Therefore, not observing an effect from passenger cars travelling in the far lane is reasonable, since they are travelling at a perpendicular distance of about 7 m away from the sensor, and the car wake under no crosswinds will only have spread enough to fill its own highway lane by 150 m behind the vehicle. Therefore, the car wake needs to be advected to the sensor, which for weak crosswind flow of 1 m s^{-1} implies a travel time of about 6 s. By this time the car wake has largely dissipated when it is sampled by the sonic anemometer and consequently it is absent from our measurements. The results here may suggest that dust suspended by heavy–duty trucks is more likely to impact the areas adjacent to the highway, compared to passenger cars and sport utility vehicles.

These results also show that the wake becomes slightly asymmetric about the wake centerline, especially for transport trucks. This may suggest that each side of the vehicle wake is advected at a different speed, that is, the portion of the wake that interacts directly with the mean wind is advected the fastest.

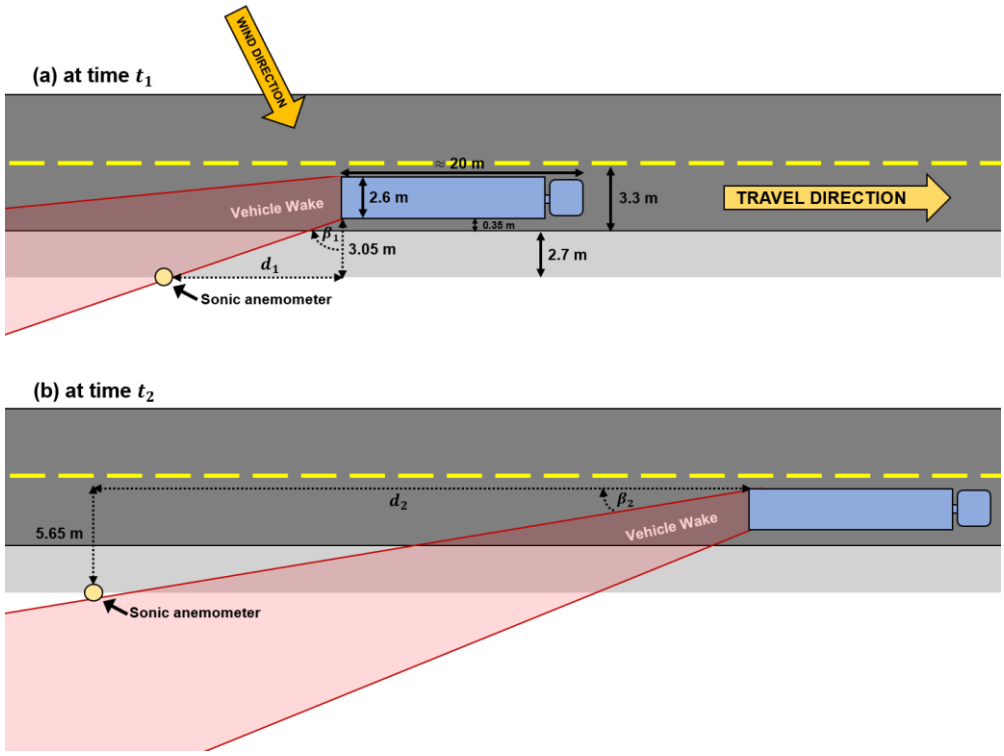

Figure 5.5: (a) Shows the initial measurement of the wake at time t_1 and (b) shows the end of the wake at time t_2, with the associated geometry superimposed. Time t_0 (not shown) is defined as the point when the front end of the vehicle (in this case the transport) is directly in front of the sonic anemometer.

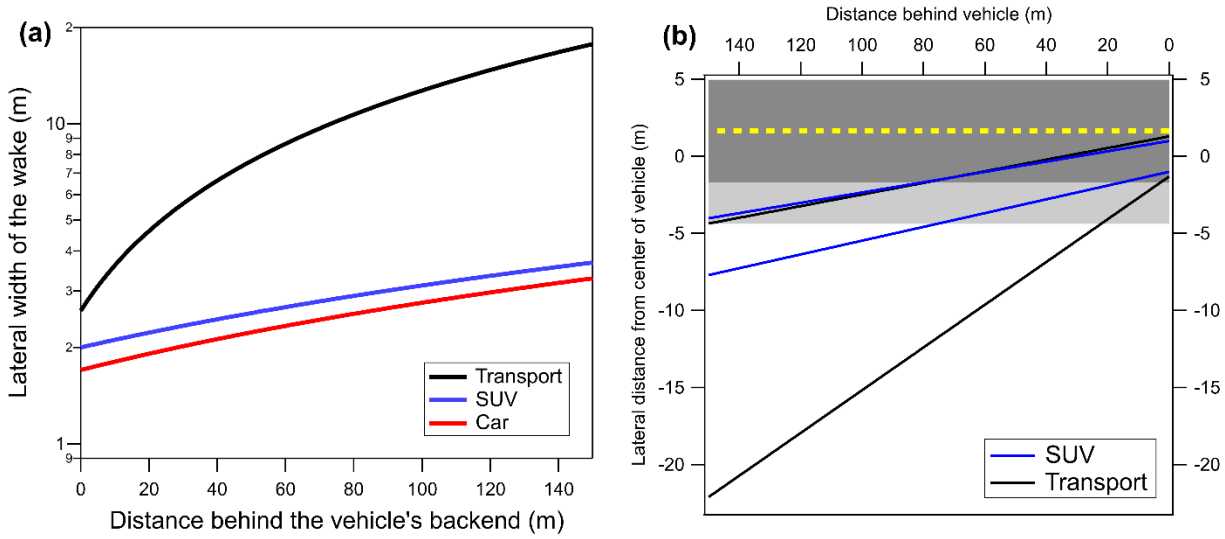

Figure 5.6: (a) The lateral width of the wake estimated as a function of distance behind the vehicle's backend. Calculated from Eq. 5.2 for each vehicle class investigated in this study. (b) Equivalent to Fig. 5.5 but determined from the tripod measurements. The solid lines represent the edge of the vehicle wake.

b Wind energy potential

It is interesting to estimate the possible wind power that could be extracted from the measured vehicle–induced flow, considering some modelling studies (see introduction) demonstrating it could be a possibility. For transport trucks with a maximum horizontal wind speed near $U = \sqrt{u^2 + v^2}$, a wind turbine with a unit area swept (A = 1 m^2), and an air density ρ = 1.2 kg m^{-3}, the corresponding wind power density (kinetic energy per unit time, per unit area) is $P_w = 0.5\rho U^3$. The available power is $P_a = C_p \eta P_w$ (Manwell et al. 2002), where C_p = 16/27 is the Betz limit and η is the drive train efficiency, assumed here to be equal to 1.0, implying perfect efficiency. Since $P_W \propto U^3$, a small increase in the wind speed, say from 4 to 5 m s^{-1}, implies that P_w is 1.95× larger. The available power calculated for transport trucks and SUVs is shown in Fig 5.7. Dashed lines give the available power at specific fixed horizontal wind speeds. For moving vehicles, the assumption of a constant flow velocity throughout the entire swept area of the wind turbine may not be valid, and rotational inertia will lower the wind turbine efficiency (Hara et al. 2012). Therefore. the results in Fig 5.7 represent a theoretical maximum available wind power.

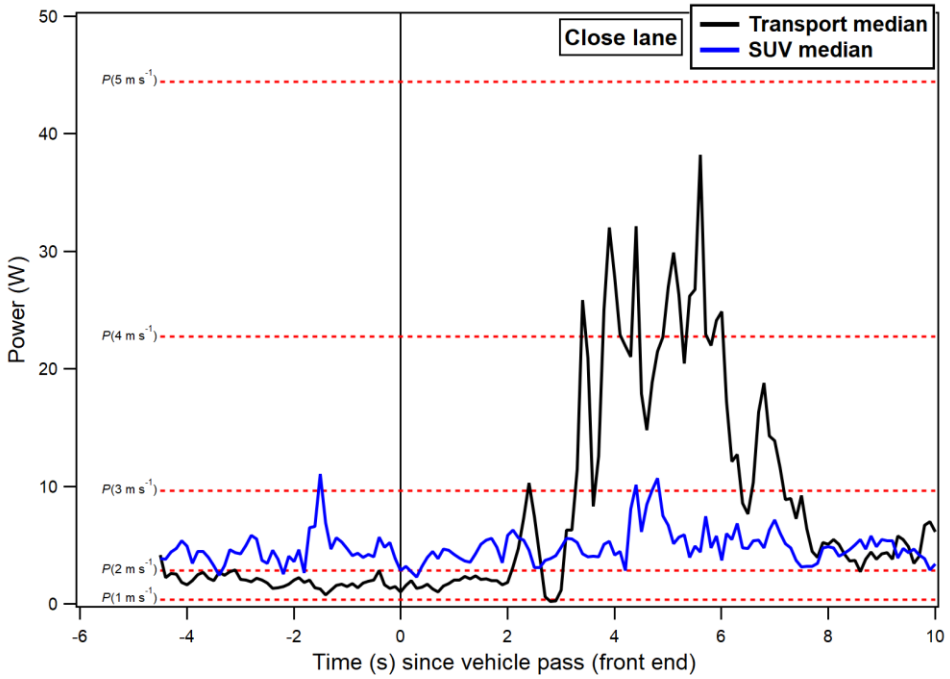

Figure 5.7: The available wind power calculated from flow induced by moving transport trucks and SUVs. Dashed lines give the available power at a specific horizontal wind speed.

Figure 5.7 demonstrates that transport trucks produce a wake flow that yields significantly more available wind power than SUVs (and passenger cars). Therefore, when considering roadside power extraction, the ideal placement will be where the amount of passing transport trucks is maximized. The

measurements here represent sparse vehicle passings, but on a real highway in heavy traffic the effect of a group of vehicles travelling together may give different results. In closely spaced traffic, the wake induced flow may not have time to return to background levels between each successive vehicle passing. In this case, the flow generated by each consecutive passing vehicle may add together to some extent, giving a larger magnitude flow at the roadside than measured in this study for isolated transport trucks and SUVs.

In high density traffic travelling at speeds between 80 to 120 km h^{-1}, typical of freeways within major metropolitan areas, there are typically greater than two highway lanes on either side of the center embankment. In Ontario, Canada, transport trucks typically travel in the "reduced speed lane", corresponding to the outermost lane near the edge of the highway, or sometimes the highway lane adjacent to it. For safety reasons, it is unlikely that wind turbines could be placed much closer to the edge of the highway than the measurement location used during this study. Therefore, the measurement location used in this work is likely to be representative of what an actual wind turbine would experience at a height of 1.4 m. Based on data available online by the Government of Canada for the year 2008, 400 series highways in the Toronto region typically experienced between 6000 and 8000 transport trucks per day. However, there is a clear diurnal trend in the amount of traffic, with the peak amount of transport trucks occurring on weekdays between 11:00 and 15:00 (MTO, 2021); some sections of Highway 401 may experience about 1100 transport trucks per hour during this peak time. For passenger vehicles, the peak traffic on weekdays occurs between 06:00 and 18:00, with the amount of passenger vehicles ranging between 4000 and 6000 per hour during this time. Furthermore, some sections of the 400 series highways have a bimodal pattern for passenger vehicles on weekdays, with the first peak between 07:00 and 09:00 and the second between 16:00 and 18:00.

For the measurements in Fig. 5.7, the spacing of transport trucks required to maintain $U \geq 3$ m s^{-1} can be estimated, assuming other vehicle wakes do not influence the flow generated by transport trucks, either constructively or destructively. The choice of $U \geq 3$ m s^{-1} is somewhat arbitrary but can be justified since at $U \geq 3$ m s^{-1} the amount of extractable power becomes large relative to the extractable power in the mean ambient flow. After a passing transport truck, $U \geq 3$ m s^{-1} for approximately 4 s. Integrating the power over this 4 s period gives an estimate of the total energy (E) produced by a single passing transport truck, with $E \approx 80$ J. For a transport truck travelling in the close lane at a vehicle speed of 22 m s^{-1}, the minimum spacing of transport trucks required to maintain $U > 3$ m s^{-1} would be 88 m, or 15 equally spaced transport trucks every minute. This implies 900 transport trucks per hour, which is less than the average hourly transport trucks reported on some sections of Highway 401; 1100 transport trucks per hour would require an equal spacing of about 73 m with 18 passing transport trucks per minute and would result in a perpetual flow that is elevated above background levels. Assuming 900 transport trucks per hour travel in the outermost highway lane, and each truck is equally spaced with no wake interactions (i.e., each successive

transport truck yields 80 J of energy), then the maximum extractable energy that could be stored during each peak hour is estimated to be 72 kJ. Peak traffic may be sustained for up to 4 hours on some sections of 400 series highways, and thus a maximum of 288 kJ of stored energy (per m^2 area swept) would result. Passing SUVs do produce a minor increase in wind energy for < 0.4 s, and so the addition of these vehicles travelling in the outermost lane with transport trucks would likely result in greater energy estimates than presented here. The energy estimates presented here assume a vehicle speed of 80 km h^{-1}, but on 400 series highways, the speed limit may range between 100 and 120 km h^{-1}, probably leading to larger wake induced flows (and energy) than measured here. Thus, these results suggest that in some locations along 400 series highways it may be possible to extract a limited amount of energy that could then be stored in a battery and used to power streetlights during the night, especially with an installation of many wind turbines that maximize the amount of swept area.

The idea of placing wind turbines in the center dividing barrier of the highway to increase the amount of passing vehicles (which would also produce enhanced vorticity) is probably not a feasible idea in Ontario, since transport trucks rarely travel in the innermost highway lane, and SUVs and passenger cars alone likely will not produce sufficient flow at the location of the wind turbine. This is supported by the findings of Nazari (2020) who performed a numerical simulation of multiple vehicles passing a wind turbine placed at the center the highway (i.e., dividing traffic flow directions). They investigated a case where only passenger cars and SUVs are present, and a case that also includes transport trucks. The case with only passenger cars and SUVs is found to yield much less available wind power compared to the case that also includes transport trucks, which is consistent with the measurements in this study. However, in regions that do have transport trucks travelling in the innermost highway lane, placement of wind turbines in the center dividing barrier of the highway is likely to be more feasible. One possible effect of placing wind turbines at the highway roadside (and in the center divide) could be a reduction in fuel efficiency due to increased turbulence generated by the turbines, however it is not possible to quantify this effect in the present work.

It is useful to compare the amount of energy that could be stored by placing a solar panel at the roadside, compared to a wind turbine. The power output by a solar panel (P_w) with an illuminated area of A_s, operating with an efficiency of E_s can be calculated as $P_w = A_s I_{ds} E_s$, where I_{ds} is the downwelling shortwave irradiance in W m^{-2} (Tiong et al., 2015). Assuming a unit area solar panel (A_s = 1 m^2) and using measurements of I_{ds} made at York University (see Fig. F1), the amount of storable energy in August is estimated to be about 1950 kJ per day while in January the amount of storable energy is lower near 560 kJ per day. This energy estimate assumes a rather poor efficiency of the solar panel, with E_s = 0.1 and assumes that the solar panel can maximize the intercepted solar irradiance by self-tilting. Therefore, even a rather inefficient solar panel will generate significantly more storable energy per unit area at the highway roadside compared to a wind turbine that harvests vehicle wake energy. For 900 equally spaced transport trucks per

hour that is sustained for 4 consecutive hours, the estimated maximum storable energy is 288 kJ (from a perfectly efficient wind turbine). This is only about 15% of the daily energy produced by a low-efficiency solar panel with a unit area. This demonstrates that it would be much more economical to use roadside solar panels opposed to wind turbines in low ambient flow conditions, especially since a wind turbine will have a much lower efficiency and hence yield lower power estimates than given here.

5.3.2 Turbulent kinetic energy

Figure 5.8 shows the turbulent kinetic energy (e) following the same conventions as Fig. 5.4. Fig. 5.8 (a) shows transport trucks, (b) sport utility vehicles and (c) passenger cars. e generated by transport trucks in the close lane begins to increase in the median and 75th percentile, within the first 0.5 s after its front end has passed the tripod, peaking at 3.5 s in the median with $e \approx 4.5$ m^2 s^{-2}. It is useful to point out that the turbulent kinetic energy includes timescales up to 2 min. The 75th percentile demonstrates that some passing transport trucks produce much more significant turbulence, with the 75th percentile peaking at 3.4 s with e = 9.8 m^2 s^{-2}, which is about 2.2× larger than the maximum median e. The roadside measurements agree with in–situ measurements obtained behind transport trucks, where e measured closely behind the trailer is large and > 6 m^2 s^{-2} (Gordon et al. 2012; Miller et al. 2019/Chapter 2). After reaching a maximum, the median e remains elevated for about 0.9 s, followed by an abrupt drop at 4.4 s, and then a gradual decrease to background levels over the next 5 s. For transport trucks, $\overline{v'^2}$ is the largest contributor to e, followed by $\overline{u'^2}$ and $\overline{w'^2}$ (not shown). For transport trucks travelling in the far lane, there is still an obvious increase in median e between 4.9 s and 8 s, but the maximum e is about 42% lower ($e \approx 1.9$ m^2 s^{-2}) than trucks travelling in the close lane. And unlike the close lane, the 75th percentile does not demonstrate nearly as much spread from the median. In the far lane, the 75th percentile maximizes at 4.8 s with $e \approx 2.4$ m^2 s^{-2}, which is about 1.3× larger than the median e.

For SUVs travelling in the close lane, the median e begins to increase about 1.5 s after the vehicle's front end passes the tripod. The increase is more gradual than passing transport trucks, and a well–defined peak is not as clear. The median e peaks near 5.4 s with e = 1.3 m^2 s^{-2}, but the 75th percentile reaches a maximum earlier at 4.2 s with $e \approx 1.9$ m^2 s^{-2}. Even in the 75th percentile, e generated by SUVs travelling in the close lane is 42% lower than the median e measured for passing transport trucks. SUVs travelling in the far lane show some increase in the median e, between 4.7 and 7.8 s, but the maximum e is much lower than the close lane, near e = 1.1 m^2 s^{-2}, and not significantly different in the 75th percentile. Passenger cars traveling in the close lane produce less turbulence than SUVs, and their effects last for less time. The motion of passenger cars travelling in the far lane does not generate visible turbulence at the tripod location.

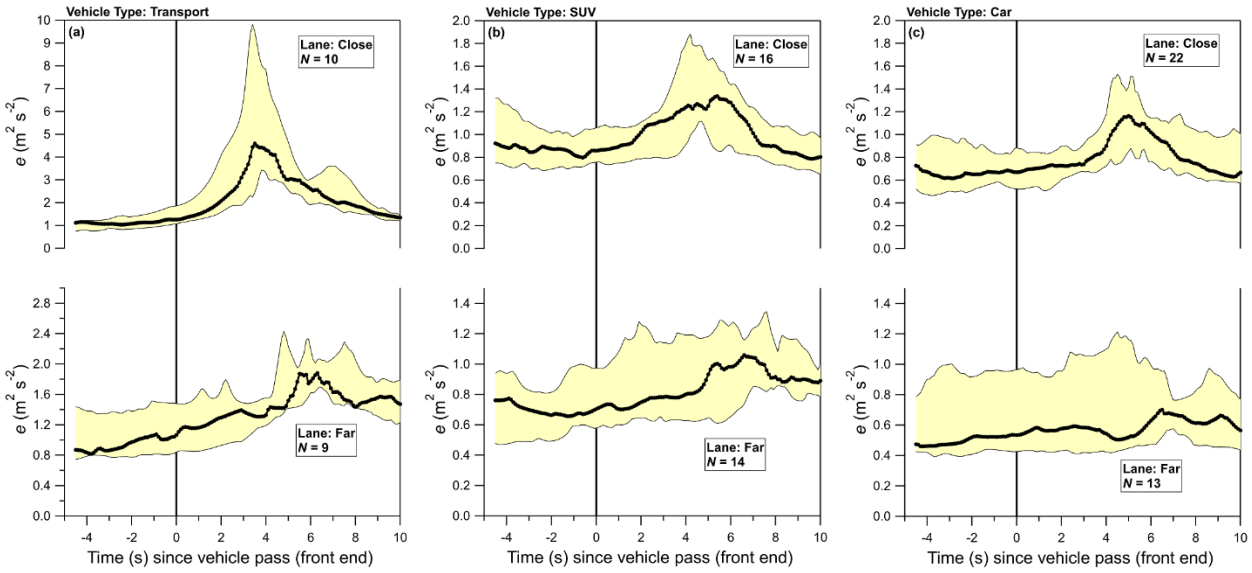

Figure 5.8: The 0.1 s turbulent kinetic energy (*e*) calculated using wavelet analysis corresponding to passing (a) transports, (b) sport utility vehicles (SUV) and (c) passenger cars. The median is shown as a solid black line bounded by two thin lines; the thin lines give the 25th (lower) and 75th (upper) percentiles. The solid vertical line gives the event start, that is, when the front end of the vehicle is directly in front of the tripod. Each panel shows measurements separated by highway lane of travel (i.e., close vs. far). *e* includes time scales up to about 2 min.

Figure 5.9 (a) shows the vertical turbulent heat flux ($\overline{w'T'}$) as transport trucks passed by the tripod. Like *e*, only timescales up to 2 min are included, which neglects contributions to $\overline{w'T'}$ that occur at longer timescales within the ambient atmosphere, and therefore background $\overline{w'T'}$ presented herein has a lower magnitude than is presented in Miller and Gordon (2022) (Chapter 3) who calculated $\overline{w'T'}$ for averaging periods between 5 and 8 min. In either lane there is an enhancement in $\overline{w'T'}$ for passing transport trucks. The same increase is not found when passenger cars or SUVs pass the tripod (not shown). $\overline{w'T'}$ for transport trucks travelling in the close lane shows an abrupt increase at 2.9 s, maximizing at 3.4 s with $\overline{w'T'} \approx 0.43$ K m s^{-1}. The 75th percentile maximizes later, at 4.1 s with $\overline{w'T'} \approx 0.70$ K m s^{-1}. An increase is also evident in the far lane, particularly in the 75th percentile between 3.8 and 5.7 s, maximizing near 4.7 s with $\overline{w'T'} \approx$ 0.43 K m s^{-1}. These heat fluxes are probably generated by the turbulence behind transport trucks rapidly mixing the air near the low–albedo asphalt surface, upward and away from the highway. This increase in the heat flux is unlikely to be related to vehicle exhaust since for transport trucks the release point is near a height of 4 m, and the heat flux is sustained over about 3.5 s.

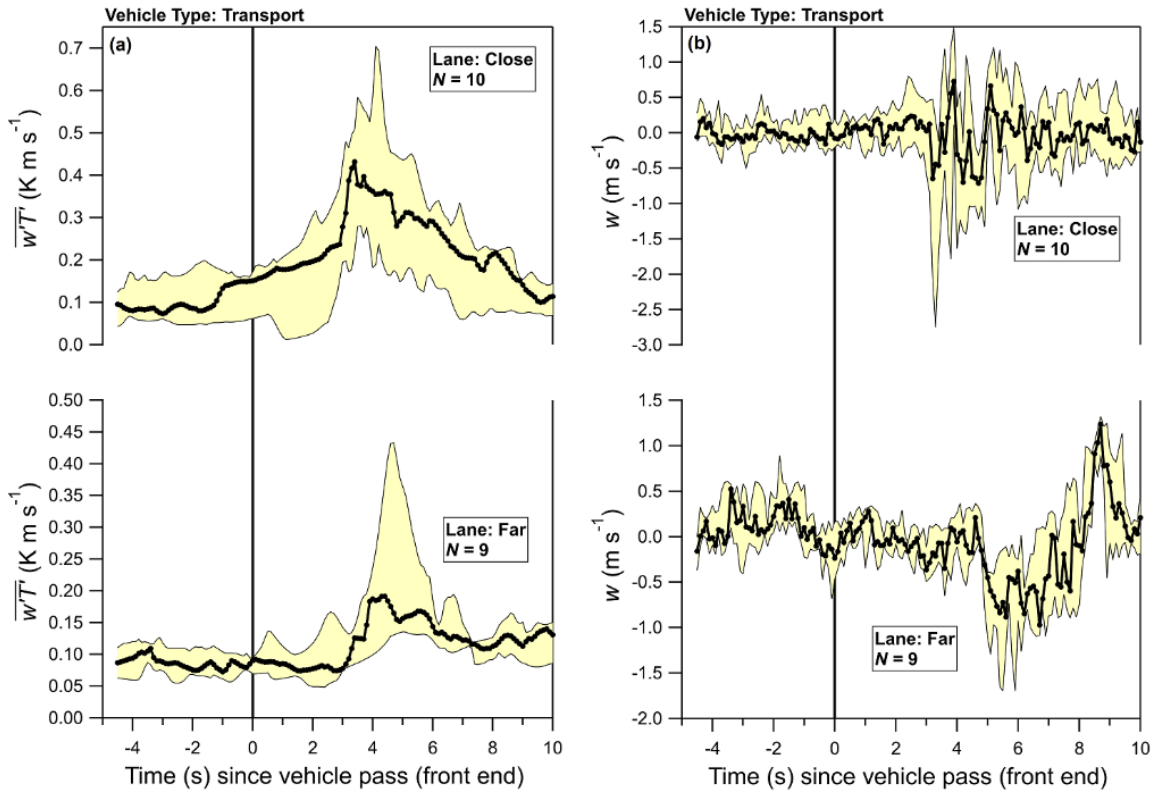

Figure 5.9: (a) The 0.1 s turbulent vertical heat flux ($\overline{w'T'}$) calculated using wavelet analysis and (b) the 0.1 s averaged vertical velocity (w). Both panels show data for passing transport trucks. This figure follows the same convention as Fig. 5.8. The vertical turbulent heat flux includes time scales up to 2 min.

Figure 5.9 (b) shows w, as in Fig. 5.4, but for transport trucks only. Like the horizontal velocities, there is a clear impact on w from transport trucks passing the tripod, but for w the effect is most pronounced from transport trucks travelling in the far lane, compared to the close lane. The impact on w from transports travelling in the far lane occurs between 4.6 and 9.7 s; w becomes negative between 5.0 and 7.7 s, with w ranging between –0.5 and –1.0 m s^{-1}, and then between 8.4 and 9.1 s, w becomes positive, maximizing at 8.7 s with $w \approx 1.24$ m s^{-1}. For transport trucks travelling in the close lane, the magnitude of w varies rapidly, and its sign switches back–and–forth between positive and negative with no clear trend.

5.3.3 Velocity spectra

Figure 5.10 shows the average wavelet spectra (averaged from N events) calculated during a 15 second period corresponding to a passing isolated transport truck. The solid black line corresponds to the background levels and is calculated for the 5 seconds preceding the measured event. The colored lines show the spectra for the 10 s following the event (i.e., after the vehicle's front end passes the tripod), calculated for 2 s averages (starting at 0, 2, 4, 6 and 8 s). Fig. 5.10 (a) are spectra for transport trucks travelling in the close lane and Fig. 5.10 (b) are for transport trucks travelling in the far lane. Fig. 5.10 (a) and (b) show

spectra for each measured velocity component, and from top to bottom are u, v and w respectively. In the first 2 seconds after an event in the close lane (0 to 2 s), the spectra are increased relative to background levels only for frequencies (f) between 0.08 and 2 Hz. For f > 2 Hz there appears to be reduced energy compared to background levels, and this is most significant for w. The period that the trailer is passing the tripod occurs in the time range between 0 and 2 s. During the next 2 seconds (2 to 4 s) the velocity spectra show maximum enhancement relative to background levels, and the enhancement is present over all f > 0.08 Hz. This period corresponds to the time just after the trailer passes the tripod, and hence when the measured turbulent kinetic energy is greatest and is likely representative of the near–wake region. For v and w the spectra have a minor broad peak near f = 0.5 Hz in the 2 to 4 s period. During the next 6 s the spectra slowly return to background levels. The broad peak near f = 0.5 Hz in the v and w spectra for transport trucks travelling in the close lane is consistent with the results presented in Baker (2001) for small non–dimensional times. Wavelet spectra presented in Baker (2001) also demonstrate a second peak in the frequency range of 0.05 to 0.1 Hz, but we do not see this peak in our measurements. In the 0.05 to 0.08 Hz frequency range the spectra remain essentially identical to the background spectra, implying no impact from vehicle–induced turbulence occurs at these frequencies.

The results measured in the far lane are similar to the close lane, except that the maximum enhancement of turbulence occurs later, during 4 to 6 s. Furthermore, the turbulence is also much less significant in the far lane which is evident in the spectra, and is consistent with the results presented in Fig. 5.4 and Fig. 5.8.

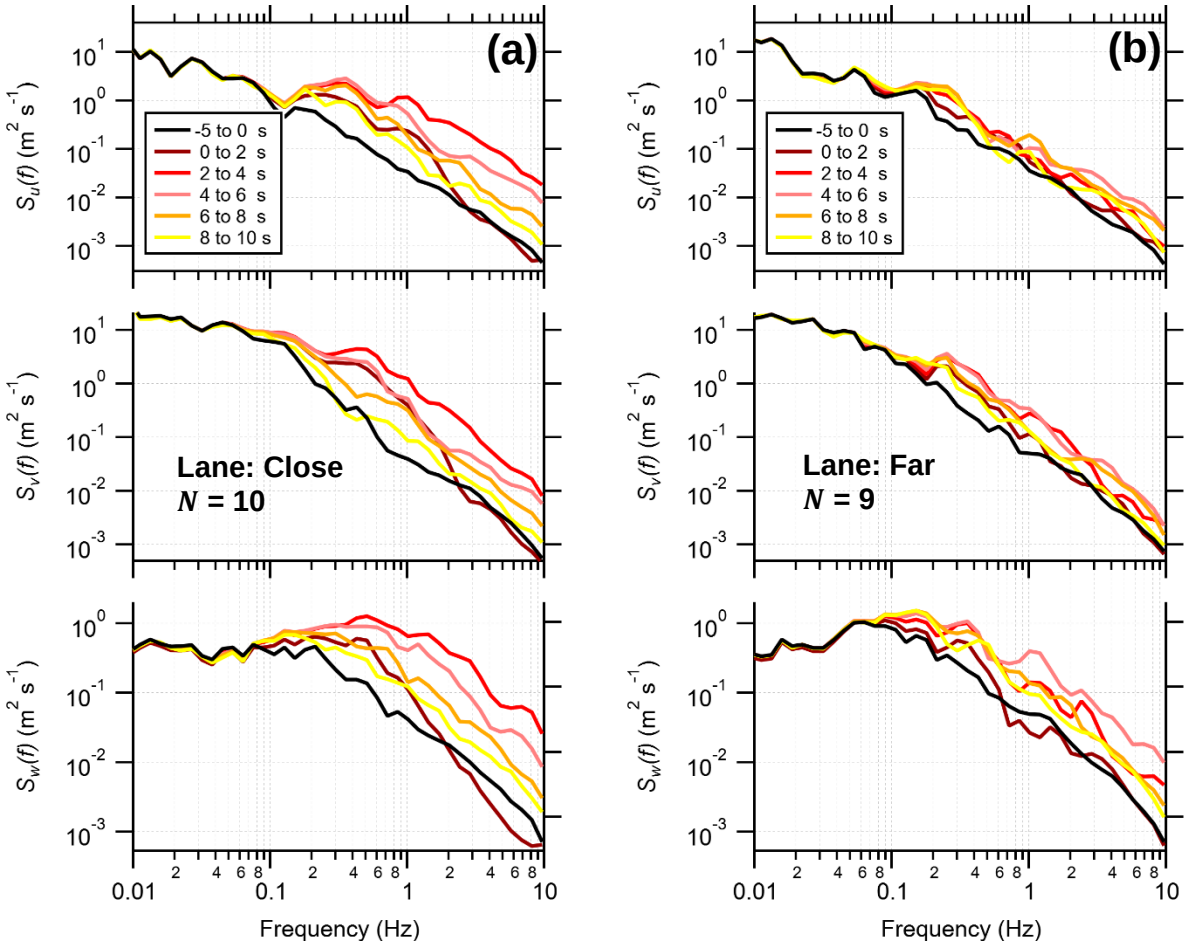

Figure 5.10: Wavelet power spectral densities for (a) the close lane and (b) the far lane. 6 spectra are shown for each velocity component (u top, v middle and w bottom). The first is calculated for the 5 second period before the vehicle's front end passes the tripod (time –5 to 0 s) and then for each 2 second increment thereafter. The period –5 to 0 s gives an approximation of the background turbulence spectra. Each spectrum is the average of all transport trucks that were recorded by the tripod dashcam and were considered isolated (i.e., 10 in the close lane and 9 in the far lane as in Fig. 5.8 and 5.9).

5.4 Conclusions

This study has presented measurements of vehicle–induced flow and turbulence attributed to individual vehicle types. The results can be summarized into a few key points:

I. Moving traffic induces a flow in the direction of vehicle motion. At a height of 1.4 m, the vehicle–induced flow is most significant for transport trucks, followed by SUVs and passenger cars. The magnitude of the measured flow induced by transport trucks exceeds the mean ambient wind speed by about a factor of 2.

II. The results suggest that to maintain a mean horizontal flow velocity of 3 m s^{-1} for use in road–side power generation, there would need to be 15 equally spaced transport trucks every minute (~900 trucks per hour). During peak traffic on 400 series highways, there can be near 18 transport trucks per minute (~1100 trucks per hour), in addition to other passenger vehicles. Since transport trucks typically travel in the outermost lane in Ontario, this suggests there may be areas where a perpetual elevated flow is produced. For a more modest case of 900 equally spaced transport trucks per hour travelling in the outermost lane, and ignoring passenger vehicles and any wake interactions, the measurements from this study suggest a maximum of 72 kJ of energy per hour (per m^2 area swept) could be stored in a battery for later use. This is true when the mean ambient wind speed is low near 1 m s^{-1} and is most relevant since under strong ambient winds there is no need for the vehicle wake to generate power. However, compared with solar panels placed at the roadside, the use of wind turbines to harvest wake energy is not economical, since even a low-efficiency solar panel can produce nearly 7x more storable energy per day (per unit area) than a perfect-efficiency wind turbine operating during low ambient flow conditions (with a unit area swept).

III. The lateral spread of the wake is about 8× greater for transport trucks than SUVs, and 150 m behind the vehicle, the lateral width of the wake is approximately 5× larger for transport trucks than SUVs or passenger cars. This may imply that road dust suspended by transport trucks has a larger impact on the areas next to the road, compared to SUVs and passenger cars.

IV. Moving traffic generates vehicle–induced turbulence, which follows a similar trend as the vehicle–induced flow. Transport trucks are found to produce significant turbulence at 1.4 m height, and passenger vehicles produce relatively little in comparison.

V. For transport trucks, the vehicle–induced turbulence is primarily the result of eddies with frequencies greater than 0.08 Hz (wavelengths < 50 m for a horizontal flow of 4 m s^{-1}). A relatively minor broad peak is present in the spectra of turbulent kinetic energy near f = 0.5 Hz (wavelength on the order of 10 m), for transport trucks passing the tripod in the close lane.

VI. Transport trucks generate significant mixing near the road surface and for the combination of sunny conditions and a low albedo asphalt, the result is a significant enhancement in the vertical exchange of heat for about 5 s following the passage of the vehicle.

CHAPTER 6: Conclusions and future research

This work used an instrumented car and a stationary monitoring system to explore vehicle wakes generated by on–road moving vehicles and investigated the wake's impact on the dispersion of emitted aerosols and nonreacting trace gases. Since only one other study has evaluated an instrumented car for its accuracy at measuring turbulence quantities, this research also aimed to quantify the performance of the car setup used in this work, to provide confidence in the representativeness of in–traffic measurements made by the system.

The study outlined in Chapter 2 examined the spatial variation of vehicle–induced turbulence (VIT) using an instrumented mobile car. Measurements were obtained behind vehicles on highways at a height of 1.7 m, while travelling at high speeds near 100 km h^{-1}. The turbulent kinetic energy (TKE) measured behind heavy–duty trucks and passenger vehicles is found to decay following a power law relationship with increasing distance downwind of the vehicle. The most significant turbulence occurs in the near wake region, closest to the vehicle, and is most intense behind heavy–duty vehicles (e.g., tractor–trailers, dump trucks, commercial buses), followed by mid sized vehicles (e.g., sport utility vehicles, minivans, pickup trucks) and passenger cars. Chapter 5 also analyzed VIT, but with measurements obtained from a stationary tripod placed near the edge of a two–lane highway, instead of from the mobile car. The sonic anemometer affixed to the tripod was placed at a height of 1.4 m, and about 2.7 m from the edge of the highway. Traffic passing the tripod was sparse such that several seconds elapsed between some vehicle passings, allowing the vehicle wake to be studied in near isolation and statistics to be generated for similar vehicle types. Like on–road measurements, the tripod measured the greatest TKE after passing heavy–duty trucks, with the maximum TKE ≈ 10 m^2 s^{-2} in the 75th percentile (the median TKE maximizes near 5 m^2 s^{-2}). After reaching its maximum ~3 s after the truck's front end passes the tripod, the TKE takes 5 to 6 s to return to background levels (background levels are near 1 m^2 s^{-2}). The TKE measured on–road behind heavy–duty trucks (using the instrumented car) maximizes near 11 m^2 s^{-2} in the 75th percentile at small following times < 1 s, a magnitude that is consistent with the tripod when background levels are considered. However, the median TKE measured on the tripod has a lower magnitude than the median TKE measured on–road using the instrumented car. This difference may be explained by (1) the vehicles sampled by the tripod travelled at lower speeds (typically 20 to 30 km h^{-1} lower), (2) the tripod measured beside the vehicle instead of directly behind it, and (3) the tripod measured at a height of 1.4 m compared to 1.7 m on the instrumented car.

Chapter 3 investigated turbulence each second as a heavy–duty truck travelled in the opposite direction (i.e., adjacent lane) as the instrumented car. The results demonstrate that even a single heavy–duty truck travelling past the instrumented car can lead to an enhancement of the measured velocity variances when they are calculated over a duration of 40 to 50 s. This is an important factor to consider, especially if

the goal is to measure the ambient atmosphere and not traffic. The same conclusion was not found for passing SUVs, since their effect may or may not be evident in the car–measured turbulence. For example, in one measurement period with only two passing SUVs there is no evidence of their effect in the measured turbulence, but in another measurement pass with a single SUV, there is enhancement evident in the horizontal velocity variances. Chapter 5 analyzed the wakes of sparse traffic, and it is estimated that at 150 m behind a heavy–duty truck, the lateral wake width is nearly 5× larger than at the same distance behind an SUV. At 150 m behind an SUV the wake has only spread enough to fill its own highway lane and very little of the adjacent lane (~0.2 m), assuming no crosswinds. Therefore, if limited crosswinds occur while an SUV passes the instrumented car (travelling in the opposite direction) the wake may not be sampled (i.e., no enhancement in the velocity variance). In the case of limited crosswinds, the wake will not spread enough laterally before dissipating to background levels, leading to no enhancement seen in the measured variances. For times with limited traffic contamination, a wavelet–based approach was developed (Chapter 3) that gives an estimate of the variance excluding the effect of the passing traffic, while still retaining contributions from the longest timescales. This technique could be useful in studies where the contamination of the velocity record by passing traffic occurs intermittently, but cannot be avoided (e.g., while measuring on low–traffic public roads).

Chapter 3 also examined the performance of the instrumented car at measuring atmospheric means, variances and covariances when not following traffic, by comparing measurements made on the car to a roadside monitoring system (a tripod). If the car can successfully measure ambient variances and covariances while travelling at high speeds, it is probable that it can successfully measure these same quantities behind traffic. The results shown in Chapter 2 and 3 demonstrate that flow distortion on the car is significant at the measurement location. For the instrumented car used in Chapter 2, 3 and 4, the measured vertical velocity has a nearly perfect linear relationship with vehicle speed. However, the results in Chapter 3 demonstrate that if appropriate corrections are applied, the mean wind speed and mean wind direction measured on the car agree well with measurements recorded by the nearby tripod. For some measurement passes, the horizontal velocity variances measured on the car are overestimated, compared to measurements logged by the tripod. However, improvement in the estimation of the horizontal velocity variances can be obtained by using wavelet analysis. Wavelet analysis is found to better resolve the low frequency contributions compared to the standard approach using eddy–covariance assumptions, giving a better estimate for some measurement periods. The vertical velocity variance and vertical turbulent heat flux measured on the car are biased low when compared to the tripod. The low bias may be related to a flux footprint mismatch between the car and tripod, or perhaps related to rapid flow distortion at the car measurement location. Another possibility is passing traffic that impacts the tripod but not the car, since as demonstrated in Chapter 5, there are impacts on the measured heat flux and vertical velocity when heavy–

duty vehicles pass the tripod. However, when sampling uncertainties are considered, the vertical momentum flux ($\overline{u'w'}$) is not found to be different from the tripod in the 95% confidence interval, and significantly different than zero for most measurement periods. Thus, Chapter 3 demonstrates that the instrumented car can successfully measure the mean turbulence near the surface, where the goal is not to measure traffic but rather the ambient atmosphere. The success using the instrumented car to measure ambient atmospheric variances and covariances gives confidence in the ability of the instrumented car at quantifying turbulent fluxes behind traffic on busy highways, where the direct comparison with a stationary tower at the roadside is much more difficult. The analysis presented in Chapter 5 supports the instrumented car's ability to quantify turbulent fluxes behind traffic, since the direction of the vertical turbulent flux of aerosols ($\overline{w'N'}$) and the vertical turbulent flux of CO_2 ($\overline{w'\rho_c{}'}$) are found to be consistent with the exhaust release point relative to the vehicle's measurement height. That is, for an exhaust located near the ground (~ 0.5 m), the car–measured $\overline{w'N'}$ and $\overline{w'\rho_c{}'} > 0$, but for an exhaust located near a height of 4 m, $\overline{w'N'}$ and $\overline{w'\rho_c{}'} < 0$.

The measurements presented in Chapter 2, combined with earlier measurements gathered by Gordon et al. (2012), suggests that TKE has a height dependence in the near–wake region of high–speed vehicles, with the vertical profile of TKE having a maximum near the vehicle's top (in the upper shear layer). Using these results, an extended parametrization was outlined in Chapter 2 that describes the total on–road TKE enhancement due to a composition of vehicles, including a vertical dependence on the magnitude of TKE. In addition to an upper shear layer along the top of the trailer, moving block shaped HDVs also have shear layers that develop along each side wall of the trailer, extending downwind. The side shear layers are characterized by a region of large horizontal Reynold's stress (i.e., a large magnitude of $\overline{u'v'}$) and enhanced turbulence (McArthur et al. 2016; He et al. 2019), and as demonstrated in Chapter 4, there is a moderate correlation between $\overline{u'v'}$ and TKE for measurements made behind HDVs (R^2 = 0.48). In comparison, $\overline{u'w'}$ has a weak correlation with TKE behind block shaped HDVs (R^2 = 0.17); the upper shear layer should be evident in the measurements as a region of large negative $\overline{u'w'}$ and enhanced turbulence near the height of the vehicle, about 4.1 m for HDVs (McArthur et al. 2016; He et al. 2019). Since the measurement height in this work is 1.7 m, the upper shear layer is less evident in the measurements made behind HDVs of height 4.1 m, and consequently there is a weak correlation between $\overline{u'w'}$ and TKE. Despite this, measurements close to HDVs (i.e., at small following distances) show a clear relationship between $\overline{w'N'}$ and $\overline{u'w'}$. Specifically, the most significant downward $\overline{w'N'}$ occur only during significant downward $\overline{u'w'}$, demonstrating a probable relationship between the upper shear layer and vertical pollutant transport. Further, these results might suggest that the upper shear layer entrains pollutants near the start of the trailer that are later released downwind into the near wake region.

The analysis presented in Chapter 5 suggests that pollutants emitted (and suspended dust) into the wake of a moving heavy–duty truck are more likely to impact the region adjacent to the highway compared to SUVs and passenger cars (especially during weak crosswinds), given the much greater lateral spread of the vehicle wake; the lateral spread of the wake is estimated to be about 8× greater for heavy–duty trucks than SUVs (assuming linear spread). For measurements made behind HDVs presented in Chapter 4, a simple Gaussian form was assumed, and a fit to the measured concentrations and vertical fluxes was determined by an optimization approach that reduced the residual between the Gaussian fit and measurements. The Gaussian solutions give estimated lateral and vertical eddy diffusivities for the wake region. The estimated vertical eddy diffusivities are similar for bottom and top exhaust vehicles. However, unlike bottom exhaust vehicles, the estimated lateral eddy diffusivity is near zero behind top exhaust vehicles, suggesting little lateral diffusion in the vehicle wake. Therefore, at the roadside, a bottom exhaust HDV will likely result in a greater dose of pollutants at pedestrian level (~ 1.5 to 2 m) compared to top exhaust vehicles. Bottom exhaust vehicles emit pollutants near the ground, resulting in a greater particle number concentration (and CO_2 concentration) at the measurement height of the instrumented car, compared to top exhaust vehicles (as demonstrated in Chapter 4). The greater near ground–level concentration is then dispersed laterally (and vertically) as the wake expands downwind of the vehicle.

The power spectral density of TKE measured in vehicle wakes were first investigated in Chapter 2. The power spectral densities in the wake region are significantly enhanced at frequencies (f) > 0.5 Hz. For a 20 to 30 m s^{-1} flow velocity, 0.5 Hz corresponds to a wavelength between 40 and 60 m, demonstrating that small eddies are responsible for all turbulent transport in vehicle wakes. Cospectra of w and N presented in Chapter 4 demonstrate that, like the TKE spectra, eddies with wavelengths < 60 m are responsible for the turbulent diffusion of aerosols in the near wake region. In–wake power spectral densities of TKE measured behind tractor–trailers and presented in Chapter 2 show a broad peak near f = 2 Hz, corresponding to a wavelength between 10 and 15 m for a 20 to 30 m s^{-1} flow velocity. This wavelength is near the length of the attached trailer, which typically has a span between 10 and 16 m. Chapter 4 also investigated the power spectral density of TKE behind heavy–duty trucks using on–road measurements, but now for a heavy–duty truck that does not have an attached trailer. In this case the broad peak near f = 2 Hz nearly disappears, although the TKE is still significantly enhanced for f > 0.5 Hz compared to background levels. Therefore, when a trailer is attached, in–wake measurements show that the main contributions to vehicle–induced turbulence are eddies with a size near the length of the trailer. Chapter 5 investigated the power spectra of each velocity component as heavy–duty trucks (with trailers) passed the roadside tripod. Compared to background levels, the velocity spectra measured on the tripod (all components) are mainly impacted at f > 0.08 Hz when a heavy–duty truck passes the tripod, which for a horizontal flow velocity between 4 and 5 m s^{-1} corresponds to eddies with wavelengths less than 50 to 60

m, consistent with on–road measurements. However, unlike the TKE spectra measured on–road behind heavy–duty trucks, the velocity spectra calculated 2 to 4 seconds after the truck passes the tripod have a much less distinct peak than on–road measurements. The tripod peak is located near 0.5 Hz and present mainly in v (oriented parallel to the travel direction) and w. For a flow velocity between 4 and 5 m s^{-1} the wavelength of this minor peak is between 8 and 10 m, slightly lower than measured on–road.

Chapter 4 characterized the size of the emitted accumulation mode particles. An abrupt decrease in the total particle number concentration and particle number concentration variance was measured behind heavy–duty vehicles near 50 m, most pronounced behind heavy–duty vehicles with a bottom exhaust. It is interesting to note that this distance is similar to the maximum wavelength noted in the TKE spectra and cospectra of w and N. Measurements behind a commercial bus demonstrate a distinct relationship between CO_2 emission and vehicle acceleration, with CO_2 emission increasing nearly exponentially with increasing vehicle acceleration. Vehicle acceleration is also found to affect the size of emitted accumulation mode particles, with periods of acceleration leading to an increase in the mode diameter of accumulation mode particles measured behind the commercial bus. There is a clear decrease in the mode diameter of accumulation mode particles emitted by heavy–duty diesel vehicles between 2016 and 2019. This decrease in mode diameter corresponds to an increasing percentage of biodiesel being mixed into diesel fuel in Ontario. This study also revealed that there is a large uncertainty in the measured emission factors behind low–emission vehicles, which may be biased high from high–emission plumes that are advected across the highway.

Consistent with past studies (Rao et al. 1978; Chock 1980), Chapter 5 demonstrated that passing heavy–duty trucks induce a significant wake flow, with flow in the wake nearly aligning with the vehicle's travel direction. The flow induced by SUVs and passenger cars is much less significant than heavy–duty trucks. Assuming 900 equally spaced transport trucks per hour travelling in the outermost highway lane (e.g., during peak traffic flow), the tripod measurements of wake induced flow suggests that a maximum of 0.02 kW h of storable energy (per m^2 area swept) is possible when the ambient wind speed is low (near 1 m s^{-1}). This estimate neglects any wake interactions that could possibly result in compounding flow and hence lead to higher flow velocities than measured by the tripod for single isolated vehicles, especially if passenger vehicles travel together in groups with heavy–duty trucks. Thus, if several wind turbines are erected near the highway edge in regions with a high amount of daily transport trucks, it may be possible to store a modest amount of wind energy that could then be used during the nighttime to power street lights, for example.

Future research

The work presented herein has demonstrated the effectiveness of an instrumented mobile car for near–ground atmospheric measurements. This includes use of the instrumented car for specific applications, such as on–road measurement of vehicle wakes and emissions, but also for general investigation of the ambient atmosphere. Future work could use the mobile car for measurements within cities, which is currently an intense area of study with increasing numerical resolution of meteorological and air pollution models. There is still a need to investigate flow distortion effects on the vehicle–measured wind and turbulence quantities, so future wind tunnel and modelling studies investigating flow distortion and its impact on car measurements would be useful. Future work should also investigate the performance of the instrumented car in other meteorological conditions, such as during the nighttime and during very windy conditions.

The instrumented mobile car may be used for other applications aside from air-quality studies. Other possible applications could investigate the placement and effect of buildings, and the wake that develops downwind at pedestrian level (which can negatively affect pedestrian comfort), or to investigate how windbreaks affect the environment downwind and close to the surface (in the vicinity of field crops). Typically, these types of investigations would be done using stationary towers, but an instrumented mobile platform may offer another method to obtain these data, but over a larger domain. Future work could also use the instrumented car for boundary layer studies, such as to investigate flow in complex terrain, study mesoscale fronts such as lake breezes, or examine intermittent turbulence that occurs in isolated locations. On-road measurements using the mobile car may also be tailored toward investigating the drag produced by moving vehicles, which could provide useful data that may help improve vehicle design and thus fuel efficiency. Other vehicle types could also be outfitted with instrumentation, which may allow mobile measurements to be made in locations that are typically difficult to sample using stationary towers, such as within a forest (i.e., using an all-terrain vehicle), or perhaps on frozen lakes (i.e., using a snowmobile).

There is a need for additional in–wake measurements of vehicle–induced turbulence to improve the parameterization of on–road TKE enhancement used in numerical models (Makar, 2021). As discussed in Chapter 2, there is a variation of TKE with height, especially behind large trucks. To fully describe the vertical profile of TKE behind a heavy–duty truck, velocity measurements at other heights are necessary, such as closer to the ground and the region above the truck (> 4 m). Future measurements should also investigate the lateral variation of TKE behind on–road vehicles, which may require more controlled conditions, since for heavy–duty trucks, the wake may spread to fill other highway lanes (Chapter 5). The measurements in this work were obtained in relatively sparse traffic. Therefore, there is a need for measurements in highly dense traffic, where the vehicle flow rate remains high and interaction between different vehicle wakes is significant. The on–road TKE enhancement parameterization outlined in Chapter

2 is based on measurements of near–isolated vehicles, but the decay of TKE with distance and height behind on–road vehicles may change in very dense traffic.

Finally, given the success of vertical flux measurements (aerosols and CO_2) while travelling at high vehicle speeds, future research should continue to investigate the use of an instrumented car for targeted on–road emissions testing. While low–emission vehicles may be problematic to isolate and measure in–situ without interference, the results presented in Chapter 4 suggest that high–emission vehicles are easily identified by in–situ measurements obtained on the instrumented car, suggesting targeting high–emission vehicles is possible. The ability of the system to measure turbulence and pollutant fluxes could be improved by using an array of sonic anemometers and pollutant analyzers to gain a more complete picture of the vehicle wake, and this may provide the data necessary to obtain better estimates of vehicle emissions from on–road, in–situ measurements.

References

Abdul–Khalek, I. S., Kittelson, D. B., Graskow, B. R., Wei, Q., & Bear, F. (1998). Diesel exhaust particle size: Measurement issues and Trends. SAE Technical Paper Series. https://doi.org/10.4271/980525

Achberger, C., & Bärring, L.: Correction of surface air temperature measurements from a mobile platform, Agricultural and Forest Meteorology, 98–99, 227–238, https://doi.org/10.1016/s0168–1923(99)00099–4, 1999.

Ahmed, S. R. (1981). Wake structure of typical automobile shapes. Journal of Fluids Engineering, 103(1), 162–169. https://doi.org/10.1115/1.3240767

Alonso–Estébanez, A., Pascual–Muñoz, P., Yagüe, C., Laina, R., & Castro–Fresno, D. (2012). Field experimental study of traffic–induced turbulence on Highways. Atmospheric Environment, 61, 189–196. https://doi.org/10.1016/j.atmosenv.2012.07.032

Anderson, A. R., Chapman, M., Drobot, S. D., Tadesse, A., Lambi, B., Wiener, G., & Pisano, P.: Quality of mobile air temperature and atmospheric pressure observations from the 2010 Development Test Environment Experiment, Journal of Applied Meteorology and Climatology, 51(4), 691–701, https://doi.org/10.1175/jamc–d–11–0126.1, 2012.

Aristodemou, E., Boganegra, L. M., Mottet, L., Pavlidis, D., Constantinou, A., Pain, C., Robins, A., & ApSimon, H.: How tall buildings affect turbulent air flows and dispersion of pollution within a neighbourhood, Environmental Pollution, 233, 782–796, https://doi.org/10.1016/j.envpol.2017.10.041, 2018.

Armas, O., Gómez, A., Mata, C., & Ramos, A. (2013). Particle size distributions from a city bus fuelled with ethanol–biodiesel–diesel fuel blends. Fuel, 111, 393–400. https://doi.org/10.1016/j.fuel.2013.03.036

Armi, L., & Mayr, G. J.: Continuously stratified flows across an alpine crest with a pass: Shallow and Deep Föhn. Quarterly Journal of the Royal Meteorological Society, 133(623), 459–477, https://doi.org/10.1002/qj.22, 2007.

BAKER, C. J. (2001). Flow and dispersion in ground vehicle wakes. Journal of Fluids and Structures, 15(7), 1031–1060. https://doi.org/10.1006/jfls.2001.0385

Ban–Weiss, G. A., Lunden, M. M., Kirchstetter, T. W., & Harley, R. A. (2009). Measurement of black carbon and particle number emission factors from individual heavy–duty trucks. Environmental Science & Technology, 43(5), 1419–1424. https://doi.org/10.1021/es8021039

Ban–Weiss, G. A., Lunden, M. M., Kirchstetter, T. W., & Harley, R. A. (2010). Size–resolved particle number and volume emission factors for on–road gasoline and diesel motor vehicles. Journal of Aerosol Science, 41(1), 5–12. https://doi.org/10.1016/j.jaerosci.2009.08.001

Bani–Hani, E. H., Sedaghat, A., AL–Shemmary, M., Hussain, A., Alshaieb, A., & Kakoli, H. (2018). Feasibility of highway energy harvesting using a vertical axis wind turbine. Energy Engineering, 115(2), 61–74. https://doi.org/10.1080/01998595.2018.11969276

Bäumer, D., Vogel, B., & Fiedler, F. (2005). A new parameterisation of motorway–induced turbulence and its application in a numerical model. Atmospheric Environment, 39(31), 5750–5759. https://doi.org/10.1016/j.atmosenv.2004.10.046

Bhautmage, U., & Gokhale, S. (2016). Effects of moving–vehicle wakes on pollutant dispersion inside a highway road tunnel. Environmental Pollution, 218, 783–793. https://doi.org/10.1016/j.envpol.2016.08.002

Belušić, D., Lenschow, D. H., & Tapper, N. J.: Performance of a mobile car platform for mean wind and turbulence measurements, Atmospheric Measurement Techniques, 7(6), 1825–1837, https://doi.org/10.5194/amt–7–1825–2014, 2014.

Bogren, J., & Gustavsson, T.: Nocturnal Air and road surface temperature variations in complex terrain, International Journal of Climatology, 11(4), 443–455, https://doi.org/10.1002/joc.3370110408, 2007.

Bonin, T. A., Newman, J. F., Klein, P. M., Chilson, P. B., & Wharton, S.: Improvement of vertical velocity statistics measured by a Doppler lidar through comparison with Sonic Anemometer Observations, Atmospheric Measurement Techniques, 9(12), 5833–5852, https://doi.org/10.5194/amt–9–5833–2016, 2016.

Britter, R. E., Hunt, J. C., & Richards, K. J.: Air flow over a two–dimensional hill: Studies of velocity speed–up, roughness effects and turbulence, Quarterly Journal of the Royal Meteorological Society, 107(451), 91–110, https://doi.org/10.1002/qj.49710745106, 1981.

Bukowiecki, N., Kittelson, D. B., Watts, W. F., Burtscher, H., Weingartner, E., & Baltensperger, U. (2002). Real–time characterization of ultrafine and accumulation mode particles in ambient combustion aerosols. Journal of Aerosol Science, 33(8), 1139–1154. https://doi.org/10.1016/s0021–8502(02)00063–0

Cai, Y., Montague, D. C., Mooiweer–Bryan, W., & Deshler, T. (2008). Performance characteristics of the Ultra High Sensitivity Aerosol Spectrometer for particles between 55 and 800nm: Laboratory and field studies. Journal of Aerosol Science, 39(9), 759–769. https://doi.org/10.1016/j.jaerosci.2008.04.007

Canagaratna, M. R., Jayne, J. T., Ghertner, D. A., Herndon, S., Shi, Q., Jimenez, J. L., Silva, P. J., Williams, P., Lanni, T., Drewnick, F., Demerjian, K. L., Kolb, C. E., & Worsnop, D. R. (2004). Chase Studies of particulate emissions from in–use New York City vehicles. Aerosol Science and Technology, 38(6), 555–573. https://doi.org/10.1080/02786820490465504

Carpentieri, M., Kumar, P., & Robins, A. (2012). Wind tunnel measurements for dispersion modelling of vehicle wakes. Atmospheric Environment, 62, 9–25. https://doi.org/10.1016/j.atmosenv.2012.08.019

Casal, C. S., Arbilla, G., & Corrêa, S. M. (2014). Alkyl polycyclic aromatic hydrocarbons emissions in diesel/biodiesel exhaust. Atmospheric Environment, 96, 107–116. https://doi.org/10.1016/j.atmosenv.2014.07.028

Cassiani, M., Bertagni, M. B., Marro, M., & Salizzoni, P. (2020). Concentration fluctuations from localized atmospheric releases. Boundary–Layer Meteorology, 177(2–3), 461–510. https://doi.org/10.1007/s10546–020–00547–4

Chang, V. W.–C., Hildemann, L. M., & Chang, C.–hisn. (2009). Dilution rates for tailpipe emissions: Effects of vehicle shape, tailpipe position, and exhaust velocity. Journal of the Air & Waste Management Association, 59(6), 715–724. https://doi.org/10.3155/1047–3289.59.6.715

China, S., Salvadori, N., & Mazzoleni, C. (2014). Effect of traffic and driving characteristics on morphology of atmospheric soot particles at freeway on–ramps. Environmental Science & Technology, 48(6), 3128–3135. https://doi.org/10.1021/es405178n

Chock, D. P. (1980). General Motors sulfate dispersion experiment. Boundary–Layer Meteorology, 18(4), 431–451. https://doi.org/10.1007/bf00119498

Chuepeng, S., Xu, H., Tsolakis, A., Wyszynski, M., & Price, P. (2011). Particulate matter size distribution in the exhaust gas of a modern diesel engine fuelled with a biodiesel blend. Biomass and Bioenergy, 35(10), 4280–4289. https://doi.org/10.1016/j.biombioe.2011.07.017

Conte, M., Contini, D., & Held, A.: Multiresolution decomposition and wavelet analysis of urban aerosol fluxes in Italy and Austria, Atmospheric Research, 248, 105267, https://doi.org/10.1016/j.atmosres.2020.105267, 2021.

Commercial vehicle flows by road network. Open Government Portal. Retrieved from https://open.canada.ca/data/en/dataset/44e4631f–152a–4042–a8fd–78965c1a59cf

Curry, M., Hanesiak, J., Kehler, S., Sills, D. M., & Taylor, N. M.: Ground–based observations of the thermodynamic and kinematic properties of Lake–Breeze Fronts in southern Manitoba, Canada, Boundary–Layer Meteorology, 163(1), 143–159, https://doi.org/10.1007/s10546–016–0214–1, 2016.

Dallmann, T. R., DeMartini, S. J., Kirchstetter, T. W., Herndon, S. C., Onasch, T. B., Wood, E. C., & Harley, R. A. (2012). On–road measurement of gas and particle phase pollutant emission factors for individual heavy–duty diesel trucks. Environmental Science & Technology, 46(15), 8511–8518. https://doi.org/10.1021/es301936c

DeCarlo, P., Slowik, J., Worsnop, D., Davidovits, P., & Jimenez, J. (2004). Particle morphology and density characterization by combined mobility and aerodynamic diameter measurements. part 1: Theory. Aerosol Science and Technology, 38(12), 1185–1205. https://doi.org/10.1080/02786826.2004.10399461

de Boer, G., Waugh, S., Erwin, A., Borenstein, S., Dixon, C., Shanti, W., Houston, A., & Argrow, B.: Measurements from mobile surface vehicles during the lower atmospheric profiling studies at elevation – a remotely–piloted aircraft team experiment (lapse–rate), Earth System Science Data, 13(1), 155–169, https://doi.org/10.5194/essd–13–155–2021, 2021.

Ebrahim, H., & Dominy, R. (2020). Wake and surface pressure analysis of vehicles in Platoon. Journal of Wind Engineering and Industrial Aerodynamics, 201, 104144. https://doi.org/10.1016/j.jweia.2020.104144

Edvardsson, K., & Magnusson, R. (2009). Monitoring of dust emission on gravel roads: Development of a mobile methodology and examination of horizontal diffusion. Atmospheric Environment, 43(4), 889–896. https://doi.org/10.1016/j.atmosenv.2008.10.052

EMOS (2016) Environmental Meteorological Observation Station (EMOS), Department of Earth and Space Science and Engineering, York University. [Available online at http://www.yorku.ca/pat/weatherStation/index.php.]

Ermak, D. L. (1977). An analytical model for Air Pollutant Transport and deposition from a point source. Atmospheric Environment (1967), 11(3), 231–237. https://doi.org/10.1016/0004–6981(77)90140–8

Eskridge, R. E., & Hunt, J. C. (1979). Highway modeling. part I: Prediction of velocity and turbulence fields in the wake of vehicles. Journal of Applied Meteorology, 18(4), 387–400. https://doi.org/10.1175/1520–0450(1979)018<0387:hmpipo>2.0.co;2

Eskridge, R. E., & Thompson, R. S. (1982). Experimental and theoretical study of the wake of a block–shaped vehicle in a shear–free boundary flow. Atmospheric Environment (1967), 16(12), 2821–2836. https://doi.org/10.1016/0004–6981(82)90033–6

Eskridge, R. E., Petersen, W. B., & Rao, S. T. (1991). Turbulent diffusion behind vehicles: Effect of traffic speed on pollutant concentrations. Journal of the Air & Waste Management Association, 41(3), 312–317. https://doi.org/10.1080/1047328 Eskridge, R. E., & Trivikrama Rao, S. (1986). Turbulent diffusion behind vehicles: Experimentally determined turbulence mixing parameters. Atmospheric Environment (1967), 20(5), 851–860. https://doi.org/10.1016/0004–6981(86)90269–6

Eskridge, R. E., Binkowski, F. S., Hunt, J. C., Clark, T. L., & Demerjian, K. L. (1979). Highway modeling. part II: Advection and diffusion of SF6tracer gas. Journal of Applied Meteorology, 18(4), 401–412. https://doi.org/10.1175/1520–0450(1979)018<0401:hmpiaa>2.0.co;2

Eskridge, R. E., Petersen, W. B., & Rao, S. T. (1991). Turbulent diffusion behind vehicles: Effect of traffic speed on pollutant concentrations. Journal of the Air & Waste Management Association, 41(3), 312–317. https://doi.org/10.1080/10473289.1991.104668489.1991.10466848

Finkelstein, P. L., & Sims, P. F.: Sampling error in eddy correlation flux measurements. Journal of Geophysical Research: Atmospheres, 106(D4), 3503–3509, https://doi.org/10.1029/2000jd900731, 2001.

Friedlander, S. K., & Wang, C. S. (1966). The self–preserving particle size distribution for coagulation by Brownian motion. Journal of Colloid and Interface Science, 22(2), 126–132. https://doi.org/10.1016/0021–9797(66)90073–7

Gong, W., & Ibbetson, A.: A wind tunnel study of turbulent flow over Model Hills, Boundary–Layer Meteorology, 49(1–2), 113–148, https://doi.org/10.1007/bf00116408, 1989.

GIECHASKIEL, B., NTZIACHRISTOS, L., SAMARAS, Z., SCHEER, V., CASATI, R., & VOGT, R. (2005). Formation potential of vehicle exhaust nucleation mode particles on–road and in the Laboratory. Atmospheric Environment, 39(18), 3191–3198. https://doi.org/10.1016/j.atmosenv.2005.02.019

Göckede, M., Kittler, F., & Schaller, C.: Quantifying the impact of emission outbursts and non–stationary flow on eddy–covariance CH4 flux measurements using wavelet techniques, Biogeosciences, 16(16), 3113–3131, https://doi.org/10.5194/bg–16–3113–2019, 2019.

Gordon, M., Staebler, R. M., Liggio, J., Li, S.–M., Wentzell, J., Lu, G., Lee, P., & Brook, J. R. (2012). Measured and modeled variation in pollutant concentration near roadways. Atmospheric Environment, 57, 138–145. https://doi.org/10.1016/j.atmosenv.2012.04.022

Gordon, M., Staebler, R. M., Liggio, J., Makar, P., Li, S.–M., Wentzell, J., Lu, G., Lee, P., & Brook, J. R.: Measurements of enhanced turbulent mixing near Highways, Journal of Applied Meteorology and Climatology, 51(9), 1618–1632, https://doi.org/10.1175/jamc–d–11–0190.1, 2012.

Grigoratos, T., & Martini, G. (2014). Brake wear particle emissions: A Review. Environmental Science and Pollution Research, 22(4), 2491–2504. https://doi.org/10.1007/s11356–014–3696–8

Gromke, C., & Blocken, B.: Influence of avenue–trees on air quality at the Urban Neighborhood Scale. part I: Quality assurance studies and turbulent schmidt number analysis for RANS CFD Simulations, Environmental Pollution, 196, 214–223, https://doi.org/10.1016/j.envpol.2014.10.016, 2015.

Grønskei, K. E. (1988). The influence of car speed on dispersion of exhaust gases. Atmospheric Environment (1967), 22(2), 273–281. https://doi.org/10.1016/0004–6981(88)90033–9

Guo, Y., Stevanovic, S., Verma, P., Jafari, M., Jabbour, N., Brown, R., Cravigan, L., Alroe, J., Osuagwu, C. G., Brown, R., D'Anna, B., & Ristovski, Z. (2019). An experimental study of the role of biodiesel on the performance of Diesel Particulate Filters. Fuel, 247, 67–76. https://doi.org/10.1016/j.fuel.2019.03.042

Hanlon, T., & Risk, D.: Using computational fluid dynamics and field experiments to improve vehicle–based wind measurements for environmental monitoring, Atmospheric Measurement Techniques, 13(1), 191–203, https://doi.org/10.5194/amt–13–191–2020, 2020.

Hanna, S. R. (1984). Concentration fluctuations in a smoke plume. Atmospheric Environment (1967), 18(6), 1091–1106. https://doi.org/10.1016/0004–6981(84)90141–0

Hanna, S. R. (1984). The exponential probability density function and concentration fluctuations in smoke plumes. Boundary–Layer Meteorology, 29(4), 361–375. https://doi.org/10.1007/bf00120535

Hanna, S. R. (1986). Spectra of concentration fluctuations: The two time scales of a meandering plume. Atmospheric Environment (1967), 20(6), 1131–1137. https://doi.org/10.1016/0004–6981(86)90145–9

Hara, Y., Hara, K., & Hayashi, T. (2012). Moment of inertia dependence of vertical axis wind turbines in pulsating winds. International Journal of Rotating Machinery, 2012, 1–12. https://doi.org/10.1155/2012/910940

Harris, S. J., & Maricq, M. M. (2001). Signature size distributions for diesel and gasoline engine exhaust particulate matter. Journal of Aerosol Science, 32(6), 749–764. https://doi.org/10.1016/s0021–8502(00)00111–7

Harrison, R. M., Rob MacKenzie, A., Xu, H., Alam, M. S., Nikolova, I., Zhong, J., Singh, A., Zeraati–Rezaei, S., Stark, C., Beddows, D. C., Liang, Z., Xu, R., & Cai, X. (2018). Diesel exhaust nanoparticles and their behaviour in the atmosphere. Proceedings of the Royal Society A: Mathematical, Physical and Engineering Sciences, 474(2220), 20180492. https://doi.org/10.1098/rspa.2018.0492

He, M., Huo, S., Hemida, H., Bourriez, F., Robertson, F. H., Soper, D., Sterling, M., & Baker, C. (2019). Detached eddy simulation of a closely running lorry platoon. Journal of Wind Engineering and Industrial Aerodynamics, 193, 103956. https://doi.org/10.1016/j.jweia.2019.103956

Hertwig, D., Gough, H. L., Grimmond, S., Barlow, J. F., Kent, C. W., Lin, W. E., Robins, A. G., & Hayden, P.: Wake characteristics of tall buildings in a realistic urban canopy, Boundary–Layer Meteorology, 172(2), 239–270, https://doi.org/10.1007/s10546–019–00450–7, 2019.

Hinds, W. C. (1999). Aerosol Technology. J. Wiley.

Hoek, G., Krishnan, R. M., Beelen, R., Peters, A., Ostro, B., Brunekreef, B., & Kaufman, J. D. (2013). Long–term air pollution exposure and cardio– respiratory mortality: A Review. Environmental Health, 12(1). https://doi.org/10.1186/1476–069x–12–43

Hosker RP Jr, Rao KS, Gunter RL, Nappo CJ, Meyers TP, Birdwell KR, White JR (2003) Issues affecting dispersion near highways: Light winds, intra–urban dispersion, vehicle wakes, and the ROADWAY–2 Dispersion Model. NOAA Tech. Memo. OAR ARL–247, 197 pp. [Available online at http://www.arl.noaa.gov/documents/reports/arl–247.pdf.]

Howell, S. G., Freitag, S., Dobracki, A., Smirnow, N., & Sedlacek III, A. J. (2021). Undersizing of aged African biomass burning aerosol by an ultra–high–sensitivity aerosol spectrometer. Atmospheric Measurement Techniques, 14(11), 7381–7404. https://doi.org/10.5194/amt–14–7381–2021

Huang, L., Gong, S. L., Gordon, M., Liggio, J., Staebler, R., Stroud, C. A., Lu, G., Mihele, C., Brook, J. R., & Jia, C. Q. (2014). Aerosol–computational fluid dynamics modeling of ultrafine and black carbon particle emission, dilution, and growth near roadways. Atmospheric Chemistry and Physics, 14(23), 12631–12648. https://doi.org/10.5194/acp–14–12631–2014

Huang, Y., Ng, E. C. Y., Surawski, N. C., Yam, Y.–S., Mok, W.–C., Liu, C.–H., Zhou, J. L., Organ, B., & Chan, E. F. C. (2020). Large eddy simulation of vehicle emissions dispersion: Implications for on–road remote sensing measurements. Environmental Pollution, 259, 113974. https://doi.org/10.1016/j.envpol.2020.113974

Hunt, J. C. R., Poulton, E. C., & Mumford, J. C.: The effects of wind on people; new criteria based on wind tunnel experiments, Building and Environment, 11(1), 15–28, https://doi.org/10.1016/0360–1323(76)90015–9, 1976.

Hudda, N., Fruin, S., Delfino, R. J., & Sioutas, C. (2013). Efficient determination of vehicle emission factors by fuel use category using on–road measurements: Downward trends on Los Angeles Freight Corridor I–710. Atmospheric Chemistry and Physics, 13(1), 347–357. https://doi.org/10.5194/acp–13–347–2013

Ježek, I., Katrašnik, T., Westerdahl, D., & Močnik, G. (2015). Black Carbon, particle number concentration and nitrogen oxide emission factors of random in–use vehicles measured with the on–road chasing method. Atmospheric Chemistry and Physics, 15(19), 11011–11026. https://doi.org/10.5194/acp–15–11011–2015

Kalthoff, N., Bäumer, D., Corsmeier, U., Kohler, M., & Vogel, B. (2005). Vehicle–induced turbulence near a motorway. Atmospheric Environment, 39(31), 5737–5749. https://doi.org/10.1016/j.atmosenv.2004.06.048

Kalafut–Pettibone, A. J., Wang, J., Eichinger, W. E., Clarke, A., Vay, S. A., Blake, D. R., & Stanier, C. O. (2011). Size–resolved aerosol emission factors and new particle formation/growth activity occurring in Mexico City during the milagro 2006 campaign. Atmospheric Chemistry and Physics, 11(17), 8861–8881. https://doi.org/10.5194/acp–11–8861–2011

Kaimal JC, Finnigan JJ (1994) Atmospheric boundary layer flows – their structure and measurement. Oxford University Press, New York, USA

Kanda, I., Uehara, K., Yamao, Y., Yoshikawa, Y., & Morikawa, T. (2006). A wind–tunnel study on exhaust gas dispersion from road vehicles—part I: Velocity and concentration fields behind single vehicles. Journal of Wind Engineering and Industrial Aerodynamics, 94(9), 639–658. https://doi.org/10.1016/j.jweia.2005.12.003

Kim, W.–G., Kim, C.–K., Lee, J.–T., Kim, J.–S., Yun, C.–W., & Yook, S.–J. (2017). Fine particle emission characteristics of a light–duty diesel vehicle according to Vehicle Acceleration and Road Grade. Transportation Research Part D: Transport and Environment, 53, 428–439. https://doi.org/10.1016/j.trd.2017.04.041

Kim, Yesul, Huang Li, Gong Sunling, Jia, Q., C.: A new approach to quantifying vehicle induced turbulence for complex traffic scenarios, Chinese Journal of Chemical Engineering, (1)(24), 71–78, https://doi.org/10.1016/j.cjche.2015.11.025, 2018.

Kim, M. Y., Yoon, S. H., Hwang, J. W., & Lee, C. S. (2007). Characteristics of particulate emissions of compression ignition engine fueled with biodiesel derived from soybean. ASME 2007 Internal Combustion Engine Division Fall Technical Conference. https://doi.org/10.1115/icef2007–1715

Kittelson, D. B., Watts, W. F., & Johnson, J. P. (2006). On–road and laboratory evaluation of combustion aerosols—PART1: Summary of diesel engine results. Journal of Aerosol Science, 37(8), 913–930. https://doi.org/10.1016/j.jaerosci.2005.08.005

Kittelson, D. B., Watts, W. F., & Johnson, J. P. (2004). Nanoparticle emissions on Minnesota Highways. Atmospheric Environment, 38(1), 9–19. https://doi.org/10.1016/j.atmosenv.2003.09.037

Kittelson, D., & Kraft, M. (2014). Particle formation and models. Encyclopedia of Automotive Engineering, 1–23. https://doi.org/10.1002/9781118354179.auto161

Kittelson, D., Johnson, J., Watts, W., Wei, Q., Drayton, M., Paulsen, D., & Bukowiecki, N. (2000). Diesel aerosol sampling in the atmosphere. SAE Technical Paper Series. https://doi.org/10.4271/2000–01–2212

Kittelson, D., Khalek, I., McDonald, J., Stevens, J., & Giannelli, R. (2022). Particle emissions from mobile sources: Discussion of ultrafine particle emissions and definition. Journal of Aerosol Science, 159, 105881. https://doi.org/10.1016/j.jaerosci.2021.105881

Klein, P. K., Berkowicz, R., & Plate, E. J. (2000). Modelling of vehicle–induced turbulence in air pollution studies for Streets. International Journal of Environment and Pollution, 14(1/2/3/4/5/6), 496. https://doi.org/10.1504/ijep.2000.000573

Kljun, N., Calanca, P., Rotach, M. W., & Schmid, H. P.: A simple two–dimensional parameterisation for Flux Footprint Prediction (FFP), Geoscientific Model Development, 8(11), 3695–3713, https://doi.org/10.5194/gmd–8–3695–2015, 2015.

Kolb, C. E., Herndon, S. C., McManus, J. B., Shorter, J. H., Zahniser, M. S., Nelson, D. D., Jayne, J. T., Canagaratna, M. R., & Worsnop, D. R. (2004). Mobile Laboratory with Rapid Response Instruments for real–time measurements of urban and regional trace gas and particulate distributions and emission source characteristics. Environmental Science & Technology, 38(21), 5694–5703. https://doi.org/10.1021/es030718p

Krayenhoff, E. S., Jiang, T., Christen, A., Martilli, A., Oke, T. R., Bailey, B. N., Nazarian, N., Voogt, J. A., Giometto, M. G., Stastny, A., & Crawford, B. R.: A multi–layer urban canopy meteorological model with trees (BEP–tree): Street tree impacts on pedestrian–level climate, Urban Climate, 32, 100590, https://doi.org/10.1016/j.uclim.2020.100590, 2020.

Langford, B., Acton, W., Ammann, C., Valach, A., & Nemitz, E.: Eddy–covariance data with low signal–to–noise ratio: Time–lag determination, uncertainties and limit of detection, Atmospheric Measurement Techniques, 8(10), 4197–4213, https://doi.org/10.5194/amt–8–4197–2015, 2015.

Lapuerta, M., Armas, O., & Gómez, A. (2003). Diesel particle size distribution estimation from Digital Image Analysis. Aerosol Science and Technology, 37(4), 369–381. https://doi.org/10.1080/02786820300970

Lapointe, C., & Gopalan, H. (2016). Numerical investigation of mini wind turbines near Highways. Journal of Solar Energy Engineering, 138(2). https://doi.org/10.1115/1.4032428

Larson, T., Gould, T., Riley, E. A., Austin, E., Fintzi, J., Sheppard, L., Yost, M., & Simpson, C. (2017). Ambient air quality measurements from a continuously moving mobile platform: Estimation of area–wide, fuel–based, mobile source emission factors using absolute principal component scores. Atmospheric Environment, 152, 201–211. https://doi.org/10.1016/j.atmosenv.2016.12.037

Lee J, Choi H (2009) Large eddy simulation of flow over a three–dimensional model vehicle. Sixth international symposium on turbulence and shear flow phenomena, 22–24 June, 2009, Seoul, South Korea.

Lee, J. P., & Lee, S. J.: PIV analysis on the shelter effect of a bank of real fir trees, Journal of Wind Engineering and Industrial Aerodynamics, 110, 40–49, https://doi.org/10.1016/j.jweia.2012.07.003, 2012.

Lenschow, D. H., Mann, J., & Kristensen, L.: How long is long enough when measuring fluxes and other turbulence statistics? Journal of Atmospheric and Oceanic Technology, 11(3), 661–673, https://doi.org/10.1175/1520–0426(1994)011<0661:hlilew>2.0.co;2, 1994.

Lenschow, D. H., Wulfmeyer, V., & Senff, C.: Measuring second– through fourth–order moments in Noisy Data, Journal of Atmospheric and Oceanic Technology, 17(10), 1330–1347, https://doi.org/10.1175/1520–0426(2000)017<1330:mstfom>2.0.co;2, 2000.

Liggio, J., Gordon, M., Smallwood, G., Li, S.–M., Stroud, C., Staebler, R., Lu, G., Lee, P., Taylor, B., & Brook, J. R. (2012). Are emissions of black carbon from gasoline vehicles underestimated? insights from near and on–road measurements. Environmental Science & Technology, 46(9), 4819–4828. https://doi.org/10.1021/es2033845

Lu, C., Wang, X., Dong, S., Zhang, J., Li, J., Zhao, Y., Liang, Y., Xue, L., Xie, H., Zhang, Q., & Wang, W. (2019). Emissions of fine particulate nitrated phenols from various on–road vehicles in China. Environmental Research, 179, 108709. https://doi.org/10.1016/j.envres.2019.108709

Lo, K. H., & Kontis, K. (2017). Flow around an articulated lorry model. Experimental Thermal and Fluid Science, 82, 58–74. https://doi.org/10.1016/j.expthermflusci.2016.11.003

Lushi, E., & Stockie, J. M. (2010). An inverse gaussian plume approach for estimating atmospheric pollutant emissions from multiple point sources. Atmospheric Environment, 44(8), 1097–1107. https://doi.org/10.1016/j.atmosenv.2009.11.039

Lyu, J., Wang, C. M., & Mason, M. S.: Review of models for predicting wind characteristics behind windbreaks, Journal of Wind Engineering and Industrial Aerodynamics, 199, 104117, https://doi.org/10.1016/j.jweia.2020.104117, 2017.

Mahrt, L., Richardson, S., Seaman, N., & Stauffer, D.: Turbulence in the nocturnal boundary layer with light and variable winds, Quarterly Journal of the Royal Meteorological Society, 138(667), 1430–1439, https://doi.org/10.1002/qj.1884, 2012.

Makar, P. A., Stroud, C., Akingunola, A., Zhang, J., Ren, S., Cheung, P., & Zheng, Q. (2021). Vehicle–induced turbulence and atmospheric pollution. Atmospheric Chemistry and Physics, 21(16), 12291–12316. https://doi.org/10.5194/acp–21–12291–2021

Makar, P. A., Zhang, J., Gong, W., Stroud, C., Sills, D., Hayden, K. L., Brook, J., Levy, I., Mihele, C., Moran, M. D., Tarasick, D. W., He, H., & Plummer, D. (2010). Mass tracking for chemical analysis: The causes of ozone formation in southern Ontario during BAQS–Met 2007. Atmospheric Chemistry and Physics, 10(22), 11151–11173. https://doi.org/10.5194/acp–10–11151–2010

Mann, J., & Lenschow, D. H.: Errors in airborne flux measurements, Journal of Geophysical Research, 99(D7), 14519, https://doi.org/10.1029/94jd00737, 1994.

Manwell, J. F., G., M. G. J., & Rogers, A. L. (2002). Wind Energy explained. John Wiley & Sons.

Markowski, P. M., Lis, N. T., Turner, D. D., Lee, T. R., & Buban, M. S.: Observations of near–surface vertical wind profiles and vertical momentum fluxes from vortex–SE 2017: Comparisons to Monin–Obukhov similarity theory, Monthly Weather Review, 147(10), 3811–3824, https://doi.org/10.1175/mwr–d–19–0091.1, 2019.

Mathissen, M., Scheer, V., Vogt, R., & Benter, T. (2011). Investigation on the potential generation of ultrafine particles from the tire–road interface. Atmospheric Environment, 45(34), 6172–6179. https://doi.org/10.1016/j.atmosenv.2011.08.032

Mauder, M., Eggert, M., Gutsmuths, C., Oertel, S., Wilhelm, P., Voelksch, I., Wanner, L., Tambke, J., & Bogoev, I.: Comparison of turbulence measurements by a CSAT3B sonic anemometer and a high–resolution bistatic Doppler lidar, Atmospheric Measurement Techniques, 13(2), 969–983, https://doi.org/10.5194/amt–13–969–2020, 2020.

Maricq, M. (2007). Chemical Characterization of particulate emissions from Diesel Engines: A Review. Journal of Aerosol Science, 38(11), 1079–1118. https://doi.org/10.1016/j.jaerosci.2007.08.001

Maricq, M. M., & Xu, N. (2004). The effective density and fractal dimension of soot particles from premixed flames and motor vehicle exhaust. *Journal of Aerosol Science*, *35*(10), 1251–1274. https://doi.org/10.1016/j.jaerosci.2004.05.002

Mayr, G. J., & Armi, L.: Föhn as a response to changing upstream and downstream air masses, Quarterly Journal of the Royal Meteorological Society, 134(635), 1357–1369, https://doi.org/10.1002/qj.295, 2008.

McArthur, D., Burton, D., Thompson, M., & Sheridan, J. (2016). On the near wake of a simplified heavy vehicle. Journal of Fluids and Structures, 66, 293–314. https://doi.org/10.1016/j.jfluidstructs.2016.07.011

Mejia Lopez, O. D., Ardila Gómez, S. A., Blanco Otero, D. E., & Muñoz Camargo, L. E. (2016). Analysis of the vorticity in the near wake of a station wagon. Journal of Fluids Engineering, 139(2). https://doi.org/10.1115/1.4034523

Miller, S., & Gordon, M. (2022). The measurement of mean wind, variances and covariances from an instrumented mobile car in a rural environment. https://doi.org/10.5194/amt–2022–163

Miller, S. J., Gordon, M., Staebler, R. M., & Taylor, P. A.: A study of the spatial variation of vehicle–induced turbulence on highways using measurements from a mobile platform, Boundary–Layer Meteorology, 171(1), 1–29, https://doi.org/10.1007/s10546–018–0416–9, 2019.

Ministry of the Environment and Climate Change, Ontario. (2016, December). Guide and director's directions – Renewable Fuel Content Requirements for Petroleum Diesel Fuel. Government of Ontario. Retrieved July 2, 2022, from http://www.downloads.ene.gov.on.ca/envision/env_reg/er/documents/2015/012–4413_FinalGuide.pdf

Mochida, A., Tabata, Y., Iwata, T., & Yoshino, H.: Examining tree canopy models for CFD prediction of wind environment at pedestrian level, Journal of Wind Engineering and Industrial Aerodynamics, 96(10–11), 1667–1677, https://doi.org/10.1016/j.jweia.2008.02.055, 2008.

Mohan, M. (1998). Analysis of various schemes for the estimation of Atmospheric Stability Classification. Atmospheric Environment, 32(21), 3775–3781. https://doi.org/10.1016/s1352–2310(98)00109–5

Moore, R. H., Wiggins, E. B., Ahern, A. T., Zimmerman, S., Montgomery, L., Campuzano Jost, P., Robinson, C. E., Ziemba, L. D., Winstead, E. L., Anderson, B. E., Brock, C. A., Brown, M. D., Chen, G., Crosbie, E. C., Guo, H., Jimenez, J. L., Jordan, C. E., Lyu, M., Nault, B. A., … Wang, J. (2021). Sizing response of the ultra–high sensitivity aerosol spectrometer (UHSAS) and Laser Aerosol Spectrometer (LAS) to changes in submicron aerosol composition and refractive index. Atmospheric Measurement Techniques, 14(6), 4517–4542. https://doi.org/10.5194/amt–14–4517–2021

Moosmüller, H., Gillies, J. A., Rogers, C. F., DuBois, D. W., Chow, J. C., Watson, J. G., & Langston, R. (1998). Particulate emission rates for unpaved shoulders along a paved road. Journal of the Air & Waste Management Association, 48(5), 398–407. https://doi.org/10.1080/10473289.1998.10463694

MTO (2016) Provincial highways: Traffic volumes – King's highways / secondary highways / tertiary roads: 1988–2016. Ministry of Transportation, Highway Standards Branch, Traffic Office. 1509 pp.

MTO ICORRIDOR. MTO iCorridor. (2021, July 16). Retrieved from https://icorridor–mto–on–ca.hub.arcgis.com/

Mylne, K. R., & Mason, P. J. (1991). Concentration fluctuation measurements in a dispersing plume at a range of up to 1000 m. Quarterly Journal of the Royal Meteorological Society, 117(497), 177–206. https://doi.org/10.1002/qj.49711749709

Nazari, S. (2020). Power Generation from Localized Wind Energy on Highways using Vertical Axis Wind Turbines (thesis, University of British Columbia).

Olfert, J. S., Symonds, J. P. R., & Collings, N. (2007). The effective density and fractal dimension of particles emitted from a light–duty diesel vehicle with a diesel oxidation catalyst. Journal of Aerosol Science, 38(1), 69–82. https://doi.org/10.1016/j.jaerosci.2006.10.002

Pagán, J. (1999). Study of particle size distributions emitted by a diesel engine. SAE Technical Paper Series. https://doi.org/10.4271/1999–01–1141

Pang, X., & Mu, Y. (2007). Characteristics of carbonyl compounds in public vehicles of Beijing City: Concentrations, sources, and personal exposures. Atmospheric Environment, 41(9), 1819–1824. https://doi.org/10.1016/j.atmosenv.2006.10.057

Park, K., Cao, F., Kittelson, D. B., & McMurry, P. H. (2002). Relationship between particle mass and mobility for diesel exhaust particles. Environmental Science & Technology, 37(3), 577–583. https://doi.org/10.1021/es025960v

Park, S. S., Kozawa, K., Fruin, S., Mara, S., Hsu, Y.–K., Jakober, C., Winer, A., & Herner, J. (2011). Emission factors for high–emitting vehicles based on on–road measurements of individual vehicle exhaust with a mobile measurement platform. Journal of the Air & Waste Management Association, 61(10), 1046–1056. https://doi.org/10.1080/10473289.2011.595981

Paterna, E., Crivelli, P., & Lehning, M.: Decoupling of mass flux and turbulent wind fluctuations in drifting snow, Geophysical Research Letters, 43(9), 4441–4447, https://doi.org/10.1002/2016gl068171, 2016.

Perrone, M. G., Carbone, C., Faedo, D., Ferrero, L., Maggioni, A., Sangiorgi, G., & Bolzacchini, E. (2014). Exhaust emissions of polycyclic aromatic hydrocarbons, n–alkanes and phenols from vehicles coming within different European classes. Atmospheric Environment, 82, 391–400. https://doi.org/10.1016/j.atmosenv.2013.10.040

PIRJOLA, L. (2004). ?sniffer??a novel tool for chasing vehicles and measuring traffic pollutants. Atmospheric Environment. https://doi.org/10.1016/s1352–2310(04)00333–4

Pope III, C. A. (2002). Lung cancer, cardiopulmonary mortality, and long–term exposure to Fine Particulate Air Pollution. JAMA, 287(9), 1132. https://doi.org/10.1001/jama.287.9.1132

Rakha, H., Lucic, I., Demarchi, S. H., Setti, J. R., & Aerde, M. V. (2001). Vehicle Dynamics Model for predicting maximum truck acceleration levels. Journal of Transportation Engineering, 127(5), 418–425. https://doi.org/10.1061/(asce)0733–947x(2001)127:5(418)

Rannik, Ü., Peltola, O., & Mammarella, I.: Random uncertainties of flux measurements by the eddy covariance technique, Atmospheric Measurement Techniques, 9(10), 5163–5181, https://doi.org/10.5194/amt–9–5163–2016, 2016.

Rao, K. S., Gunter, R. L., White, J. R., & Hosker, R. P. (2002). Turbulence and dispersion modeling near Highways. Atmospheric Environment, 36(27), 4337–4346. https://doi.org/10.1016/s1352–2310(02)00353–9

Rao, T. S., Sedefian, L., & Czapski, U. H. (1979). Characteristics of turbulence and dispersion of pollutants near major highways. Journal of Applied Meteorology, 18(3), 283–293. https://doi.org/10.1175/1520–0450(1979)018<0283:cotado>2.0.co;2

RISTOVSKI, Z., MILJEVIC, B., SURAWSKI, N., MORAWSKA, L., FONG, K., GOH, F., & YANG, I. (2012). Respiratory health effects of diesel particulate matter. Respirology, 17(2), 201–212. https://doi.org/10.1111/j.1440–1843.2011.02109.x

Rönkkö, T., Virtanen, A., Vaaraslahti, K., Keskinen, J., Pirjola, L., & Lappi, M. (2006). Effect of dilution conditions and driving parameters on nucleation mode particles in diesel exhaust: Laboratory and on–road study. Atmospheric Environment, 40(16), 2893–2901. https://doi.org/10.1016/j.atmosenv.2006.01.002

Sabaliauskas, K., Jeong, C.–H., Yao, X., Jun, Y.–S., Jadidian, P., & Evans, G. J. (2012). Five–year roadside measurements of ultrafine particles in a major Canadian city. Atmospheric Environment, 49, 245–256. https://doi.org/10.1016/j.atmosenv.2011.11.052

Salmond, J. A.: Wavelet analysis of intermittent turbulence in a very stable nocturnal boundary layer: Implications for the vertical mixing of ozone, Boundary–Layer Meteorology, 114(3), 463–488, https://doi.org/10.1007/s10546–004–2422–3, 2005.

Salmond, J. A., & McKendry, I. G.: A review of turbulence in the very stable nocturnal boundary layer and its implications for Air Quality, Progress in Physical Geography: Earth and Environment, 29(2), 171–188, https://doi.org/10.1191/0309133305pp442ra, 2005.

Schaller, C., Göckede, M., & Foken, T.: Flux calculation of short turbulent events – comparison of three methods, Atmospheric Measurement Techniques, 10(3), 869–880, https://doi.org/10.5194/amt–10–869–2017, 2017.

Schiehlen, W.: White noise excitation of road vehicle structures, Sadhana, 31(4), 487–503, https://doi.org/10.1007/bf02716788, 2006.

Sedefian, L., Trivikrama Rao, S., & Czapski, U. (1981). Effects of traffic–generated turbulence on near–field dispersion. Atmospheric Environment (1967), 15(4), 527–536. https://doi.org/10.1016/0004–6981(81)90182–7

Sistla, G., Samson, P., Keenan, M., & Rao, S. T. (1979). A study of pollutant dispersion near Highways. Atmospheric Environment (1967), 13(5), 669–685. https://doi.org/10.1016/0004–6981(79)90196–3

Smith, S. A., Brown, A. R., Vosper, S. B., Murkin, P. A., & Veal, A. T.: Observations and simulations of cold air pooling in Valleys, Boundary–Layer Meteorology, 134(1), 85–108, https://doi.org/10.1007/s10546–009–9436–9, 2009.

Starkenburg, D., Metzger, S., Fochesatto, G. J., Alfieri, J. G., Gens, R., Prakash, A., & Cristóbal, J.: Assessment of despiking methods for turbulence data in Micrometeorology, Journal of Atmospheric and Oceanic Technology, 33(9), 2001–2013, https://doi.org/10.1175/jtech–d–15–0154.1, 2016.

Sterken, L., Sebben, S., & Löfdahl, L. (2016). Numerical implementation of detached–eddy simulation on a passenger vehicle and some experimental correlation. Journal of Fluids Engineering, 138(9). https://doi.org/10.1115/1.4033296

Straka, J. M., Rasmussen, E. N., & Fredrickson, S. E.: A mobile mesonet for Finescale Meteorological Observations, Journal of Atmospheric and Oceanic Technology, 13(5), 921–936, https://doi.org/10.1175/1520–0426(1996)013<0921:ammffm>2.0.co;2, 1996.

Strunin, M. A., & Hiyama, T.: Applying wavelet transforms to analyse aircraft–measured turbulence and turbulent fluxes in the atmospheric boundary layer over Eastern Siberia, Hydrological Processes, 18(16), 3081–3098, https://doi.org/10.1002/hyp.5750, 2004.

Su, J., Wang, L., Gu, Z., Song, M., & Cao, Z.: Effects of real trees and their structure on pollutant dispersion and flow field in an idealized Street Canyon, Atmospheric Pollution Research, 10(6), 1699–1710, https://doi.org/10.1016/j.apr.2019.07.001, 2019.

Taylor, P. A., & Salmon, J. R.: A model for the correction of surface wind data for sheltering by upwind obstacles, Journal of Applied Meteorology, 32(11), 1683–1694, https://doi.org/10.1175/1520–0450(1993)032<1683:amftco>2.0.co;2, 1993.

Taylor, N. M., Sills, D. M., Hanesiak, J. M., Milbrandt, J. A., Smith, C. D., Strong, G. S., Skone, S. H., McCarthy, P. J., & Brimelow, J. C.: The understanding severe thunderstorms and Alberta Boundary Layers Experiment (unstable) 2008, Bulletin of the American Meteorological Society, 92(6), 739–763, https://doi.org/10.1175/2011bams2994.1, 2011.

Thompson, R. S., & Eskridge, R. E. (1987). Turbulent diffusion behind vehicles: Experimentally determined influence of Vortex Pair in vehicle wake. Atmospheric Environment (1967), 21(10), 2091–2097. https://doi.org/10.1016/0004–6981(87)90343–x

Tian, W., Song, B., & Mao, Z. (2020). Numerical investigation of wind turbines and turbine arrays on Highways. Renewable Energy, 147, 384–398. https://doi.org/10.1016/j.renene.2019.08.123

Tiong, Y. K., Zahari, M. A., Wong, S. F., & Dol, S. S. (2015). The feasibility of wind and solar energy application for oil and gas offshore platform. IOP Conference Series: Materials Science and Engineering, 78, 012042. https://doi.org/10.1088/1757-899x/78/1/012042

Torrence, C., & Compo, G. P.: A practical guide to wavelet analysis, Bulletin of the American Meteorological Society, 79(1), 61–78, https://doi.org/10.1175/1520–0477(998)079<0061:apgtwa>2.0.co;2, 1998.

Trivikrama Rao, S., Sedefian, L., & Czapski, U. H. (1979). Characteristics of turbulence and dispersion of pollutants near major highways. Journal of Applied Meteorology, 18(3), 283–293. https://doi.org/10.1175/1520–0450(1979)018<0283:cotado>2.0.co;2

Turner, D, B.,: Comparison of three methods for calculating the standard deviation of the wind direction, Journal of Climate and Applied Meteorology, 25(5), 703–707, https://doi.org/10.1175/1520–0450(1986)025<0703:cotmfc>2.0.co;2, 1986.

Van de Wiel, B. J., Moene, A. F., Jonker, H. J., Baas, P., Basu, S., Donda, J. M., Sun, J., & Holtslag, A. A.: The minimum wind speed for sustainable turbulence in the nocturnal boundary layer, Journal of the Atmospheric Sciences, 69(11), 3116–3127, https://doi.org/10.1175/jas–d–12–0107.1, 2012.

Virtanen, A. K., Ristimäki, J. M., Vaaraslahti, K. M., & Keskinen, J. (2004). Effect of engine load on diesel soot particles. Environmental Science & Technology, 38(9), 2551–2556. https://doi.org/10.1021/es035139z

von der Heyden, L., Deventer, M. J., Graus, M., Karl, T., Lamprecht, C., & Held, A.: Aerosol particles during the Innsbruck Air Quality Study (INNAQS): The impact of transient fluxes on total aerosol number exchange, Atmospheric Environment, 190, 389–400, https://doi.org/10.1016/j.atmosenv.2018.07.041, 2018.

von der Weiden, S.–L., Drewnick, F., & Borrmann, S. (2009). Particle loss calculator – a new software tool for the assessment of the performance of Aerosol Inlet Systems. Atmospheric Measurement Techniques, 2(2), 479–494. https://doi.org/10.5194/amt–2–479–2009

Wang, J. M., Jeong, C.–H., Zimmerman, N., Healy, R. M., Wang, D. K., Ke, F., & Evans, G. J. (2015). Plume–based analysis of Vehicle Fleet Air Pollutant Emissions and the contribution from high emitters. Atmospheric Measurement Techniques, 8(8), 3263–3275. https://doi.org/10.5194/amt–8–3263–2015

Wang, J., & Rakha, H. A. (2017). Fuel consumption model for heavy duty diesel trucks: Model Development and testing. Transportation Research Part D: Transport and Environment, 55, 127–141. https://doi.org/10.1016/j.trd.2017.06.011

Wang, S., & Wang, X. (2021). Modeling and analysis of highway emission dispersion due to noise barrier and automobile wake effects. Atmospheric Pollution Research, 12(1), 67–75. https://doi.org/10.1016/j.apr.2020.08.013

Wang, Y. J., & Zhang, K. M. (2009). Modeling near–road air quality using a computational fluid dynamics model, CFD–Vit–Rit. Environmental Science & Technology, 43(20), 7778–7783. https://doi.org/10.1021/es9014844

Wang, Y. J., & Zhang, K. M. (2012). Coupled turbulence and aerosol dynamics modeling of vehicle exhaust plumes using the CTAG model. Atmospheric Environment, 59, 284–293. https://doi.org/10.1016/j.atmosenv.2012.04.062

Wang, Y. J., DenBleyker, A., McDonald–Buller, E., Allen, D., & Zhang, K. M. (2011). Modeling the chemical evolution of Nitrogen Oxides near roadways. Atmospheric Environment, 45(1), 43–52. https://doi.org/10.1016/j.atmosenv.2010.09.050

Wang JY, Yang CH, Hu XJ, Guo B (2013) Aerodynamic optimization of a simplified SUV. Fourth international conference on digital manufacturing and automation, 29–30 June, 2013, Qindao, Shandong, China.

Webb, E. K., Pearman, G. I., & Leuning, R. (1980). Correction of flux measurements for density effects due to heat and water vapour transfer. Quarterly Journal of the Royal Meteorological Society, 106(447), 85–100. https://doi.org/10.1002/qj.49710644707

White, L. D.: Mobile observations of a quasi–frontal transient moisture boundary in the Deep South, Weather and Forecasting, 29(6), 1356–1373, https://doi.org/10.1175/waf–d–14–00009.1, 2014.

Wilczak, J. M., Oncley, S. P., & Stage, S. A.: Sonic anemometer tilt correction algorithms, Boundary–Layer Meteorology, 99(1), 127–150, https://doi.org/10.1023/a:1018966204465, 2001.

Williams, D. S., Shukla, M. K., & Ross, J. (2008). Particulate matter emission by a vehicle running on Unpaved Road. Atmospheric Environment, 42(16), 3899–3905. https://doi.org/10.1016/j.atmosenv.2008.02.003

Wilson, D. J., Robins, A. G., & Fackrell, J. E. (1985). Intermittency and conditionally–averaged concentration fluctuation statistics in plumes. Atmospheric Environment (1967), 19(7), 1053–1064. https://doi.org/10.1016/0004–6981(85)90189–1

Wren, S. N., Liggio, J., Han, Y., Hayden, K., Lu, G., Mihele, C. M., Mittermeier, R. L., Stroud, C., Wentzell, J. J., & Brook, J. R. (2018). Elucidating real–world vehicle emission factors from mobile measurements over a large metropolitan region: A focus on isocyanic acid, hydrogen cyanide, and Black Carbon. Atmospheric Chemistry and Physics, 18(23), 16979–17001. https://doi.org/10.5194/acp–18–16979–2018

Wulfmeyer, V., Pal, S., Turner, D. D., & Wagner, E.: Can water vapour raman lidar resolve profiles of turbulent variables in the convective boundary layer? Boundary–Layer Meteorology, 136(2), 253–284, https://doi.org/10.1007/s10546–010–9494–z, 2010.

Wyngaard, J. C.: The effects of probe–induced flow distortion on atmospheric turbulence measurements: Extension to scalars, Journal of the Atmospheric Sciences, 45(22), 3400–3412, https://doi.org/10.1175/1520–0469(1988)045<3400:teopif>2.0.co;2, 1988.

Xie, J., Liu, C.–H., Mo, Z., Huang, Y., & Mok, W.–C. (2020). Near–field dynamics and plume dispersion after an on–road truck: Implication to remote sensing. Science of The Total Environment, 748, 141211. https://doi.org/10.1016/j.scitotenv.2020.141211

Xue, J., Li, Y., Wang, X., Durbin, T. D., Johnson, K. C., Karavalakis, G., Asa–Awuku, A., Villela, M., Quiros, D., Hu, S., Huai, T., Ayala, A., & Jung, H. S. (2015). Comparison of vehicle exhaust particle size distributions measured by SMPS and EEPS during steady–state conditions. Aerosol Science and Technology, 49(10), 984–996. https://doi.org/10.1080/02786826.2015.1088146

Yli–Tuomi, T., Aarnio, P., Pirjola, L., Mäkelä, T., Hillamo, R., & Jantunen, M. (2005). Emissions of fine particles, NOx, and co from on–road vehicles in Finland. Atmospheric Environment, 39(35), 6696–6706. https://doi.org/10.1016/j.atmosenv.2005.07.049

Yokelson, R. J., Burling, I. R., Urbanski, S. P., Atlas, E. L., Adachi, K., Buseck, P. R., Wiedinmyer, C., Akagi, S. K., Toohey, D. W., & Wold, C. E. (2011). Trace gas and particle emissions from open biomass burning in Mexico. Atmospheric Chemistry and Physics, 11(14), 6787–6808. https://doi.org/10.5194/acp–11–6787–2011

Young, L.–H., Liou, Y.–J., Cheng, M.–T., Lu, J.–H., Yang, H.–H., Tsai, Y. I., Wang, L.–C., Chen, C.–B., & Lai, J.–S. (2012). Effects of biodiesel, engine load and diesel particulate filter on nonvolatile particle number size

distributions in heavy–duty diesel engine exhaust. Journal of Hazardous Materials, 199–200, 282–289. https://doi.org/10.1016/j.jhazmat.2011.11.014

Yu, Y., Liu, J., Chauhan, K., de Dear, R., & Niu, J.: Experimental study on convective heat transfer coefficients for the human body exposed to turbulent wind conditions, Building and Environment, 169, 106533, https://doi.org/10.1016/j.buildenv.2019.106533, 2020.

Zimmerman, N., Wang, J. M., Jeong, C.–H., Ramos, M., Hilker, N., Healy, R. M., Sabaliauskas, K., Wallace, J. S., & Evans, G. J. (2016). Field measurements of gasoline direct injection emission factors: Spatial and seasonal variability. Environmental Science & Technology, 50(4), 2035–2043. https://doi.org/10.1021/acs.est.5b04444

Appendix A: Following distance calculation

Figure A–1 displays the pixel geometry and Fig. A–2 displays the physical geometry. In Fig. A–1, P_H is the pixel distance between the attachment points on the hood of the sport utility vehicle, (corresponding to the physical distance Y_H in Fig. A–2) and P_r is the pixel width of the road (corresponding to physical road width Y_r in Fig. A–2). Noting that the ratio between P_H and the image width W (Fig. A–1) is equal to the ratio between Y_H and the width of the field of view at this location, $Y_{W,H}$ (Fig. A–2) gives

$$\frac{Y_H}{Y_{W,H}} = \frac{P_H}{W}. \tag{A1}$$

Likewise, the ratio between P_r (at the location of the vehicle's shadow) and the image width W (Fig. A–1) is equal to the ratio between road width Y_r and the width of the field of view at this location $Y_{W,r}$ (Fig. A–2),

$$\frac{Y_r}{Y_{W,r}} = \frac{P_r}{W}. \tag{A2}$$

From Fig. A–2, similar triangles gives

$$\frac{Y_{W,H}}{X_H} = \frac{Y_{W,r}}{x_m}, \tag{A3}$$

where x_m is the following distance and X_H is the measured distance between the dashcam and the attachment points at the front of the vehicle (see Fig. 2.3). Using Eq. A1 and Eq. A2 in Eq. A3 yields

$$\frac{Y_H W}{P_H X_H} = \frac{Y_r W}{P_r x_m}. \tag{A4}$$

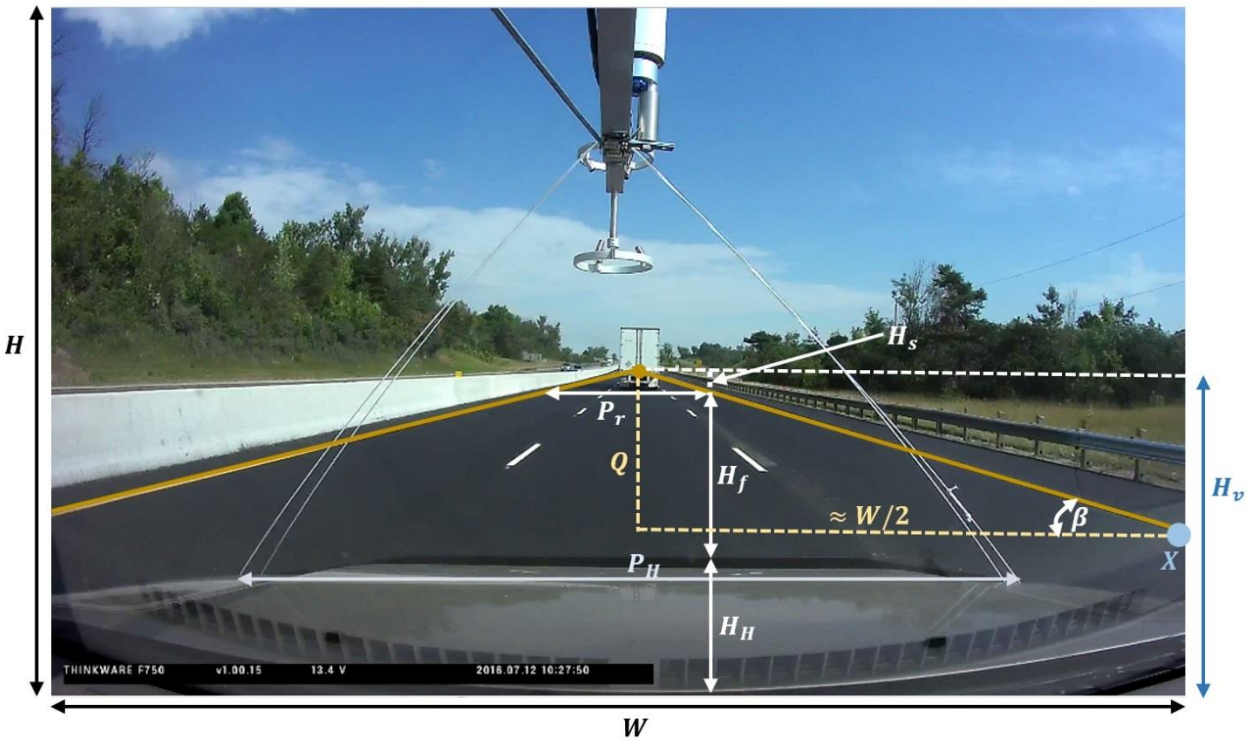

Figure A–1: A still image while vehicle chasing a HD–B truck on 12 July. Superimposed is the pixel geometry used to estimate the following distance. All distances in this image are in units of pixels (px). Automated software was developed to determine the value of $H_f + H_H$. The red circle represents the location of the vanishing point.

Noting that the highway intersects the image frame at X (see Fig. A.1) which is also equal to image frame width, W, then

$$\frac{Q}{W} = \frac{H_s}{P_r} \Longrightarrow P_r = \frac{WH_s}{Q}, \tag{A5}$$

where H_s is the pixel difference between the vanishing point H_v and the target distance $H_f + H_H$ (at location P_r) and Q is the distance in pixels between W (denoted $W/2$ in Fig. A–1) and the vanishing point.

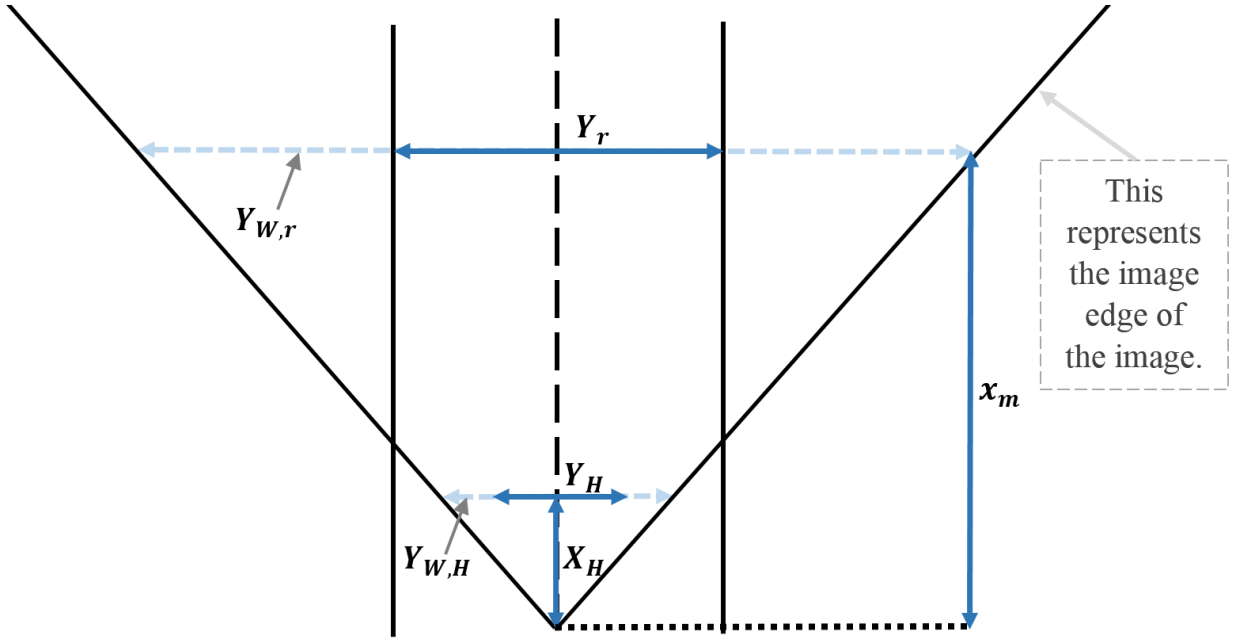

Figure A–2: The physical geometry. All distances in this figure are in units of m. Refer to Fig. 2.3 which displays the measured physical geometry (i.e., X_h and Y_H).

Substituting Eq. A5 into Eq. A4 gives

$$\frac{Y_H W}{P_H X_H} = \frac{Y_r Q}{H_s x_m}. \tag{A6}$$

If it is assumed that the calculated vanishing point is centred about W, then

$$\tan\beta = \frac{Q}{W/2} \Rightarrow \frac{\tan\beta}{2} = \frac{Q}{W}. \tag{A7}$$

and the following distance in physical units can be expressed as

$$x_m = \frac{Y_r P_H X_H \tan\beta}{2 Y_H H_s}. \tag{A8}$$

Since $H_s = H_v - H_f - H_H$, x_m can be written as

$$x_m = \frac{Y_r P_H X_H \tan\beta}{2 Y_H (H_v - H_f - H_H)}. \tag{A9}$$

Finally, since x_m is defined as the distance between the measurement location (i.e., the sonic anemometer) and the back end of the target vehicle (i.e., its shadow), the measured distance between the dashcam and the anemometer ($\approx X_H$) needs to be removed from Eq. A9, giving

$$x_m = \frac{Y_r P_H X_H \tan\beta}{2Y_H(H_v - H_f - H_H)} - X_H. \quad \text{(A10)}$$

In Eq. A10, Y_r is estimated from a Google Earth satellite. Since the terrain was generally flat and the dashcam was adhered to the windshield, a single calibration image is used to determine the pixel values of H_v, H_H, P_H and β. Physically, H_H includes the distance between the dashcam and the vehicle's front end, and some of the highway surface immediately in front of the vehicle (it cannot be seen by the dashcam). Therefore, H_H places a lower limit on the domain of x_m. To determine the target distance H_f, automated software was developed to locate the step change in greyscale values between the sunlit highway surface and the shadow behind the vehicle. It should be noted that Eq. A10 approaches infinite distance near the horizon (i.e., as $H_f + H_H \to H_v$), and therefore a small error in the pixel location near the horizon results in a large error in the following distance. Consequently, the measurement domain is limited to a maximum following distance of 100 m to limit error related to image resolution (except Sect. 2.5). Equation A10 was tested in a parking lot using distances measured up to 70 m. The results determined from Eq. A10 were generally within ± 1 m of the measured distances.

Appendix B: Meteorological measurements obtained near Highway 400

Table B1: Stationary measurements obtained near Highway 400 during this study. Shown is the stop identifier (see Fig. 2.2 for the geographic location) and the date and time of the measurements. T is the averaging period used to calculate the mean wind at a height of 1.7 m ($\overline{u}_{1.7}$), the wind direction ($\gamma_{1.7}$) and the turbulent kinetic energy (e). Also shown are the longitudinal, lateral, and vertical turbulent velocity variances, $\overline{u'^2}$, $\overline{v'^2}$ and $\overline{w'^2}$ respectively.

Stop	Date	Time	T (min)	$\overline{u}_{1.7}$	$\gamma_{1.7}$	$\overline{u'^2}$	$\overline{v'^2}$	$\overline{w'^2}$	e
			(min)	(m s^{-1})	(° true)	(m^2 s^{-2})	(m^2 s^{-2})	(m^2 s^{-2})	(m^2 s^{-2})
Stop 1	12 July	10:39:00	15	1.09	170	0.78	1.65	0.29	1.36
Stop 2	12 July	12:05:30	30	2.54	170	0.73	1.28	0.13	1.07
Stop 3	12 July	13:18:00	15	2.52	150	1.03	1.06	0.21	1.15
Stop 3	14 July	10:46:00	30	1.71	180	0.73	0.85	0.17	0.88
Stop 3	15 July	10:26:00	15	2.21	290	1.43	1.73	0.32	1.74

Appendix C: Details related to the spectra presented in Fig. 2.8

Table C1: Details related to the spectra presented in Fig. 2.8. Units are not shown in the table. x_m is the following distance (m), V is the vehicle speed (m s^{-1}), u_s is the wind speed parallel to vehicle motion (m s^{-1}), $\overline{u_s'^2}$, $\overline{v_r'^2}$, and $\overline{w_r'^2}$ are the longitudinal, lateral and vertical velocity variances respectively and e is the turbulent kinetic energy. Averages, corresponding to the 1–min spectra, are denoted by overbars.

Case	Description	x_m	$\overline{V}$	$\overline{u_s}$	$\overline{u_s'^2}$	$\overline{v_r'^2}$	$\overline{w_r'^2}$	e
		(m)	(m s^{-1})	(m s^{-1})	(m^2 s^{-2})	(m^2 s^{-2})	(m^2 s^{-2})	(m^2 s^{-2})
A	Behind HD–B	$4.0h \le x_m \le 7.3h$	26.3	–9.61	4.93	5.18	2.75	6.43
B	Behind HD–B	$11h \le x_m \le 18h$	27.2	–7.44	2.66	2.46	1.59	3.36
C	Behind bus	$5.0h \le x_m \le 9.0h$	25.9	–1.82	5.30	3.40	2.57	5.64
D	Behind car	$13h \le x_m \le 20h$	27.8	–4.36	2.42	1.57	0.84	2.42
E	Isolated	—	13.7	2.31	1.56	1.23	0.17	1.48
F	Isolated	—	21.5	1.90	1.22	1.08	0.16	1.23
G	Isolated	—	30.7	–2.14	1.70	1.09	0.13	1.46

Appendix D: Figures and tables relevant to Chapter 3

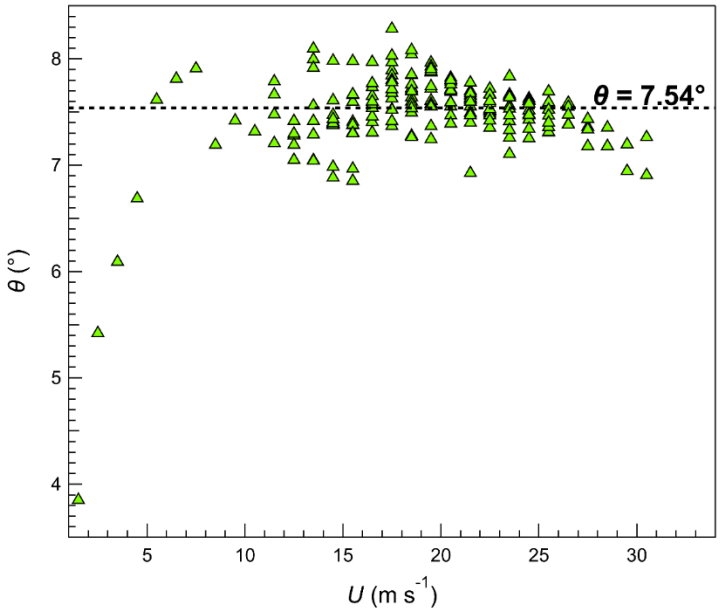

Figure D1: The flow distortion correction angle calculated for each binned value shown in Fig. 3.3. The dashed black line shows the median value of the set.

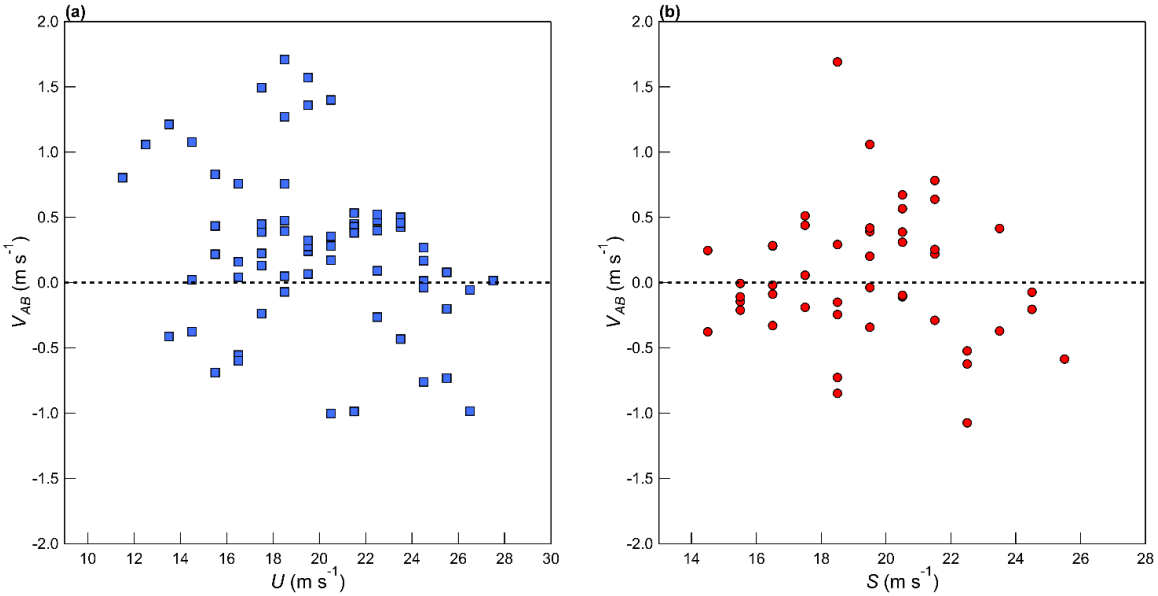

Figure D2: (a) The measured lateral velocity V_{AB} plotted as a function of the measured U; (b) the measured lateral velocity V_{AB} plotted function of the vehicle speed (S). Measurements are binned using a bin size of 1 m s^{-1}. Data shown are for both 20 and 22 Aug.

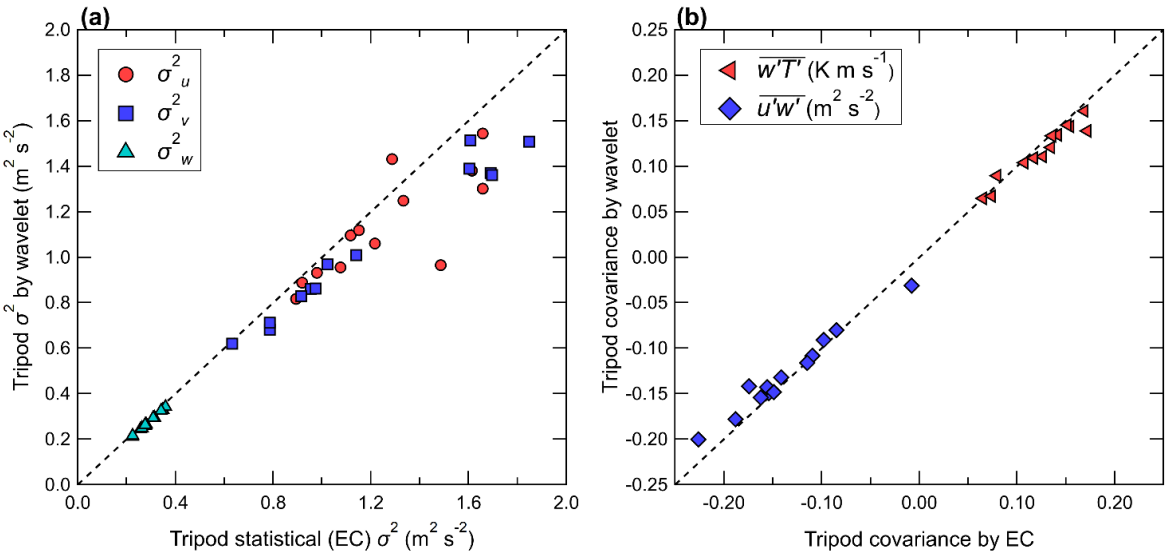

Figure D3: A comparison of the (a) velocity variances and (b) covariances measured on the tripod, using two calculation methods: the variances and covariances are calculated with eddy–covariance (x–axis) or wavelet analysis (y–axis). All passes from 20 and 22 Aug are included, and calculations are done as in Fig. 3.7. However, wavelet analysis is completed using the Mexican hat analyzing wavelet instead of the Morlet analyzing wavelet. The Morlet analyzing wavelet is not used since some passes would include edge effects in the calculation of variances and covariances, since the tripod record was ended soon after the final vehicle pass on both 20 and 22 Aug.

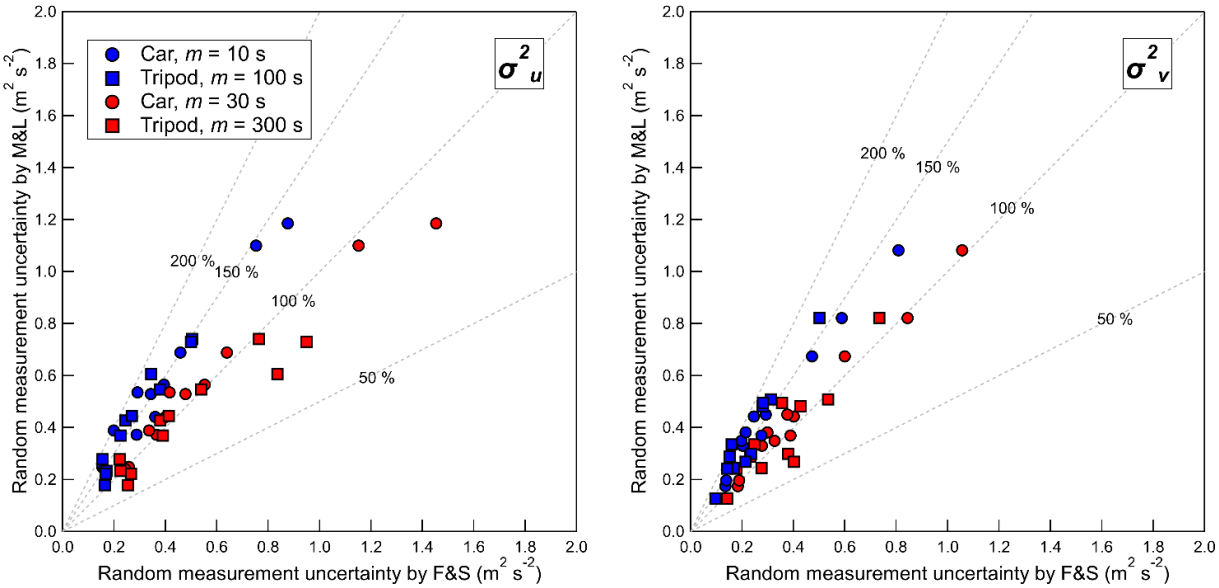

Figure D4: A comparison of uncertainty estimate by F&S and M&L of the horizontal velocity variances for two choices of parameter *m*: (1) car uses *m* = 10 s and the tripod uses *m* = 100 s and (2) the car uses *m* = 30 s and the tripod uses *m* = 300 s.

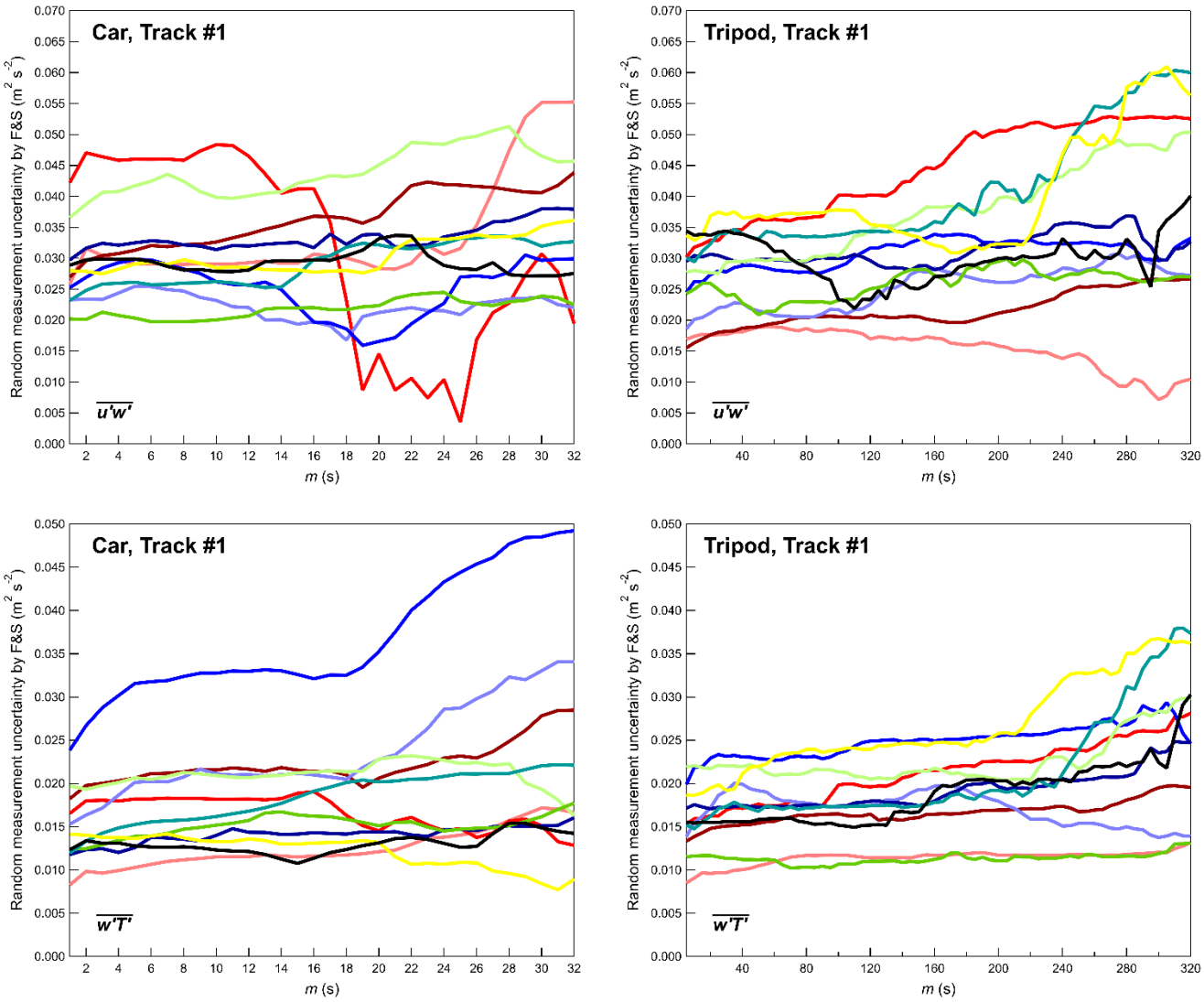

Figure D5: The uncertainty calculated using F&S (i.e., Eq. 3.17) as a function of parameter *m*. Tripod measurements are shown in the right panel and mobile car measurements are shown in the left panel.

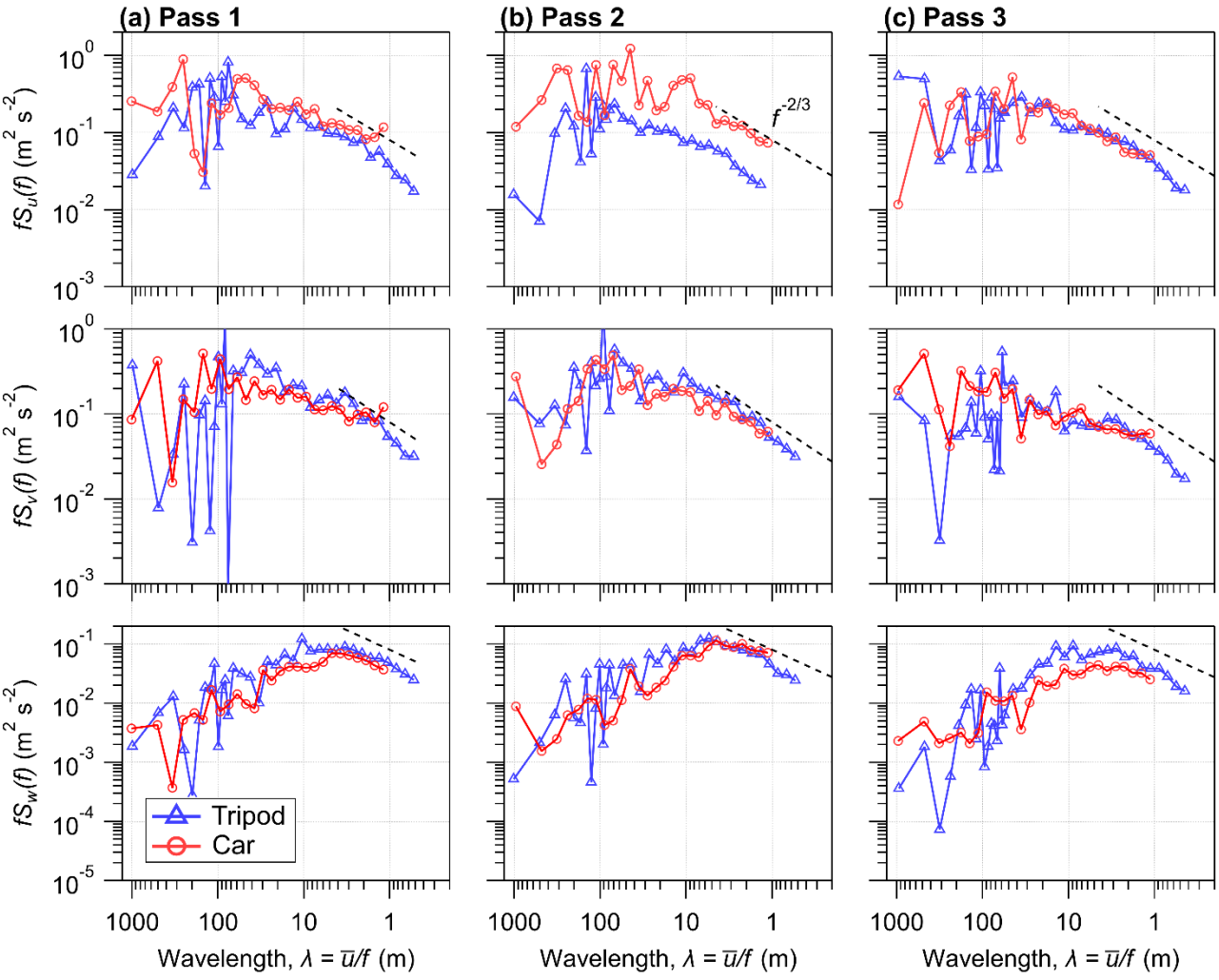
(a) Pass 1
(b) Pass 2
(c) Pass 3
$fS_u(f)$ (m^2 s^{-2})
$fS_v(f)$ (m^2 s^{-2})
$fS_w(f)$ (m^2 s^{-2})
$f^{-2/3}$
Tripod
Car
Wavelength, $\lambda = \overline{u}/f$ (m)

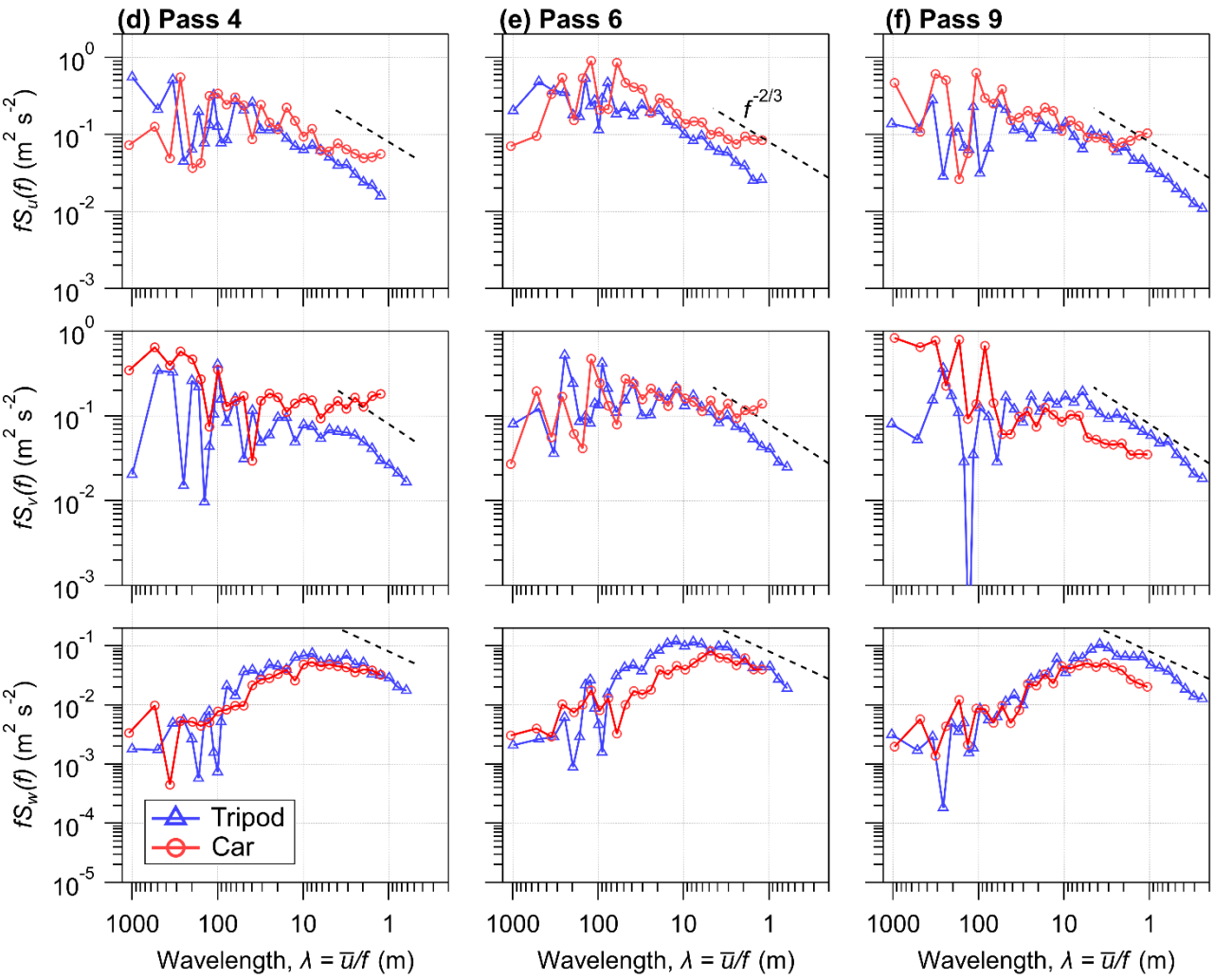

Figure D6: Spectra of u (top), v (middle) and w (bottom) measured on some additional measurement passes of Track #1.

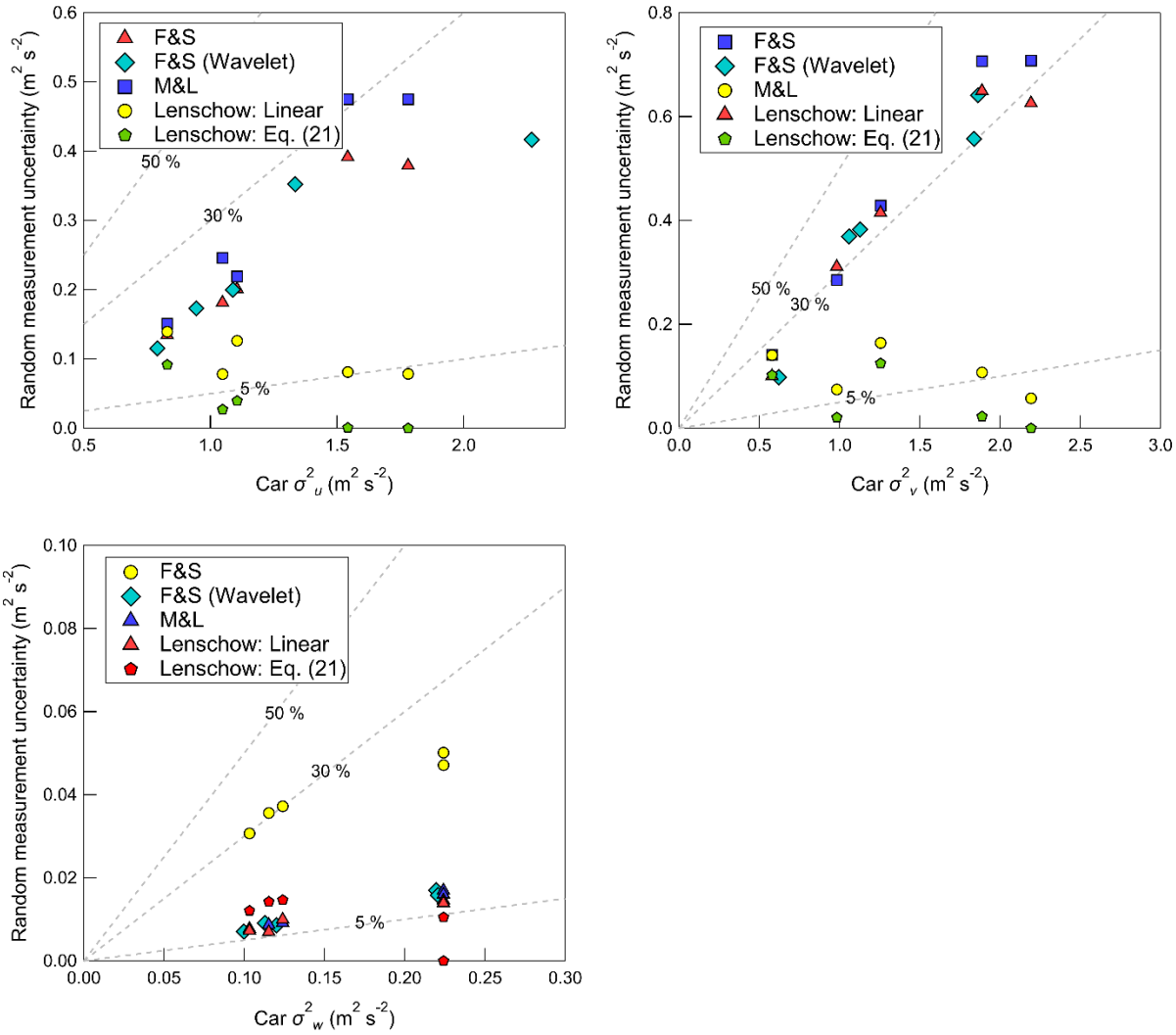

Figure D7: Random measurement uncertainty as a function of the measured velocity variances while driving on a gravel road.

Table D1: Statistics calculated over all passes in Track #1 only.

	MBE_{EC}	MBE_W	$RMSE_{EC}$	$RMSE_W$	$Mean_{EC}$ Car	$Mean_W$ Car	$Mean_{EC}$ Tripod
$\overline{u'^2}$ (m² s⁻²)	0.48	0.37	0.85	0.70	1.74	1.63	1.26
$\overline{v'^2}$ (m² s⁻²)	0.23	0.07	0.55	0.38	1.36	1.19	1.18
$\overline{w'^2}$ (m² s⁻²)	–0.10	–0.10	0.10	0.11	0.18	0.17	0.29
$\overline{u'w'}$ (m² s⁻²)	0.01	0.03	0.07	0.07	–0.13	–0.11	–0.14
$\overline{w'T'}$ (K m s⁻¹)	–0.05	–0.05	0.06	0.06	0.07	0.08	0.13
$\bar{u}$ (m s⁻¹)	0.15	—	0.43	—	2.54	—	2.42

Table D2: Statistics calculated over all passes in Track #2 only.

	MBE_{EC}	MBE_{W}	RMSE_{EC}	RMSE_{W}	Mean_{EC} Car	Mean_{W} Car	Mean_{EC} Tripod
$\overline{u'^2}$ ($m^2\ s^{-2}$)	1.26	0.51	1.79	0.79	2.50	1.74	1.26
$\overline{v'^2}$ ($m^2\ s^{-2}$)	0.23	0.07	0.63	0.44	1.40	1.23	1.20
$\overline{w'^2}$ ($m^2\ s^{-2}$)	–0.11	–0.11	0.13	0.13	0.17	0.16	0.29
$\overline{u'w'}$ ($m^2\ s^{-2}$)	–0.001	0.02	0.09	0.09	–0.13	–0.11	–0.14
$\overline{w'T'}$ (K $m\ s^{-1}$)	–0.04	–0.03	0.05	0.05	0.08	0.09	0.13
$\bar{u}$ ($m\ s^{-1}$)	–0.01	—	0.71	—	2.36	—	2.40

Table D3: Turbulence statistics measured on the instrumented car during the 1000 m track.

Track 1	**1**	**2**	**3**	**4**	**5**	**6**	**7**	**8**	**9**	**10**	**11**
Statistics on instrumented car: 1000 m track											
I_u **(s)**	1.11	0.69	0.64	0.68	0.99	0.55	2.25	2.06	1.88	1.34	1.01
I_v **(s)**	0.82	1.32	1.72	1.60	0.60	0.43	1.29	1.03	3.33	1.72	1.20
I_w **(s)**	0.11	0.07	0.09	0.08	0.06	0.12	0.04	0.12	0.06	0.05	0.14
I_{uw} **(s)**	0.07	0.05	0.08	0.14	0.08	0.03	0.04	0.02	0.06	0.04	0.04
I_{wt} **(s)**	0.10	0.04	0.11	0.06	0.13	0.04	0.04	0.08	0.05	0.03	0.03
$\lvert R_{uw} \rvert$	0.24	0.24	0.35	0.30	0.30	0.20	0.18	0.19	0.17	0.16	0.27
$\lvert R_{wT} \rvert$	0.34	0.23	0.32	0.25	0.31	0.24	0.21	0.17	0.30	0.15	0.24
T **(s)**	48	48	48	49	57	49	42	41	51	41	40
$\bar{S}$ **(m s^{-1})**	20.5	20.7	20.9	20.4	17.5	20.4	23.8	24.1	19.5	24.4	25.2

Table D4: Turbulence statistics measured on the tripod corresponding to the 1000 m track.

Track 1	**1**	**2**	**3**	**4**	**5**	**6**	**7**	**8**	**9**	**10**	**11**
Statistics on tripod, period corresponding to 1000 m track											
I_u **(s)**	4.58	3.94	25.2	21.7	12.0	9.78	6.19	11.1	11.6	14.1	12.6
I_v **(s)**	10.6	3.62	16.0	10.5	16.1	5.14	14.8	3.60	8.38	23.7	8.93
I_w **(s)**	0.66	0.59	0.44	0.44	0.47	0.44	0.30	0.39	0.25	0.28	0.31
I_{uw} **(s)**	0.40	0.42	0.42	0.41	0.42	0.33	0.20	0.37	0.19	0.15	0.21
I_{wt} **(s)**	0.30	0.26	0.44	0.41	0.33	0.25	0.24	0.25	0.22	0.27	0.21
$\lvert R_{uw} \rvert$	0.26	0.29	0.24	0.30	0.01	0.25	0.18	0.37	0.23	0.26	0.17
$\lvert R_{wT} \rvert$	0.42	0.36	0.36	0.40	0.20	0.42	0.33	0.48	0.32	0.29	0.33
T **(s)**	420	420	420	360	300	360	480	360	420	480	420

Appendix E: Figures and tables relevant to Chapter 4

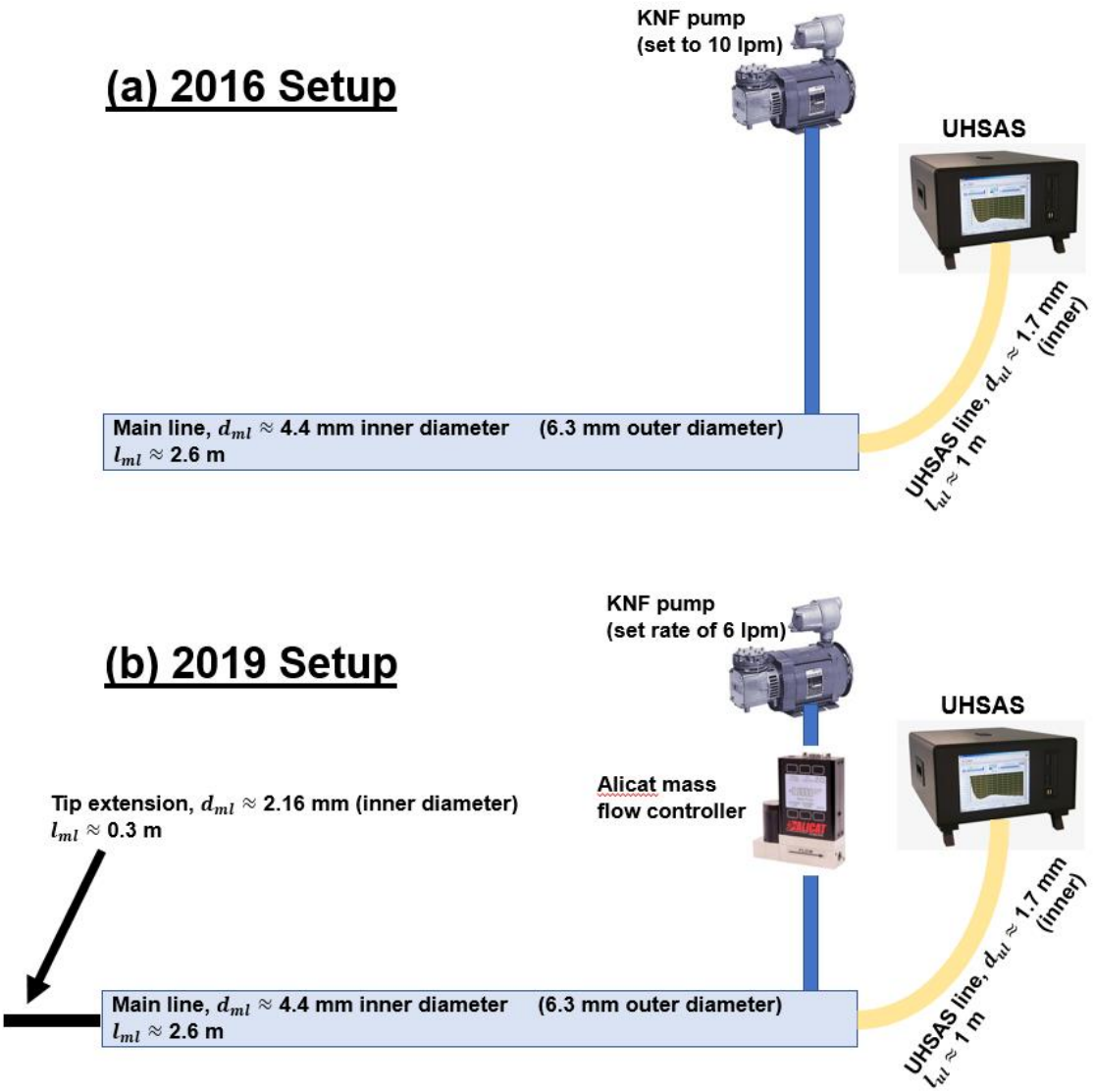

Figure E1: The aerosol sampling setup in (a) 2016 and (b) 2019. Some important points: (1) 2019 had a filter before the flow controller, but it is not shown in (b), and (2) the main line shown in the figure has no curvature, but in reality there was about a 30° curvature over its entire length, since the UHSAS sampled from the passenger window, but the main line had an entrance at the vehicle's centerline. We estimate the curvature to be about 30°. This curvature has been considered in the particle loss calculation shown in Fig. S2.

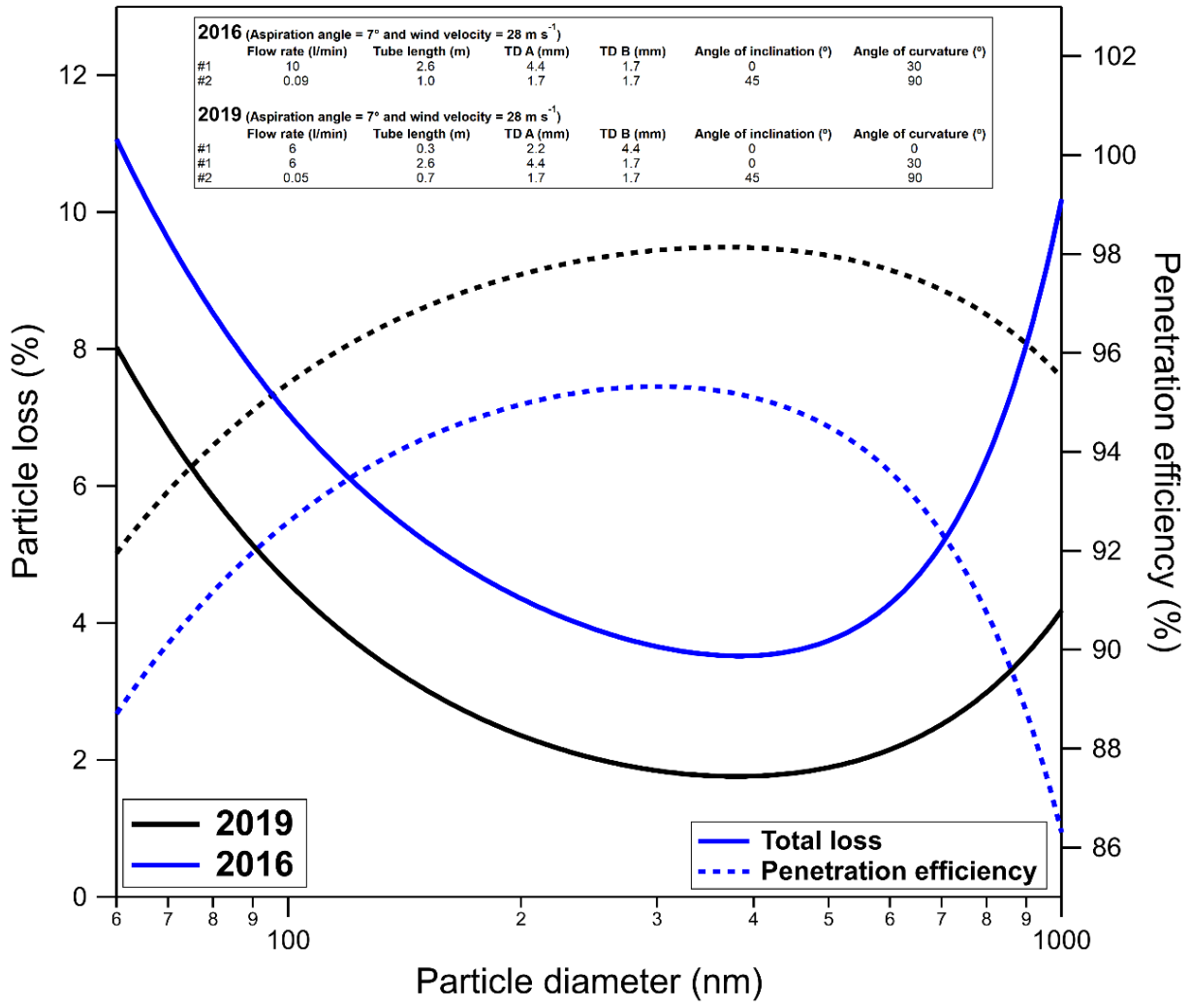

Figure E2: The particle loss and penetration efficiency for the 2016 and 2019 study calculated from the particle loss calculator provided by von der Weiden et al. (2009). Parameters used for particle loss and penetration efficiency estimations are given in the figure. Penetration efficiency includes losses from gravitation settling (i.e., sedimentation) and diffusion to the walls of the tube.

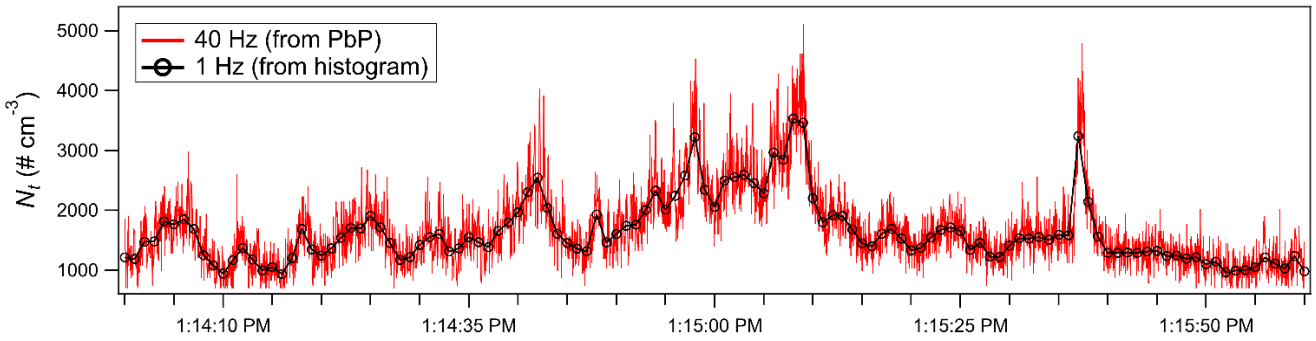

Figure E3: Example of a 40 Hz time series generated by the particle–by–particle data. Also shown is the total 1 s count from the histogram record.

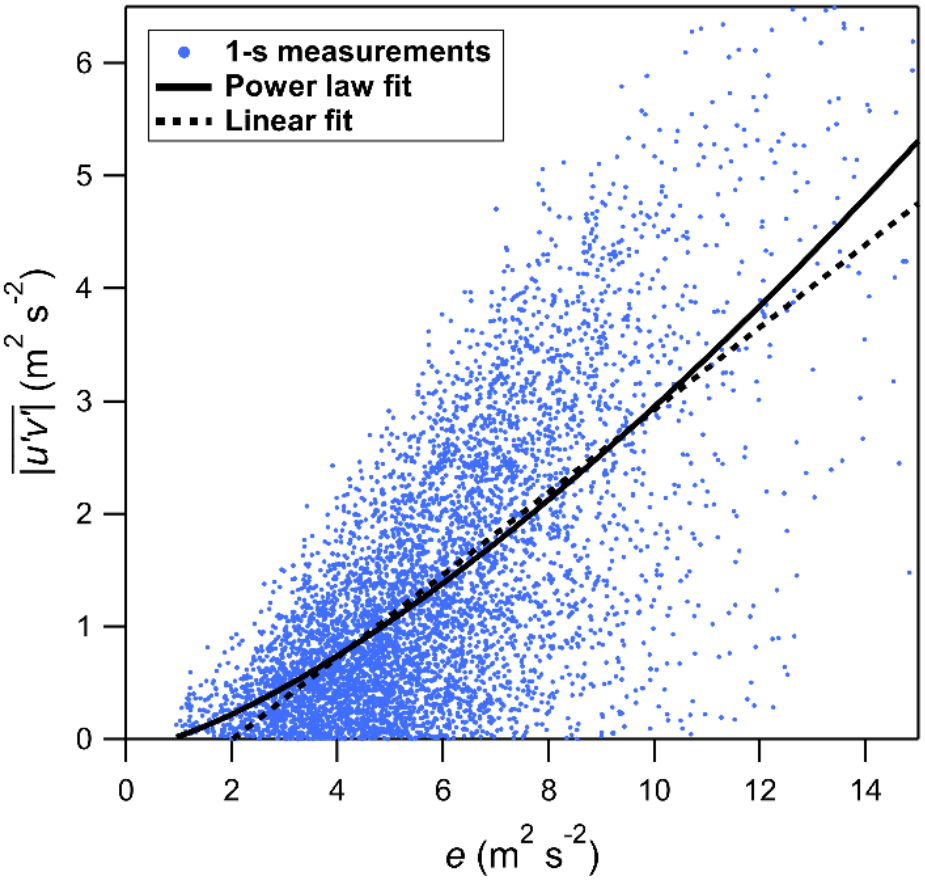

Figure E4: A scatter plot of the absolute value of the 1 s horizontal turbulent momentum ($|\overline{u'v'}|$) flux plotted as a function of the turbulent kinetic energy (e). A linear least squares fit and a power law fit are superimposed. Measurements are TE–HDVs.

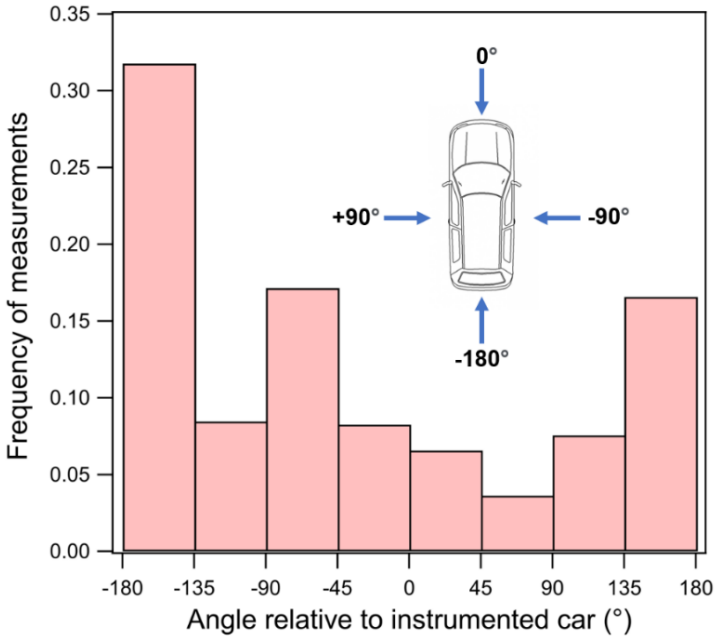

Figure E5: A histogram of the estimated ambient wind impact direction on the instrumented car. Impact angles (∅) are calculated by assuming a single wind direction for each daily measurement record, and using the GPS recorded vehicle heading to estimate ∅. There is a relatively large uncertainty in these calculations since the wind direction varied over each measurement day and there were most probably localized flow variations that are not accounted for in this analysis. This precludes binning according to ∅ using a bin size less than 30 deg. ∅ = 0° implies ambient flow toward the vehicle's front end, ∅ = –90° implies ambient flow toward the vehicle's passenger side, ∅ = –180° implies ambient flow toward the vehicle's backend and ∅ = 90° implies ambient flow toward the vehicle's driver side. Measurements are TE–HDVs.

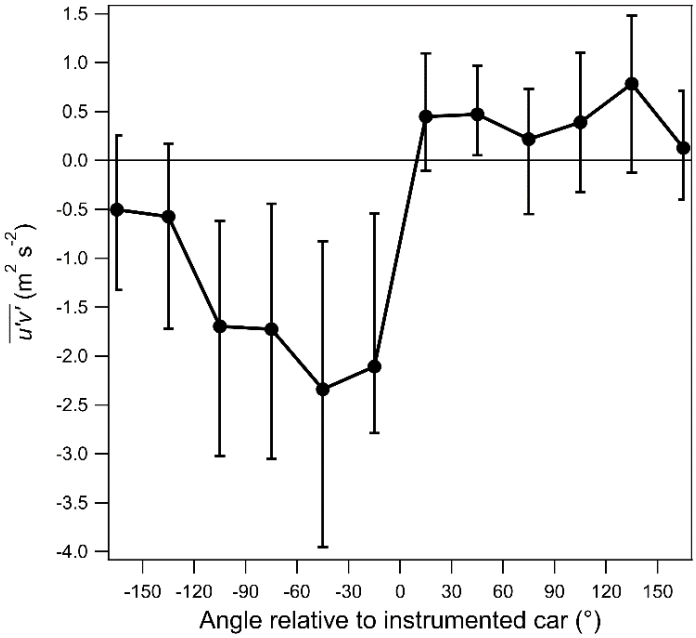

Figure E6: The 1 s horizontal turbulent momentum flux ($\overline{u'v'}$) binned according to the ambient wind impact direction. See Fig. S3 for for graphical description of the meaning of the angles. Measurements are TE–HDV.

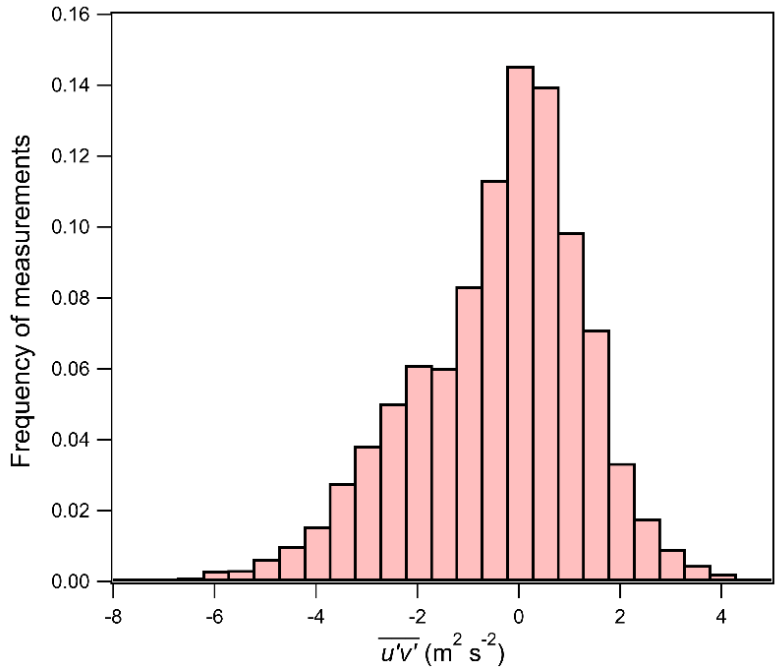

Figure E7: Histogram of the 1 s horizontal turbulent momentum flux ($\overline{u'v'}$) measured behind TE–HDV.

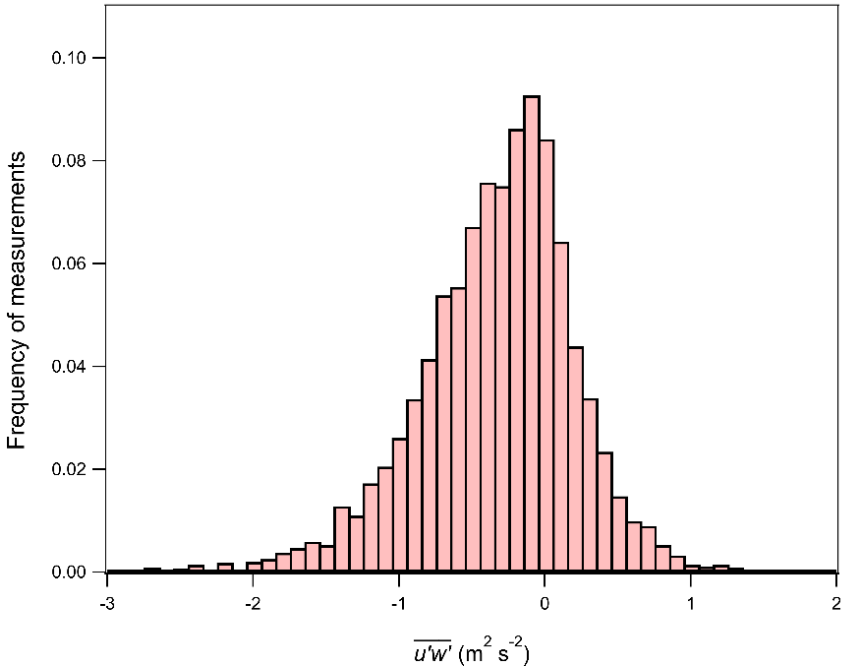

Figure E8: Histogram of the 1 s vertical turbulent momentum flux ($\overline{u'w'}$) measured behind TE–HDV.

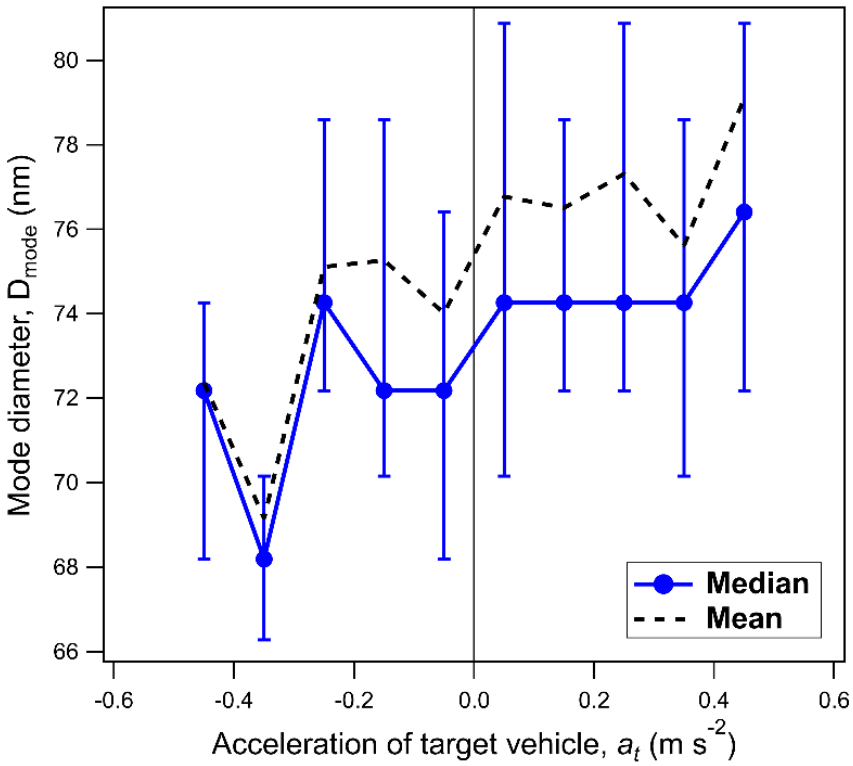

Figure E9: The measured mode diameter behind the commercial bus, binned according to the estimated acceleration of the commercial bus, identical to Fig. 4.

Table E1: Parameters describing the aerosol sampling setup used in 2016 and 2019. Refer to Fig. E1.

Line	Inner diameter, d_i (mm)	Length, L	Flow velocity, U (m s^{-1})	Travel time (s)	Volumetric flow rate, Q (m^3 s^{-1})	Reynolds number	Regime
2016							
Main	4.4	2.6	11	0.2	1.7×10^{-4}	3200	Transition
UHSAS	1.7	1.0	0.7	1.4	1.5×10^{-6}	80	Laminar
2019							
Tip	2.2	0.3	26	0.01	1.0×10^{-4}	3800	Transition
Main	4.4	2.6	6.6	0.4	1.0×10^{-4}	1900	Laminar
UHSAS	1.7	0.7*	0.4	1.8	8.3×10^{-7}	50	Laminar

***The UHSAS tubing length has shortened over time from each successive experiment**

Appendix F: Figures and tables relevant to Chapter 5

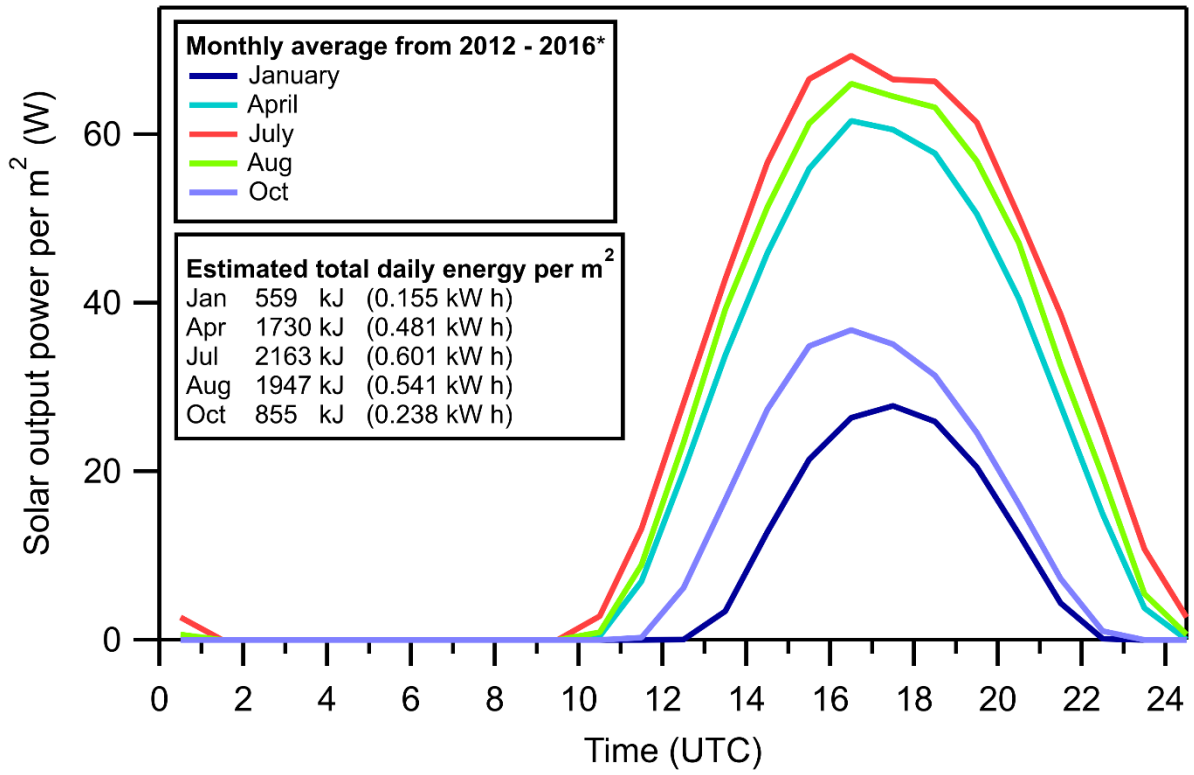

Figure F1: The solar power calculated using the average downwelling shortwave irradiance measured during different months, using data from 2012 to 2016. The data are from the York University Earth and Space Science Meteorological Observation Station (EMOS, 2016). Also shown is the estimated total daily energy per m^2 area, as determined by integrating the solar output power over all hours. The solar output power is calculated as $P_s = A_s(I_{dw})E_s$, where I_{dw} is the downwelling shortwave irradiance (W m^{-2}), A_s is the area of the solar panel (here set to 1 m^2), and E_s = 0.1 is the efficiency of the solar panel.